SEISMIC PERFORMANCE EVALUATION OF PORT CONTAINER CRANES ALLOWED TO UPLIFT

A Thesis
Presented to
The Academic Faculty

by

Benjamin David Kosbab

In Partial Fulfillment
of the Requirements for the Degree
Doctor of Philosophy in the
School of Civil and Environmental Engineering

Georgia Institute of Technology
May, 2010

SEISMIC PERFORMANCE EVALUATION OF PORT CONTAINER CRANES ALLOWED TO UPLIFT

Approved by:

Dr. Reginald DesRoches, Advisor
School of Civil and Environmental Engineering
Georgia Institute of Technology

Dr. Glenn J. Rix
School of Civil and Environmental Engineering
Georgia Institute of Technology

Dr. Roberto T. Leon
School of Civil and Environmental Engineering
Georgia Institute of Technology

Dr. Donald White
School of Civil and Environmental Engineering
Georgia Institute of Technology

Dr. Alan Erera
School of Industrial and Systems Engineering
Georgia Institute of Technology

Date Approved: 3/30/2010

ACKNOWLEDGEMENTS

A wise man once said that if you read something at face value, then you're missing the point. I believe that to be true. In the literal sense, that means that a much closer reading "between the lines" of this document will reveal a much more interesting story than a purely sequential reading might provide. I leave it to the fervent and meticulous reader to untangle that yarn. However, the casual reader can interpret this in a more figurative sense, and understand that the writing of this document represents the contributions, tangible or otherwise, of many individuals besides myself. Although I certainly can not fully thank them in these few pages, their contributions to my journey through graduate school should be recognized.

First, I truly appreciate all of the guidance, support, opportunity, and insight provided by my graduate advisors, Dr. Reginald DesRoches and Dr. Roberto Leon. While my patience with this process has at times been underwhelming, they convinced me that I could and would reach the finish line. Nearing it now, I recognize the generosity with which they offered their limited time to advise me through this experience.

The other members of my graduate committee, Drs. Glenn Rix, Donald White, and Alan Erera, deserve thanks for their insights and critical assessment. They have been instrumental in shaping the scope and outcomes of this work, and challenged me to uncover some intriguing wrinkles that I might have overlooked on my own.

My time at Georgia Tech has been fruitful and rewarding, made possible by support from the National Science Foundation and the Georgia Tech Institute Fellowship fund. Their generous support enabled me to comfortably pursue my graduation education as the sole professional focus during my tenure as a graduate student. Additionally, the Network for Earthquake Engineering Simulation has provided immeasurable and unique opportunities for travel, growth, and development for which I am indebted.

Fortunately, the department of Civil and Environmental Engineering has a wealth of excellent graduate students which have made my time here memorable from a personal level as well. My colleagues here have challenged me to live and grow beyond the confines of technical research. Thanks to my great officemates from Mason 325: Monique, Jamie, Masahiro, Suzanne, Jazalyn, and Niki. A special note of appreciation goes to Laura, who showed tremendous patience throughout her invaluable contributions, without which this work would not have been complete. Thanks also to my other friends in the department who always brought much-needed smiles and laughter: Robert, Jonah, Amal, Jun, Matthew, Abdollah, Karthik, Jonathan, Andrew, and countless others.

To my family, I am truly grateful for the unconditional support you have provided and for the perspectives on reality that have served me well throughout my life. The foundation and grounding you have provided me is the best gift you could give. Finally, to my dearest wife Beth, you are a saint through and through. Your enduring and selfless love, confidence, and patience have made this journey possible and worthwhile. Thank you.

TABLE OF CONTENTS

LIST OF TABLES

LIST OF FIGURES

SUMMARY

The seismic behavior of port container cranes has been largely ignored–by owners, operators, engineers, and code officials alike. This is despite their importance to daily port operations, where historical evidence suggests that port operational downtime following a seismic event can have a crippling effect on the affected local, regional, and national economies. Because the replacement time in the event of crane collapse can be a year or more, crane collapse has the potential to be the "critical path" for post-disaster recovery. Since the 1960's, crane designers allowed and encouraged an uplift response from container cranes, assuming that this uplift would provide a "safety valve" for seismic loading; i.e. the structural response at the onset of uplift was assumed to be the maximum structural response. However, cranes have grown much larger and more stable such that the port industry is now beginning to question the seismic performance of their modern jumbo container cranes.

This research takes a necessary step back, and reconsiders the fundamental effect that uplift response has on the seismic demand of portal-frame structures such as container cranes. One primary objective of this work is to develop methodologies for realistically modeling this effect, and to serve as a foundation for the design and evaluation of new and existing container cranes. Portal uplift theory, derived here to meet that objective, is a major contribution. Using this unique new theoretical tool to estimate the dynamic structural demand during seismically-induced uplift events, the "safety valve" design assumption for container cranes is found to be unconservative. With implications to all

structures which exhibit reduced shear stiffness during uplift events, portal uplift theory is verified with detailed finite element models incorporating frictional contact elements and experimental shake-table testing of a scaled jumbo container crane allowed to uplift.

Understanding that container cranes may be subjected to higher seismic demands than expected, characterizing their risk is critical. Thus, using the verified models developed in this work, fragility curves and downtime estimates are developed for three representative container cranes to provide insight into their seismic vulnerability. These fragility curves are conditional probability statements which describe the potential for exceeding certain damage thresholds during an earthquake of a given intensity. Throughout the analysis, appropriate levels of uncertainty and randomness are evaluated and propagated. Because the damage levels are defined globally and according to specific repair models, probabilistic estimates of the operational downtime due to a given earthquake are also developed. The results indicate that existing container cranes, especially stout cranes and those not specifically detailed for ductility, are not expected to achieve the seismic performance objectives of many ports. Due to their potential for damage and/or collapse, container cranes designed using previous and current standards can significantly contribute to port seismic vulnerability. To address this deficiency, performance-based design recommendations are provided which encourage the comparison of demand and capacity in terms of the critical portal deformation, using the derived portal uplift theory to estimate seismic deformation demand. Simplified methods and basic design factors are proposed and demonstrated which enable practitioners to conveniently design for reliable achievement of seismic performance objectives.

CHAPTER 1

INTRODUCTION AND MOTIVATION

1.1 Motivation

1.1.1 Port Vulnerability

Earthquakes pose a significant threat to the largest of US seaports such as Los Angeles, Long Beach, Seattle, Oakland, Charleston, Savannah, and others, which serve as critical gateways for international trade (Figure 1.1). As the world's largest trading nation, the US economy is exceedingly vulnerable to significant damage at one of its critical ports.

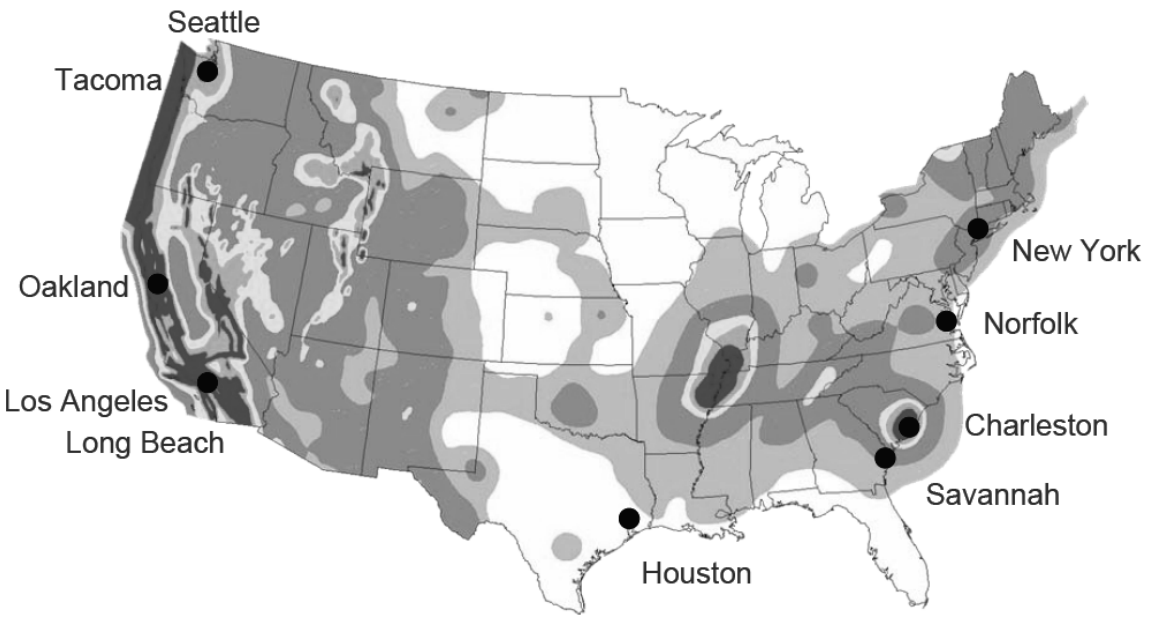

Figure 1.1. Many of the largest container ports in the US are vulnerable to seismic damage, as they are inconveniently located in areas of high seismic hazard.

Ports have received little attention compared with other infrastructure systems (i.e., buildings, bridges, water and power), despite their economic importance; a 2002 10-day

labor lockout at west coast ports cost the national economy an estimated $1 billion daily [1]. Historically, one needs to look no further than the 1995 Hyogoken-Nanbu earthquake, which heavily damaged the Port of Kobe, to see the lasting economic effects of heavy port damage. While the port struggled to perform repairs, shipping companies were forced to continue their shipping operations elsewhere. With little incentive for shipping companies to return, the Port of Kobe never recovered to full pre-earthquake container traffic volume [2]. Thus, a city struggling to rebuild after a devastating earthquake had to also deal with a drastically reduced economic base. In the US, where container traffic is expected to continue growing, protecting the nation's ports should be a paramount concern.

Heavy damage to a port can also greatly hamper emergency response in many parts of the world. For example, the port in Port-au-Prince, Haiti was nearly destroyed during the devastating earthquake of January 12, 2010 which left much of the city in ruins and injured or killed hundreds of thousands of people. International emergency response was severely limited by the inability to get humanitarian aid supplies, including medical supplies and food, into the crippled country. With the port out of commission, the small Haiti airport was the only major avenue for receiving goods, and was quickly overwhelmed. Over 50% of the port was destroyed, including the only true container terminal, leaving the sole container crane partially submerged in water, as shown in Figure 1.2 [3]. Two weeks after the earthquake, limited supplies were being ferried in to the port, but only at about 10% of pre-earthquake capacity [4]. As of February 12, 2010, salvage and harbor-clearing teams were still working to clear dangerous debris out of the

port, including the sole container crane, in order to bring in floating piers for longer-term operations [5].

Figure 1.2. Partially submerged container crane at the port in Haiti following the January 12, 2010 earthquake. Photo courtesy of Glenn Rix [3]

What makes ports particularly vulnerable to crippling damage from earthquakes is the fact that they are a system of systems. The successful daily operation of a port is dependent on a number of intertwined elements. Poor performance of one element can cause the entire system to perform inadequately, or not at all. In the case of earthquake response, a port's performance is tied to a number of sub-system responses depicted in Figure 1.3: soil, piles, wharf, and crane. The interdependency in a port system in a post-disaster environment cannot be ignored.

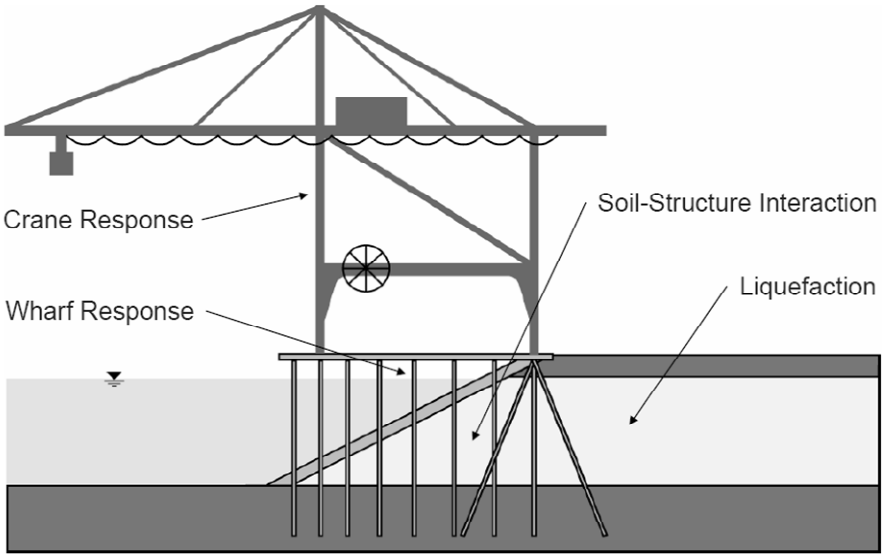

Figure 1.3. Relevant responses to a port's seismic performance.

1.1.2 Container Crane Vulnerability

One of the most vulnerable components of a port is the container crane stock that plays the crucial role of loading and unloading container ships. At most ports, container cranes are the sole means of ship-to-shore (STS) operations. However, the seismic performance of container cranes has been largely ignored. The premier and comprehensive port seismic design guide [6], published by the International Navigation Association (PIANC), acknowledges that container cranes are crucial to continued operation of container ports after a seismic event, and that they may be vulnerable to different levels of potentially large damage. However, little is said relative to ensuring adequate performance of the container crane themselves, but rather guidelines are offered to suggest designs which are sensitive to the requirements of the container cranes. All said, only 6 of 474 pages of those provisions directly apply to container cranes.

In the US, the situation is perhaps worse, due to a perceived sense of security. Based on the limited number of past seismic events impacting ports, the ASCE publication, *Seismic Guidelines for Ports* [7], suggest that container cranes generally perform well during earthquakes. It is reported that normally, cranes are strong enough that they will uplift before the structure fails, and that this tipping limits the internal forces in the structure. However, because container cranes have been rapidly growing in size [8], it has been recently suggested in the industry that many newer cranes may actually be damaged or fail prior to uplifting because their larger gage length makes them more stable and resistant to uplifting yet they have been designed without a similar increase in strength [9, 10]. While this is certainly a concern, there is in fact a more fundamental problem: the understanding of uplift response of container cranes and its effect on internal forces underlying the typical design assumption has been simplistic and incomplete. The upshot is that container cranes have been designed based on an assumption of performance [10] that is no longer, or may never have been, valid.

The Port of Los Angeles, the largest container port in the US, uses well-developed performance-based design guidelines for the seismic design of port structures [11]. In fact, container cranes are explicitly considered. It is required that cranes are not damaged by an operating level earthquake, and should not collapse due to an ultimate level earthquake, yet no guidelines are provided for how to ensure these performance requirements can be met. Further, more importance seems to be placed on the potentially detrimental effect that the presence of a crane can have on wharf behavior. Still, the fact that container cranes are beginning to be recognized indicates that port stakeholders are

beginning to understand the potential risk associated with their poor performance. Other ports, such as Oakland and Tacoma, appear to be considering the addition of crane criterion in their own design guidelines as well [10], but there appears to be no realistic and thorough treatment, existing or on the horizon, that deals with the specific design concerns related to container cranes.

This apparent neglect is in spite of the fact that container crane performance is especially critical to post-earthquake downtime. Container cranes, in contrast to built-on-site structures, are built abroad and sent via ship to their home port, leading to replacement times often much longer than the rebuilding of other damaged port components. While an individual crane is relatively inexpensive, the indirect losses and effect on post-disaster recovery caused by damaged cranes can be staggering. The extensive damage to container cranes at Kobe after the earthquake of 1995–in the form of local buckling of plates and stiffeners, global buckling of legs, and derailment [12], shown in Figure 1.4–is thought to have played a large role in the port's decline.

Figure 1.4. Container crane damage at the Port of Kobe, 1995. White, grey, and black arrows indicate derailment, local buckling, and collapse, respectively.

With these ideas in mind, understanding the performance of container cranes during earthquakes is critical. Despite this, most port owners would agree that the seismic performance of container cranes has been largely ignored. In fact, many port stakeholders are still unaware of the potential vulnerability of cranes or how crane damage can affect the overall port system vulnerability.

1.2 Scope

1.2.1 Problem Statement

The observed port performance during the Kobe earthquake, as well as other minor events, provides a general idea as to the seismic vulnerability of container cranes. While ideas exist about the general seismic response of container cranes, little work has been done to rigorously understand the observed behavior or quantify the vulnerability. Currently, no known method exists or has been applied to accurately model or design a container crane realistically considering the complicated uplift response. In order to develop more resilient ports, a better understanding of the dynamic behavior of container cranes is required, especially regarding the effect of uplift on seismic demand.

1.2.2 Objectives

In order to address the problem statement, several objectives are defined for this research. The objectives are to:

- Identify the critical response of container cranes for consideration and evaluation of seismic performance.

- Understand and describe the complicated uplift response potentially exhibited by container cranes and other portal frame structures, as well as its effect on the identified critical response. A generalized portal uplift theory is sought which will provide a physics-based estimate of dynamic structural demand for uplifting portal frame structures as it relates to system input, such as earthquake excitation.
- Develop and verify detailed and simplified analytical models of representative container cranes from three operational classifications, accounting for the nonlinear boundary condition and inelastic structural behavior.
- Characterize and quantify the uncertainties associated with container crane seismic performance.
- Produce a set of fragility curves for each crane classification, each including several levels of structural damage and derailment where applicable, to serve as a vital component of overall port system seismic risk analysis.
- Recommend capacity and demand factors for application to seismic design and retrofit of container cranes.
- Propose and demonstrate general performance-based design guidelines for future and existing container cranes.

1.2.3 Limitations

This study considered the seismic performance of container cranes, and the analysis is performed under the assumption that they can be evaluated as an independent system. Thus, several limitations to the approach taken in this study arise, as summarized below.

- As pointed out by overall port seismic design guidelines [6, 7], a container crane may perform poorly if the underlying wharf or soil layers perform poorly. For instance, differential movement of the crane rails may cause large structural deformations beyond a container crane's capacity, as was the case during the Kobe earthquake [12]. From personal communication with Stu Werner (March 31, 2008, Atlanta GA), the author's understanding is that this deficiency has been or is being addressed in modern wharf construction in the USA through retrofits that directly tie the crane rails together. Therefore, this failure mode is not considered herein, as these measures are expected to drastically reduce the likelihood of occurrence.
- Further, this study assumes that, because the fundamental period of a typical crane is much higher than that of a typical wharf, and because the majority of the mass of a crane is far from the mass of the wharf deck, no significant dynamic coupling effects occur between the wharf and the crane.
- Serviceability of a crane following an earthquake depends on the condition of the crane rails and the presence of uninterrupted and reliable electrical power. While certainly important, these issues are outside the scope of this study, which considers performance of the container crane itself.
- Finally, it is assumed that the nonstructural components of a container crane vital to efficient operation following a seismic event have a capacity roughly equivalent to the structural system itself. The relative flexibility of container cranes is believed to minimize the accelerations transferred to machinery and equipment, damage to which is presumably acceleration-sensitive. The stairwells

and elevators are assumed to be designed to specifications approximately equivalent to the fatigue, serviceability, and operational criterion that typically control the structural design, and thus are not expected to fail prematurely. However, it is always possible that a container crane may be rendered inoperable even if there is no sign of structural damage, but that possibility is not considered herein.

1.3 Organization and Outline

This dissertation is composed of 9 chapters, 2 appendices, and a list of references at the end. This chapter has presented the motivation for the research, and defined the scope in terms of objectives and limitations. For those unfamiliar with container cranes, some important and helpful container crane terminology is highlighted and defined in the beginning of Appendix A, specifically as it relates to a typical modern A-frame crane. Chapter 2 is intended to provide an overall review of the current state-of-the-art of the distinct research areas necessary to thoroughly consider the seismic performance of container cranes. The topics fall into four main categories: dynamic behavior of container cranes, behavior of uplift-capable systems, behavior of steel stiffened hollow box sections, and probabilistic seismic performance evaluation. The remaining chapters specifically address the unique research performed to meet the defined research objectives.

A theoretical approach to uplift behavior as it relates to container crane structures and similar portal frame structures is taken in Chapter 3. Most importantly, portal uplift theory is developed, which helps explain why the seismic performance has been misunderstood for so long, and provides closed-form physics-based estimates for seismic demand of uplift-capable portal-frame structures in order to correct this fundamental misunderstanding. With this theory and its implications in mind, Chapter 4 gives a thorough description of the modeling and analysis approach taken for the remainder of the research; specifically, how critical features of the response are handled and why, especially in the context of finite element models. Then, Chapter 5 discusses a relatively small-scale shake table experiment devised to verify and validate the chosen modeling approach, how it compares with the models and theory, and some conclusions which can be drawn to aid and simplify further analysis.

Inelastic material and element behavior is introduced in Chapter 6. First, a predictive method for determining and modeling the inelastic and cyclic behavior of a given slender stiffened box section is presented. Then, limit states specific to potential container crane repairs are introduced and discussed. Finally, the limit states are quantified for three specific representative container cranes. Specific details regarding each representative crane are described in Appendix A. Chapter 7 considers the same representative container cranes probabilistically, and develops fragility curves for the various limit states representing the probability of different damage given a specific earthquake. The suite of ground motions used to develop these fragility curves is presented in Appendix B. Additionally, the fragility curves are used in Chapter 7 to estimate the expected damage-

related downtime for each crane, given specific earthquake intensity. In Chapter 8, intuitive performance-based design and retrofit guidelines are proposed, followed by a demonstration of their application to simple examples using the results and methodologies of the previous chapters.

Finally, the main conclusions and outcomes of the dissertation are reiterated in Chapter 9, together with recommendations of future work to refine and extend the developed results. Made possible by the pioneering development of portal uplift theory, this research is the first systematic and comprehensive assessment of seismic behavior and vulnerability of container cranes. Taken together, these chapters are intended to define a new state-of-the-art for evaluating the seismic performance of container cranes, and therefore provide the guidance necessary to develop safer, more robust container cranes for ports worldwide.

CHAPTER 2

REVIEW AND ASSESSMENT OF THE STATE OF THE ART

2.1 Introduction

In order to perform relevant and contextually-significant research, it is important to understand the current state-of-the-art. This chapter reviews and surveys the significant literature in a number of areas critical for evaluating the seismic performance of container cranes. First, prior literature regarding the dynamic behavior of container cranes is considered, with emphasis on studies specifically evaluating seismic behavior. This serves as a high-level starting point for the research of this study, and highlights the need for an improved understanding of how uplift affects seismic demand in order to describe container crane seismic behavior. Thus, current understanding regarding the behavior of uplift-capable structures is evaluated next, specifically addressing the knowledge gap about portal frame type structures. Logically, seismic performance relies on capacity as well, so an extensive review of the current state-of-the-art for evaluating and estimating the inelastic and cyclic behavior of stiffened steel box sections is presented, as that is the typically employed construction method. With a full understanding of demand and capacity, it is possible to probabilistically evaluate the seismic performance of container cranes, one of the key objectives of this research. To this end, the concept of fragility curves and the underlying risk framework is discussed and reviewed in the concluding section. The diverse topics covered in this chapter highlight the nature of earthquake engineering: there are always several interacting features which must be considered for a realistic representation of seismic performance.

2.2 Dynamic Behavior of Container Cranes

The capability of a modern FEM to capture the dynamic characteristics of a container crane structure was first demonstrated by Dinevski et al. [13]. By performing forced vibration tests and monitoring ambient vibrations of a container crane in the field, mode shapes and frequencies were compared with a relatively simple 3D FEM. Two boom torsion modes were evident (approximately 2 sec. and 1 sec. period), as well as a portal sway mode (noted as important for operation, at approximately 1.4 sec. period) and a vertical boom mode (approximately 1.2 sec. period) as the four primary modes, all with damping estimated near 1% of critical damping. The FEM was able to predict the observed vibration frequencies within 2% without extensive calibration; however no further efforts beyond system identification were made to evaluate the dynamic response.

A study by container crane consultant Liftech, Inc. [14] considered the issue of operational serviceability being hampered by portal sway. It was noted that the swinging of the hanging load can excite the portal sway mode and cause excessive operator discomfort, leading to significantly decreased productivity. The main recommendation was to limit the period of the portal sway mode to be 1.5 seconds or less. This serviceability criterion is important for the design of new cranes, but has implications for dynamic and seismic behavior that should be more fully understood.

A series of studies in Japan were performed following the Kobe earthquake, which severely damaged several cranes, to study the uplift phenomenon and its effect on the dynamic behavior of container cranes, beginning with a 1:25th scale model of a typical

30m gage Japanese container crane [15]. The scale model was subjected to uniaxial seismic excitation in the direction of trolley-travel with the aim of describing rigid body rocking of a container crane. It was observed that uplift and subsequent rocking can result from even moderate earthquakes. A finite element model was developed in parallel to the physical test, accounting for the nonlinear boundary condition through the use of gap elements: essentially pinned with no upward vertical constraint when in contact with the rail, completely free while uplifting, and constrained by friction when derailed. The model's capability to adequately simulate the uplift and rocking was verified by comparison with dynamic tests of the physical specimen. However, real container cranes are not rigid structures, and the effect of structural deformation response may significantly alter the overall rocking behavior.

This initial work was extended via a 1:8th scale shake-table model based on the same prototype in order to investigate the coupling of elastic response with the rocking phenomenon [16]. Overall, comparisons of response between the physical test and the analytical model, updated to account for elastic structural response, were favorable. This response can be described as follows, depicted in Figure 2.1: (a) structure displaces seaward due to seismic load; (b) landside wheels translate laterally (derail) and uplift when total gravity load transferred to waterside legs; (c) as a result, load increases on waterside legs, and they deform further; (d) landside wheels land inside the rail, resulting in residual inward displacement of each leg (bowing of the portal frame). Together with the observation that response in the trolley-travel direction was critical under seismic loading, it was noted that complete crane collapse could occur from the additional load

on the waterside legs due to uplift of the landside legs. This significant conclusion has important implications, as many cranes are designed assuming that the uplift response will actually prevent damage, as noted in Chapter 1. Thus, it becomes centrally important to fully understand how the uplift response affects seismic demand, a key objective of the current research. While the experimental data suggested that derailment dominated the base displacements during the early stages of uplift events, this potentially important observation was not discussed.

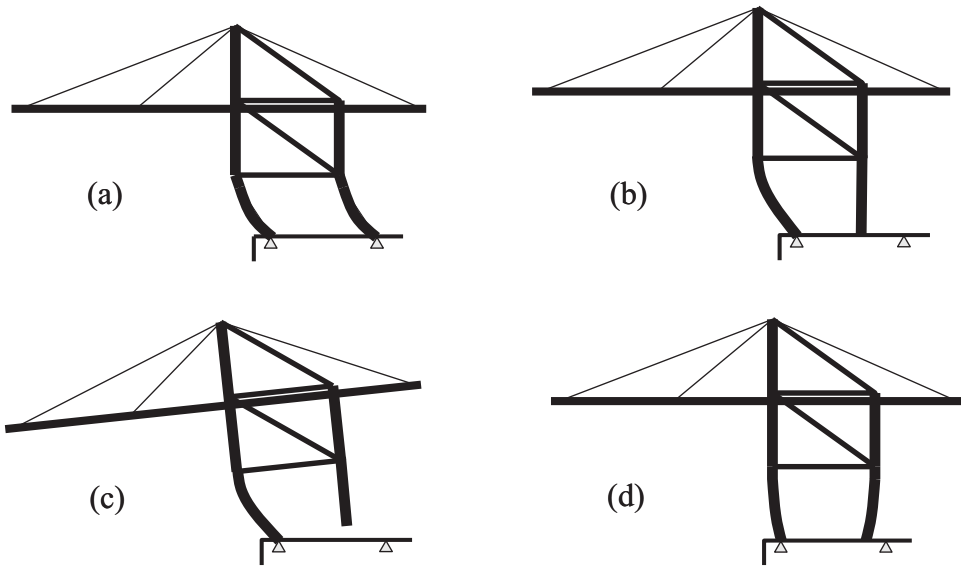

Figure 2.1. Schematic of coupled elastic and uplift container crane response.

Despite the overall good agreement between experiment and analyses results, the fact that an uplifted leg vibrates like a cantilever column caused some discrepancies in the leg's landing point, especially at later cycles of rocking, as the landing point is dependent on the duration of the uplift event. A discrepancy in landing point contributes to greater

discrepancy in the ensuing rocking cycle; thus, the accuracy of the predicted response deteriorated with each rocking cycle, although the response remained qualitatively alike.

To address the numerical accuracy of a gap element approach to simulating the changing boundary condition, a multi-body dynamics modeling method was used to model the container crane from the earlier shake-table tests, both 2D [17] and 3D [18]. Contact markers at the corners of the wheel, rail, and ground next to the wheel are defined. Contact is detected when a contact marker passes a contact line connecting the contact markers. The contact force is then described by different nonlinear springs and nonlinear dampers which must be tuned by several unknown constants. This approach is not wholly compatible with finite element analysis, so the flexible crane structure was represented by the finite segment method, with rigid bodies connecting revolute joints. The modeled response of the crane structure is therefore limited to a crude estimate, which can only be adequate for simple elastic and prismatic members. This effect is most easily seen by the fact that this approach results in a much less favorable prediction of the first mode elastic frequency than does FEM, when compared with the experiment specimen. Overall, while the contact marker approach to boundary modeling appeared to achieve more accurate rocking predictions, the elastic structural response was adversely impacted, and a potential extension to include inelastic behavior is limited using the finite segment approach. Thus, because the goal for improved treatment of the uplift response is to more fully understand its effect on the seismic demand of the uplifting structure, the contact marker and finite segment approach is judged as inferior. By developing a quantifiable, physics-based understanding as is done in the current research, one can

directly judge how closely any boundary modeling technique meets that goal, rather than rely solely on comparisons of leg base kinematics which may or may not correspond to overall seismic demand.

Understanding the general implication of these early studies that container cranes had the potential to collapse even without large differential displacements of the crane rails, the Port and Airport Research Institute (PARI) of Japan, formerly the Port and Harbour Research Institute (PHRI), began considering response of container cranes to seismic loads. Using a 1:15 elastic model of a similar prototype crane as [16], shake table tests were performed for sine wave and earthquake excitation, and compared with analytical response predictions from both simple mass-spring systems and a 3D FEM model [19]. The increase in maximum bending moment of the grounded legs due to the unloading of uplifted legs was verified, though it was noted that the increase due to dynamic loads was much lower than for static loads. However, the leg's bending moment within a range of horizontal force immediately preceding uplift and derailment was higher during dynamic loading than static forces. This discrepancy again points to a need for a more fundamental understanding of the effect that uplift has on seismic demand, a key contribution of the current research. Still, the 3D FEM, utilizing a gap element at the boundary, could sufficiently predict the response, including uplift and derailment, while the simple mass-spring model was adequate for smaller earthquakes but could not capture the increased force due to dynamic loading at higher excitation levels. Results of the shake table tests indicated that a threshold of center-of-mass (CoM) acceleration as determined from a pseudo-static tipping analysis could correctly indicate uplift and

subsequent derailment. While this result emphasizes the fact that these previous researchers recognized the importance of uplift to seismic demand, they do not fully address this issue.

The interaction between a pier-type wharf and its associated container crane was considered using the same 1:15 scale crane model placed atop a simple model of a wharf and tested on the shake table [20]. It was found that in general, a simple double decked mass-spring model could sufficiently capture interaction effects where crane uplift does not occur. Allowing crane uplift appeared to increase the crane's maximum acceleration response, but decrease the pier's maximum acceleration response under both sinusoidal and seismic excitation. Finally, full 3D FE analyses were able to capture the coupled crane/wharf response, even when including uplift. While a range of pier natural frequencies were modeled using the simple coupled system, the crane's period was held constant; further, analysis including uplift was only performed at the minimum excitation that caused uplift. Because of these limitations, it is still unclear as to when coupling effects becomes important. However, the relative effect of crane/wharf coupling can never be contextually addressed without first understanding the effect of uplift.

Noting that little was known about the true (i.e. potentially inelastic) behavior or demand of a container crane after uplift has occurred, base isolation was proposed as a way to drastically reduce response by altering the fundamental mode and thus avoid uplift altogether [21]. Again, the 1:15 scale container crane experimental model was utilized, and tested on a shake table under a variety of conditions, including base isolation. It was

found that the crane's dynamic behavior was unaffected by a hanging mass representing the container being loaded/unload. Further, having the boom in its lowered, rather than stowed, position was the critical configuration, albeit only slightly so. The addition of properly designed base isolators, located between the gantry trucks and leg bases, had the desired effect: they reduced overall deformations and prevented uplift. However, they required shear pins for operational serviceability as well as displacement-limiting links, moment-support rollers, and the damping device, amounting to an expensive option considering four are required per crane. Still, they effectively decreased the risk of container crane damage during a major event caused by excessive deformations or derailment, and are now being produced by Mitsubishi Heavy Industries (MHI). It was later shown [22] that simplified models could effectively capture seismic response including uplift, even when base isolators were used, and were important tools for design of new container cranes.

At first glance, it could appear that the previous research has sufficiently characterized the seismic behavior of container cranes and "solved" the potential problem of uplift contributing to seismic damage. While effective, it is important to emphasize that base isolation to avoid uplift is required only because the true response and behavior of an uplifting container crane structure is not fully understood. Further, base isolation has not been readily adopted for container cranes outside of Japan, so uplift is still the expected response. With the thorough understanding developed here of how uplift affects seismic demand, container cranes can be efficiently designed or retrofitted with a capacity to match that demand without the need for costly base isolation.

2.3 Behavior of Uplift-Capable Systems

The seismic response of systems capable of exhibiting uplift and subsequent rocking motion has attracted significant attention over the past decades. The seminal work by Housner [23] considered the rocking response of rigid block structures on a rigid surface. This prompted many studies to consider the rocking response of rigid blocks (e.g. [24-28]), including simplified displacement-based design procedures incorporating soil-structure interaction [29] based on the nonlinear static procedure utilized in FEMA 356 [30]. Approximating an uplifting structure as a rigid body has limitations however, and it is not always appropriate to represent rocking structures with an "equivalent" SDOF oscillator [31]. Rather, it is often necessary to consider rocking more explicitly as it relates to structural deformation response. This approach can be traced back to Meek [32], who considered the dynamic behavior of a SDOF elastic oscillator on a rigid foundation mat allowed to uplift from rigid soil, thus coupling elastic and rocking behaviors. The idea of flexible uplifting structures was extended to include two-spring foundations by Chopra and Yim [33], and later, Winkler foundations [34]. Extensive parametric analyses were performed by Psycharis [35] in order to better understand how the dynamic effects impact earthquake loading.

In general, it was observed that the earthquake response of a system after uplift is nearly independent of the ground shaking, and depends mainly on the kinematic conditions at the onset of uplift. Thus, it was possible to propose simplified methods for earthquake analysis of uplifting flexible structures [32, 34, 35]. For structures of typical vibration periods, the overall effect of allowing uplift was a reduction in structural deformations

and forces when compared with the same system with bonded contact. Uplift acts as a type of "isolation," or "safety valve" [32] as it interrupts the build-up of seismic energy and limits the transfer of shear from ground shaking, the effect of which could be observed easily using response reduction curves.

Early experimental work echoed these findings. Shake-table tests of steel building frames with columns permitted to uplift [36] found that a structure would be more likely to survive an extreme earthquake, or incur less damage, if column uplift were allowed. More recent experiments sought to take advantage of the isolation effect by proposing column-base details to provide controllable rocking response of steel frames [37-39].

Despite the seeming consensus regarding the benefits of allowing uplift and rocking of flexible structures, uplift is not a guarantee for improved performance. Following the 1995 Kobe earthquake many port container cranes were destroyed, with uplift identified as a direct cause of collapse for some [16]. Here, the "isolation" from uplift did not occur. Similarly, unintentional uplift occurring with failure of an anchoring system can lead to collapse such as the Kinzua Viaduct [40]. These cases, at first glance, seem to be in contrast to the prior research work regarding uplift.

A rarely emphasized, but necessary criterion underlying the assumption of benefit from uplift is a constant shear stiffness of the uplifting structure. In the analytical formulations concerning uplift of a foundation mat, this criterion is intuitively satisfied. The early experiments used a "shear key" to prevent column migration during uplift [36], which

allowed the uplifting columns to carry shear, and thus enforced the constant shear stiffness criterion. Midorikawa's experiment [37] intentionally designed an uplift-capable detail that could carry shear. The specimen used by Pollino & Bruneau [38] had a truss-member connecting the column bases, which creates a system without loss of shear stiffness during uplift. In the case of uplifting container cranes, the uplifted columns are free to displace laterally, and thus cannot carry shear or contribute to shear stiffness. Similarly, yielding column base connection details are not always capable of resisting shear. There is a knowledge gap on the subject of these types of uplift-capable systems, which the current research addresses.

Regardless of the structural deformation response of the system during uplift, and assuming sufficient resistance to overturning, a structure's uplifted elements must always return to the ground, and does so via impact. Impact between structural elements has been extensively studied under the moniker of pounding, a typical issue for adjacent buildings or bridge decks subjected to seismic excitation. There are essentially four methods to numerically model pounding: linear elastic [41], linear viscoelastic [42], non-linear elastic [43], and non-linear viscoelastic [44]. Muthukumar and DesRoches [45] present a comparison study of all four methods to determine their situational appropriateness. Guidelines for selection of the impact stiffness parameter are presented. It was shown that when energy loss due to impact is important, such as at high levels of excitation, then the non-linear viscoelastic model is most appropriate, though the linear-viscoelastic model performs nearly as well, though a mild tension force develops during separation. The damping parameter is analytically related to an assumed coefficient of

restitution in either case. Under smaller excitations, when energy loss due to impact is less critical, the non-linear elastic model is generally adequate.

2.4 Behavior of Steel Stiffened Hollow Box Columns

The portal frame of a container crane is generally constructed of stiffened steel box columns using rather slender plate elements. These sections are very similar to some Japanese steel bridge piers built since the 1960s, whose ultimate strength, often controlled by local buckling phenomena, has been studied in depth ([46-49]). Early experimental work (e.g., [50-52]) aimed to evaluate the ductility capacity, but it was not until the 1995 Kobe earthquake that it was generally understood that these sections were exceedingly vulnerable to seismic motion; thin-walled steel welded sections are prone to the loss of strength and ductility caused by severe local and overall buckling interaction [53-55]. As a result, significant further experimental and analytical work was performed to characterize the cyclic performance of these sections and to aid in the accurate characterization of the load-deflection response under this complicated buckling interaction. The following sub-sections comprehensively evaluates this previous research in order to determine the most appropriate and applicable modeling, design, and retrofit methods for the current study. However, it is perhaps most important to understand the basic, generalized behavior of these types of sections under large lateral loading, which is summarized here.

The most typical structural configuration considered in the previous research has been that of cantilever columns of height h, as depicted in Figure 2.2(a), loaded with a constant

axial load P. Transverse stiffeners, or diaphragm stiffeners, are spaced at a distance a, creating h/a separate "stub-columns." Each stub-column normally has the same cross section, with a typical section depicted in Figure 2.2(b), where B and D represent the outside dimensions of width and depth, respectively, and t_f and t_w represent the flange and web thicknesses. The flange and webs are separated into n_f and n_w number of subpanels by longitudinal stiffeners, each with length b_s and width t_s. The columns were then subjected to pseudo-static and dynamic reversed cyclic loading using horizontal load H.

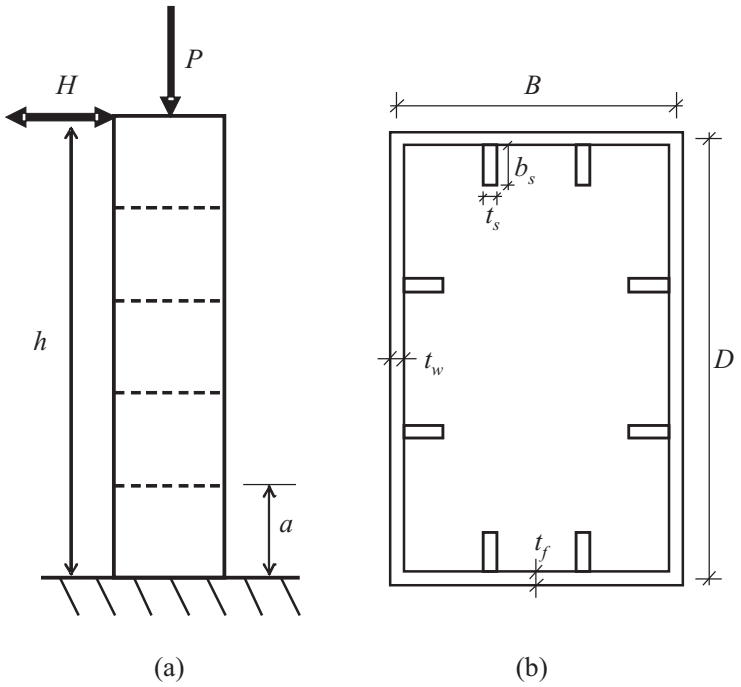

Figure 2.2. Typical Japanese bridge pier specimens: (a) cantilever column, (b) stiffened hollow box cross-section

In general, behavior is controlled by section buckling at the fixed base below the first transverse stiffener [56], always beginning in the flange and gradually transferred to the webs. The shape of the cyclic skeleton (envelope or backbone) curves resembled that of Figure 2.3. At point Y, initial yielding of the section occurs, with some evidence of

minor local buckling. Flange plates generally deform inward. Upon reaching the maximum capacity at point M, flange stiffeners have significantly deformed laterally, enabling large second-order local forces to cause further deformations. This causes rapid progression of further buckling until point N, chosen as the point of maximum ductility, after which no reliable capacity exists due to the unstable progression of local buckling until fracture. The typical skeleton curve (Figure 2.3) and the associated member damage descriptions are summarized in Table 2.1.

Table 2.1. Summary of cyclic behavior

Range		*Envelope Curve*	*Member Damage*
1	$\delta < \delta_y$	Linear elastic	None
2	$\delta_y < \delta < \delta_m$	Decreasing rate of resistance growth	Occurrence of local buckling
3	$\delta_m < \delta < \delta_u$	Minor strength degradation	Growth of local buckling
4	$\delta > \delta_u$	Rapidly increasing rate of degradation	Unstable progression of local buckling, potential crack occurrence

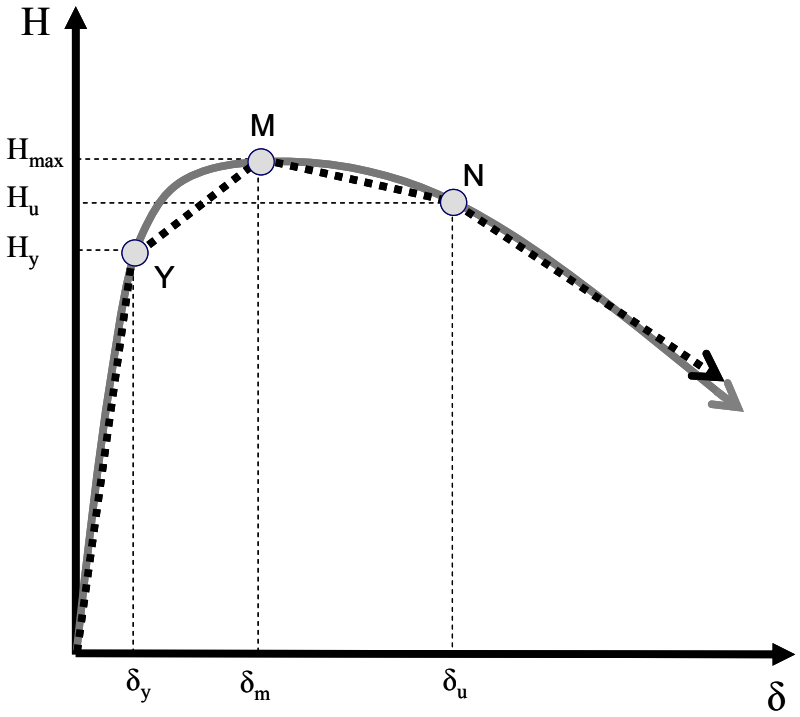

Figure 2.3. Typical cyclic behavior skeleton curve

The choice of the "ultimate" point N depends in large part on expert judgment. However, while earlier studies generally assumed reliable behavior until the capacity decreases to the yield load (e.g. [50, 51]), since the Kobe earthquake it is now more commonly assumed that the ultimate state is when the load decreases to 95% of the maximum load (e.g. Usami et al., 2000).

2.4.1 Early Experimental Studies

The first experimental study of the behavior of steel stiffened hollow box columns [46] began as an extension of studies regarding unstiffened hollow steel box columns [47, 48]. These early studies were concerned with ultimate strength of sections, and found that plate slenderness parameters could be defined in order to define empirical formulas for evaluating the ultimate strength, which could be plotted as interaction curves of compression and bending. Interaction relationships were later extended to include torsion for the case of unstiffened sections [49].

The Public Works Research Institute (PWRI) of Japan performed an extensive series of experiments to determine the ductility of typical steel bridge piers used in Japan, and to quantify the effect of slenderness on strength degradation. Preliminary results [51, 57] present results for 22 specimen, 4 of which were partially filled with concrete. Of the 22 specimens, 18 were subjected to reversed cyclic loading with 10, 5, 3, or 1 cycle to each displacement target, while 4 were subjected to shaking table testing of a historic earthquake motion. From the cyclic loading tests it was found that, while 1 cycle of loading achieved the highest ductility, there was very little difference in hysteretic

response between 10, 5, or 3 cycles, despite significant wall or panel buckling at higher deformations. Results of the shaking table tests showed significant residual deformations, very little load reversal, and thus significantly less energy dissipation than would be predicted by the cyclic testing. Many specimens failed by fracture, but only after major buckling caused significant loss of strength and stiffness.

Using the results of these tests and elastic plate buckling theory [58], a first attempt at estimating the deformation capacity of hollow steel bridge piers was proposed [59]. The concept of an equivalent plastic hinge length was used to propose a semi-rational methodology, which assumes a compact section according to Japanese bridge design code of the time [60] as well as development of the full moment capacity. While these criteria are satisfied for many steel bridge piers, the methodology allows little insight to noncompact, slender sections. However, the stiffeners' relative flexural rigidity γ can be used to determine whether buckling due to slenderness will decrease a section's strength. This is accomplished by comparing γ with the minimum required ratio of longitudinal stiffener stiffness to plate stiffness γ_{req} [61], explained in detail in the next section.

Details of specimen construction, testing procedures, detailed results, and discussion can be found in the final experiment report [51]. The suggested design procedure was refined based on a tri-linear approximation of the backbone curve and the application of the equal energy method. An equivalent elasto-plastic hysteresis curve was proposed, and shown to be appropriate for determining an equivalent strength-reduction factor (R-factor) for stiffened steel hollow box columns. The effect of partially filling with concrete had

mixed results, and decreased the ultimate deformation capacity despite increasing ultimate strength in some instances. Final recommendations and results [61] include 2 additional tests of larger versions of parametrically similar specimens to verify the lack of size effects, especially on initial imperfections and weld details.

Concurrently, experiments were conducted at Nagoya University to consider the behavior of steel bridge columns to cyclic loading. The first set included 25 specimens [50], of which 16 were stiffened box columns. Rather than rely exclusively on gamma ratios to characterize the slenderness, an additional two slenderness parameters were utilized:

$$R_f = \frac{B}{t}\sqrt{\frac{12\left(1-\nu^2\right)}{4n^2\pi^2}}\sqrt{\frac{\sigma_y}{E}} \tag{2.1}$$

$$\bar{\lambda} = \frac{kh}{r\pi}\sqrt{\frac{\sigma_y}{E}} \tag{2.2}$$

Where R_f = flange plate slenderness parameters, λ=column slenderness parameter, B = flange width, t_f = flange plate thickness, E = Young's modulus, ν = Poisson's ratio, k = buckling coefficient n = number of subpanels separated by longitudinal stiffeners, h = column height, r = radius of gyration of the cross section, and σ_y = yield stress. Similar cyclic behaviors were observed as for the PWRI experiments, but presented as envelope rather than backbone curves. In addition to the slenderness, the axial load ratio also adversely affected the strength degradation and energy absorption capacity. For all tests, 3 cycles at each displacement target were performed. Improved behavior was noted where stiffener rigidity, γ, was significantly higher than the optimum value as determined by linear buckling theory [58]. A sequel study [62, 63] tested for improvements in the ductility and energy absorption capacity by using stepped stiffeners, higher yield steel in

longitudinal stiffeners, partially filling with concrete, and greatly increasing effective stiffener rigidity. It was found that no appreciable gain was to be had by increasing stiffener rigidity beyond three times the optimum from linear buckling theory, γ_{req}, but that decreasing overall slenderness or increasing the yield stress of the stiffener steel greatly improved ductility. Providing partial concrete fill appeared to significantly enhance both ultimate strength and ductility, but seemed to exhibit a more brittle failure.

2.4.2 Estimating Buckling Potential

Early attempts to quantify the buckling potential of stiffened steel box sections, or more particularly to determine whether buckling will occur prior to reaching the desired section strength, were based on elastic buckling theory [58]. These methods remain a valuable tool for evaluating the behavior of slender sections, and are presented here, based on their particular application by the research team at PWRI [51, 59, 61].

Perhaps the most common, and simple, method for evaluating slenderness of plate elements is by using a width/thickness ratio (e.g. AISC, AASHTO), where new designs are limited by some upper limit depending on the configuration, location, material, etc. This approach is easily applied to stiffened steel box sections, where the width/thickness ratio is expressed in terms of a subpanel between two longitudinal stiffeners:

$$B/t = k_s f n \tag{2.3}$$

where k_s = general limiting width-thickness ratio and f = coefficient related to the stress gradient. In general, it is conservatively assumed that f = 1.0 in plates which yield. In Japan, k_s = 28 for grade SS41 steel (f_y = 245 MPa) and k_s = 24 for grade SM50 (f_y = 323

MPa) for stiffeners to be used in the sections in question. In the US, flanges of rectangular box sections are compact if less than ~27, and slender if greater than ~34 (50ksi steel). It has long been known, however, that width-thickness ratios are insufficient to characterize the buckling potential of stiffened steel box sections [64]. For this, a more detailed analysis is required.

A steel stiffener's relative flexural rigidity can be described by the parameter γ [61]:

$$\gamma = I_t \Big/ \frac{Bt^3}{11} \tag{2.4}$$

where I_t = stiffener's section inertia moment with respect to its end connected to the plate. Then, the equation to determine the required ratio γ_{req} depends on the stiffness of transverse stiffeners (i.e. diaphragms). If the flange plate aspect ratio α (length between diaphragms a divided by plate width B) is less than the critical aspect ratio α_0, and the transverse stiffener second moment about the surface of the main plate I_d is greater than the required stiffness $I_{d,req}$, then γ_{req} can be determined by

$$\gamma_{req} = \begin{Bmatrix} 4\alpha^2 n\left(\frac{t_0}{t}\right)^2\left(1+n\frac{b_s t_s}{Bt}\right) - \frac{\left(\alpha^2+1\right)^2}{n}; \left(t \geq t_0\right) \\ 4\alpha^2 n\left(1+n\frac{b_s t_s}{Bt}\right) - \frac{\left(\alpha^2+1\right)^2}{n}; \left(t < t_0\right) \end{Bmatrix} \tag{2.5}$$

$$I_{d,req} = \frac{Bt^3}{11} \cdot \frac{1+n\gamma_{req}}{4\alpha^3} \tag{2.6}$$

$$\alpha_0 = \sqrt[4]{1+n\gamma} \tag{2.7}$$

where t_0 = the minimum plate thickness which satisfies Eq. 2.3. If the requirements for Eq. 2.5 are not met, then the effect of transverse stiffeners is ignored and the governing equation is

$$\gamma_{req} = \begin{cases} \frac{1}{n}\left[\left\{2n^2\left(\frac{t_0}{t}\right)^2\left(1+n\frac{b_s t_s}{Bt}\right)-1\right\}^2 - 1\right]; (t \geq t_0) \\ \frac{1}{n}\left[\left\{2n^2\left(1+n\frac{b_s t_s}{Bt}\right)-1\right\}^2 - 1\right]; (t < t_0) \end{cases} \quad (2.8)$$

If $\gamma/\gamma_{req} > 1.0$, and $b_s t_s/Bt > 0.10/n$, then it is expected that the stiffeners are sufficient to prevent premature wall buckling.

While buckling may be avoided prior to reaching the yield strength by following the above criteria, it cannot always be avoided completely. In fact, local buckling is still the likely failure mechanism, leading to the strength and stiffness degradation described previously. Buckling can occur as panel buckling or wall buckling, as depicted in Figure 2.4.

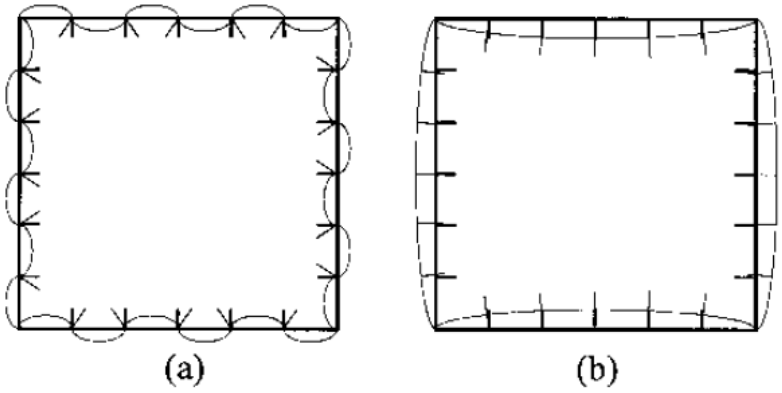

Figure 2.4. Stiffened steel box section buckling modes: (a) panel buckling; (b) wall buckling, reproduced from [61]

The mode of failure can be determined according to theory [64], utilizing the ratio of γ/γ^*. If $\gamma/\gamma^* > 1.0$, then panel buckling is the expected initial buckling mode. If $\gamma/\gamma^* < 1.0$, then wall buckling is expected to dominate. Here, γ^* is defined similarly to γ_{req}:

$$\gamma^* = \begin{cases} 4\alpha^2 n\left(1 + n\frac{b_s t_s}{Bt}\right) - \frac{\left(\alpha^2+1\right)^2}{n}; (\alpha \le \alpha_0) \\ \frac{1}{n}\left[\left\{2n^2\left(1 + n\frac{b_s t_s}{Bt}\right) - 1\right\}^2 - 1\right]; (\alpha > \alpha_0) \end{cases} \tag{2.9}$$

These combined criteria lead to a convenient representation of the allowable design space for new sections based on expected behavior, as depicted in Figure 2.5. To avoid premature wall buckling, $\gamma > \gamma_{req}$. General local buckling is mitigated by requiring $t > t_0$, thus $\gamma_{req} > \gamma^*$. Allowable section designs are expected to behave in one of three ways, described by the zones indicated in Figure 2.5. Sections are expected to fail according to their zone:

1. overall wall buckling
2. panel buckling
3. fracture

Although the theoretical limit between zones 1 and 2 is $\gamma/\gamma^* = 1$, experiments indicate that when $1 < \gamma/\gamma^* < 2$, wall buckling caused failure even though panel buckling may have initiated first [61]. Sections described by zone 3 are not expected to fail by buckling, because their buckling stiffnesses are high, but rather through fracture [51]. However, the tests from Nagoya University [63] indicate that while fracture may be the final state of specimens with high γ/γ_{req} ratios, significant strength and stiffness degradation is still present prior to fracture and no appreciable improvement in ductility can be achieved with γ/γ_{req} greater than roughly three.

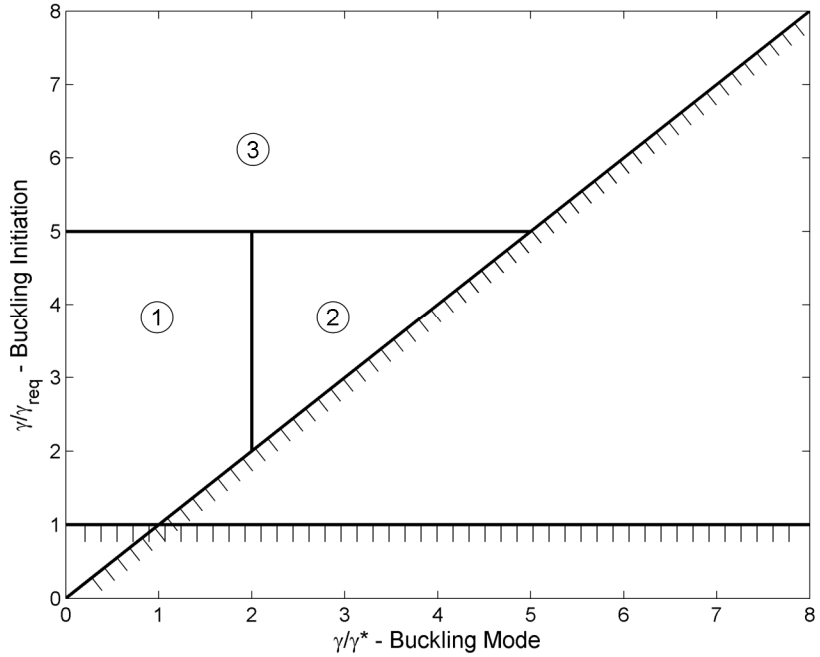

Figure 2.5. Allowable design parameters and behavior types of stiffened steel box sections, inspired by [51]

2.4.3 Modeling Hysteretic Response

There have been several studies suggesting the appropriateness for various hysteretic models to effectively capture the response observed from the early experimental work regarding these thin-walled steel sections. The suggestions have ranged from common and simple to complex and unique, and are described and compared below.

2.4.3.1 Bilinear and Trilinear Models

The most basic hysteretic model is bilinear, with elastic and perfectly plastic branches. This sort of model was suggested based on the early experiments by PWRI [51], using the equivalent energy method. The effective yield point was determined such that the perfectly plastic yield plateau had the same energy as a two-line approximation to the

inelastic action. While simple, this method highlights an important consideration: that both strength and deformation are important to the earthquake resistance of these sections.

Ikeda et al. [65] also used a bilinear model, but rather than enforce an equal energy assumption (that would likely require an experiment to calibrate), amplified the yield point uniformly for all specimen, and included hardening until the load reached 95% of the empirically predicted maximum load, where an empirically predicted ductility has been reached. It was seen that, for the specimens considered, this approach yielded nearly equivalent accumulated energy as experimental cyclic tests. Also, trilinear models were proposed; elastic, followed by hardening until 95% of the maximum empirically predicted load is achieved, followed by a plastic plateau until the empirically predicted maximum ductility is achieved. This trilinear approach had lower accumulated energy, but was slightly less conservative with load capacity within the range of applicability than the bilinear. It was concluded that neither could accurately reproduce the hysteretic response at large deformations, but that if the ultimate point was chosen to be where the load decreased to 95% of the maximum load, then the bilinear and trilinear models were a decent conservative estimate.

2.4.3.2 Phenomenological 2-Parameter Model

The usefulness of bilinear and non-degrading trilinear hysteretic models is limited, however, given the restriction above. Suzuki et al. [66] developed a more realistic hysteresis model specifically for thin-walled steel bridge piers. It is a typical phenomenological model that simulates hysteretic behavior by enforcing specific

hysteretic rules and defining several empirical parameters. The original skeleton curve is essentially trilinear, with elastic, hardening, and degrading branches. The hardening branch extends from the yield point to the point of maximum load under cyclic loading. The degrading branch then descends at a degrading stiffness equal to that of a monotonic pushover. The skeleton curve is then updated and shrunk depending on the accumulated hysteretic energy. This approach was shown to capture the general behavior of cyclic tests well, even at large deformations [66]. Further, this approach performed well for dynamic time history analysis, and provided reasonably accurate estimates of maximum and residual deformations for a variety of steel bridge piers subjected to several ground motions. This type of model is hereafter referred to as the 2-paramater model.

2.4.3.3 Degradation Damage Model

Defining damage in terms of maximum deformation has limitations, especially when degradation is due to local buckling, since the hysteresis curves then depend on the loading history [50]. A damage model was thus proposed to account for this, and the effects of various factors on the evaluation of damage were studied using 10 additional experimental specimens [67]. Monotonic, constant-amplitude, and three-cycle quasi-static reversed cyclic testing was performed to evaluate the effect of loading history. To verify that the damage model was useful for earthquake loading rather than simple loading histories capable during quasi-static testing, pseudodynamic tests were performed on hollow steel box column specimens [68]. A relatively complex evolutionary-degrading hysteretic model for steel hollow box sections was proposed, based on the damage index verified for quasi-static and pseudodynamic testing [69].

The proposed damage model, referred to as an evolutionary-degrading (E-D) damage model, updates a trilinear envelope curve (elastic, hardening, and plastic plateau branches) incrementally using a calculated damage index, D, based on the past loading history.

$$D = (1-\beta)\sum_{j=1}^{N_1}\left(\frac{\delta_{\max,j}-\delta_y}{\delta_u-\delta_y}\right)^c + \beta\sum_{i=1}^{N}\left(\frac{E_i}{H_y(\delta_u-\delta_y)}\right)^c \tag{2.10}$$

where, δ_y = yield displacement; δ_u = ultimate displacement under monotonic loading; $\delta_{max,j}$ = maximum displacement produced for the jth time; E_i = energy dissipated in the ith half-cycle; H_y = effective yield load; N = number of half-cycles; N_1 = number of cycles producing $\delta_{max,j}$ for the first time such that $\delta_{max,j} > \delta_{max,j-1} + \delta_y$; and β and c are parametric constants [69]. This damage index is clearly a more generalized version of those proposed by Park and Ang [70] and Krawinkler and Zohrei [71]. Here, parameter β sets the relative importance of both deformation-based and hysteretic energy-based damage. Parameter c controls the relative importance of larger half-cycles, as well as relates the damage achieved between different loadings (for example: monotonic vs. cyclic). Such flexibility allows for reasonably accurate inelastic behavior modeling, but only after significant calibration with experimental results to identify appropriate values for β and c. This challenge was addressed at length when the damage index was used for cylindrical bridge piers [72].

While the parametric constants present a challenge, the application of the E-D damage index for seismic design verification was shown to be effective for both stiffened box

[73] and pipe steel bridge piers [74]. However, these systems could readily be assumed to act as SDOF systems, which greatly simplify the hysteresis analysis so that the use of the E-D damage index and envelope updating process was practical to apply. For more complex systems, where the damage index would have to be employed at many discrete locations for several degrees-of-freedom, the damage index would need to be codified within a finite element framework – a non-trivial matter. Further, using the E-D damage index for hysteretic modeling still requires ductility and strength estimates to define the starting skeleton curve. If an accurate skeleton curve could be determined in the absence of experimental data, then the additional complexity of the E-D damage would need to provide significantly better response predictions to be favored over other, more conventional hysteretic modeling approaches.

2.4.3.4 Model Comparison Studies

A broad comparison of hysteretic models was done by Liu et al. [75, 76] using pipe-section steel bridge piers. They first considered four models: bilinear (elastic, hardening), trilinear (elastic, hardening, degrading no skeleton curve updating), 2-parameter (elastic, hardening, degrading with skeleton curve updating), and E-D damage model (elastic, hardening, plastic with damage accumulation). Each method could adequately capture the maximum response within a specific range. The bilinear model, as before, must be limited to some small range of ductility. The trilinear model, as defined in this study, was unconservative for moderate to large ductility levels, but was superior to the bilinear model all around. Both the 2-parameter and the E-D models were reasonably accurate at predicting maximum as well as residual displacements due to seismic motions (except

when the motion was long duration on soft soil, where the E-D model overestimates the residual). Characterization of the appropriateness of the E-D model versus the 2-parameter model was later refined [76]. In general, it was concluded that either model adequately simulates the hysteretic response, but that caution should be given when considering the residual deformations for long duration ground motions. Essentially, the weakness of both models is the degradation after the capacity has dropped below the yield capacity; the E-D model is only calibrated to the post-maximum yield point, where the 2-parameter model degradation is based on an assumed path. Therefore, neither model can predict displacements with certain accuracy. However, both models perform adequately for normal excitations [76].

In general, simple hysteretic models are adequate when only slight to moderate inelastic action is reached. If an analyst desires adequate predictions further into the inelastic range, then two sources of degradation must be accounted for when modeling these thin-walled steel sections: deformations and accumulated energy. Both the 2-parameter and E-D damage models satisfy this criterion. However, for any model to accurately predict response in the absence of physical experiments, accurate ways to predict the strength and ductility measures necessary for the skeleton curve are necessary, as well as a robust enough experimental database to thoroughly characterize the parametric constants.

2.4.4 After Introduction of Numerical Methods

The development and implementation of a modified two-surface plasticity material model (2SM) at Nagoya University [77, 78] based on the material model proposed by Dafalias

and Popov [79], has allowed for much more accurate elastoplastic large deformation finite element analysis of thin-walled steel sections subjected to cyclic loads, considering both material and geometrical nonlinearity as well as initial imperfections and residual stresses [80, 81]. With this new tool, the database of specimens used to develop and improve empirical relationships could be readily expanded at significantly reduced cost. Many new studies were performed to look closer at the behavior of these thin-walled sections, each one extending the previous. The first major report from these studies considered stiffened plates, tubes, and stiffened box sections [82], showing the superiority of the 2SM approach, and detailing updated empirical strength and ductility relationships in terms of the critical slenderness parameters. When considering stiffened sections, the stiffener's equivalent slenderness ratio parameter was introduced, defined by

$$\bar{\lambda}_s = \frac{1}{\sqrt{Q}} \frac{a}{r_s} \frac{1}{\pi} \sqrt{\frac{\sigma_y}{E}} \tag{2.11}$$

in which r_s = radius of gyration of the T-shape cross section consisting of one longitudinal stiffener and the adjacent subpanels, and Q = local buckling strength of a plate enclosed by two adjacent diaphragms and stiffeners, defined as

$$Q = \frac{1}{2R_f}\left[\beta - \sqrt{\beta^2 - 4R_f}\right] \tag{2.12}$$

When the nondimensionalized compressive residual stress and initial out-of-flatness are assumed to be 1/150, parameter β can be determined from

$$\beta = 1.33R_f + 0.868 \tag{2.13}$$

A more in-depth presentation of the described cyclic behavior (discussed earlier) as it relates to stiffened steel box columns is presented [56] in unison with a more thorough treatment of the parametric studies leading to proposed empirical strength and ductility

relationships [83]. First, it is found that a two-sided cyclic loading is conservative but most representative of an earthquake loading. Then, the parametric study considered the effects of flange plate width-thickness ratio, column slenderness ratio, stiffener's equivalent slenderness ratio, and axial load magnitude on strength and ductility. Here, it was found that a modified stiffener equivalent slenderness ratio could better describe the contribution towards coupled instability leading to degradation, presented as

$$\bar{\lambda}_s' = \frac{1}{\sqrt[5]{\alpha}} \bar{\lambda}_s \tag{2.14}$$

where α represents the section aspect ratio of the flange plate between two diaphragms (a/B).

In general, it was found that ultimate strength and ductility suffer with higher values of width-thickness ratio, column slenderness, and modified stiffener's equivalent slenderness ratio. Empirical relationships describing the strength and ductility are presented, which agree well with experimental [50, 63] and analytical [82, 83] results. These empirical relationships form the cyclic envelope curve based on points Y, M, and N from Figure 2.3, where point N is defined as the deformation where the capacity decreases to 95% of the maximum strength.

$$\frac{H_{\max}}{H_y} = \frac{0.10}{\left(R_f \bar{\lambda} \bar{\lambda}_s'\right)^{0.5}} + 1.06 \qquad (S = 0.07) \tag{2.15}$$

$$\frac{\delta_m}{\delta_y} = \frac{0.22}{R_f \sqrt{\bar{\lambda}} \bar{\lambda}_s'} + 1.20 \qquad (S = 0.59) \tag{2.16}$$

$$\frac{\delta_{95}}{\delta_y} = \frac{0.25}{\left(1 + P/P_y\right) R_f \sqrt{\bar{\lambda}} \bar{\lambda}_s'} + 2.31 \qquad (S = 0.64) \tag{2.17}$$

Here, S is the standard deviation of the curve fit to the computed values from finite element analyses. The reported range of applicability, based on the parameter values for the specimens considered, is

$$0.25 \leq R_f \leq 0.56,\ 0.20 \leq \lambda \leq 0.50,\ P/P_y \leq 0.3,\ \gamma/\gamma^* \geq 1.0 \qquad (2.18)$$

The mean empirical relationships, as well as the mean minus S and mean minus $2S$ curves, are shown graphically in Figure 2.6 in relation to the appropriate parameters.

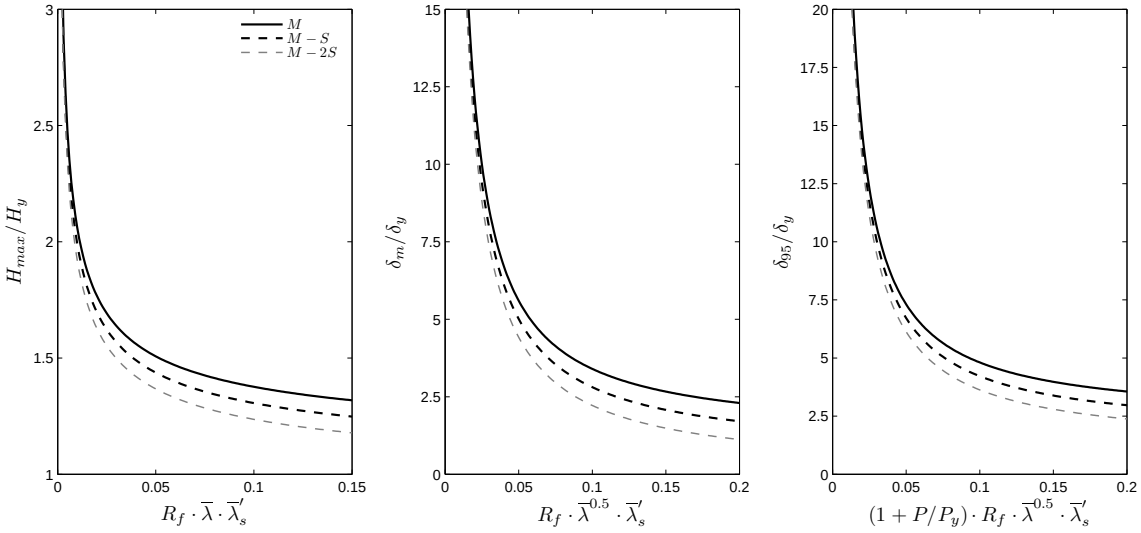

Figure 2.6. Empirically-determined ultimate strength and ductility curves [83]

As an alternative to empirical relationships defining an envelope curve in terms of load vs. deflection, a strain-based ductility evaluation methodology has been proposed [84, 85]. Using the same specimens and a similar parametric analysis, an effective failure strain is defined corresponding to the point of ultimate ductility. When the average strain on the compression flange along an effective failure length of a stiffened hollow box section, assuming a typical nonlinear material model, reaches the effective failure strain, then the ultimate ductility is assumed to have been reached. The effective failure length was found to be the minimum of a or $0.7B$. Then, empirical relationships for the mean

effective failure strain and strain at maximum capacity are determined presented [84], and shown predict the point of ultimate ductility well for a cantilever and frame structure [85]. While this type of an approach can be easily used for ductility evaluation during design, where a desired ductility must not be surpassed, it cannot be used for performance evaluations of structures which are expected to surpass their ultimate ductility. This is because no real-time degradation happens in the hysteretic model due to the use of standard nonlinear material models, but rather some maximum strain is determined "offline." Thus, this type of an approach is ideal for deterministic evaluation (pass/fail) or during design iterations, but is not suitable for more detailed types of analysis.

A different form of the strain-based ductility evaluation methodology was later proposed [86], specifically emphasizing its use for seismic verification of new or existing thin-walled steel bridge piers. Here, the equal energy method is used to determine capacity based on a factored global ductility, and compared with demand, determined by the seismic coefficient method. Again, the method provides the means for checking a new or retrofit design, or verifying adequacy of a built structure, without having to develop and verify a full nonlinear model, but with the same limitations to extension as [84, 85].

Rectangular-shaped hollow stiffened steel bridge piers were evaluated through experiment and finite element analysis [87] in order to determine whether the B/D ratio altered the strength or ductility. While specimens appeared to exhibit differences in strength and ductility with changes in rectangularity, they appeared small (<15%), and then only with large differences in B/D (0.33→2). In general, strength and ductility

appeared at a maximum when B/D was in the range of 1.5-2, but that differences could generally be ignored, even if considering energy absorbed. It was also briefly shown that the effect of the axial load varying with the changing lateral load made a negligible difference when considering the envelope curves of specimens.

The issue of axial force fluctuations was expanded [88], and its influence on the ductility of short steel box columns was studied in depth. It was found that varying the axial load with the variations in lateral load could increase the post-peak ductility, but had no effect on strength. Therefore, an adjusted empirical relationship was proposed for the effective ultimate strain which accounted for axial force fluctuations, which could be used where the prior equations, assuming constant axial load, was too conservative. The effect is small however, and is not likely to have an impact on generalized hysteretic behavior.

2.4.5 Retrofit Concepts

Several techniques to improve the ductility and inelastic behavior of thin-walled stiffened steel box sections have been proposed and studied. This section describes several of the more common and most interesting techniques, and outlines their basic limitations.

Because of the promising preliminary results of partially filling a thin-walled steel column with concrete [62], considerable further effort was later devoted to concrete-filled columns (e.g., [89, 90]). In general, concrete-filled columns exhibit significant improvement in strength, ductility, and energy-absorption capacity when subjected to cyclic loads by bracing the flange and web plates from buckling inwards [89]. However,

the added mass due to the necessary concrete can potentially overload the foundation system, which is seldom designed with large excess load-bearing capacity. Further, the failure of concrete-filled sections can be brittle [62].

Several studies (e.g. [91, 92]) have evaluated a number of supplemental stiffening strategies. It was found that a minimal stiffening of the corners was effective in improving the ductility and energy dissipation of the section. Noticeable increases in overstrength and greater energy absorption capacity was noted for the cases when the number of longitudinal stiffeners was increased and when the corners were significantly stiffened. Regardless of the stiffener retrofit, however, the general envelope curve was similar in shape, with significant degradation following the peak strength. If increases in ductility or overstrength are all that is required to bring a section into conformance, then stiffener retrofits may be an appropriate technique to consider.

Another innovative retrofit technique was proposed by Susantha et al. [93], where low-yield-strength (LYS) steel was used to replace the lowest cross section of a cantilevered column. It was found that a carefully proportioned replacement panel was capable of increasing both ductility and energy absorption capacity. However, in addition to the expense of total panel replacement, this approach tends to decrease the overall stiffness, resulting in longer periods that could be disruptive to serviceability. A similar concept, strategically replacing segments with energy absorption segments, has similar benefits [92], but also requires the expense of replacement after only moderate earthquakes.

Internal bracing of the webs and flanges has been considered as well [94], where reduced-shank threaded rods are inserted into holes drilled through the webs and/or flanges, so that both webs and/or both flanges buckle together, in the same direction. Slight to moderate improvements were noted in terms of ductility and energy absorption, but less than other retrofit strategies. Though adding internal braces is an attractive option due to the low cost, one must know precisely where the buckle will initiate in order to determine where to add the braces. This is difficult, even with the most advanced FE modeling capabilities, and thus has too much risk to have gained widespread acceptance.

Base-isolation has been proposed for steel bridge piers constructed of thin-walled stiffened box sections, and lead-rubber bearings have been shown to economically reduce the seismic demands [95]. However, the system dynamics change as the rubber ages, leading to unpredictable seismic performance and an intensive maintenance schedule [96].

On the whole, many different retrofit strategies exist, and can be effective under the right circumstances. No current retrofit strategy can meet the needs of all deficient sections. Therefore, it is important to better understand the seismic demands in order to implement appropriate concepts with acceptable compromises.

2.5 Probabilistic Seismic Performance Evaluation

Successful structural engineering design must offer economical methods of reliably achieving certain minimum performance limits. The unknowns associated with any

structural system design can be quite large, forcing the designer to create a more nominally conservative structure in order to reliably reach the specified performance objectives. In the past 30 years, this has been dictated through probability-based limit state design as specified in building codes, which has matured with advances in reliability theory and the supporting statistical data [97]. However, applying the same load-factor type methodology for earthquake-resistant design presents many challenges [98, 99]. In fact, it has been shown [100] that early attempts to incorporate earthquakes into load combinations resulted in far less reliable systems than with more typical (dead, live, wind, etc.) loads. Further, code-compliant buildings have caused significant economic losses during recent earthquakes while meeting the life-safety requirement, prompting interest in further performance objectives [101]. The industry thus began incorporating and refining probabilistic risk assessment techniques used by the nuclear power industry [102] in order to quantifiably approach the issue of seismic performance evaluation. This sort of an approach to safe design is becoming increasingly important, as policymakers want to see, and be part of, the risk characterization and evaluation stages of the risk-informed decision making process [103].

At the heart of a structure performance evaluation or seismic risk assessment are *fragility curves*, which describe the probability of failure of a system to reach a performance level as a function of the seismic demand [104, 105]; it not only provides the probability of reaching limit states given a specific earthquake, but is also needed to estimate maximum probable losses. The fragility curve concept was first applied to civil infrastructure in the ATC-13 [106] report, and now forms the backbone of the well-known FEMA-sponsored

loss estimation software tool, HAZUS [107]. While these tools are generally based on professional judgment and expert opinion, they have been shown to be immensely helpful, and have thus spurred efforts to develop more meaningful, data-driven fragility relationships. The simplest of these types are empirical in nature, where damage data (either real data from past earthquakes or simulated data from computational analyses) is used to fit a fragility curve with some assumed cumulative distribution function (CDF) shape (e.g. [108, 109]). In this approach, however, there is no physical meaning behind the CDF variability term, and thus it is difficult to determine what system aspects are major contributors to the overall vulnerability. More advanced methods have since been introduced [98, 110, 111], which will be described in detail in the following sections. These new methods are attractive due to their ability to account for explicit characterization of different sources of dispersion, rendering them meaningful, flexible and transparent.

2.5.1 Uncertainties

There are many factors which affect the performance of a structure during an earthquake. Uncertainties in demand, or the earthquake characteristics that must be resisted by the structure, come from the lack of knowledge regarding the next earthquake and how the structure will react to it. Capacity uncertainties arise due to unknowns relating to how much resistance may be provided before reaching specified limit states. In addition, the actual process of predicting a structure's capacity entails significant uncertainty, as does forecasting the demand that will actually be experienced. All of these uncertainties in capacity and demand can be further characterized as aleatory and epistemic uncertainties.

Aleatory uncertainty, or randomness, stems from factors that are inherently random at the scale of understanding, and cannot be reduced by acquiring further information. For example, one cannot know with certainty the characteristics of the next earthquake (location, intensity, etc.). Further, the precise material properties throughout the structure can never be known exactly, despite coupon tests, core samples, etc, due to inherent randomness in the materials.

Epistemic uncertainty, or uncertainty in general, stems from various assumptions, lack of knowledge, and/or limitations to supporting databases. They can be reduced with more complete (generally costly) analysis or improved information. For example, a chosen analysis method may not capture the actual behavior accurately due to simplifications (2D vs. 3D model) or approximations (linear vs. nonlinear) made during modeling. In addition, epistemic uncertainties come from our general lack of complete knowledge regarding the behavior of structures under earthquake loading.

While somewhat unpredictable, many of these uncertain factors exhibit statistical regularity and can be dealt with using rational tools from probability and statistics [112]. Often, uncertainties are expressed as Gaussian or lognormal distributions [113], which are typically described by two parameters: the mean and the coefficient of variation.

Uncertainty in structural strength and stiffness are characterized by imperfect knowledge of material properties, idealized constitutive models, discrepancies between as-drawn and

as-built member dimensions, and more. It is common to account for these uncertainties using two independent variables: yield stress f_y, and Young's modulus E. Distributions of these uncertainties are presented for use in the development of LRFD by Galambos & Ravindra [114]. A more detailed and updated report, distinguishing between various steel specifications, is presented by Liu et al. [115].

Structural mass is especially important in dynamic analyses, beyond simply producing gravity load. The mass of any structure is dependent on the material choices, structural dimensions, nonstructural elements, and more. Each component has an associated uncertainty that, when combined, form uncertainty in structural mass. Ellingwood et al. [116] suggest a simple model for the probability distribution of dead load, where uncertainty in mass is considered together as one lumped parameter.

While sources of uncertainty are nearly infinite, previous studies (e.g. [117-120]) have shown that the uncertainty in seismic demand often dominates the overall response variability. Therefore, so long as other sources of uncertain are accounted for elsewhere [121], probabilistic seismic demand analyses and performance evaluations can often be performed assuming that all uncertain structural properties are at their expected mean, so that total behavior uncertainty is vested in the ground motions, greatly reducing the number of time-consuming analyses [110]. To make this assumption, a supporting sensitivity analysis is highly desirable.

2.5.2 Risk Framework

Risk of loss (life, finances, time, etc.) is characterized by the more fundamental occurrences damages conditioned on the occurrence of some hazard. More specifically and in the context of seismic risk, the loss itself is dependent on some damage state (DS), which is itself dependent on the occurrence of some subsystem limit state. That limit state (LS) is dependent on the occurrence of some seismic intensity (SI) with occurrence described by traditional probabilistic seismic hazard analysis [122]. From the theorem of total probability [123], this can be expressed as:

$$P[Loss > c] = \sum_{s} \sum_{LS} \sum_{d} P[Loss > c \mid DS = d] P[DS = d \mid LS] P[LS \mid SI = s] P[SI = s] \quad (2.19)$$

in which P[SI=s] is the probability of a seismic event with SI=s, from the standard hazard curve; P[LS|SI=s] is the probability of reaching a limit state LS, given the occurrence of SI=s; P[DS=d|LS] the probability of damage state DS, given limit state LS; and P[Loss>c|DS=d] the probability that loss exceeds c, given that DS=d. This sort of an approach clearly delineates contributors to the overall risk model: a seismologist provides P[SI=s], a structural engineer provides P[LS|SI=s], and a building economist and loss expert provides P[Loss>c|DS=d] [101]. The term P[DS=d|LS] has a less clear contributor, but plays the important role of linking quantitative limit states to qualitative damage states. When many subsystem or component level limit states contribute to a global damage state, the P[DS=d|LS] term acts as the unifier. However, when the limit states themselves are global in nature, limit states can be defined such that they are one-to-one with damage states.

Interstory drift has been deemed an appropriate engineering demand parameter (EDP) to define structural limit states for seismic reliability analysis, as it provides insight to local and global collapse behaviors [98, 101, 111, 124-126], and requires no calibration. When interstory drift, or simply drift from here on, is chosen as the EDP, it is common to assume damage states are perfectly correlated to limit states.

While it has been customary in the past to use the peak ground acceleration as the seismic intensity for hazard analysis, it is now more common to use the spectral acceleration at the structure's fundamental period, as this has been shown to be an effective intensity measure which can generally be well correlated with typical EDPs, including drift [98, 111, 125, 127, 128].

Using drift and spectral acceleration, it is convenient to express the probability of surpassing some specified drift level,

$$P[D > d] = \sum_{x_i} P[D > \theta | S_a = x_i] P[S_a = x_i] \tag{2.20}$$

The inner term forms the basis for fragility analysis.

2.5.3 Fragility

As described earlier, the $P[D > \theta | S_a = s]$ term describes structural fragility. In this form, it describes the probability of the structure surpassing a certain drift level when subjected as a function of an excitation's spectral acceleration. Dating back to the original work by the U.S. NRC [102], fragility is commonly modeled as a lognormal cumulative distribution function [98, 108, 111], with the form

$$F_R(x) = \Phi\left[\ln(x/m_R)/\beta_R\right] \tag{2.21}$$

where m_R represents the *median* capacity with logarithmic standard deviation β_R representing inherent randomness in seismic capacity. The notation Φ[] indicates the standard normal probability integral. However, there are also associated epistemic uncertainties, which can be vested in the median capacity estimate m_R. To first order, then, m_R can be replaced with random variable M_R, which has which has mean m_R and logarithmic standard deviation β_U [98]. Thus, Equation 2.21 represents the *mean* fragility, and total uncertainty β_R is expressed as

$$\beta_R = \sqrt{\beta_{RR}{}^2 + \beta_U{}^2} \tag{2.22}$$

where the aleatory (β_{RR}) and epistemic (β_{RU}) uncertainties each contribute to the total uncertainty. Going one step further, the aleatory uncertainty can be separated into uncertainty in both demand and capacity

$$\beta_{RR}{}^2 = \sqrt{\beta_{RD}^2 + \beta_{RC}^2} \tag{2.23}$$

where β_{RD} and β_{RC} represent aleatory uncertainty in demand and capacity, respectively [101]. The use of the symbol β, used here to quantify dispersions, is not to be confused with the reliability index β used for first-order second moment (FOSM) or first-order reliability method (FORM); the use of β here follows from its origins in the nuclear industry [102].

As proposed by the SAC/FEMA project [111], an exponential relationship between drift and spectral acceleration can be represented in the areas of interest as

$$\theta_{\max} = a \cdot S_a^b \cdot \varepsilon \tag{2.24}$$

where ε is a lognormal random variable with median 1 and logarithmic standard deviation $\sigma_{\ln\varepsilon}$. After performing a number of nonlinear analyses, a regression on ln $\theta_{\max}$ *vs*. ln S_a to characterize the mean and standard deviation results in a mean value for substitution of m_R in Eq. 2.21 as [101]

$$\hat{\theta}_{\max} = a \cdot S_a^b \tag{2.25}$$

The standard deviation $\sigma_{\ln\varepsilon}$, written as $\beta_{D|Sa}$ when the uncertainty is vested in the ground motions [101, 129], represents the seismic demand uncertainty, and is here represented by β_{RD}. Consistent with the equal displacement rule [130], it can be assumed that the exponent $b \approx 1$, as proposed by Cornell et al. [111], for structures with moderate fundamental periods (>1sec), such as steel moment frames. However, this simplification is not necessary is a suite of nonlinear time history analyses will be performed regardless.

Under the assumptions discussed, the mean fragility curve for a drift limit θ can be described by the CDF, manipulated from Equation 2.21

$$F_R(\theta) = \Phi\left[\ln[\theta/(a \cdot S_a{}^b)]/\beta_{TU}\right] \tag{2.26}$$

or

$$P\left[D > \theta \middle| S_a = s\right] = 1 - \Phi\left[\ln[\theta/(a \cdot S_a{}^b)]/\beta_{TU}\right] \tag{2.27}$$

where

$$\beta_{TU} = \sqrt{\beta_{RD}^2 + \beta_{RC}^2 + \beta_U^2} \tag{2.28}$$

This approach to fragility analyses has been successfully applied to steel frames [101, 129], reinforced concrete buildings [101, 131-133], unreinforced masonry buildings [110, 134], bridges [135, 136], and a multitude of other structures.

While the common demand model is logarithmic (Equation 2.25), the lognormal assumption behind fragility (Equation 2.21) does not necessitate a purely log-log linear demand relationship between EDP and SI. Ramamoorthy et al. [131, 132] found that, in their case, a bilinear piecewise logarithmic fit was superior, and evaluated the lognormal fragility piecewise, accordingly. In fact, any demand relationship can be used, assuming that the lognormality assumption is still valid.

2.5.4 Limit States

Defining appropriate limit states is important for any comprehensive performance assessment or fragility analysis in general. While the link between qualitative damage states and quantitative limit states was alluded to earlier, the methodology for determining them was not discussed. Limit states, or the points at which a structure or component is no longer capable of satisfying a desired function or at a desired performance, are generally given qualitatively. Thus, the engineer must determine the relevant quantitative limits for design or evaluation. The most comprehensively documented set of structural limit states are found in FEMA 356 [30], described as *performance levels*:

1. Immediate Occupancy (IO) – occupants are allowed immediate access into the structure following the earthquake and the pre-earthquake design strength and stiffness are retained
2. Life Safety (LS) – building occupants are protected from loss of life with a significant margin against the onset of partial or total structural collapse

3. Collapse Prevention (CP) – building continues to support gravity loading, but retains no margin against collapse

FEMA 356 presents typical, representative values for a number of common structural systems, however other values have been proposed elsewhere (e.g. [137-140]). Still, one set of values may not be arbitrarily accepted over another without due consideration for the structure in question, as capacity limits may be highly variable from one structure to another, even within the same class designation.

Another way of defining limit states quantitatively is based on levels which can be identified analytically using nonlinear pushover techniques [110], taking care to use the most critical loading patterns. The two common levels are

1. First Yield (FY) – deformation at which a single member initiates yielding under imposed lateral loading
2. Plastic Mechanism Initiation (PMI) – deformation at which a plastic mechanism initiates under imposed lateral loading

An additional level can be determined from an incremental dynamic analysis [141, 142] to determine the collapse point, or the average deformation from a suite of incrementally amplified ground motions which cause the stiffness to degrade by a certain amount (generally to 20% of initial, elastic stiffness).

In general, if the choice of limit state is not dictated by an owner or building code, they can be chosen according to the analyst, since performance assessments are generally done as comparisons, where relative differences are more important than absolute numbers.

However, care must be taken to ensure that limit states are chosen consistently in order to make fair comparisons.

2.5.5 HAZUS

As mentioned earlier, HAZUS [107] provides lognormal fragility curves based on expert opinion for a number of structural systems. In addition, estimated restoration timelines are given for most systems. Included are several port transportation components, including cranes/cargo handling equipment, described in the HAZUS Technical Manual [107]. Five damage states are defined: none, slight/minor, moderate, extensive, and complete. Table 2.2 gives a qualitative description of the damage states for unanchored/rail-mounted port cranes.

Table 2.2 Description of HAZUS damage states for unanchored/rail-mounted port cranes [107].

Damage	*Description*
slight/minor	Minor derailment or misalignment without any major structural damage to the rail mount. Minor repair and adjustments may be required before the crane becomes operable.
moderate	Derailment due to differential displacement of parallel track. Rail repair and some repair to structural members is required.
extensive	Considerable damage to equipment. Toppled or totally derailed cranes are likely to occur. Replacement of structural members is required.
complete	Same as extensive.

The probability of reaching a given damage state $D=d$ is given by

$$P[D \geq d \mid IM] = \Phi\left[\frac{1}{\beta}\ln\left(\frac{IM}{IM_D}\right)\right] \tag{2.29}$$

where IM_D is the median value of the intensity measure, IM, at which the structure reaches the threshold of the damage state D, β is the standard deviation of the natural

logarithm of *IM* for the damage state, and Φ indicates the standard normal cumulative distribution function (CDF). Two intensity measures are defined: peak ground acceleration (PGA), which indicates damage due to ground shaking, and permanent ground deformation (PGD), indicating damage due to lateral spreading. The fragility curve parameters and mean downtimes for unanchored/rail-mounted cranes are presented in Table 2.3.

Table 2.3. Fragility and restoration parameters of HAZUS damage states for unanchored/rail-mounted port cranes [107].

	Fragility			Restoration	
	PGA median (g)	PGD median (in)	β	Mean (days)	σ
slight/minor	0.15	2	0.6	0.4	0.35
moderate	0.35	4	0.6	6	6
extensive	0.8	10	0.7	30	30
complete	0.8	10	0.7	75	55

Because fragility functions are defined for both PGA and PGD, a simple multi-hazard analysis must be done to determine the damage state probabilities.

CHAPTER 3

ANALYTICAL DESCRIPTION OF PORTAL UPLIFT BEHAVIOR

3.1 Introduction

Container cranes built in regions of moderate to high seismicity sit on wheels on top of crane rails built into a wharf deck. The crane stays in place due to the effects of gravity and the lateral restraint provided by a small flange on each wheel. Therefore, they can uplift and lose lateral constraint in its legs as a result of seismic excitation, as discussed in Chapter 2. Early design assumptions in the United States assumed that allowing uplift and the subsequent rocking was desirable for seismic loading, and act as the type of "isolation" demonstrated by pure uplift (Section 2.3), thus limiting internal forces and protecting the crane from damage [10]. In fact, the most applicable design guide, the ASCE Seismic Design Guidelines for Ports, says that "if a leg does lift, the forces are limited to the load required to lift a leg" [7]. Performance of early container cranes during past moderate earthquakes, especially the 1989 Loma Prieta earthquake, appears to back this assumption [7]. Thus, tie-downs to restrict uplift are reserved for areas where wind loads from hurricanes or typhoons control lateral load design [143]. As a result, wharf structures in regions of seismicity but low wind are not designed with tensile crane uplift forces in mind, and would have very little uplift resistance capacity even with tie-downs installed due to the high cost of providing such capacity. As container cranes continue to grow in response to the continued demand for ever-larger container ships [8], it is therefore important to revisit the assumption of "isolation" from the uplift response with the understanding that uplift cannot be economically prevented.

A first clue that "isolation" does not always occur for uplifting container cranes came after the 1995 Kobe earthquake, where uplift was identified as a direct cause of collapse for some of the failed cranes [16]. Still, these failures were attributed in the US to lateral spreading of the crane rails from liquefaction [7], and little further attention was given to the issue of container crane uplift behavior. In Japan, container crane vulnerability was addressed through expensive base isolation techniques [21] which have not gained traction in the US for various reasons [9].

This chapter reevaluates uplift behavior as it relates to structures like container cranes, which behave essentially like a portal frame when excited by seismic motion. Recall from Section 2.3 that a key assumption for classic uplift is that shear stiffness remains constant before, during, and after an uplift event. In the case of a container crane, or a portal frame structure in general, uplifted elements cannot carry base shear and thus do not contribute to overall shear stiffness during uplift events. This observation can be made for any structure which can uplift due to seismic excitation and that loses horizontal restraint during uplift, resulting in "wandering" of the column base. This form of uplift response is referred to here as "softened uplift with initial sliding," or "portal uplift." A simplified approach similar to classic uplift as derived by Meek [32] and Chopra & Yim [34] is taken, evaluating the free vibration response after the onset of uplift for systems with typical vibration periods. To avoid unnecessary complication, single-mass models are used. The effect of structure slenderness, excitation magnitude, and shear stiffness reduction are considered. Comparisons are made with the pure uplift case, where shear

stiffness is preserved during uplift. An example of the simplified methodology is presented in the form of response spectra.

3.2 System Considered

The simplest structural system which exhibits the response of interest is considered here to provide the greatest flexibility and relevance. For this purpose, a simple one-story one-bay elastic portal frame with initially pinned base connections is chosen, as shown in Figure 3.1. Mass, m, is assigned only at the midpoint of the portal beam. Dimensions H and $2E$ represent portal height and portal gage, respectively. For simplicity, it is assumed that the portal flexibility is provided by the elastic behavior of the columns, while the portal beam is effectively rigid. Therefore, the columns of a portal frame with vibration period T have a section modulus of

$$I = \frac{m \cdot H^3}{6E_s}\left(\frac{2\pi}{T}\right)^2 \tag{3.1}$$

where E_s is the elastic modulus of the base material, assumed here to be steel. Additionally, damping ratio ξ is assumed present in the flexible columns.

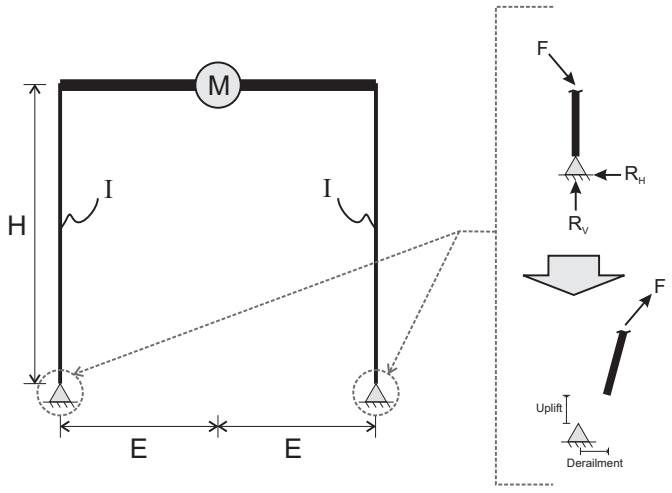

Figure 3.1. SDOF portal frame used for uplift study, illustrating removal of constraint during uplift

Two geometric parameters, R and α, are defined for convenience. R is the diagonal distance from the mass to a column base in the undeformed condition ($R^2 = E^2 + H^2$), while α is an aspect ratio ($\alpha = E/H$) or a measure of structure slenderness.

The boundary condition is not a traditional pin; it cannot produce tensile reactions, and thus cannot provide restraint to uplift. Moreover, lateral restraint is provided only while there is some axial compressive reaction (see Figure 3.1). In other words, the horizontal restraint is active only while the column base is in contact with the ground. This form of unbonded contact allows uplift and subsequent lateral displacement (derailment) of the column base. The lateral displacement during uplift events can cause "walking" of the portal frame, or simply migration of the uplifted column base from the point of initial contact.

Further, it is assumed that the boundary condition is sufficient to avoid the possibility of total-structure sliding, where the structure slides relative to the ground prior to any uplift. The reader is referred to the literature (e.g. [144]) for the analysis of coupled elastic and total-structure sliding response.

Uplift occurs when the overturning moment overcomes the restoring moment provided by gravity:

$$M > mgE \tag{3.2}$$

The overturning moment for undamped structures is

$$M = kHu_{cr} \tag{3.3}$$

where u_{cr} is the critical structural deformation required for initial uplift. Making the appropriate substitutions and simplifying, this critical displacement is

$$u_{cr} = \frac{\alpha \cdot g}{\omega^2} \tag{3.4}$$

Throughout this paper, the dynamic response of this simple portal frame with unbonded-contact is compared with that of its bonded-contact counterpart, the pinned-base case. However, the counterpart to some other generalized unbonded-contact structure could have some other type of a fixed-base boundary; the terminology used here for portal frames is not meant to reduce the generality of the results.

3.3 Response Behavior

With an excitation of sufficient magnitude, the free vibration response of such a system has three sequential phases, as shown in Figure 3.2: (a) elastic, (b) sliding, and (c) tipping. During the tipping stage, the total displacement of the mass is from structural deformation, u, and rigid body rotation, $x = H \cdot \sin\theta$. During each phase, the structural deformation response can be described by a linear differential equation as a sum of the complementary solution with constants depending on the initial conditions and a particular solution corresponding to the excitation [32, 34]. Continuity between stages is enforced through the initial conditions. Thus, the total deformation response is nonlinear in nature, but is a piece-wise combination of linear responses.

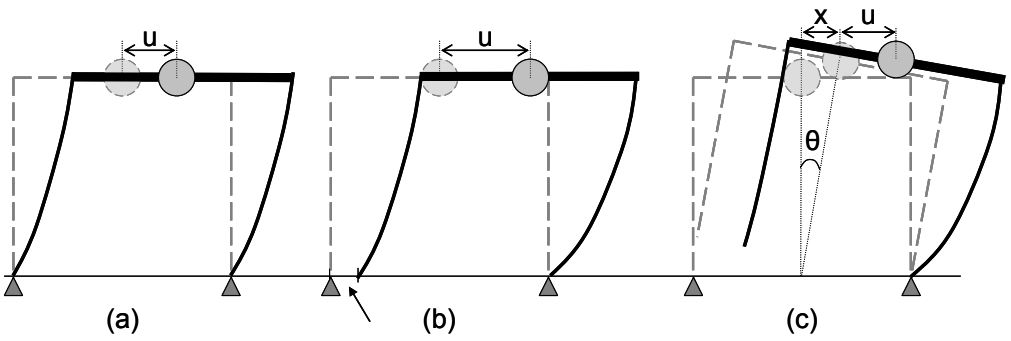

Figure 3.2. Schematic of uplift response of portal frame with unbonded contact, exhibiting three-stage behavior: (a) elastic, (b) sliding, (c) tipping.

Idealized rules governing the structural deformation, u, of each phase and their transitions when subjected to earthquake excitations are described in the ensuing sections. Small angle theory is applied, so that $\sin\theta$ and $\cos\theta$ are approximated as θ and 1, respectively. In addition, because $mg/kH \ll 1$, p-δ effects are ignored, simplifying the governing differential equations from order 4 to 2 [32].

3.3.1 Stage 1: Elastic

Initially, the structure behaves linearly, no different than the behavior with bonded contact. Therefore, the standard equation of motion (EOM) for a single-degree-of-freedom (SDOF) system applies:

$$\ddot{u} + 2\xi\omega\dot{u} + \omega^2 u = -\ddot{u}_g(t) \tag{3.5}$$

in which $\omega = 2\pi/T$ = the natural frequency, and $\xi = c/2m\omega$ = the damping ratio. The undamped free vibration response can be approximated by sinusoidal motion with amplitude u_0:

$$u = u_0 \sin(\omega t) \tag{3.6}$$

At some critical point, uplift will occur, and this EOM no longer governs. This occurs when $u > u_{cr}$, shifting the response to stage 2.

3.3.2 Stage 2: Sliding

Once structural deformation surpasses a critical displacement (Eq. 3.4), one column no longer carries axial load. Intuitively, one could imagine that column beginning to uplift. However, when that column no longer carries axial compression, it can no longer provide lateral resistance. Therefore, the shear stiffness decreases. For generalization, n is used to represent the reduction in shear stiffness; in this case, when shear stiffness is reduced in half (as is the case with our portal frame), n = 2. This reduction in stiffness corresponds with a change in frequency and critical displacement. The new frequency and critical displacement is

$$\overline{\omega} = \frac{\omega}{\sqrt{n}},\ \overline{u}_{cr} = n \cdot u_{cr} \tag{3.7}$$

Note that the critical displacement is increased as a result of the reduction in stiffness, which increases the overturning moment, thereby requiring increased displacement for uplift to occur. Therefore, the freed leg can slide along the "ground" surface (or if infinite friction is assumed, incrementally "jump" along the surface). Ignoring the force from friction for simplicity (which is necessarily small due to being "activated" only under very small axial loads), a new EOM is defined:

$$\ddot{u} + 2\overline{\xi}\overline{\omega}\dot{u} + \overline{\omega}^2 u = -\ddot{u}_g(t) \tag{3.8}$$

in which $\overline{\xi} = \xi / n$, a reduction in damping due to the fact that only the leg still in ground contact contributes to damping related to structural deformation u.

As Meek proposed [32], an idea later reinforced by Chopra and Yim [34], a good estimate of response may be found if the ground acceleration is neglected, as it does not greatly affect the structural deformation after reaching the initial critical deformation, or while the structure is rocking. Once a structure reaches the initial critical deformation, its response is dominated by the free vibration. In other words, it is assumed that the maximum deformation occurs in the first cycle or two after shifting from the elastic response stage, a result shown to be true for uplift-susceptible structures of typical (>~0.4s) vibration periods [34, 35]. Therefore:

$$\ddot{u} + 2\bar{\xi}\bar{\omega}\dot{u} + \bar{\omega}^2 u = 0\,,\ u(0) = u_{cr} \tag{3.9}$$

with solution

$$u = e^{-\bar{\xi}\bar{\omega}t'}\left[u_{cr}\cos(\bar{\omega}t') + \frac{\dot{u}_{cr}}{\bar{\omega}}\sin(\bar{\omega}t')\right] \tag{3.10}$$

where t' is the time after loss of base lateral resistance.

The initial velocity of stage 2, the velocity at the point of initial critical deformation, can be approximated from the sinusoidal motion of the initial bonded-contact system:

$$\dot{u}_{cr} = \omega\sqrt{u_0^2 - u_{cr}^2} \tag{3.11}$$

Thus the solution deformation during sliding is:

$$u = u_{cr}e^{-\bar{\xi}\bar{\omega}t'}\left[\cos(\bar{\omega}t') + \sqrt{n\left[\left(\frac{u_0}{u_{cr}}\right)^2 - 1\right]}\sin(\bar{\omega}t')\right] \tag{3.12}$$

with maximum value

$$\bar{u}_0 = u_{cr} e^{-\bar{\xi}\phi} \sqrt{1 + n\left[\left(\frac{u_0}{u_{cr}}\right)^2 - 1\right]} \tag{3.13}$$

$$\text{where } \phi = \frac{\pi}{2} - \tan^{-1}\left\{\left(n\left[\left(\frac{u_0}{u_{cr}}\right)^2 - 1\right]\right)^{-1/2}\right\} \tag{3.14}$$

If $\bar{u}_0 > \bar{u}_{cr} = n \cdot u_{cr}$, uplift occurs, and the response moves to stage 3.

3.3.3 Stage 3: Tipping

When the structure deforms beyond the critical deformation modified for having lost pure base contact, uplift occurs, resulting in a tipping response. Total displacement of the portal frame, measured from the midpoint of the portal beam, is a result of structural deformation, *u*, and translational motion associated with rigid rotation, *x*. Assuming small angles, $x = H \cdot \sin(\theta)$, as shown in the earlier figure, part (c). When this stage occurs, two EOMs govern the response:

$$\begin{aligned} &\ddot{u} + H\ddot{\theta} + 2\bar{\xi}\bar{\omega}\dot{u} + \bar{\omega}^2 u = -\ddot{u}_g(t) \\ &\ddot{u} + \frac{R^2}{H^2}\left(H\ddot{\theta}\right) = -\ddot{u}_g(t) \mp g\frac{E}{H} \end{aligned} \tag{3.15}$$

The algebraic sign of the restoring moment corresponds with uplift of the left and right column. Combining, manipulating, and simplifying these two equations results in one EOM:

$$\ddot{u} + 2\zeta\lambda\dot{u} + \lambda^2 u = -\left[\ddot{u}_g(t) \mp g\frac{H}{E}\right] \tag{3.16}$$

$$\text{where } \lambda = \bar{\omega}\frac{R}{E} = \frac{\omega}{\sqrt{n}}\frac{R}{E}, \text{ and } \zeta = \bar{\xi}\frac{R}{E} = \frac{\xi}{n}\frac{R}{E}$$

Notice that the frequency and damping of the uplifted structure increase, proportional to *R/E*, a result previously observed and explained for simpler uplifting structures [32, 34].

Making the same simplification regarding ground acceleration as in stage 2 response, we can find a good estimate for the response using the free vibration EOM:

$$\ddot{u} + 2\zeta\lambda\dot{u} + \lambda^2 u = \pm g\frac{H}{E},\ u(0) = \bar{u}_{cr} \tag{3.17}$$

The solution of this differential equation is

$$u = n \cdot u_{cr}\frac{H^2}{R^2} + e^{-\zeta\lambda\tau}\left[n \cdot u_{cr}\frac{E^2}{R^2}\cos(\lambda\tau) + \frac{\bar{\dot{u}}_{cr}}{\lambda}\sin(\lambda\tau)\right] \tag{3.18}$$

where τ is the time after uplift. Applying a similar technique as before, we can use the free vibration stage 2 response to estimate the modified critical velocity, or velocity at uplift:

$$\bar{\dot{u}}_{cr} = \bar{\omega}\sqrt{\bar{u}_0^2 - \bar{u}_{cr}^2} = \bar{\omega}u_{cr}\sqrt{\left(\frac{\bar{u}_0}{u_{cr}}\right)^2 - n^2} \tag{3.19}$$

Subsequently:

$$u = n \cdot u_{cr}\frac{H^2}{R^2} + e^{-\zeta\lambda\tau}\left[n \cdot u_{cr}\frac{E^2}{R^2}\cos(\lambda\tau) + \frac{E}{R}u_{cr}\sqrt{\left(\frac{\bar{u}_0}{u_{cr}}\right)^2 - n^2}\,\sin(\lambda\tau)\right] \tag{3.20}$$

which has maximum value

$$u_{\max} = u_{cr}\left\{n\frac{H^2}{R^2} + \frac{E}{R}e^{-\zeta\varphi}\sqrt{n^2\frac{E^2}{R^2} + \left[\left(\frac{\bar{u}_0}{u_{cr}}\right)^2 - n^2\right]}\right\} \tag{3.21}$$

$$\text{where } \varphi = \frac{\pi}{2} - \tan^{-1}\left\{\left(n\frac{E}{R}\right)\left[\left(\frac{\bar{u}_0}{u_{cr}}\right)^2 - n^2\right]^{-1/2}\right\} \tag{3.22}$$

3.3.4 Undamped Response

When damping can be considered negligible or some conservatism is desired, the overall solution can be considerably simplified. The maximum deformation with no damping during the sliding stage is

$$\bar{u}_0 = u_{cr}\sqrt{1+n\left[\left(\frac{u_0}{u_{cr}}\right)^2-1\right]} \tag{3.23}$$

This is much simpler than Eq. 3.13 and can be substituted into Eq. 3.21. After some manipulation and simplification, the maximum deformation during the tipping stage is

$$u_{\max} = u_{cr}\left\{n\frac{H^2}{R^2}+\frac{E}{R}\sqrt{1+n\left[\left(\frac{u_0}{u_{cr}}\right)^2-1\right]-n^2\frac{H^2}{R^2}}\right\} \tag{3.24}$$

In terms of α rather than E, H, and R, the maximum deformation during tipping is:

$$u_{\max} = u_{cr}\left\{\frac{n}{1+\alpha^2}+\frac{\alpha}{\sqrt{1+\alpha^2}}\sqrt{1+n\left[\left(\frac{u_0}{u_{cr}}\right)^2-1\right]-\frac{n^2}{1+\alpha^2}}\right\} \tag{3.25}$$

3.3.5 Combined Response

When the excitation magnitude is sufficient, the total response will include instances of all three response stages. The combination is piece-wise, with initial conditions providing continuity between each stage. Prior to uplift, the response is sinusoidal with amplitude u_0 and frequency ω (Eq. 3.6). Once structural deformation reaches u_{cr} (Eq. 3.4), the response shifts to sinusoidal with amplitude $\bar{u}_0$ (Eq. 3.13) and frequency $\bar{\omega}$ (Eq. 3.7). Structural deformation then reaches $\bar{u}_{cr}$ (Eq. 3.7), and the response oscillates about

$u = n \cdot u_{cr}/(1+\alpha^2)$ with peak deformation $u_{\max}$ (Eq. 3.21) and increased frequency λ. The uplifted column then lands, the deformation cycle reverses, the opposite leg loses contact, and the rocking cycle continues.

When damping is present, the assumptions behind this simplified methodology are even more suitable, as it is even more likely that the peak displacement occurs in the first cycle or two, because the increased damping during the uplift stage quickly degrades or even eliminates the high-frequency oscillation.

A measure of the magnitude of excitation can be defined based on the amplitude of oscillation of the bonded-contact system, u_0, in relation to the initial critical deformation of the uplift-capable system, u_{cr}. As proposed by Psycharis [35], this measure of excitation strength is then

$$\beta = \frac{u_0}{u_{cr}} \tag{3.26}$$

Two qualitative examples of the piece-wise combined response for an undamped system are shown in Figure 3.3 for $\alpha = 0.4$ and (a) $\beta = 1.8$ and (b) $\beta = 4$. The time scales for the two graphs are different and critical and peak deformations are labeled. Notice that at some levels of excitation amplitude β, such as in Figure 3.3(a), the peak deformation of the uplift-capable system ($u_{\max}$) is greater than the peak deformation of the comparable pinned (bonded-contact) system (u_0), indicating response amplification. However, for greater excitations, such as in Figure 3.3(b), the peak deformation of the uplifting structure ($u_{\max}$) is less than that of the comparable bonded-contact system (u_0), indicating response reduction. This behavior is quite different than the pure uplift case presented by

previous researchers (i.e. [32, 34, 35]), where uplift resulted in some amount of response reduction, no matter the magnitude of excitation for structures of typical vibration periods.

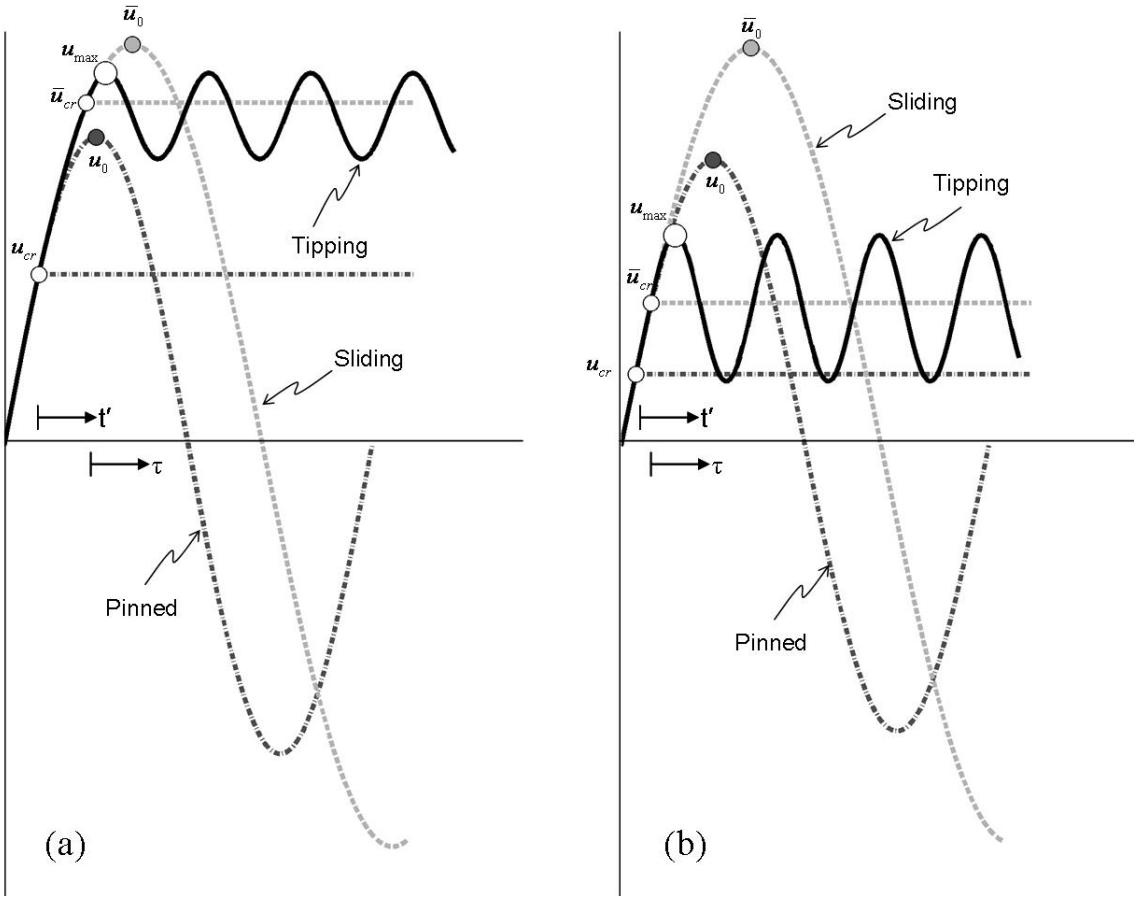

Figure 3.3. Qualitative free vibration response representation of three-stage behavior using approximate method of analysis, where α = 0.4 and (a) β = 1.8, causing response amplification and (b) β = 4, causing response reduction.

3.4 Response Modification Curve

From the equations of maximum deformation, it is clear that a relationship exists between the hypothetical bonded-contact response, u_0, and the true maximum response, u_{max}. Meek [32] referred to this relationship as a response reduction, though the terminology is generalized here due to the possibility of response amplification, as shown in the prior

section. The response modification (RM) relationship is plotted in Figure 3.4 for several values of α with $n = 2$. Rather than strictly considering deformations, values of base shear V are plotted, nondimensionalized with respect to weight, mg. The base shear of the uplifting structure, $V = ku_{max}$, is plotted with respect to that of the equivalent bonded-contact system, $V = ku_0$. Thus, the abscissa is a measure of hypothetical lateral force coefficient for a bonded-contact structure, while the ordinate represents the true lateral force coefficient for the uplifting system considered. The dashed line with slope equal to unity indicates the maximum response of a bonded-contact system. Therefore, a value on the RM curve above the dashed line indicates amplification, while a value under the dashed line indicates reduction.

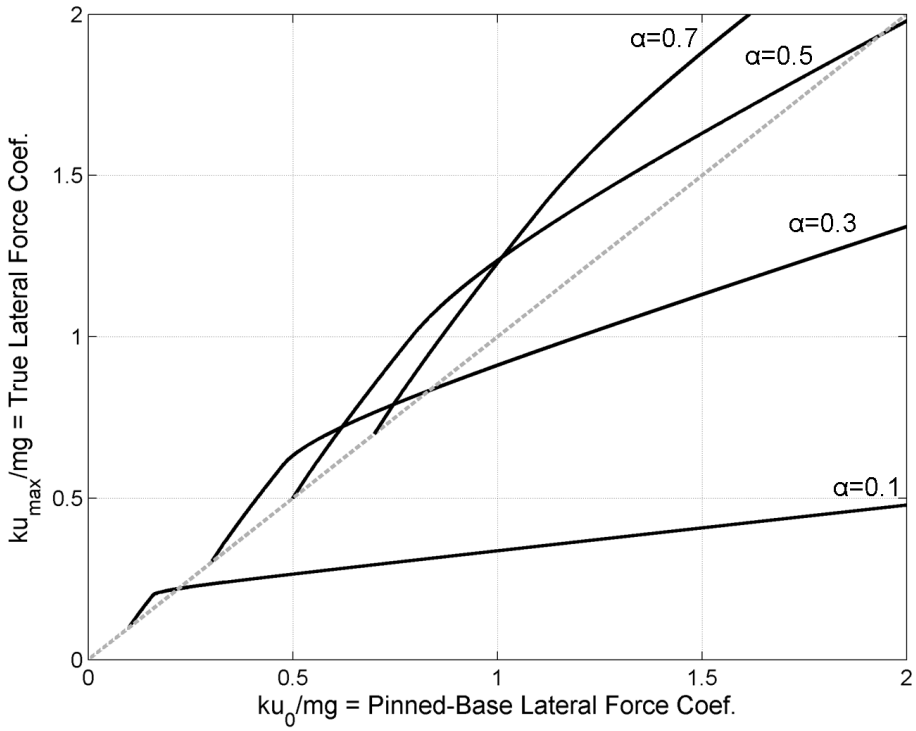

Figure 3.4. Response modification curves for unbonded contact of undamped portal frames ($n = 2$) with various values of structure slenderness.

For all values of α, the response is no different than the pinned case up to a lateral force coefficient of α, where $u_{\max} = u_{cr}$. From that point on, the system with reduced shear stiffness deforms more than the bonded-contact structure. For some range of excitation, or pinned-base lateral force coefficient, the response continues to amplify. This range of amplification is much smaller for more slender structures (i.e. α~0.1), but can extend significantly for more stocky structures (i.e. α>~0.5). At some excitation, however, the true response crosses the bonded-contact response line, and is reduced for all greater excitations. This switch-point occurs in the tipping stage and, for undamped structures, occurs where:

$$\frac{u_0}{u_{cr}} = \frac{n + \sqrt{(n-1)^2\left(n+1+\alpha^2\right)}}{1+\alpha^2-n\alpha^2} \tag{3.27}$$

This switch-point marks the shift from response amplification to response reduction.

3.5 Maximum Response Amplification

The relative amplification and reduction is a function of n, the magnitude of loss of shear stiffness. With higher n, the RM curve has higher slope after initial uplift, later switch-point for a given α, and greater amplification over the case of pure uplift. An example of this is shown in Figure 3.5, where $\alpha = 0.4$, and $n = 1.1, 1.5, 2, 3$. An RM curve where $n = 1$ is identical to the case of pure uplift described for undamped structures by Meek [32] and for damped structures by Chopra & Yim [34], exhibiting no amplification.

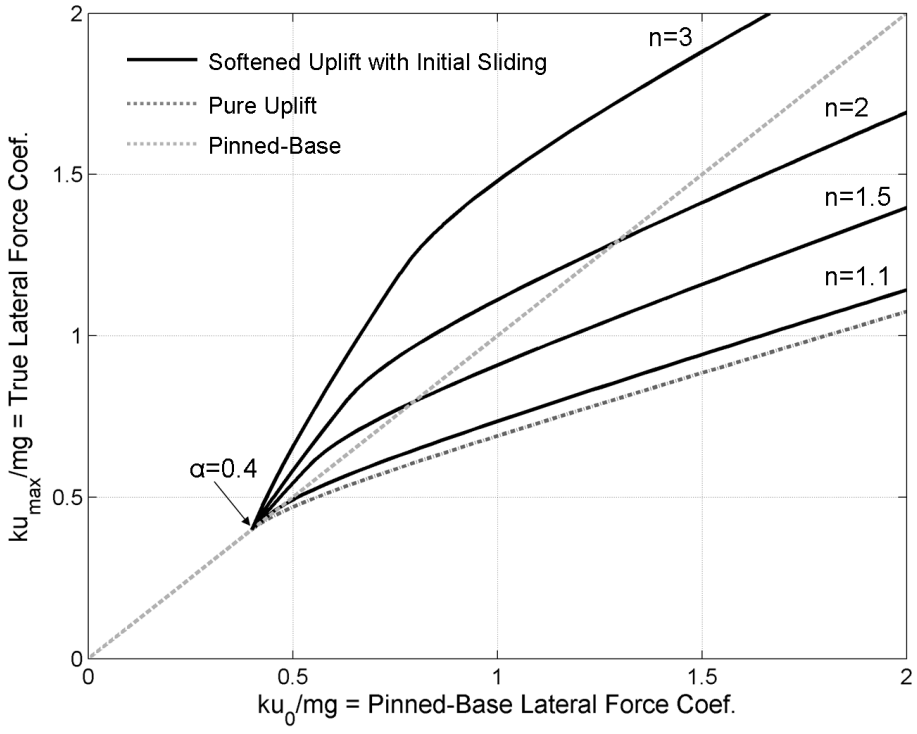

Figure 3.5. Response modification curves for unbonded contact of undamped structures with various amounts of shear stiffness reduction, $\alpha = 0.4$.

With $n > 1$, the slope of the RM curve is greater than unity in the sliding stage, but lower when in the tipping stage. Thus, the maximum amplification from the bonded-contact response occurs at the threshold between the sliding and tipping stages, where $u_{\max} = n \cdot u_{cr}$, or $\beta = n$. This maximum amplification can be calculated for undamped systems as

$$\left(\frac{u_{\max}}{u_0}\right)_{\max} = \frac{n}{\sqrt{\frac{n^2-1}{n}+1}} \tag{3.28}$$

Hence, the maximum amplification is a function only of n, and does not depend on the structure slenderness, α. In the case of the portal frame, where $n = 2$, the maximum amplification is 1.265, or 26.5%.

3.6 Comparison with Pure Uplift

The response modification (RM) curves can easily be compared with those of pure uplift scenarios, when either the foundation mat uplifts, or wherever else the shear stiffness is unaffected by uplift ($n = 1$). Figure 3.6 compares these response modification curves for $n = 2$ and $\alpha = 0.1$, 0.3, and 0.5.

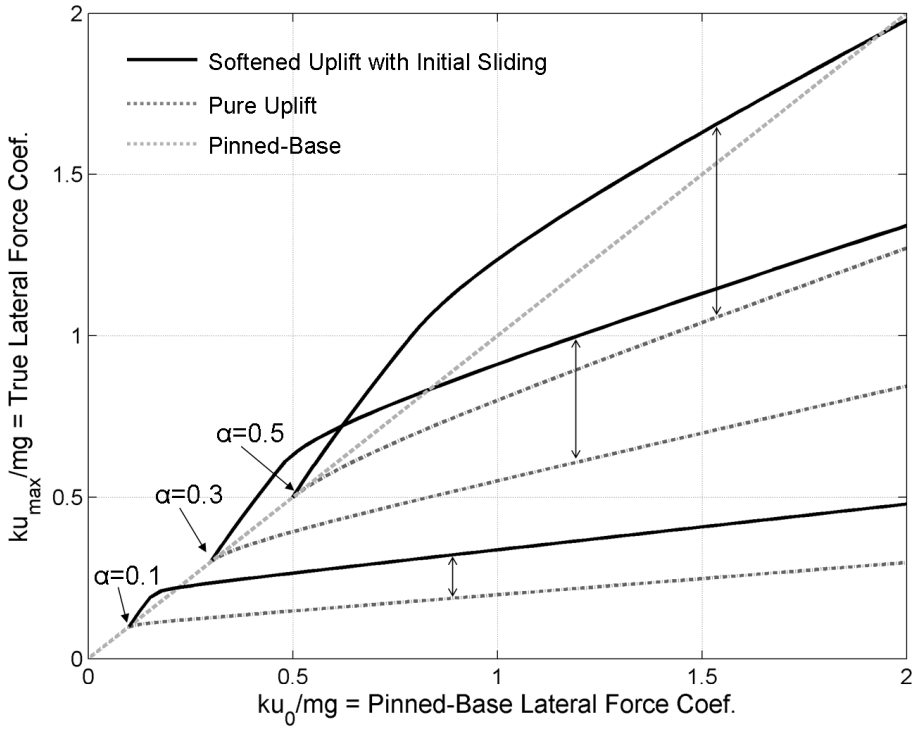

Figure 3.6. Response modification curves for unbonded contact of undamped portal frames ($n = 2$) with different aspect ratios as compared with pure uplift ($n = 1$).

It is clear that pure uplift ($n = 1$) does not cause amplification under any condition of excitation, but rather provides a form of isolation, limiting the peak structural response. However, uplift of the kind considered here ($n > 1$) exhibits response amplification when excited more than the initial critical excitation, but less than the switch point. The slope of the RM curve for the considered structures asymptotically approaches that of pure

uplift as excitation increases, but its magnitude is always greater, with a larger difference for more stocky structures. Thus, the damaging effects of decreased shear stiffness during uplift become more significant with less slender structures.

3.7 Finite Element Verification

A finite element model is constructed within OpenSees [145] to verify the response predicted by the analytical formulations. The system is developed as described previously. A zero-length, node-to-node frictional contact element is used at the base of the columns to couple the horizontal restraint to vertical reaction magnitude. The coefficient of friction is chosen as $\mu = 0.9$, which ensures that total sliding does not occur prior to reaching the initial critical deformation.

In order to cause free-vibration response, a rectangular pulse force is used. This approach is advantageous, as free vibration and peak deformation occurs in the first cycle, thus avoiding numerical difficulties associated with impact.

A rectangular pulse force is applied at the mass, with magnitude p_0 and duration t_d. The response to this force has two parts, the forced-vibration and free-vibration phases, which are described in detail by Chopra [146]. Here, $t_d/T_n = 1/10$, which ensures that there is no peak during forced-vibration. Rather, the response continues to build to some displacement and velocity achieved at the end of the pulse, which serve as the initial conditions for the free-vibration. From [146], the maximum dynamic deformation of the bonded-contact system due to this force is known to be

$$u_0 = 2\frac{p_0}{\omega^2 m}\sin\left(\frac{\pi t_d}{T_n}\right) \tag{3.29}$$

Making some substitutions and manipulating, the magnitude of the pulse with a chosen duration that achieves a desired deformation of the bonded-contact system can be determined:

$$p_0 = \frac{\beta\alpha \cdot mg}{2\sin\left(\pi\frac{t_d}{T_n}\right)} \tag{3.30}$$

Therefore, the maximum deformation of the uplift-capable system, $u_{\max}$, caused by the described rectangular pulse force, can be directly compared with the associated bonded-contact system.

This analysis is performed for a range of β. The peak deformation is identified, which occurs during the first cycle of free vibration, as expected. A plot comparing the peak deformations of the FE analyses and predicted response for α = 0.2 and 0.4 and with negligible damping is shown in Figure 3.7.

Notice that the FEM agrees well with the predicted response throughout the range of input force. It can be seen that the FEM results show slightly less amplification when compared to the bonded-contact response within the sliding stage. This is a result of ignoring the force from friction in the analytical formulation, which acts to increase the effective damping during this stage. Relying on the slight reduction due to friction is not advised, however, as the true friction coefficient is not known. Further, if the column base becomes temporarily restrained, such as by an exceedingly rough patch or localized

ground damage, infinite friction could be assumed. Therefore, the slightly conservative estimate provided by the analytical formulation is deemed appropriate.

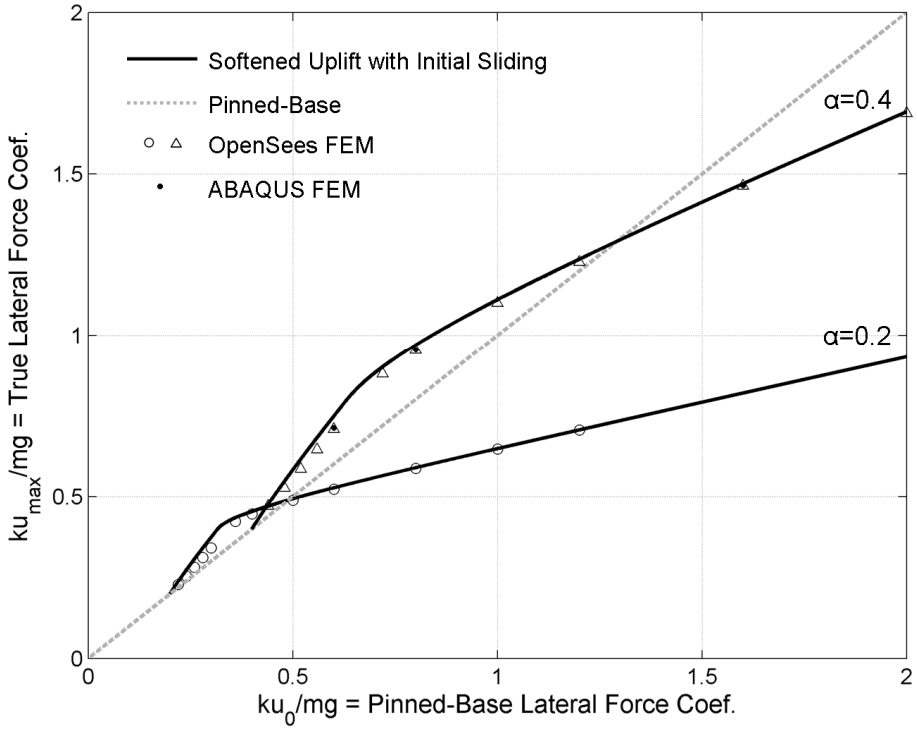

Figure 3.7. Response modification curves for unbonded contact of undamped portal frames (n = 2) and the corresponding finite element results.

When damping is included, it is much more difficult to calculate the switch-point and maximum amplification due to the reliance on angles φ and Φ. However, it is useful to compare the predicted response with that of the FEM. Figure 3.8 shows the same analyses and predictions as in the figure above, but with ξ = 5% rather than negligible damping. Again, the FEM agrees well with predicted responses. As before, neglecting the friction force causes a slightly conservative estimate of deformation response in the sliding region. It is worth noting that damping has a similar relative impact for pure uplift, as presented by Chopra & Yim [34].

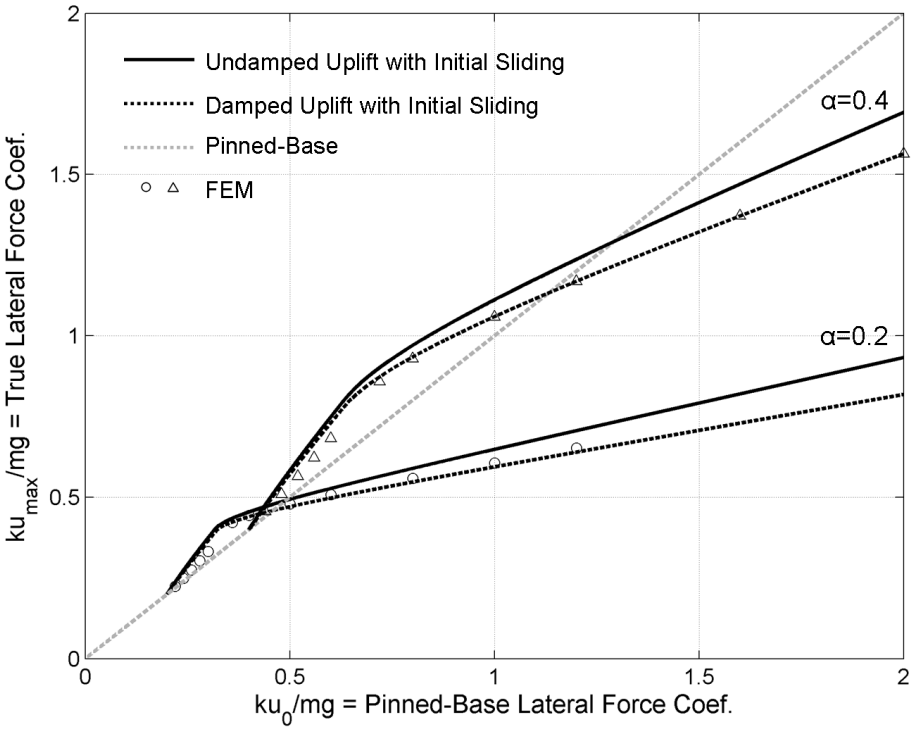

Figure 3.8. Response modification curves for unbonded contact of portal frames (n = 2) with and without damping ξ = 5%, and the corresponding finite element results.

3.8 Effect of Friction Coefficient

In deriving the approximate analytical formulations of peak displacement, it was assumed that the effect of friction is negligible. However, there is some effect when including the coefficient of friction which alters the RM curve. To show what these effects are, the OpenSees FEM model discussed above is used. Figure 3.9 shows zoomed-in RM curves for μ = 0.5, 0.9, and 1.5, as well as the analytical approximation, for a structure with α = 0.4 and negligible damping.

As μ decreases, the structure enters the sliding stage earlier, resulting in slight amplification at a lower excitation. This occurs because the effective critical deformation is reduced: the leg can begin to slide at a higher axial load. As μ increases, the additional damping effect due to the dissipation of energy through friction during the sliding stage is increased, resulting in a lower overall RM curve, most notably in the sliding stage.

In reality, a system may be restrained until the true critical deformation occurs, such as with the flanged wheel of a container crane on top of a crane rail, or where an anchorage system fails. Then, when sliding occurs, the resulting dissipated energy may be small. In this type of scenario, the approximate analytical formulation is quite appropriate, as it assumes infinite friction prior to sliding, but no friction-induced dissipated energy during sliding. The approximate analytical formulation, however, results in slightly conservative estimates of the peak deformations greater than the critical deformation for realistic values of idealized friction coefficient. Where the analytical formulation is slightly unconservative, the friction idealization is not realistic (sliding while significant axial load remains, or where friction coefficient is small enough to result in total structure sliding).

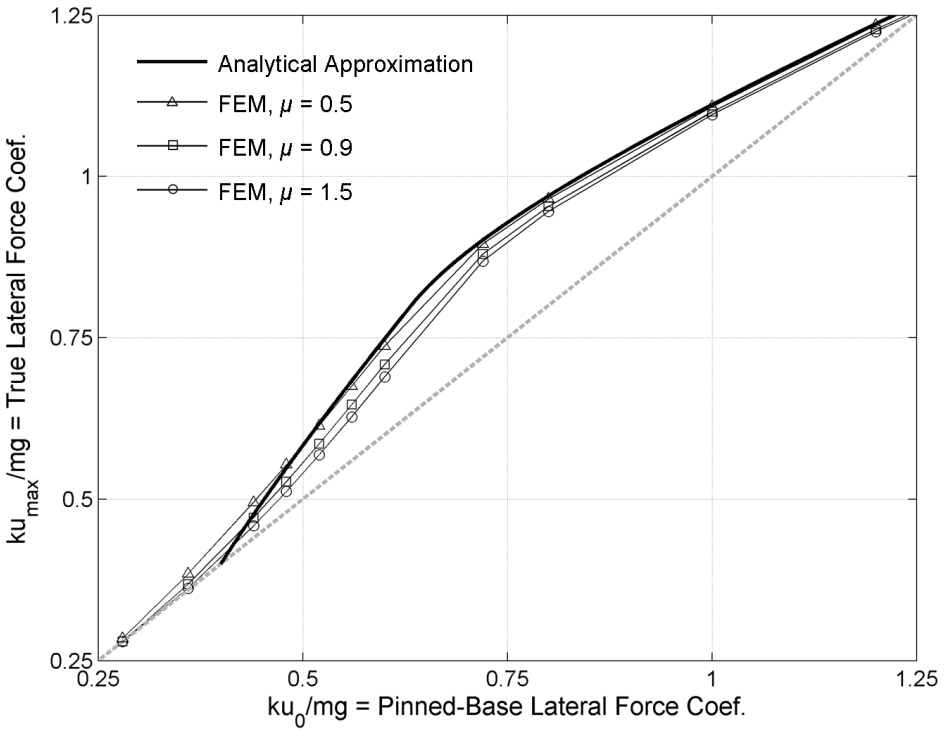

Figure 3.9. Response modification curves for unbonded contact of undamped portal frames (n = 2) and the corresponding finite element results with various assumed coefficients of friction.

3.9 Simplified Earthquake Analysis

It has been shown that the maximum deformation of an uplift-capable elastic structure which loses some amount of shear stiffness during uplift events can be determined from Eq. (3.6), (3.13), or (3.21), provided that the peak deformation of the linear system with bonded contact, u_0, is known, and that the vibration period is that of a typical structure. In the case of earthquake analysis, the largest of all peaks of the damped linear response history is known from the displacement response spectra, $S_d(\omega,\xi)$. One can estimate the corresponding deformation of an uplift-capable structure by assuming that this peak

deformation would occur at roughly the same instant, or within the same cycle, as the peak bonded-contact response. This assumption is quantified by Equation 3.31.

$$u_0 \approx S_d(\omega, \xi) \tag{3.31}$$

This approximation can be substituted into Eq. (3.6), (3.13), and (3.21) to determine the spectral displacement for the uplift-capable system, $S_d'(\omega,\xi)$. The pseudo-acceleration response spectra is computed as

$$S_a'(\omega, \xi) = \omega^2 \cdot S_d'(\omega, \xi) \tag{3.32}$$

This approach is easily applied to any known linear response spectra. Figure 3.10 presents response spectra for the Kobe Earthquake of 1995, as recorded by the Kobe Port Island station, at a depth of 0m. Damaged container cranes at the Port of Kobe had an uplift threshold of approximately 0.45 g (α = 0.45) [22] and a period of 1.74 sec [16]; the portal frame configuration yields n = 2. Modified spectra corresponding to this uplift threshold are shown in Figure 3.10, and notated at the Kobe cranes' fundamental period. The methodology of Chopra & Yim [34], which assumes shear continuity, indicates a 26% reduction in response of an uplift-capable structure. However, the methodology presented here, which does account for shear stiffness reduction during uplift, indicates a 16% amplification of response from the bonded-contact situation. This amplification of response explains the discrepancy between the findings that uplift contributed to crane collapse at Kobe [16] and the common belief that uplift inherently protects a structural system. In addition, it provides explanation for the dynamic amplification during uplift events that was observed in previous container crane shake table studies [19].

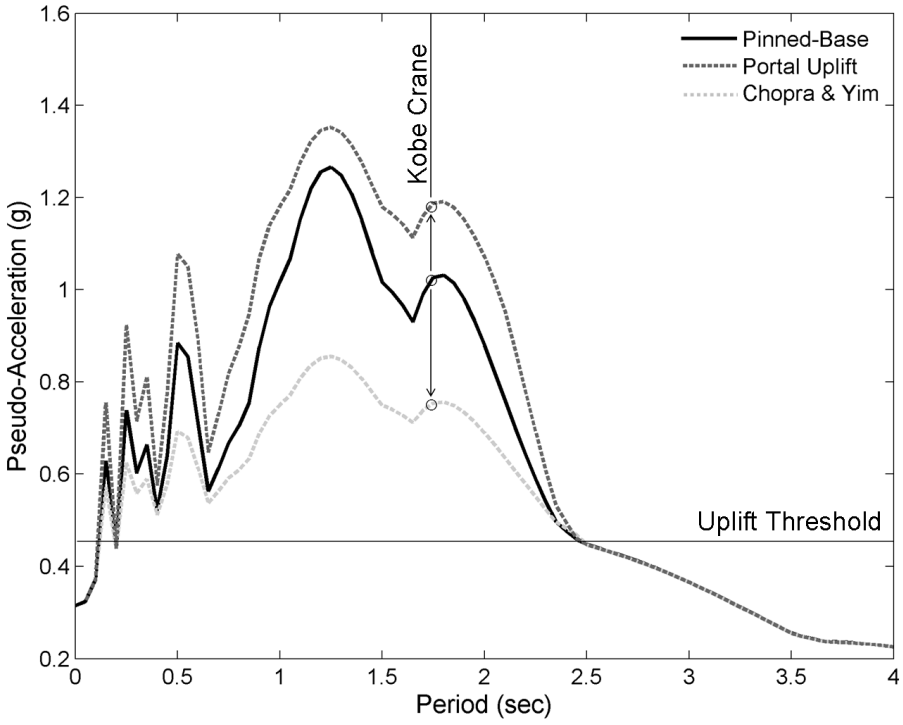

Figure 3.10. Pseudo-acceleration response spectra (2% damping) for Kobe earthquake (Port Island station, 0m depth), modified for uplift as assumed by Chopra & Yim (1985) and as proposed for unbonded contact with $n = 2$.

Still, this does not explain why older cranes in the United Stated have performed reasonably well in past earthquakes. The two main US earthquakes which were felt at port facilities were the Loma Prieta earthquake in 1989 and the Northridge earthquake in 1994. The Port of Oakland (POAK) is located approximately 55 miles northwest of the epicenter of the magnitude 6.9 Loma Prieta earthquake. The Port of Los Angeles (POLA) and Port of Long Beach (POLB) are approximately 40 miles southeast of the magnitude 6.7 Northridge earthquake's epicenter. Container cranes went essentially undamaged through both earthquakes. It is important to realize that the epicenter of the damaging magnitude 6.9 Kobe earthquake of 1995 occurred only approximately 12 miles from the Port of Kobe. Thus, the ground accelerations at the Port of Kobe were much

larger than those at POLA/POLB and POAK during the Northridge and Loma Prieta earthquake respectively.

However, there is another aspect to consider. Recall that growth of container cranes has occurred primarily since 1995. The majority of cranes in use during the historic US earthquakes were much smaller than current cranes, and had gage lengths of 50ft. This lower gage length resulted in the typical structural slenderness being approximately α = 0.3. From Figure 3.4, it is clear that at higher levels of excitation, higher slenderness (lower α) results in lower seismic demand. This is because, like with classic uplift, the seismic energy in the structure at incipient uplift is greater for more stocky structures. For example, at a pinned-base lateral force coefficient of 1, a structure with slenderness α = 0.45 has a true lateral force coefficient of approximately 1.18. However, a structure with slenderness α = 0.3 requires a pinned-base lateral force coefficient of approximately 1.62 to reach the same demand. To illustrate the same thing in a different way, the modified Kobe earthquake response spectra for portal uplift where α = 0.3 and 0.45 are shown in Figure 3.11. For the same reason, the more slender container crane has a significantly lower seismic demand estimate in the entire period range of typical container cranes (~1.2s-1.8s).

This type of simplified earthquake analysis for first-mode dominant uplift-capable structures provides a powerful tool for evaluation of existing container cranes and for the design of new cranes. Just as historic spectra can be modified to account for portal uplift, design spectra can be adjusted as well, using the same methodology.

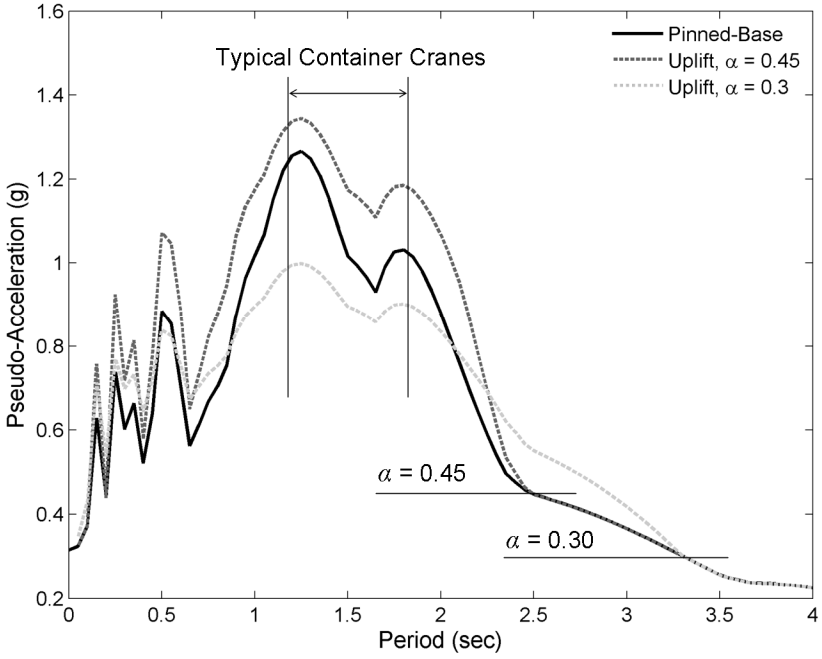

Figure 3.11. Pseudo-acceleration response spectra (2% damping) for Kobe earthquake (Port Island station, 0m depth), modified for portal uplift with α = 0.3 and 0.45 (n = 2).

3.10 Limitations

The results, methodology, and simplifications presented provide a basic understanding of the effects on structural response of uplifting elastic structures which have a reduced shear stiffness during uplift events. There are certain limitations, however, that should not be ignored. Soils and foundations are assumed to have negligible flexibility as compared with the lateral structural system. Also, while the analytical formulations of maximum structural deformations are derived in the general sense, they have been verified by finite element studies exclusively using portal frames. In addition, they are valid only for structures with periods of typical uplift-susceptible structures (>~0.4s), although typical container cranes are well within this range. Regardless, the equations proposed are meant as an estimate only, keeping in mind the fundamental assumptions.

Still, they provide unique insight to the consequences of uplift response when shear capacity is compromised, and highlight the importance of the base connection for systems which rely on uplift for a reduction in seismic demand.

3.11 Summary and Conclusions

Much of the prior research on flexible elastic structures allowed to uplift has assumed continuity in shear stiffness, even during uplift events, resulting in a generally reduced structural response. While new building designs and retrofits can be made to satisfy this assumption by providing a means of transferring shear during uplift events, the extension of this result cannot be generalized to all cases of uplift. Systems not intentionally designed to uplift may in fact exhibit uplift if the anchoring system is insufficient and fractures. Other structures have no anchoring systems, such as container cranes, and can exhibit unconstrained uplift under sufficient lateral loading. This chapter develops portal uplift theory, a simplified analysis describing the behavior of such systems through closed-form estimates of seismic demand dependent on the excitation intensity, with an emphasis on container cranes. Several conclusions can be made regarding this behavior:

1.) The response of elastic structures exhibiting unconstrained uplift with reduced shear stiffness has three stages. Each stage is linear in nature, but the piece-wise combination of stages results in an overall nonlinear response to a given excitation. The structure initially exhibits response identical to that of a bonded-contact system. Upon reaching some initial critical response amplitude, some

portion of the structure loses its shear capacity, and begins to slide. At the second critical response amplitude, those sections that exhibited sliding then uplift.

2.) The maximum response amplitude of the uplift-capable system can be estimated well using the solutions of the simplified equations of motion governing each response stage. The overall maximum structural response depends on the excitation, determined from the EOM of the highest response stage. There is a range of excitation, beginning during sliding, which causes amplification of the response compared with the bonded-contact case. However, at excitation beyond the switch point, the response of the uplifted structure is reduced compared with the bonded-contact system. The switch point, always in the tipping stage, is a function of the shear stiffness reduction during uplift and the structure slenderness.

3.) The relative magnitude of amplification and reduction of response in relation to bonded-contact over all excitation ranges is easily viewed in a response modification curve. More stocky structures stay in the initial elastic stage longer, and have a higher switch-point. Higher reduction in shear stiffness leads to increased amplification, and a higher switch-point. The maximum amplification is a function of shear stiffness reduction, and not structure slenderness.

4.) Finite element models incorporating frictional contact elements can capture the response described above well. While the transitions between stages, especially the initial entry into sliding, is somewhat sensitive to the assumed value of the

coefficient of friction, the proposed response modification curves are slightly conservative for realistic friction values for a structure's base, and are deemed appropriate.

The developed portal uplift theory can be easily applied to response spectra. Spectra modified using the proposed response modification method provides a simple method for estimating the true structural response of systems exhibiting uplift with reduced shear stiffness. Depending on the structure's slenderness, relative shear reduction during uplift, and the seismic intensity, the modified spectra indicate the relative amplification or reduction from the standard elastic spectra. Put together, the proposed method and resulting observations behind portal uplift theory help explain the apparent discrepancy between typical uplift "isolation" and container crane failure directly caused by uplift. Portal uplift theory, as derived and presented here, provides the physics-based technical tool necessary to realistically estimate the dynamic seismic demand of uplift-capable portal frame structures such as container cranes without complicated finite element dynamic time-history analysis.

CHAPTER 4

GENERAL CONTAINER CRANE MODELING AND ANALYSIS

4.1 Introduction

Seismic performance evaluation is most economically achieved by the development of detailed mathematical models representing the structure in question. With such models, different loading conditions and analysis methods can be performed to ascertain the expected structural performance in various situations.

When considering container cranes, an accurate and useful analytical model for seismic studies must account not only for the action of structural members, but must also allow for the possibility of uplift. The uplift and associated rocking response mechanism can significantly alter the dynamic behavior of a structural system (see Chapter 3), and thus considerably alter the seismic demand. Development of a mathematical model to represent this behavior must accurately capture the coupling between elastic structural response and the uplift/rocking mechanism. This can be done effectively through advanced finite element techniques.

This chapter first discusses the basic structural modeling approach adopted for representing elastic container cranes. Then, several approaches to modeling of the boundary condition are presented, including some which allow uplift response. In addition, several simplified models are presented, and their appropriateness and

limitations are addressed. Finally, numerical strategies for solving the nonlinear dynamic response are discussed.

4.2 General Modeling

While very detailed finite element models are helpful in determining precise responses to various loadings, seismic analysis often requires many time-history analyses, which can become onerous and uneconomical. Further, the impossibility of predicting future ground motions makes seismic analysis probabilistic by nature, as there are significant uncertainties associated with every aspect of modeling and analysis (see Section 2.5 and Chapter 7). Therefore, it is sufficient and often beneficial to create models which are significantly less complex, yet still able to accurately capture key response quantities. It is this philosophy that drives the modeling steps outlined in the following sections.

4.2.1 Evaluation Platform

The Open System for Earthquake Engineering Simulation (OpenSees) is an open source, object-oriented, earthquake engineering software framework developed at the University of California, Berkeley to provide researchers with a versatile finite element analysis framework for advanced structural and geotechnical system analysis [145, 147]. The OpenSees framework utilizes the Tcl/Tk [148] scripting language in its interpreter, allowing fully-programmable model definitions and solution procedures.

OpenSees has been chosen as the computational platform for this work for a number of reasons. First, the versatility and breadth of the material and element libraries allow for

great flexibility in defining model characteristics [145]. Second, the ability to define and control the solution procedures and algorithms using a wide range of available techniques allows the user to handle highly nonlinear systems, such as those with uplift, even with severe numerical sensitivities [149]. Third, the ability to provide scripting within the model definitions and analysis makes it ideal for parametric studies and repetitive dynamic analyses.

4.2.2 Finite Element Models

The OpenSees models developed in this study use a centerline approximation, and omit the effects of the panel zones. This modeling approach is chosen based on the assumption that the additional flexibility introduced to the system due to centerline dimensions compensates for the omission of panel-zones.

The container crane models are realistically symmetrical about the trolley-travel direction, with two parallel structural frames joined at top and bottom by trolley girder support beams (TGSBs) and sill beams, respectively. Each frame is comprised of a portal frame on the first story and a braced frame second story. Atop the main frame is an A-frame system joining at the apex, or top beam. The trolley girder is rigidly attached to the bottom of the TGSBs, and often supported by a backstay. The boom is pinned to the trolley girder on the waterside, and held by inner and outer forestays. The stays are assumed to have enough loading under gravity loads that they remain in tension throughout a seismic loading. The reader is referred to Appendix A for a more detailed

description of typical container crane configuration and terminology. A basic schematic of the structural configuration is shown in Figure 4.1.

Based on the findings and recommendations of previous studies [21], the boom is modeled in its lowered, operating position, as that is the critical configuration and leads to slightly higher internal forces during seismic excitation than when stowed. Because the hanging payload was found to only have a negligible effect on the dynamic response of the crane structure [21], it is modeled as static point mass at the boom tip, and so the "swinging" of the payload under seismic excitation is ignored.

The complex system of equalizer beams, balance beams, and trucks to which the sill beams are affixed are idealized as a semi-rigid column in each corner. These pseudo-trucks are offset from the base of the lower legs to correspond with the physical truck mounting locations.

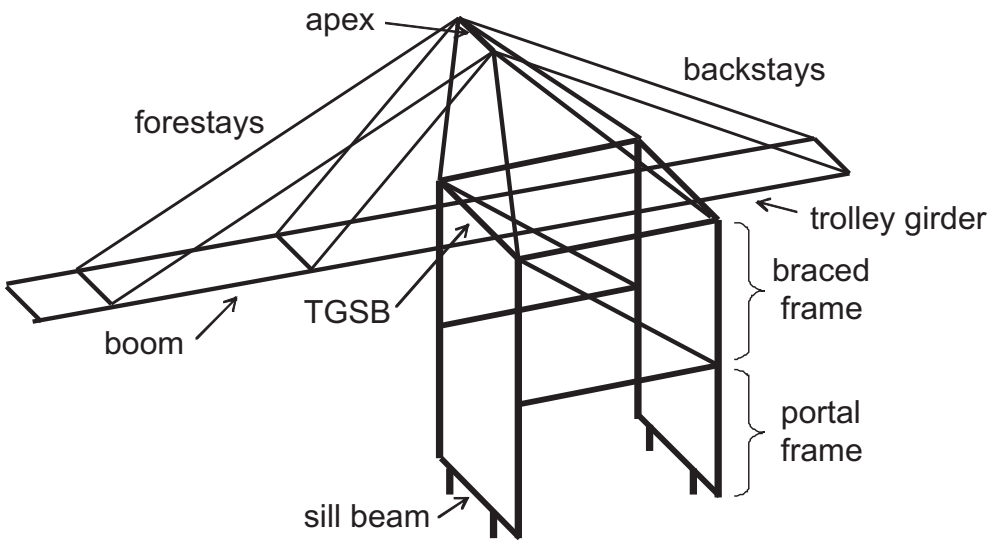

Figure 4.1. Schematic of analytical container crane model.

4.2.3 Modeling of Beams and Columns

Beams and columns are modeled using a flexibility-based frame finite element, as proposed by Neuenhofer and Filippou [150]. While the commonly-used stiffness-based frame elements are based on approximate interpolation functions for displacements along a member, the flexibility-based formulation is based on interpolation functions for the internal forces. The flexibility approach used employs a user-specified number of integration points where curvature is monitored, and equilibrium is enforced. In a general sense, it has been shown that the flexibility formulation allows for significantly fewer elements along a member length to achieve desired accuracy [150], especially when considering nonlinearities.

Although this chapter deals with elastic response, where the selection of appropriate polynomials in a stiffness-based element is straightforward, the geometric nonlinearities and uplift responses benefit from the flexibility-based formulation. In addition, utilizing the flexibility-based elements to analyze the elastic response allows consistency when comparing with the later inelastic analysis. As per the recommendations of Neuenhofer and Filippou [150], a single element with 5 integration points along the length is used for each prismatic member. This is accomplished within OpenSees using the available `nonlinearBeamColumn` elements. Elastic properties are assigned via an `Elastic` section definition.

As described in Chapter 2, previous work and experience has found that the flexible lower portal frame is the crucial component to overall response behavior, especially in the portal joints. For this reason, stiffeners are accounted for explicitly in the portal frame's areas and moments of inertia. Due to the relative stiffness of the second story braced frame as compared with the portal frame, the stiffeners above the portal frame are neglected in terms of contributing to element stiffness. In addition, the junction of beams and columns at the portal joints are modeled as rotational springs. These flexural springs are assigned a very high initial stiffness, so that the elastic behavior of the framing elements determines the overall structure stiffness. When only elastic response is desired, the rotational springs act essentially rigid. However, when nonlinear portal frame behavior is desired, such as in later chapters, it is a simple matter of defining the nonlinear behavior of the joints. A schematic of this type of portal frame model is shown in Figure 4.2.

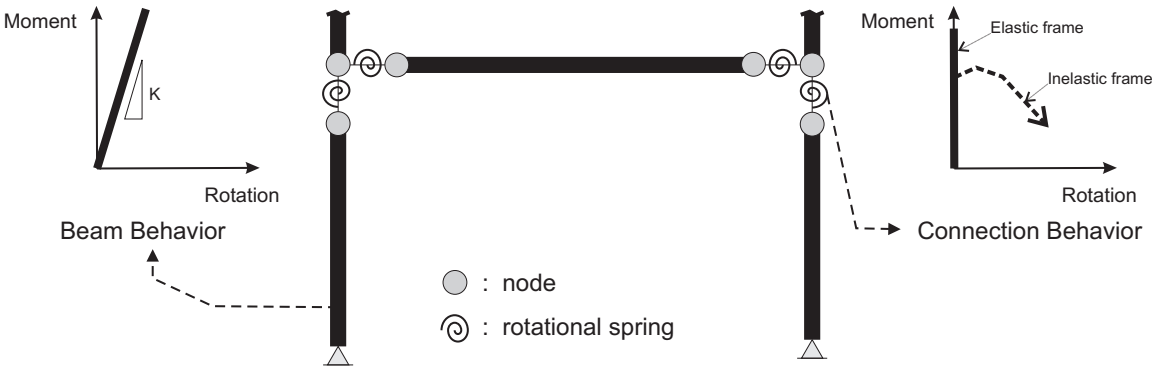

Figure 4.2. Centerline elastic portal frame model with potentially inelastic connection behavior

This popular type of centerline approach neglecting panel zones for seismic analysis has been shown to be somewhat conservative by slightly under-predicting capacity and over-

predicting demand for many steel frame structures [151], but is a reasonable and attractive model for probabilistic seismic performance evaluation .

Boom and trolley girder properties are estimated averages of the physically varying cross sections. It is assumed that the effect of the boom and trolley girder on global response is dominated by its associated and attached mass, both in terms of quantity and location. The boom and trolley girder constitutes a significant contribution to total mass and is the driving influence on a torsional response, but is a relatively insignificant contribution to global structural stiffness in terms of the dominant portal frame response.

4.2.4 Geometric Nonlinearities

The relative flexibility of the portal frame can result in significant portal sway displacements of the crane's first story. The considerable mass above the portal frame can therefore significantly increase the internal forces via second-order (P-Δ) effects and cause potential instability. For this reason, the second-order effects must be accurately modeled in order to realistically evaluate the seismic performance. Within OpenSees, this can be accomplished via the `PDelta` transformation applied to portal frame elements, which performs a linear geometric transformation of element stiffness and resisting force from the local to global coordinate system. It should be noted that this approach ignores the influence of axial force on element flexural stiffness (P-δ effect). This approach is deemed acceptable because in general, container crane portal frames are controlled by bending requirements, resulting in significantly oversized columns in relation to axial force demand. If a more accurate transformation is required, the

OpenSees `Corotational` transformation [152] could be used, which performs an exact geometric transformation and can account for large deformations. However, this transformation limits utilization of other aspects of the software framework, such as axially distributed loads and rigid joint offsets.

Local geometric nonlinearities are considered in Chapter 6 in the context of inelastic behavior and material nonlinearities, as these are the cause of local buckling of steel subcomponents. This chapter assumes linear behavior of structural elements.

4.2.5 Modeling of Viscous Damping

A form of classical damping is used which has frequency dependent damping, and is a combination of both mass and stiffness proportional damping. This damping, typically referred to as Rayleigh damping, is somewhat consistent with experimental data [146]. It can be represented as

$$[C] = a_0[M] + a_1[K] \tag{4.1}$$

Where [*M*] is the mass matrix, [*K*] is the stiffness matrix at the last-committed state, and [*C*] is the damping matrix. This formulation results in a damping ratio of the *n*th mode of

$$\zeta_n = \frac{a_0}{2}\frac{1}{\omega_n} + \frac{a_1}{2}\omega_n \tag{4.2}$$

For most traditional structures, it is reasonable to assume that two modes, ω_i and ω_j, have equal damping ratios. When that is the case, coefficients a_0 and a_1 can easily be found to be

$$a_0 = \zeta\frac{2\omega_i\omega_j}{\omega_i + \omega_j} \qquad a_1 = \zeta\frac{2}{\omega_i + \omega_j} \tag{4.3}$$

However, it is not always reasonable to assume equal damping ratios while still desiring the benefits of Rayleigh-type frequency-dependent damping. In this case, coefficients a_0 and a_1 can be found to be

$$a_0 = \frac{2\omega_i\omega_j\left(\omega_i\varsigma_j - \omega_j\varsigma_i\right)}{\left(\omega_i + \omega_j\right)\left(\omega_i - \omega_j\right)} \qquad a_1 = \frac{2\zeta_i}{\omega_i} - \frac{2\omega_j\left(\omega_i\zeta_j - \omega_j\zeta_i\right)}{\left(\omega_i + \omega_j\right)\left(\omega_i - \omega_j\right)} \tag{4.4}$$

Rayleigh damping is applied within OpenSees using the `Rayleigh` command, and specifying the appropriately calculated coefficients.

4.2.6 Modeling of Gravity Loads

Gravity loads are applied as nodal loads equal to the associated seismic mass multiplied by the gravitational constant. This approach is chosen due to the experimentation with geometric transformations, and the discovery that the corotational transformation implementation of OpenSees is not yet capable of handling distributed loads. Because the response of interest is in general localized within the portal frame, the use of nodal loads was judged to be an adequate representation of the gravity load.

4.3 Modeling of Boundary Condition

As described earlier, the wheels of a container crane are not generally positively tied to the crane rails or wharf deck in regions of known seismicity. Therefore, it is possible for the wheels to uplift from the rail. Further, if a wheel uplifts more than the height of the wheel flange (see Figure 4.3), it can displace laterally relative to the rail. Thus, dynamic container crane uplift can be a complicated response, requiring specialized boundary elements to accurately capture the important features. (The reader is referred to Chapter 3 for a detailed treatment of this type of uplift response.)

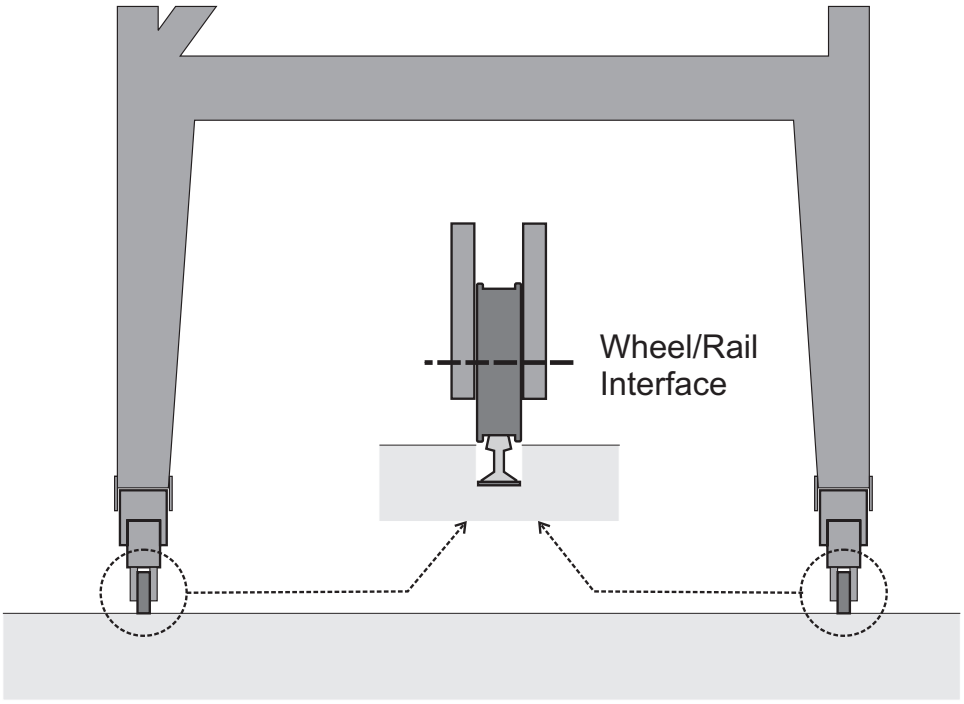

Figure 4.3. Container crane boundary condition with wheel/rail interaction

Depending on the response required, several strategies for boundary modeling may be acceptable. The general modeling approach for three boundary condition idealizations, as well as their appropriateness and limitations, are presented below. As summarized in Figure 4.4 and in order of increasing complexity they are: pinned, elastic-no-tension, and frictional contact. While a container crane's legs are in contact with the ground such that compressive vertical reactions are developed, the boundary conditions are comparable, and act essentially pinned. However, if the (generally dynamic) response of a crane is such that the vertical reaction decreases to zero and would require tension to satisfy static equilibrium, the strategies discussed behave quite differently.

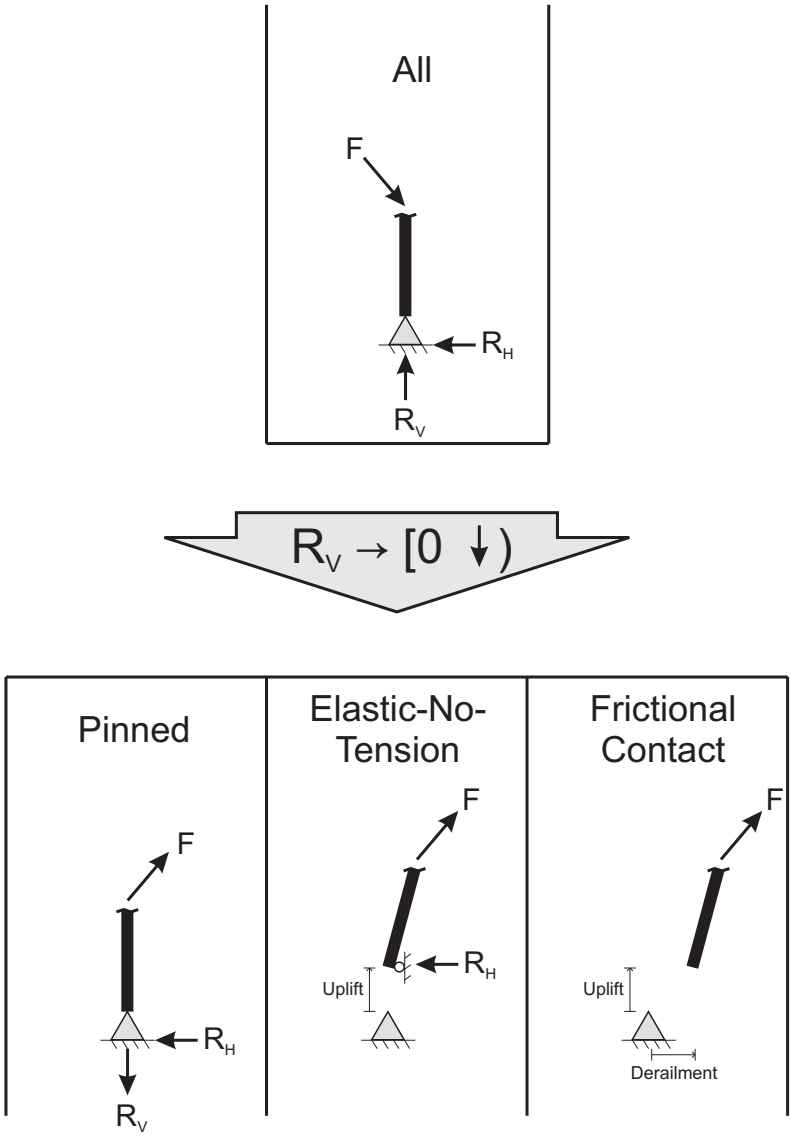

Figure 4.4. Schematic showing behavior of idealized boundary conditions under general loadings (compressive vertical reaction) and those which cause uplift (would-be tensile vertical reaction).

4.3.1 Pinned

The simplest strategy for a boundary condition idealization is to use a simple pin where the crane interfaces with the crane rail. Under this assumption, neither uplift nor derailment is permitted. Therefore, there is no computational limit to the range of reaction either in the vertical or horizontal direction, as shown in Figure 4.4.

The pinned boundary is simple and readily available in all structural modeling software packages, and is thus an attractive choice. For many types of analysis it is sufficient, as capturing the uplift response is not essential. For typical static analyses (gravity, service, wind, etc.) where uplift should be avoided, a pinned base is adequate to use during design iterations. Further, a pinned base is appropriate for dynamic analyses where the level of loading does not cause a response greater than the uplift threshold. For stocky cranes with a high uplift threshold, or for cranes in regions of low seismicity, a pinned base may be all that is needed for an entire design or seismic evaluation. Where ports utilize container crane tie-downs due to large wind loads, generally due to hurricanes, a pinned base would be a reasonable choice of boundary model, though some additional complexities associated with the tie-downs [143] would need to be addressed.

When a pinned base is assumed, a simple check should be performed to ensure that all vertical reactions throughout the analysis, either static or dynamic, remain compressive. If a tensile vertical reaction is noted, the analysis should be repeated after adjustments have been made, either in the design or in the boundary idealization.

4.3.2 Elastic-No-Tension (ENT)

The natural progression from a purely pinned boundary condition is to one which utilizes elastic-no-tension (ENT) elements between the structure and the ground. (Using the OpenSees platform, this can be achieved using the `uniaxialMaterial ENT` assigned to an `element zeroLength`.) In this way, compressive vertical reactions

may be developed under general loading. However, when a static or dynamic loading causes a vertical reaction to decrease to zero, rather than a tensile reaction developing, the leg base is free to displace upward, or uplift, as shown in Figure 4.4. Still, the use of an ENT element does not by itself remove the horizontal constraint during uplift events. In fact, the ENT approach does not link horizontal to vertical behavior in any way. Therefore, derailment is not possible, as the leg base is continuously constrained horizontally despite uplifting, so the leg base moves perfectly vertical.

One consequence of perfectly vertical uplift is that the uplifted leg base, in reality free to displace and unable to transfer shear to the wharf, causes a horizontal reaction to develop. This artificial reaction falsely redistributes the internal forces so that the uplifted leg carries some portion of the transferred shear. Thus, the moment computed at the critical portal joint of the non-uplifted side is artificially decreased, and unconservative.

An approach used by the industry [153] to correct for this has been to evaluate the capacity of the non-uplifted side of the portal frame under the maximum combined base shear from both the uplifted and non-uplifted sides, computed from dynamic time history analysis. Thus, it is ensured that the crane can withstand the total computed base shear demand. However, uplift modeled in this way can be thought of as the "pure" or "classic" uplift discussed in Chapter 3, where shear stiffness is kept constant during uplift events. Recall that pure uplift results in a significant reduction in structural deformation response, and thus base shear demand, at loadings greater than the uplift threshold for structures with fundamental period and structural slenderness typical of large container

cranes ($T \approx 1.5$s; $\alpha \approx 0.4$). In reality, as the derivations in Chapter 3 argue, a sliding stage exhibiting significant derailment occurs prior to notable uplift occurring when uplifted elements cannot contribute to overall shear stiffness. In that sliding stage, and early in the tipping stage, the total base shear demand can actually be amplified from the comparable pinned-base system. In fact, the base shear demand for this type of portal uplift is higher than that for classic uplift for all loadings which cause loss of contact. Thus, using ENT elements as described here to model uplift of container cranes is an unconservative approach, and should be avoided.

4.3.3 Frictional Contact (FC)

In order for a model to allow derailment during uplift events, the horizontal constraint must be related to the vertical force. If there is no compressive vertical reaction, then the horizontal constraint should be removed at that location. While simple in theory, this is a challenging concept to incorporate into most finite element codes.

Frictional contact (FC) boundary elements relate the horizontal force capacity to compressive vertical force, typically through Mohr-Coulomb friction.

$$F_{H,\max} = \mu \cdot F_V \tag{4.5}$$

In other words, the maximum horizontal force which can be resisted prior to sliding occurs is equal to some frictional coefficient (μ) multiplied by the vertical force. In this form of the friction law, the frictional force during sliding is the maximum resisted force – no distinction is made between static and kinetic friction. (Using the OpenSees platform, this is achieved using the `element zeroLengthContact`.) By choosing

an appropriate coefficient of friction, sliding can be avoided until the vertical force is essentially zero. It was shown in Chapter 3 that friction coefficients in the range of 0.6-0.9 are generally effective in limiting premature sliding to a negligible range for uplifting portal frame structures excited by seismic loads. Once uplift occurs, there is no compressive reaction and thus the maximum frictional force is zero. Thus, there is no horizontal constraint to limit derailment during uplift events.

In order to cause the impact after uplift to be an elastic collision, so that momentum can be conserved without a perfectly inelastic collision, it is helpful to add a stiff spring between the contact surface and the "ground." Even a very stiff spring that does not appreciably alter the overall system dynamics (period, etc.) can be very effective in reducing numerical challenges. A damper in parallel to this spring allows for energy dissipation during impact. In light of the discussion in Section 2.3, a combination of a linear spring and viscoelastic damper can be used to achieve linear viscoelastic pounding behavior.

The stiff spring constant (k_k) is assumed to be 25,000 kip/in as suggested by Muthukumar and DesRoches [45], which has been shown to be relatively insensitive to changes of an order of magnitude [41, 154]. The damping coefficient (c_k) is selected based on the coefficient of restitution (*e)* by equating the energy loss during impact.

$$c_k = 2\zeta\sqrt{k_k m}\,; \qquad \zeta = -\frac{\ln e}{\sqrt{\pi^2 + (\ln e)^2}} \tag{4.6}$$

Here, m represents the structural mass contributing to dynamic vibration of the stiff spring (roughly equal to the total mass divided by the number of contact points), and ζ is

the damping ratio. The coefficient of restitution is assumed $e = 0.6$, also based on the recommendations of Muthukumar and DesRoches [45].

The frictional contact boundary idealization can thus capture the critical uplift and derailment responses in a realistic, but simplified way. For this reason, nonlinear dynamic time-history analysis of uplifting container cranes in this study utilize frictional contact elements.

4.3.4 Comparison Example

To demonstrate the differences in predicted seismic response using different boundary modeling approaches, an example is presented. Consider a typical uplift-capable container crane structure in a region of high seismicity. It has a portal sway mode at T = 1.5s, height to center of mass of 100ft, and an overall slenderness ratio $\alpha = 0.4$. A contingency level earthquake (CLE) design spectra, having a 10% probability of exceedance in 50 years, is defined such that the spectral acceleration S_a(1.5s) = 0.7g. One can use the methodology of Chapter 3 to estimate the portal deformations calculated during dynamic time history analyses for a spectrally-compatible earthquake under different boundary assumptions.

The predicted portal deformations under various boundary conditions are shown in Figure 4.5. If the boundary were modeled as pinned, the predicted portal deformation would be approximately 15.4in, but a computed tensile vertical reaction would indicate uplift would occur. The traditional assumption is that portal deformation demand would

not increase beyond the level causing uplift, or in this case approximately 8.8in. However, using the ENT boundary assumption, the portal deformation demand is predicted by classic uplift theory to be 12.4in. Using a FC boundary idealization, portal deformation demand is predicted by portal uplift theory to be 19.4in. Thus in this case, using an ENT boundary idealization results in a seismic demand prediction that is approximately 36% lower than the more realistic FC boundary; the FC boundary predicts demand approximately 21% higher than even the case of a fully pinned base.

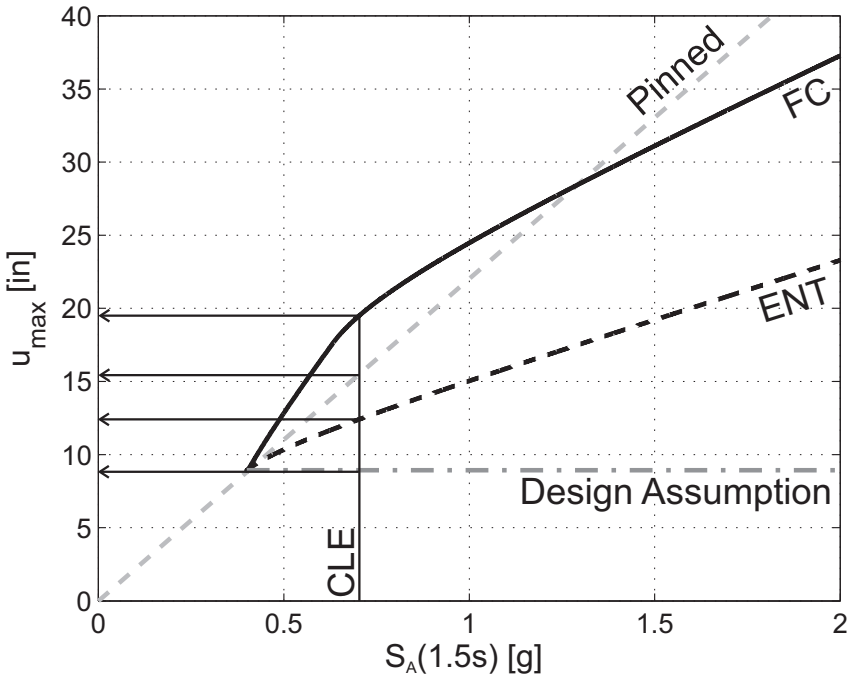

Figure 4.5. Response modification curves indicating structural deformation predicted by three boundary condition idealizations

4.4 Transient Analysis Solution Strategy

In OpenSees, the transient analysis which moves the model from its state at time t to its state at time $t+\Delta t$ is controlled by several different objects. The analysis objects coordinate to solve the general equation of transient equilibrium

$$F_I\left(\ddot{U}\right) + F_R\left(U, \dot{U}\right) = P(t) \tag{4.7}$$

where F_I is the inertial force vector (dependent on acceleration), F_R is the damping and stiffness resisting-force vector (dependent on velocity and displacement, respectively), and $P(t)$ is the external applied-force vector at time t. Because of uplift and the impact that occurs shortly afterward, there are several challenges to ensuring numerical stability and accuracy throughout a transient analysis. These challenges, and the rationale for choosing specific analysis objects, are described below.

4.4.1 Algorithm

The solution algorithm determines the progression of iterations to solve the non-linear equation of motion at a given time step. Generally, the Newton-Raphson method is the default method to advance to the next time step, where the tangent at the current iteration is used to update the tangent towards convergence. (In OpenSees, this is accomplished using the `algorithm Newton`.) However, an uplift event changes global stiffness extremely rapidly, leading to possible overshoots while searching for convergence. This can lead to divergence from which it is difficult or impossible to recover. Therefore, a modified Newton algorithm incorporating a line search technique (in OpenSees, `algorithm NewtonLineSearch`) is used, which limits the ratio between residuals before and after the incremental update. Here, that limiting ratio is set to 0.8. If the limiting ratio is violated, an algorithm developed by Crisfield [155] is used to improve convergence.

At the end of each iteration, a convergence tolerance must be performed in order to determine whether convergence has been achieved. The check is performed based on

$$K\Delta U = R \tag{4.8}$$

where K represents stiffness, ΔU represents displacement increment, and R represents the unbalanced load. Here, a norm displacement increment (`test NormDispIncr`) is performed, ensuring that

$$\sqrt{\Delta U^T \Delta U} < tol \tag{4.9}$$

This type of convergence check is chosen because it does not involve force components, which can change even more rapidly than displacements when uplift and impact are involved. Thus, a lower tolerance may be prescribed, achieving higher accuracy with fewer iterations and larger time steps than other convergence check approaches. Here, a maximum tolerance of *tol* = 1e-7 is chosen. In addition, 2000 iterations are allowed prior to accepting that convergence will not be satisfied, due to the numerical challenges associated with the rapid system stiffness changes during uplift and impact.

4.4.2 Integrator

The integrator object determines how time-stepping is achieved. An integrator must exhibit two characteristics, consistency and stability, which are necessary and sufficient for convergence according to the Lax equivalence theorem. The most well-known time-stepping integration method for structural dynamics is the classical Newmark method [156], which uses two parameters to define the variation of acceleration over time (γ) and determine the stability and accuracy characteristics (β). (In OpenSees, the

implementation is with `integrator Newmark`.) It is commonly reported (e.g. [146]) that unconditional stability may be achieved when

$$\gamma \geq \frac{1}{2}, \beta \geq \frac{\gamma}{2} \tag{4.10}$$

These parameter values satisfy the conditions necessary to keep $|A| < 1$, where A is the amplification factor which compounds the error associated with each time step. If $|A| < 1$, then A^n converges to 0 where n is the number of time steps.

Second-order accuracy may be achieved if and only if $\gamma = ½$ however [157]. When $\gamma = ½$ and $\beta = ¼$, Newmark's method is referred to as the average acceleration method, or trapezoidal rule. Because it is unconditionally stable and second-order accurate, the trapezoidal rule is economical and thus widely used. When $\gamma = ½$, and $\lambda^h \Delta t >> 1$, $A \approx -1$, where λ^h is the system's highest eigenvalue [157]. Thus, although the method is stable in the strict definition that disastrous growth will not occur, a "sawtooth" pattern in time shows up in computation when a high-frequency component is excited. When an uplifted structure lands back on the ground, impact occurs, which excites high-frequency vertical modes of the structure. It has been shown that viscous damping is ineffective in decaying these high-frequency modes [158], and exciting them is unavoidable for uplifting structures. Therefore, another approach must be taken to counteract the sawtooth behavior.

Often, the excited high-frequency modes of a finite element model are artifacts of the discretization process, or numeric modes, and are not truly representative of the physical behavior of the modeled system [157]. Thus, preserving the resulting response is not

necessary. A commonly used method is to provide algorithmic damping, or numerical dissipation, to the generalized Newmark method by selecting $\gamma > ½$ (McKenna, personal email, May 2007). High-frequency dissipation can then be maximized while still maintaining unconditional stability by enforcing [157]

$$\beta \geq \frac{(\gamma + 1/2)^2}{4} \tag{4.11}$$

Recall that when $\gamma \neq ½$, accuracy of the Newmark method decreases to first-order, thus requiring a compromise in accuracy for algorithmic damping, and the sawtooth behavior is avoided. In addition, a damped Newmark implementation cannot avoid contributing algorithmic damping at reasonably low modes, where structural response is critical. In fact, when $\gamma > ½$, the percent of critical damping caused by algorithmic damping (ζ_N) can be approximated as a linear relationship with the ratio of time step to system period ($\Delta t/T$) [157]

$$\zeta_N = \pi\left(\gamma - \frac{1}{2}\right) \cdot \frac{\Delta t}{T} \tag{4.12}$$

As an example, consider a typical container crane with period T = 1.5s, and assume an analysis time step equal to $dt/2$, where dt = ground motion time step = 0.02. Assume a choice of $\gamma = 0.8$. Thus, $\zeta_N \approx$ 0.63%. This lightly damped portal sway mode can have as low as 1% of critical damping (see Appendix A). Hence, the algorithmic damping provided by such an implementation of the Newmark method represents a significant increase in the relative damping, and thus can provide unconservative estimates of seismic demand during dynamic analysis.

Considerable research efforts have been spent on the development of alternative integration schemes which damp the higher modes without significantly affecting the important lower modes [157]. One method, the α-method, or Hilber-Hughes-Taylor method [159] (in OpenSees, `integrator HHT`), shows considerable promise. This method uses a modified version of the time-discrete equation of motion so that parameters γ and β may be represented by a single parameter α. If parameter selection is such that α is within the range [-⅓, 0] and $\gamma = (1 - 2\alpha)/2$, $\beta = (1- \alpha)^2/4$, then the method is unconditionally stable and second-order accurate [157]. When a typical value of α is chosen and the same example as above is used, Figure 9.3.2 of [157] indicates that the algorithmic damping provided in the structural mode is negligible, while significantly higher is provided in the high-frequency artifact modes than a damped Newmark approach. While this method appears extremely promising for quickly dissipating the artificial impact modes of an uplifting container crane, OpenSees user discussions and personal experience has found that its OpenSees implementation is not completely reliable, and thus should be for complex problems until its "bugs" are corrected.

When second-order accuracy is required and the α-method is unavailable or the damped Newmark method contributes too much damping to the important modes, one simple way of avoiding seeing the sawtooth behavior when using γ = ½ is to report step-to-step averages $(d_{n+1} + d_n)/2$,since $(-1)^{n+1} + (-1)^n = 0$. However, this is effective only when the response between two time steps is reasonably close, as is typical for structural response. However, when uplift and impact are involved, the drastic stiffness changes between two adjacent time steps results in step-to-step averages that are not sufficiently accurate. A

"brute force" approach can be sometimes used to avoid harmful high-frequency sawtooth behavior. Recall that $A \approx -1$ only when $\lambda^h \Delta t >> 1$. Thus, a time step sufficiently small relative to the highest system eigenvalue will ensure that $|A| < 1$ without being too close to the critical value of -1.

4.4.3 Required Time Step

When choosing a time step, an analyst must consider the stability condition, and dissipation and dispersion errors of any considered integration scheme. For efficiency in computation, it is desirable to choose the largest permissible time step which achieves the desired accuracy. To determine the required time steps for the integration schemes discussed here, the example presented earlier is used, where the dominant mode of a typical container crane $T = 1.5$s. Assume that the highest period of importance could be a torsion mode, $T_T = 3T$, and that a stiff impact mode could be excited, $T_I = T/100$. Also assume that engineering accuracy requires relative period error (PE) and amplitude decay (AD) be no more than 5 percent during any cycle for these important modes. Because the considered schemes are all unconditionally stable, stability criterion will not control the time step. Figures 9.3.2 and 9.3.3 are used from reference [157] to determine the PE and AD for each method in the following discussion.

First consider the damped Newmark method, where $\gamma = 0.6$. Amplitude decay is limited such that

$$\varsigma_N \le \frac{0.05}{2\pi} \cong 0.008 \Rightarrow \frac{\Delta t}{T_T} \le 0.03 \Rightarrow \frac{\Delta t}{T_I} \le 1\times10^{-4} \\ \rightarrow \Delta t \le 1.5\times10^{-6} \tag{4.13}$$

It is safe to assume that, in the case of damped Newmark, error associated with dissipation error will require a smaller time step than with period errors.

Second, consider the α-method, where α =-0.3. Two conditions must be considered, dissipation and period errors, such that

$$\begin{aligned}
&\varsigma_N \le 0.008 \Rightarrow \frac{\Delta t}{T_T} \le 0.13 \Rightarrow \frac{\Delta t}{T_I} \le 4.3\times10^{-4} \\
&\frac{\overline{T}-T}{T} \le 0.05 \Rightarrow \frac{\Delta t}{T_T} \le 0.10 \Rightarrow \frac{\Delta t}{T_I} \le 3.3\times10^{-3} \\
&\rightarrow \Delta t \le 5.0\times10^{-6}
\end{aligned} \tag{4.14}$$

Finally, consider the undamped Newmark method, assuming the trapezoidal rule. This method has no algorithmic damping, but the amplification factor must be kept sufficiently far from -1 to avoid a "sawtooth" response, in addition to period decay, such that

$$\begin{aligned}
&\frac{\overline{T}-T}{T} \le 0.05 \Rightarrow \frac{\Delta t}{T_T} \le 0.125 \Rightarrow \frac{\Delta t}{T_I} \le 4.2\times10^{-4} \\
&|A| << 1 \Rightarrow \lambda^h \Delta t \le 50 \Rightarrow \Delta t \cdot \left(\frac{2\pi}{T_T}\right)^2 \le 50 \Rightarrow \Delta t \cdot \left(\frac{2\pi}{T_I}\right)^2 \le 0.17 \\
&\rightarrow 9.5\times10^{-7}
\end{aligned} \tag{4.15}$$

In reality, the impact mode is not 100 times stiffer than the portal sway mode. Additionally, the accuracy can be relaxed to some degree for the impact mode, thus loosening the requirements for largest permissible time step. Still, this example illustrates the importance of a small time step for uplifting systems, especially when using an undamped Newmark method such as the trapezoidal rule. In light of these

conditions, a time step of *dt*/500 or *dt*/1000 is utilized wherever uplift and the associated impact are expected, where *dt* is the recording time step from the earthquake strong motion (typically 0.02s, 0.01s, or 0.005s).

At first glance, the fact that a small time step is required only when an impact mode is excited would indicate that a variable time step could be used to improve computational efficiency. However, the common implementation of a variable time step, where the step size is reduced when convergence does not occur, presents challenges in this situation. One difficulty lies in the fact that the convergence check can be satisfied at initial impact, but the solution at the time step leads to a physically-unrealizable solution, which lead to convergence problems one or two time steps later. Therefore, the time step must be reduced just prior to impact, before strict convergence problems occur, requiring some predictive capability such as a logical if/then displacement monitor. Implementing such a variable time step efficiently is outside the scope of this study.

4.4.4 Other Analysis Objects

Several other analysis objects exist in OpenSees, and are briefly discussed here. Due to the OpenSees implementation of the frictional contact element, the choice of how the constraint equations are enforced in the analysis is limited. Here, constrained degrees of freedom are handled through matrix condensation, through the OpenSees command `constraints Transformation`. The system degrees-of-freedom are renumbered through the `numberer RCM` method, which renumbers to minimize the matrix band-width using the Reverse Cuthill-McKee algorithm. Because of the frictional contact

element, the stiffness matrix is unsymmetric. Therefore, the systems of equations are stored and solved according to the system `BandGeneral`, which is a direct solver for banded unsymmetric matrices.

4.5 Simplified Crane Models

Several simplified, idealized analytical models of container cranes were developed in order to more easily study specific behaviors, and isolate certain responses of interest. Use of these simple models allows for certain conclusions to be made which can simplify the overall seismic performance evaluation of container cranes. These models are described in the following sections, in order of decreasing complexity. Their adequacy for use in various situations is discussed in later chapters, as relevant.

4.5.1 2D Crane

As discussed in Chapter 2 and elsewhere, the critical seismic response of a typical container crane is a portal sway mode. Therefore, a simplified 2D analytical crane model representing the trolley-travel direction is sometimes useful, and often sufficient. In general, the symmetry of the crane structure makes this simplified modeling straightforward, as shown by the nodes and elements in Figure 4.6, so that the stiffness is consistent with one half of the full structure, while the mass is exactly half. Connecting elements, however, should be properly considered. Their mass is easily accounted for with additional nodal masses, but accounting for their flexibility requires some thoughtfulness as described below and in Figure 4.6 for the waterside trolley-girder support beam (TGSB).

Because of the significant mass and inertia associated with the boom/trolley girder substructure, the flexibility due to the offset (along the z-axis of Figure 4.6) of the boom from the plane of the structural frame can significantly impact dynamic response. This flexibility can be idealized as point effects in three directions, with separate zero-length springs placed between the corners of the structural frame (point *A*) and the attached boom and trolley girder (point *C*). The trolley-girder support beams (TGSBs), which connect the structural frames at the top of the braced second story, have flexibility in the trolley-travel (translational spring oriented along x-axis between *A* and *B*), vertical (translational spring oriented along y-axis between *B* and *C*), and torsional (rotational spring oriented along z-axis between *A* and *B*) directions. Their stiffness may be estimated from the load-displacement relationship of a simply-supported TGSB.

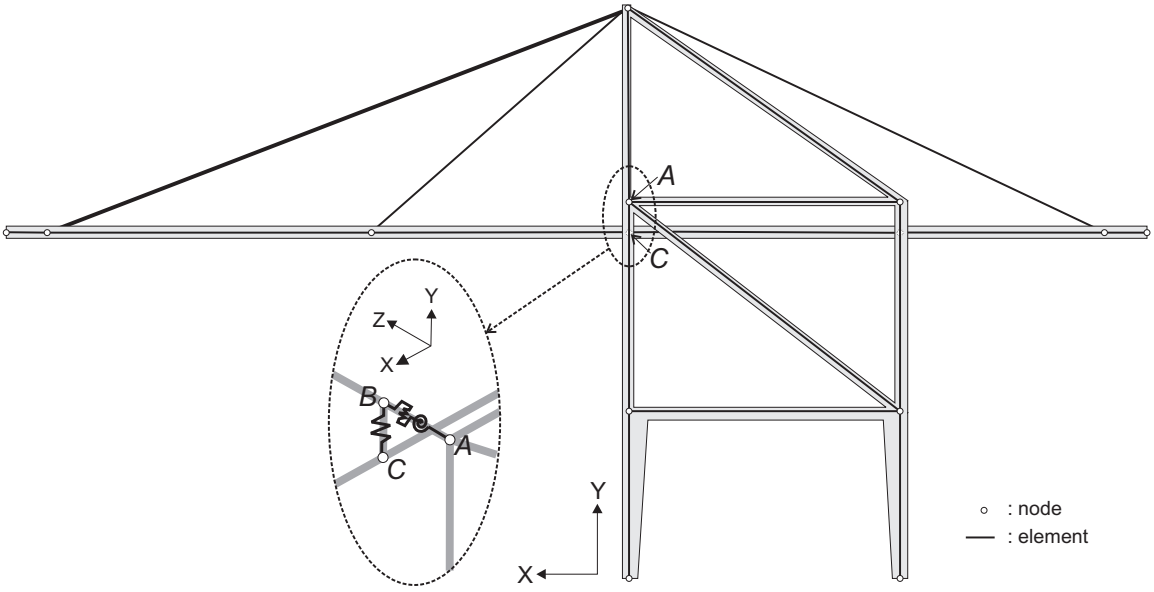

Figure 4.6. Schematic of simplified 2D crane model, accounting for flexibility of out-of-plane member

The sill beams, which connect the structural frames near the base, also contribute flexibility. They are modeled in the same idealized fashion as the TGSBs. Separate

zero-length springs are placed between the portal legs and the pseudo-trucks representing the relative translational and rotational degrees of freedom.

4.5.2 Simple Frame

Because the critical seismic response is a portal sway mode, then in some instances it may be sufficient to model the container crane in two dimensions even more simply than as described above. Recognizing that structural deformation in the trolley-travel direction is concentrated in the portal frame, and more specifically in the lower legs, a simple portal frame with a properly placed center of mass (CoM) is proposed, as shown in Figure 4.7. The simple frame has two flexible columns spaced according to the representative crane's gage length. Their length is equal to the portal height, (H_1). A rigid beam connects them, with an attached rigid column extending vertically to the crane's CoM.

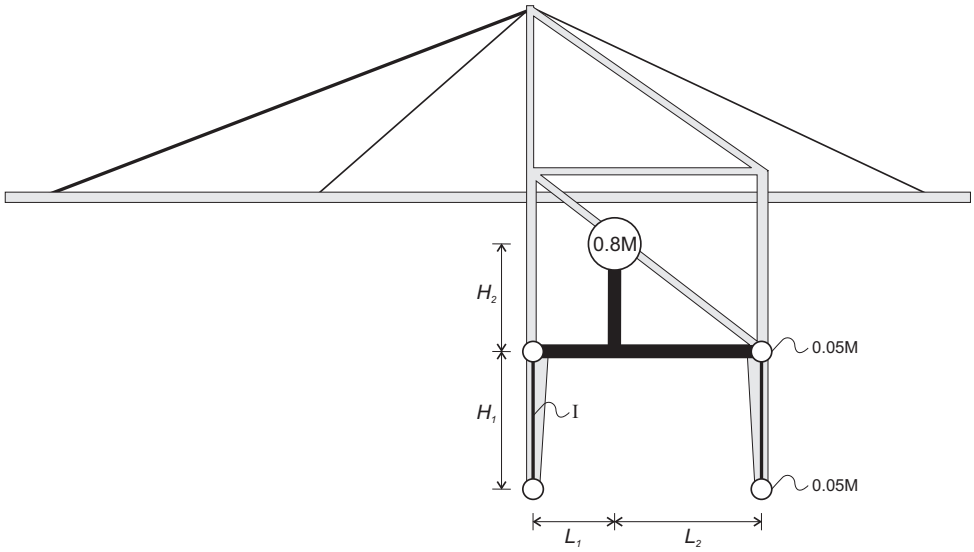

Figure 4.7. Schematic of simple frame model superimposed on 2D crane.

Normally, all of the seismic mass (M) would be placed as a point mass at the top of the rigid column. However, if uplift is considered, a realistic amount of mass should be placed at the base of the flexible columns, so that the elastic unloading and vibration of the uplifted leg resembles the representative crane behavior. Therefore, $0.8M$ is placed at the C/M, and $0.05M$ is placed at the tops and bottoms of each flexible column. While this adjustment of mass location slightly shifts the CoM for the simple frame lower than the true crane, this fact is not believed to significantly impact dynamic response. Further, these types of models will generally be used based on an estimate of the true CoM, where data would come from a preliminary portal frame design or from an inspection for seismic evaluation.

The column stiffness is selected so that the portal sway mode (comprising $0.9M$), is equal to the representative crane's dominant mode. This is accomplished simply, using the following equation.

$$\frac{2\pi}{T} = \sqrt{\frac{k}{0.9M}} \tag{4.16}$$

where T is the period, and k is the frame's portal sway stiffness (or twice the column stiffness, k_c). Therefore,

$$2\frac{3EI}{H_1^{\,3}} = k = 0.9M\left(\frac{2\pi}{T}\right)^2 \tag{4.17}$$

Or rearranged, the appropriate section modulus for the column of a simple frame model can be expressed as

$$I = \frac{0.9M\left(\frac{2\pi}{T}\right)^2 H_1^{\,3}}{6E} \tag{4.18}$$

This type of simple frame model is very similar to that proposed by the PARI (with the addition of mass at the leg bases for uplift modeling), which was shown to capture the seismic response in the trolley-travel direction nearly as well as a 2D or full 3D model [22]. While simple to formulate, it has the ability to capture the critical coupling between structural behavior in the portal legs and uplift response. It is therefore a powerful tool for simplified seismic analysis of container cranes.

4.5.3 Single Degree-of-Freedom (SDOF)

For container cranes that do not uplift, the critical seismic response can be described as first-mode dominant, where the portal sway mode captures the highly concentrated structural deformations. Therefore, a single-degree-of-freedom (SDOF) system representation is attractive due to its simplicity, and can be a reasonable choice. This type of model is represented in Figure 4.8. Only two parameters are needed to define an elastic SDOF system: mass and stiffness. Mass is typically a well-known quantity, as wheel loads on the crane rails are a critical design parameter and are well-documented for port personnel. If not explicitly known, an approximate elastic stiffness can be determined based on an estimated period and the known mass. The portal sway period can be determined with ease using data from in situ monitoring during normal operation. In the absence of that data, an estimate based on operational characteristics and expert judgment can give reasonable approximations.

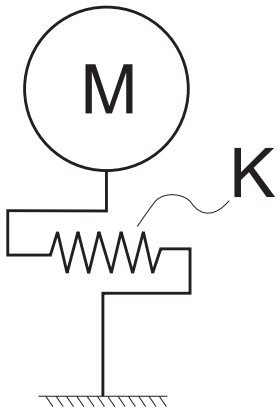

Figure 4.8. Schematic of SDOF system representation.

A SDOF system representation is not limited to elastic behavior though. In fact, the spring behavior can be represented by an infinite number of load-deflection relationships, such as elastic, elastic-perfectly plastic, hardening, and softening, etc. The seismic behavior of SDOF systems has been studied in great depth since the birth of earthquake engineering, and our understanding of it is reasonably mature. Therefore, when SDOF response can be assumed, many techniques, methods, theories, and ideas can be applied, making it an attractive choice. However, the present formulation does not allow for uplift, and thus cannot capture the coupled structural/uplift response of many container cranes subjected to moderate or large seismic motions.

4.6 Summary

Mathematical modeling of container cranes provides an economical means to further study their seismic behavior in a quantifiable way. This is achieved through finite element (FE) models; the FE platform of choice here is the OpenSees simulation framework. The models are built with elastic force-based beam-column elements, and include geometric nonlinearities where important. Inelastic behavior can be accounted

for in the critical portal frame through the use of rotational springs at the portal joint connections.

Because container cranes sit on rails without any positive restraint in regions of expected moderate seismicity, the resulting uplift response can be a challenge to model. Three boundary idealizations are discussed: pinned, elastic-no-tension (ENT), and frictional contact (FC). The benefits and limitations of each are described. While pinned-base idealizations can be used with care in some cases of lower excitation, the ENT idealization brings false confidence but is unconservative and not recommended. The FC boundary idealization results in the most realistic prediction of seismic deformation demands, and is used throughout the following chapters.

The uplift response and following impacts create challenges for transient analysis. Several aspects of solution strategies are discussed, including the algorithm, integrator, and required time-step. In general, it is found that performing Newton-Raphson iteration at each step of Newmark integration is an appropriate and recommended solution strategy. However, this approach requires very small time steps and large number of iterations to achieve clear and accurate numerical behavior.

Three simplifications to a full 3D finite element model are proposed: 2D model, simple frame, and SDOF. Aspects requiring special attention for each model are described. All four model types are used at various stages of the study, as described in later chapters.

CHAPTER 5

VERIFICATION OF GENERAL MODELING APPROACH

5.1 Introduction

Physical experiments are an important part of ensuring that mathematical models accurately represent the desired critical behaviors, and serve as a point of verification. In order to help characterize the dynamic response behavior of a container crane exposed to seismic loads, a relatively small-scale shake table experiment was devised based on the J100 container crane. Results from this experiment could then be used to validate and verify the developed finite element models and analytical tools. The verified models and tools can then be extrapolated to predict the response of similarly-constructed prototype-level cranes.

This chapter describes the scaled shake-table experiment specimen and protocol, and briefly describes the finite element models of the specimen. Then, the dynamics of each model are compared, followed by a discussion of the critical aspect of seismic response and behavior. The ability of both the 3D and the 2D model to capture and quantify the critical responses is considered. These critical responses are the elastic behavior, namely the portal sway response, and the uplift and derailment response.

5.2 Shake Table Experiment Description

Because the type of uplift exhibited by container cranes has not been previously fully understood, it is important to physically demonstrate the response analytically predicted

by the derivations in Chapter 3. Thus, while inelastic structural action is critically important to the ultimate behavior of container cranes, the coupled elastic and uplift response was targeted as the response of interest for this preliminary experiment. In this way, many experiment runs could be performed spanning a wide range of excitations without changing the effective structural stiffness through yielding.

5.2.1 Scaling

In order for a small-scale physical model to accurately reflect the true response of the prototype structure, considerable attention must be paid to the appropriate scaling relationships in order to maintain structural similitude. The practice of using small-scale physical models to predict the elastic earthquake response of structures has become commonplace since it was first reported in the 1930s [160]. Today, methods have been developed so that scale models can be used even when considering complex inelastic and cyclic structural behavior while still maintaining similitude with a prototype structure [161]. When the elastic and rigid body (uplift/rocking) responses are the focus of a scaled experiment, the process is now well-understood, and sufficient similitude can be achieved at rather small scales [162].

Proper scaling to achieve similitude starts with dimensional analysis. Recall from Section 2.2 that the expected critical container crane structural response to earthquake loading is the portal sway mode, which involves bending of structural elements. To achieve sufficient similitude for a scaled model to accurately reflect the prototype response requires that three independent dimensionless quantities be chosen, which then

establish scaling laws for all other physical quantities. The first dimensionless product describes length, which is chosen to be scaled by 1:20 in order for the model to be physically manageable. Gravity and inertial loads are critical to the uplift response, so the acceleration scale factor is chosen to be 1:1. It is attractive to use the prototype material for the structural model (in this case, steel), which sets the elastic modulus scale factor to be 1:1. This approach is taken here.

In order to achieve a "true replica" model, the model material must be quite flexible, extremely dense, or both. Because this criterion is not directly satisfied due to using the prototype material, it becomes necessary to augment the structural mass with structurally ineffective mass, or "artificial" mass to achieve similitude. This form of an “adequate” scaling model for shake table testing is considered in depth by Moncarz and Krawinkler [162], and shown to be quite effective for predicting seismic behavior of elastic structures. Time is scaled in the appropriate way, considering the choice of dimensionless parameters. Table 5.1 summarizes the important scaling relationships used in this study.

Table 5.1. Scale factors for 1:20 scale model of a container crane

Quantity	*Symbol*	*Factor*
Geometric Length, l	λ_l	20
Elastic Modulus, E	λ_E	1
Acceleration, a	λ_a	1
Mass, m	λ_m	400
Time, t	λ_t	$\sqrt{20}$

5.2.2 Specimen Design and Construction

The J100 container crane, described in Appendix A, is used as the prototype crane because it has the most typical configuration of both structural elements and mechanical

equipment (which act as dead load during seismic analysis). Because response is kept in the elastic range, structural capacity is not considered and the experiment considers elastic demand only. Thus, the selection of an elastic J100 prototype crane ensures that the results and observations of the scaled model experiment can be extended to the broadest range of general container cranes.

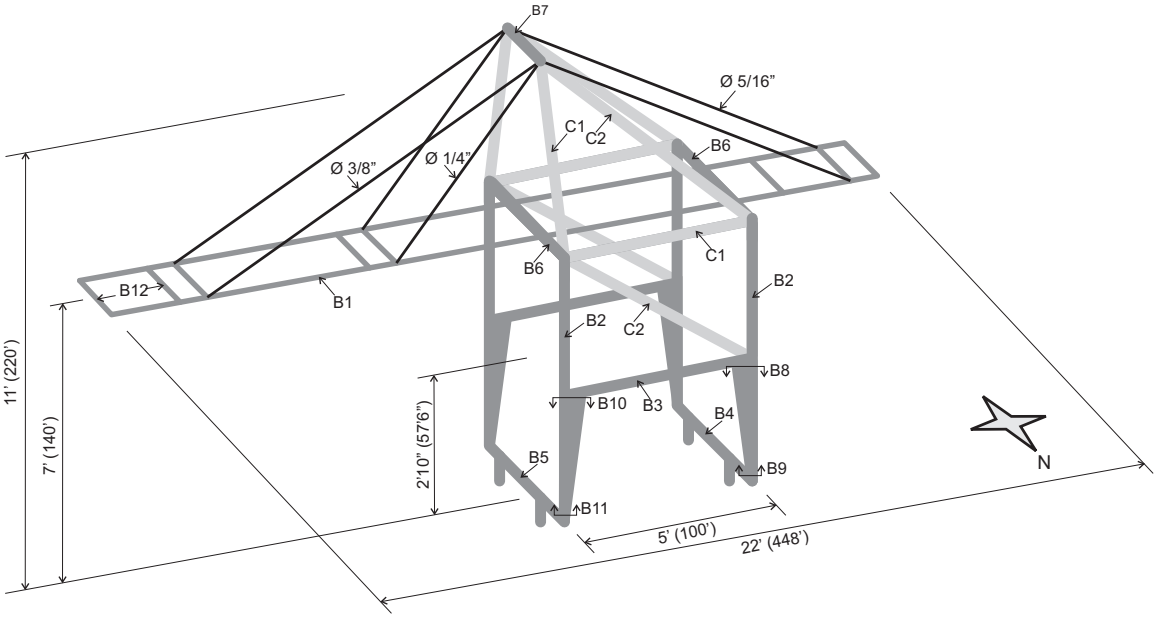

Figure 5.1. Overall dimensions of 1:20 scale experiment model (prototype dimensions in parentheses), as well as section property assignments, defined in Table 5.2.

Relative overall dimensions of the prototype crane are preserved, as well as the general structural configuration. Therefore, the model crane is 11ft tall and 22ft from landside tip of the trolley girder to waterside tip of the boom. Figure 5.1 shows the dimensions of the model with prototype dimensions in parenthesis. The portal frame, which controls the critical portal sway mode, is 5ft wide and 2.8 ft tall. The O-frame is 3.3ft wide and 7ft tall. The prototype structure is made of built-up stiffened box sections and tube sections; main model sections are hollow rectangular or round tube sized according to scaled

moment of inertia. Forestays and backstays are made from multi-strand steel cables that are sized to have equivalent axial stiffness to the corresponding scaled member. Dimensions of the section names referenced in Figure 5.1 are described in Table 5.2.

Because the portal frame incorporates tapered members and is of such critical importance, each model portal frame (N and S) is constructed as a whole using built-up welded plates to achieve hollow rectangular sections with continuity at the portal joints. Otherwise, tube section members are welded together to form four main subsections: the N and S structural frames, trolley girder, and boom. Bolted construction joints are then employed to piece the frames together with the TGSBs and sill beams. The bolted connections in the main structural frame were then welded for rigidity. Stays were attached using loops, clips, and thimbles, each incorporating a turnbuckle for final length adjustment.

Table 5.2. Summary of member dimensions for 1:20 scale container crane model

Box Member	***h*** *in*	***b*** *in*	***t*** *in*	***A*** in^2	***Iz*** in^4	***Iy*** in^4	***J*** in^4
B1	2.5	1.5	0.120	0.90	0.74	0.33	0.69
B2	2	1.5	0.120	0.78	0.43	0.27	0.50
B3	2.875	2	0.164	1.49	1.66	0.93	1.79
B4	3	2	0.250	2.00	2.07	0.64	2.57
B6	3	1.5	0.188	1.55	1.68	0.53	1.24
B5	4	2	0.250	2.75	5.31	1.68	3.92
B12	2	1.25	0.083	0.51	0.28	0.13	0.27
B8	2	1.875	0.164	1.21	0.65	0.58	0.91
B9	2	3.75	0.164	1.61	3.21	1.17	2.63
B10	2	1.625	0.164	1.08	0.58	0.41	0.72
B11	2	3.5	0.164	1.74	2.70	1.10	2.38
B7	3	1.5	0.188	1.55	1.68	0.53	1.24

Tube Member	***d_o*** *in*	***t*** *in*	***A*** in^2	***I*** in^4	***J*** in^4
C1	1.66	0.140	0.67	0.19	0.39
C2	1.315	0.133	0.49	0.09	0.17

Several aspects of model section design and construction are important to note. First, due to the small required size of model sections, it was impractical to include stiffeners. However, their effect on stiffness is included as the calculated moment of inertia of each prototype section included the effect of stiffeners, which was then scaled based on the similitude requirements to find the required dimensions of the model sections. Second, a minimum wall thickness of 0.2125in is imposed on all model sections due to concerns about distortions from the welding process. As a result, even though scaled moments of inertia are preserved, cross-sectional areas of model members are oversized relative to a perfectly scaled prototype structure. This has the effect of increasing the axial stiffness and strength above what is required by similitude, though because axial properties have a negligible influence on the uplift and elastic response, this is not viewed as detrimental. In addition, the oversized sections increase the moment capacities of the sections above what is required by similitude. However, because this experiment targets elastic response, increased moment capacities have the effect of increasing the allowable excitation prior to yielding. For the reasons described, these issues for section design do not compromise the aims of the experiment to characterize the elastic and uplift behaviors.

The structural elements of the shake-table model have a mass of only 600lbs, thus requiring 6390lbs of non-structural, "artificial," mass to enforce proper similitude (including non-structural point masses found on the prototype crane, such as mechanical equipment). The non-structural mass is added in three ways. The sill beams and rigid base columns are filled with a total of 100lbs of steel shot. Second, steel plates are stacked and tack-welded at appropriate locations along the boom to act as concentrated

masses. Lastly, lead ingots are attached to the members of the portal and O-frames, where displacements are expected to be concentrated; the use of lumped mass is less appropriate due to the second-order effects related to the large deformations. Using lead ingot allows for compactly adding distributed mass along the members with a negligible change in stiffness. Figure 5.2 shows the distribution of masses on the scaled model. Despite using dense material for the artificial mass, the volume of added material is large relative to the size of the scaled structure. Therefore, the large "stacks" of steel masses contributed rotational inertia in addition to the desired translational inertia from non-structural mass, and the strings of lead ingot could not be distributed along the entire member lengths due to space constrictions at the ends. However, these issues are not expected to significantly alter the dynamic response from an ideally scaled specimen, and thus do not limit how experiment observations apply to the prototype container crane.

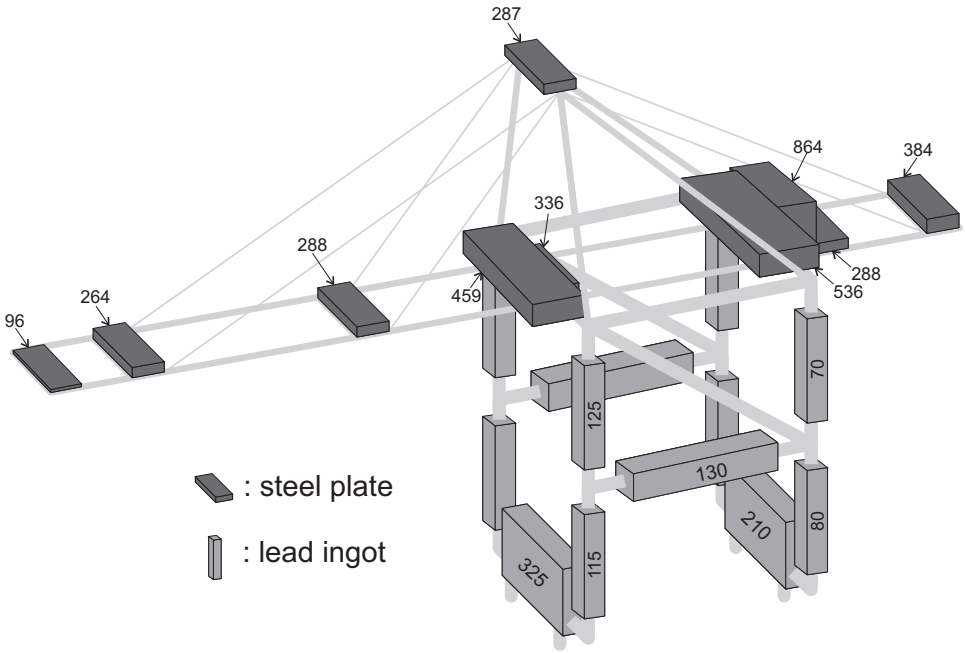

Figure 5.2. Achieved distribution of artificial masses to enforce scaling relationships in distorted scale model.

Experimentally modeling the prototype boundary condition, which has been described extensively in Chapters 2-4, is important to ensure that the uplift response of the scaled model reflects that of the prototype container crane. Because of the small model scale, it is not feasible to explicitly model the complex system of balance beams, equalizer beams and wheels (trucks), as depicted in Figure 5.3. Rather, this system is simplified in the experimental model to a stiff column that is 2in by 4 in, as can be seen in Figure 5.3 (b) and referred to as a "pseudotruck."

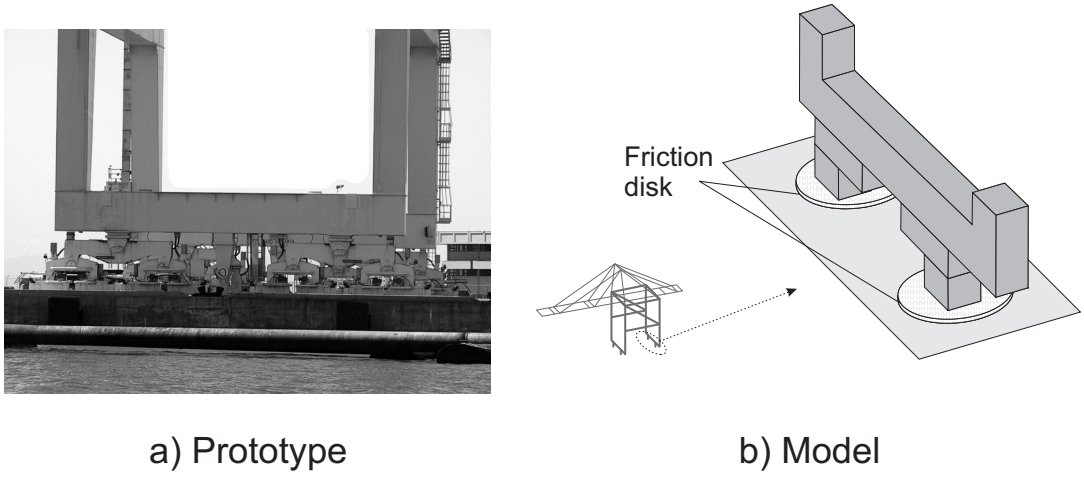

Figure 5.3. Container crane boundary condition of (a) the prototype structure consisting of a system of balance beams, equalizer beams, and wheels/trucks and (b) the experimental scale model, utilizing friction disks to simulate behavior.

Still, two issues must be accounted for: first, the boundary condition is essentially pinned except that there is no vertical restraint to uplift, and second, horizontal restraint is removed during uplift to allow for transverse motion of the uplifted legs (derailment). Experimentally, this response is achieved by using a friction-enhancing disk placed between the bottom of the column and the top of the steel base plate on the shake table, with a rough side touching both. An inclined-plane friction test indicates that the

effective coefficient of friction between the disk and clean steel is in the range of 0.6-0.8. In Chapter 3, it was shown that this friction approach is effective in causing a leg base to act essentially pinned until uplift, at which point it behaves freely.

5.2.3 Instrumentation and Facilities

The experimental container crane shake table tesing is conducted in the NEES-sponsored Structural Engineering Earthquake Simulation Laboratory (SEESL) at the University at Buffalo [163]. They are performed on one of the six-degree-of-freedom shake tables at the facility, which allows for excitation in two horizontal directions as well as a vertical component.

In order to achieve the goals of the experiment, several important response quantities are measured, including: the accelerations and displacements of the boom and portal frame, vertical and horizontal displacements of the leg bases, stresses in the portal frame, and vertical reactions at the base. Tracking the acceleration and displacement of the boom assist in characterizing the modes and mode shapes of the crane and their contributions to the overall response. Observations regarding the displacement of the legs and the vertical reactions facilitate the characterization of uplift behavior under seismic loading, including the initiation of uplift. Recording the stresses in the portal joint is also important for verifying that the model response is representative of the prototype crane, and for extrapolating potential damage scenarios of the prototype crane. Together, all of these response quantities are important for validating the analytical models and for further characterizing the container crane seismic behavior.

To measure these response quantities, an instrumentation scheme is developed that uses load cells, accelerometers, string potentiometers, extensometers and strain gages, as summarized in Table 5.3. An advanced Krypton 3D coordinate tracking system is used as a redundant measure of absolute and relative leg base movement. Eight video cameras are placed at various locations, according to Figure 5.4. Two high-speed (300 fps) cameras are employed to capture the short-duration uplift events. Close-up views of each leg base are used to further clarify each leg's individual uplift events. While all the measured responses together provide a full picture of qualitative and quantitative response, certain measurements provide particularly insightful data. For example, the difference between E-W displacements at the level of the portal beam and the leg bases describe portal sway deformations, while the deformations in all directions at the leg bases describe the uplift behavior. For that reason, quantitative analysis of model response focuses on data from these channels, with supporting data from other channels and qualitative observations from the digital video recordings.

Table 5.3. Instrumentation summary.

Instrument	*Number*
Accelerometer	56
Linear Potentiometer	25
Strain Gauge	96
Load Cells	4
TOTAL	181

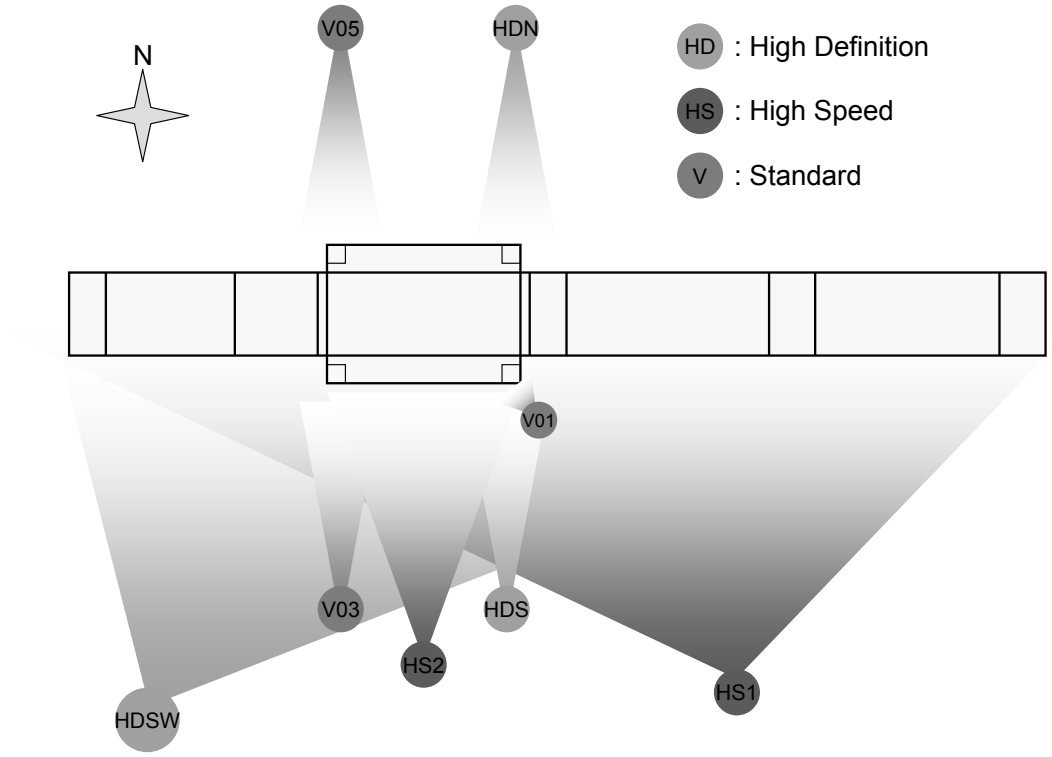

Figure 5.4. Plan view of video camera layout and their fields of view.

5.2.4 Ground Motions

Seismic ground motions are selected for these preliminary experiments that are representative of expected port motions. One particularly applicable set is a Loma Prieta acceleration time history set that was recorded by the California Geologic Survey (CGS) at station 58472. This station was created as part of the California Strong Motion Instrumentation Program (CSMIP), and is comprised of 12 accelerometer channels positioned at various locations in and around Berth 24 of the Port of Oakland. Channels 8, 9, and 11 chosen as the three orthogonal components used in this study. Channels 8 and 9 are located in the wharf deck, and represent the gantry-travel (H2) and trolley-travel (H1) excitations, respectively. Channel 11 is located in the backlands, and is the

only available vertical motion. To the authors' knowledge, this was the only significant seismic event to actually be recorded on a US wharf deck at the time of experiment design.

Additional ground motions were chosen to represent the two design level earthquakes defined for the Port of Los Angeles and Port of Long Beach. The operating-level earthquakes (OLE) represent a 72-yr return period event, while the contingency-level earthquakes (CLE) represent a 475-yr event. Spectrum-compatible time histories are chosen and spectrally matched to the 5% damping design spectra adjusted for site-specific soil conditions [164, 165]. For this study, two sets of each design level are chosen. OLE sets contain two components (H1 and H2), while CLE sets contain three components (H1, H2, and V). The ground motions selected for use here are summarized in Table 5.4.

Table 5.4. Ground motions used for 1:20 scale experiment, including POLA/POLB design level spectrally compatible modified historic records (OLE/CLE) and Loma Prieta historic motion recorded on Port of Oakland Berth 24.

Set	*Earthquake*	*Station*	*Mag.*	*Dist. (km)*
OLE1	1979 Imperial Valley	EC CO Center FF	6.5	7.6
OLE2	1992 Erzikan	Erzikan	6.9	2.0
CLE1	1999 Duzce	Lamont 1059	7.1	4.0
CLE2	1940 Imperial Valley	El Centro	7.0	6.0
LP	1989 Loma Prieta	CGS 58472	6.9	88

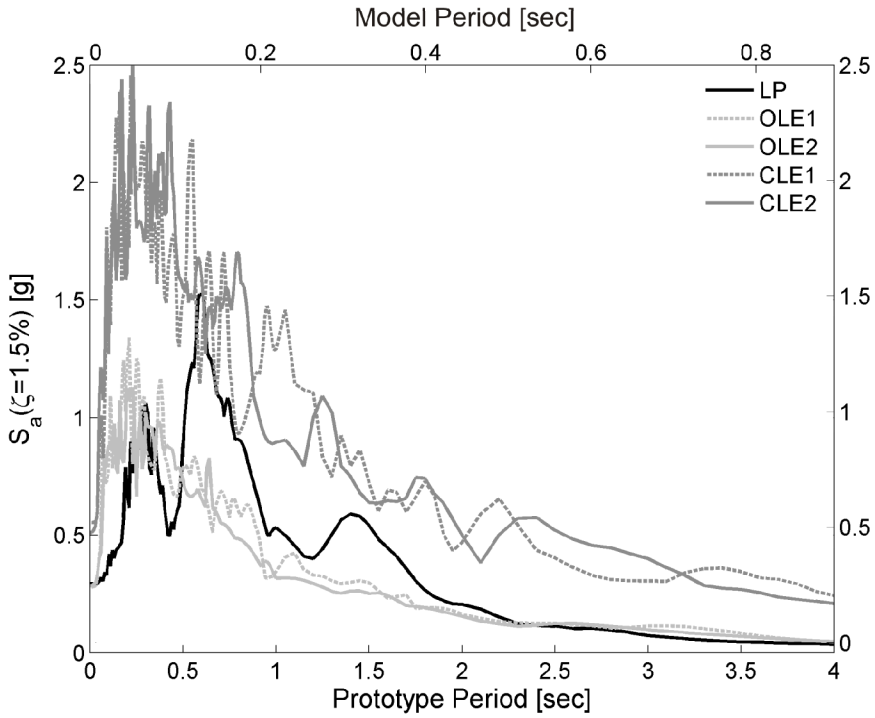

Figure 5.5. Unscaled response spectra of chosen ground motions' trolley-travel (E-W) components.

The test structure is subjected to the suite of ground motions in increasing order of acceleration amplification: 1/6. 1/4, 1/2, 3/4 and 1. The time step is reduced according to the scaling laws. The unscaled (amplitude and time) H1-component (E-W, or trolley-travel direction) response spectra at 1.5% of critical damping is shown for each earthquake in Figure 5.5, while Figure 5.6 depicts their acceleration time histories. In addition to historic earthquake motions, a low amplitude white noise base excitation is used for system identification purposes, such as for determining vibration frequencies and damping.

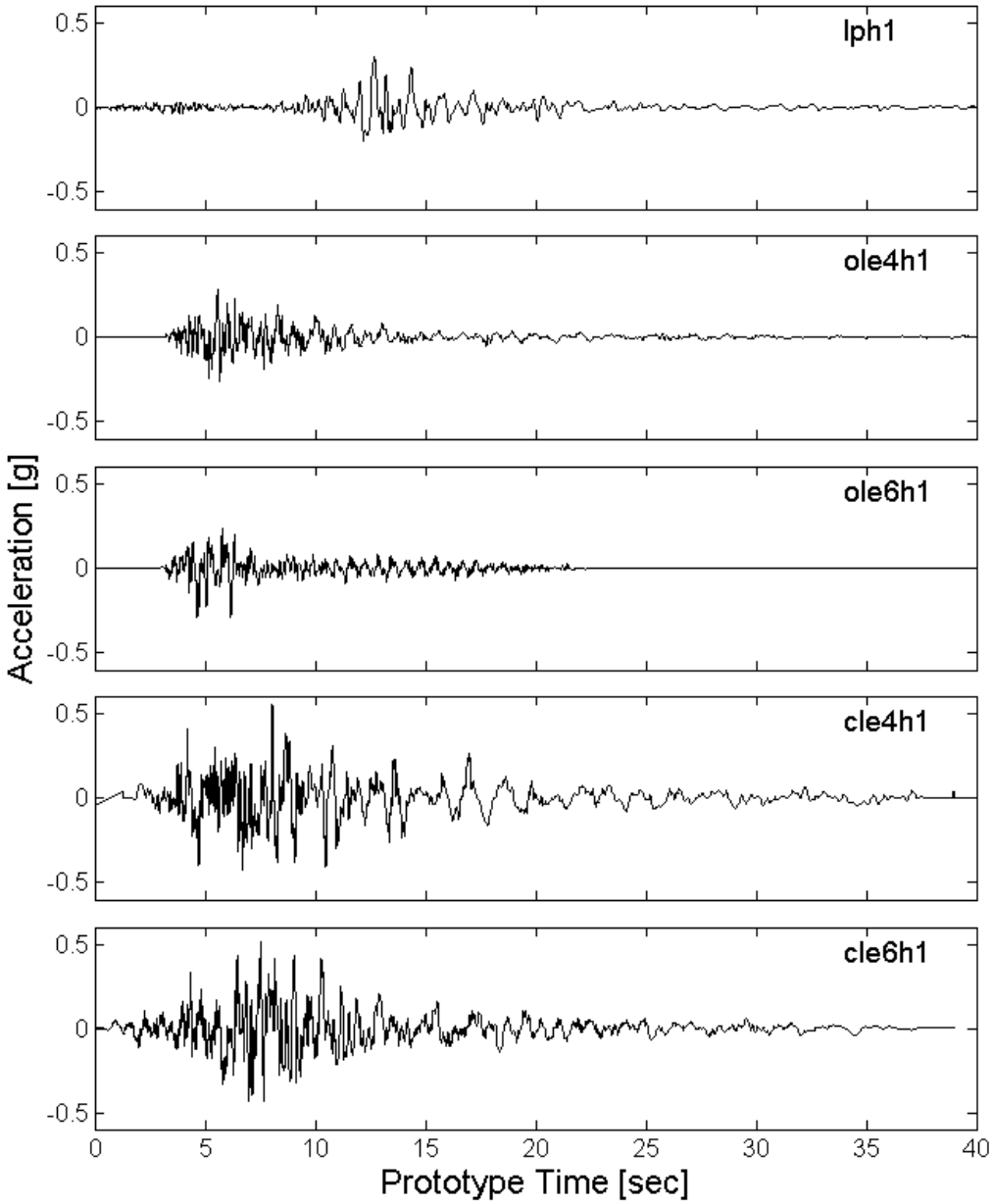

Figure 5.6. Unscaled (amplitude and time) acceleration time-histories of chosen ground motions' trolley-travel (E-W) components.

5.3 Finite Element Model Description

A finite element model (FEM) is built in parallel with the experimental program, which serves as a calibration point. A verified analytical model serves as a vital tool to further understand the system dynamics and response characteristics, which can then be used to

extend the results to the prototype model level and include inelastic behavior. The finite element model is built according to the methodology presented in Chapter 4, summarized briefly here.

The structural finite element model is based on the scaled physical test structure, and thus has the same geometry, section and material properties, mass distribution, and boundary condition as the physical model. Mass, including the experimental artificial mass due to scaling, is applied as nodal masses. The stiffening effect of the steel plate masses is accounted for by applying rigid diaphragm effects between boom ties. Gravity load is applied via point loads corresponding to the nodal masses, with the exception of horizontal members, which have uniformly distributed vertical loads. Geometric nonlinearity is taken into account by the use of the PDelta (P-Δ) geometric transformation. All elements are force-based beam-column elements with elastic section properties, allowing the use of a single element for each member with 5 integration points along the length [150], with one exception: the tapered lower legs are discretized into five elements each, with each element having the dimensions as at the midpoint of its length. Young's modulus is taken as 200 GPa (29000 ksi). Rayleigh damping is applied at two modes using the equations presented in Section 4.2.5, based on the experimentally determined half-power bandwidth damping of the portal sway and boom torsion modes.

In order to capture the prototype-level boundary condition discussed previously, a frictional contact element [145, 166] approach has been taken. This approach has been shown in Chapters 3 and 4 to realistically capture the response of systems exhibiting

portal uplift. Based on the recommendations discussed there and the estimated physical range of the experiment, a value of 0.75 is assumed for the friction coefficient in the finite element model.

A simplified 2D analytical crane model, representing the trolley-travel (E-W) direction, is also developed to test the adequacy of such an approach for accurately capturing the critical portal sway response. In general, the symmetry of the crane structure makes this simplified modeling straightforward, so that the stiffness is consistent with one half of the full structure, while the mass is exactly half. This type of model is described in further detail in Section 4.5.1, including the methodology for properly accounting for the flexibility of connecting element between parallel frames.

5.4 Elastic Behavior

5.4.1 Dynamics

Using standard system identification methods, recorded data from the experimental white noise input give information about the dynamic characteristics of the crane including natural frequencies, modes shapes and damping. The natural frequencies, reported as periods here, are found by transforming the acceleration response into the frequency domain and identifying peaks. Mode shapes are determined by observing the displaced shapes and comparing frequency-domain acceleration response in the three directions at different accelerometer locations. Using the half power bandwidth method, modal damping ratios can be estimated from the acceleration response in the frequency domain. Values of the natural periods and damping for the four most significantly excited modes

are summarized in Table 5.5, and sketched in Figure 5.7. These modes consist of two torsion modes – boom dominated (Fig. 5.7a) and frame dominated (Fig. 5.7b) – the sway in the portal frame (Fig. 5.7c), and a vertical boom displacement (Fig. 5.7d).

Table 5.5. Natural frequencies and damping of four significant modes from 1:20 scale experiment

Mode	*T Exp.* [sec]	*ζ Exp.* [%]	*T FEM* [sec]
Portal sway	0.306	0.84	0.306
Torsion (boom)	0.612	2.29	0.620
Torsion (frame)	0.549	1.45	0.539
Vertical boom motion	0.143	2.33	0.154

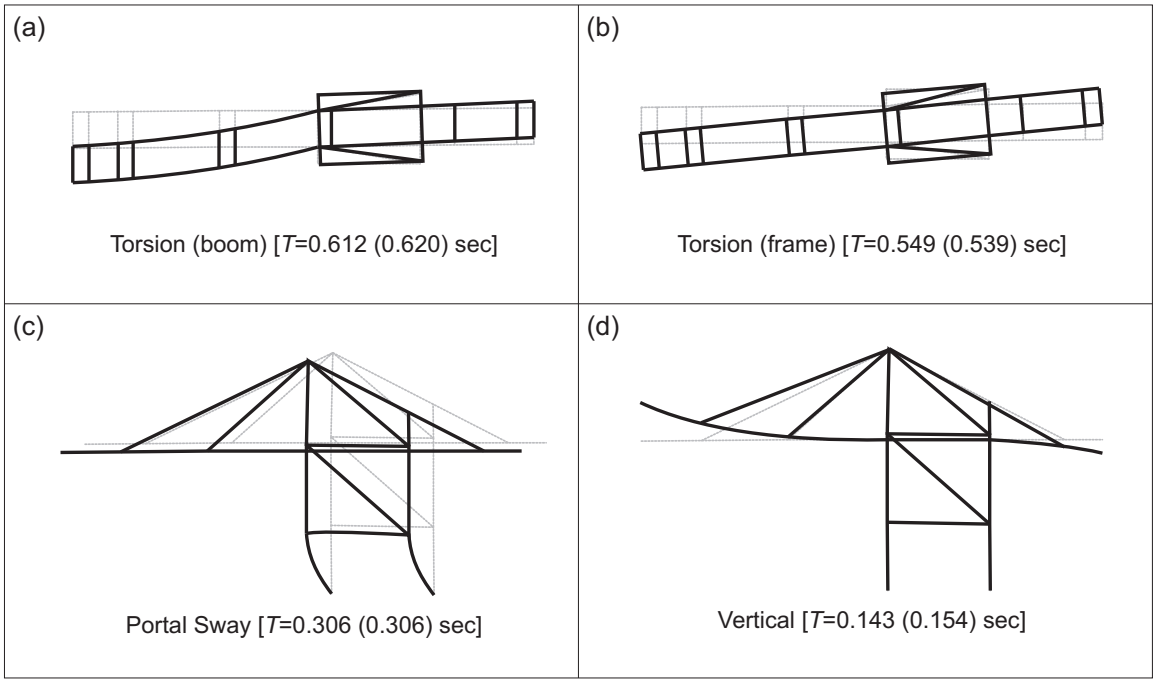

Figure 5.7. Observed experimental (and numerical) fundamental periods and mode shapes.

As an initial comparison with the experimental model, the periods of the corresponding modes of the finite element model are listed in Table 5.5 and in parentheses in Figure 5.7. When comparing experiment to FEM periods, only the vertical mode is more than 2%

different. In fact, the critical portal sway mode (deemed critical by previous studies, e.g. [16], and preliminary analysis) of both the experiment and FE models are the same. Using simple modal analysis and the FEM, this mode was found to have a modal participation ratio of >90% in the trolley-travel (E-W) direction.

5.4.2 Elastic Response

During seismic excitation small enough that uplift does not occur, the crane is observed to respond predominantly in the portal sway mode, regardless of input motion or whether a vertical (up-down) and/or gantry-travel (N-S) direction excitation components are included. This portal sway response is seen experimentally and analytically in the measurements of the displacement along the height of the crane, where horizontal boom tip deformations are within 1% of those measured at the portal beam. Additionally, the axial loads oscillate in the legs of the portal frame consistent with the portal sway mode, along with bending stresses in the portal joints.

Despite apparent portal sway dominance, several other modes are observable from experimental shaking. The crane responds in the two torsion modes, though they are indistinguishable during seismic excitation. The occurrence of the torsion modes are verified from the displacement and acceleration measurements in the direction perpendicular to the boom in both the experiment and analytical model. Also, the boom experiences some vertical vibration associated with higher modes, reflected in vertical displacement and acceleration channels along the boom.

5.4.2.1 Torsion

Because the structure is non-regular with respect to symmetry about the N-S axis, and because torsion response is easily observed during elastic response, the potential for the torsion response to contribute to critical stresses must be evaluated. More specifically, the contributions to portal drift, defined as the drift angle between the portal beam and a particular leg base, are considered here because the sway in the portal frame has been shown to be the critical seismic response. It has been shown by others [167] that the portal flexibility contributes little to torsional flexibility. To verify that result in this case, a push-twist analysis is performed on the calibrated 1:20 scale analytical model of the jumbo container crane. In this analysis a horizontal load is applied to the boom tip, perpendicular to the boom. The boom tip is displaced incrementally through a static analysis and the portal drift is recorded for both portal frames. The deflected shape and the associated displacements of interest of the crane can be seen in Figure 5.8, where Δ is the N-S boom tip deflection and δ is the E-W portal deformation.

It is found that when Δ = 8in, the associated portal deformation (δ) is such that portal drift is 1%. The initial yield of the prototype J100 crane occurs at a portal drift of 2% (see Chapter 6). Thus, significant transverse boom displacement is necessary in order for torsional response to significantly contribute to the critical portal sway response. During experimental shake table testing, the input with the highest intensity is the full-scale multi-component CLE4 ($H1_{pba}$=0.5531g, $H2_{pba}$ = 0.1618g), which resulted in Δ_{max} = 0.92in. In other words, the torsion response only contributes a maximum of 0.12% portal drift to the portal sway response, or 6% of the yield drift, in this high intensity excitation.

The input with the highest *transverse* intensity is the full scale multi-component LP ($H1_{pba}$ = 0.5117g, $H2_{pba}$ = 0.2936g, V_{pba} = 0.0652g), which resulted in Δ_{max} = 0.67in. This corresponds to the torsion response only contributing a maximum of 0.08% portal drift, or 4% of the yield drift. From these observations, it can be concluded that even with significant seismic excitation, the peak possible contribution to portal drift caused from torsion response is small relative to drift capacity. Because the prototype structure represents the typical container crane structural configuration, it is expected that this conclusion can be extended to most typical A-frame container cranes, as suggested by previous researchers (see Chapter 2).

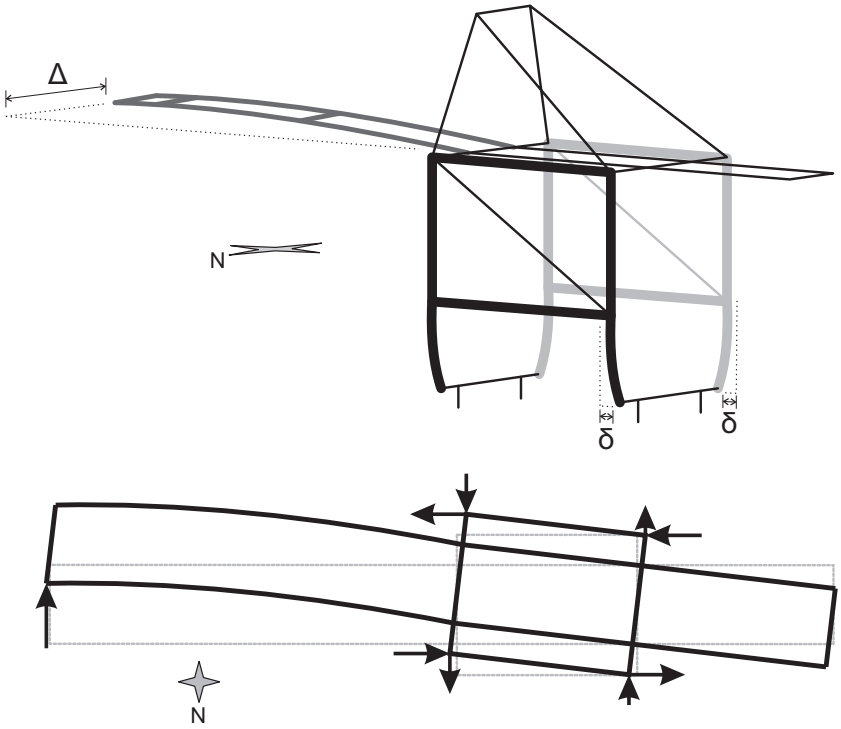

Figure 5.8. Deflected shape for push-twist analysis, emphasizing opposing portal sway deflections (δ) corresponding to gantry-travel boom tip displacement (Δ).

To further test this hypothesis, it is useful to compare experimental maximum portal drift observed between scenarios with only an E-W excitation component (H1) and when both

E-W and N-S excitation components (H1+H2) are included. In this way, it can be determined whether significantly exciting the torsion response leads to consistently higher observed maximum portal drift. Figure 5.9 shows such a comparison, using all data pairs where an earthquake at a given amplitude is used with H1 as well as H1+H2 excitations (the indicator for derailment is discussed later, in Section 5.5.2)

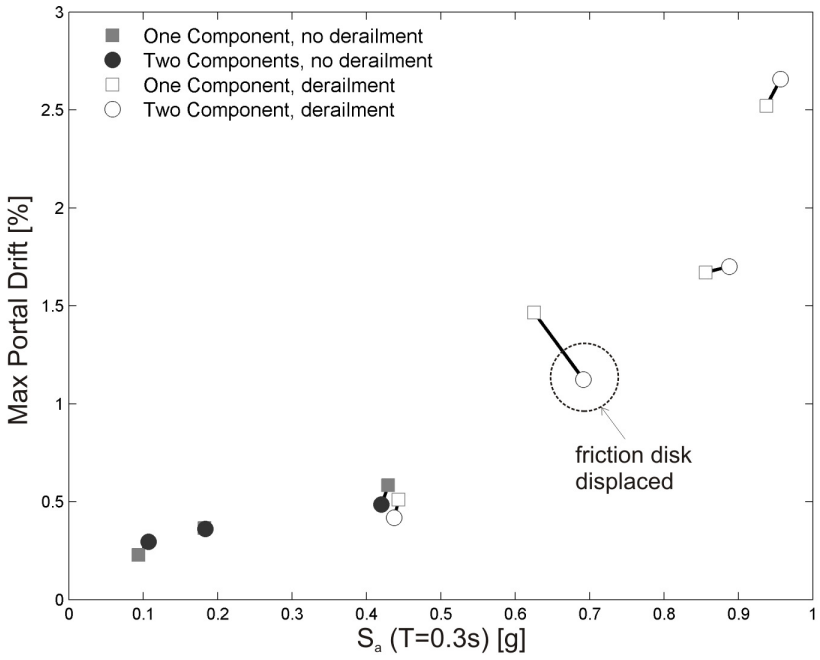

Figure 5.9. Comparison of response pairs for a given earthquake and amplitude, indicating max observed portal drift with H1 and H1+H2 excitation.

For all levels of excitation, the average difference between the responses of data pairs in Figure 5.9 is 0.1% drift or 5% of the yield drift. In some cases, the drift is larger when the second component was added, yet in some cases the opposite is true. In one instance, where earthquake's H1 spectral acceleration was approximately 0.7g, it appears that the two-component excitation resulted in a large decrease in portal drift, despite a higher achieved excitation intensity. However, closer evaluation of the video recordings reveals

that the friction disk was ejected from underneath the leg base during the two-component excitation, an anomaly that was not repeated during any other test. This resulted in lower portal drift levels throughout the specific earthquake run, as base sliding occurred, limiting the seismic energy transferred to the structure. Thus, after direct comparison it can be concluded that significantly exciting the torsion modes of the container crane does not significantly contribute to the critical portal drift. For the same reasons as described earlier, this result is not limited to the experiment model, or even the prototype crane.

An additional consideration for the potential contribution of the torsional response is the difference in period between the torsional modes and the critical portal sway mode. In this case, the torsional modes are at a significantly longer period than the portal sway mode, and so the response spectra indicate significantly lower earthquake intensity for torsional modes. This natural period disparity is typical of most container cranes [14, 167]. Thus, even for the strongest earthquakes, the torsional excitation will generally be less than the portal sway mode.

In summary, three aspects are considered above to determine the contribution of torsional response to the critical portal sway response. In general, the nature of earthquakes means that the long-period torsional response is only lightly excited. Further, even when significantly excited, the torsional response contributes little towards portal deformations. This has been verified through comparing experiment runs with H1 and then H1+H2 component excitations. For these reasons, it is assumed that the torsional response may be ignored when evaluating the seismic performance of the portal frame response.

5.4.2.2 Model Comparison with Experiment

For comparing the elastic response of the experimental and analytical models, the ¼ scale CLE2 excitation having a peak base acceleration of 0.11 g is chosen, as it provided the highest response without causing some amount of uplift. Because portal sway is deemed the critical response of interest, and for the reasons in support of neglecting torsion discussed above, only input in the trolley-travel direction is considered.

The qualitative responses of the experimental and analytical models are in good agreement. Figure 5.10 shows the horizontal displacement of the portal beam as measured at the NW portal joint of the experiment and analytical models. Both exhibit similar displacement trends, indicating that the analytical models are capable of capturing the dominant elastic system dynamics.

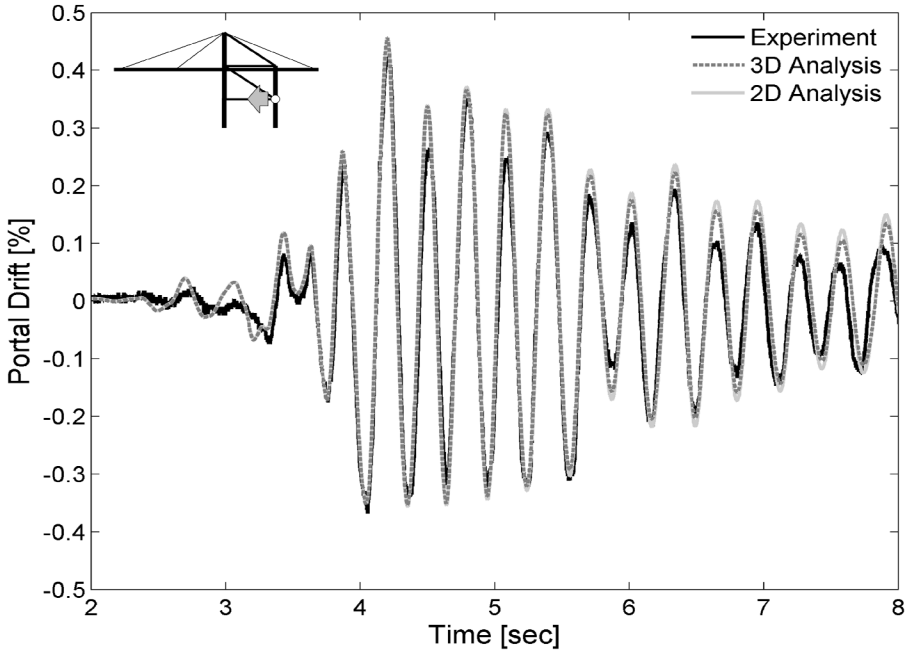

Figure 5.10. Observed portal sway drift of experiment compared with 3D and 2D analytical models for ¼ scale CLE2 excitation.

Noticeable differences between analytical and experimental response are evident, however. One reason for this discrepancy is an incidental torsion response that began where indicated in Figure 5.11, at ~4.25 seconds. Here, the seismic excitation caused a crane leg to slightly "settle" under gravity load, causing the crane's local trolley-travel axis to be slightly askew of the table excitation direction. The resulting inadvertent off-axis excitation caused a slight torsion response, which oscillates at a longer period than the portal sway response. This torsion impacts the portal sway, most noticeable at locations such as at ~4.5 and ~5.1 seconds (indicated in Figure 5.11), where the torsion and portal sway responses are out-of-phase, resulting in a reduction in portal sway deformation. While this incidental torsion is unavoidable, its relative impact is significantly less for larger excitations. Recall that a low-amplitude excitation is chosen here, so that uplift does not occur and the elastic response can be observed alone. Thus the elastic response is small (<0.5% portal drift) by necessity. As discussed in the previous section, for larger excitations where the portal sway mode responds more significantly, the torsion contribution is not significant. Further, the onset of incidental torsion is generally after the peak portal sway deformation (even if immediately so). Therefore, this phenomenon does not compromise the finite element model's capability to capture the dynamic response of container cranes.

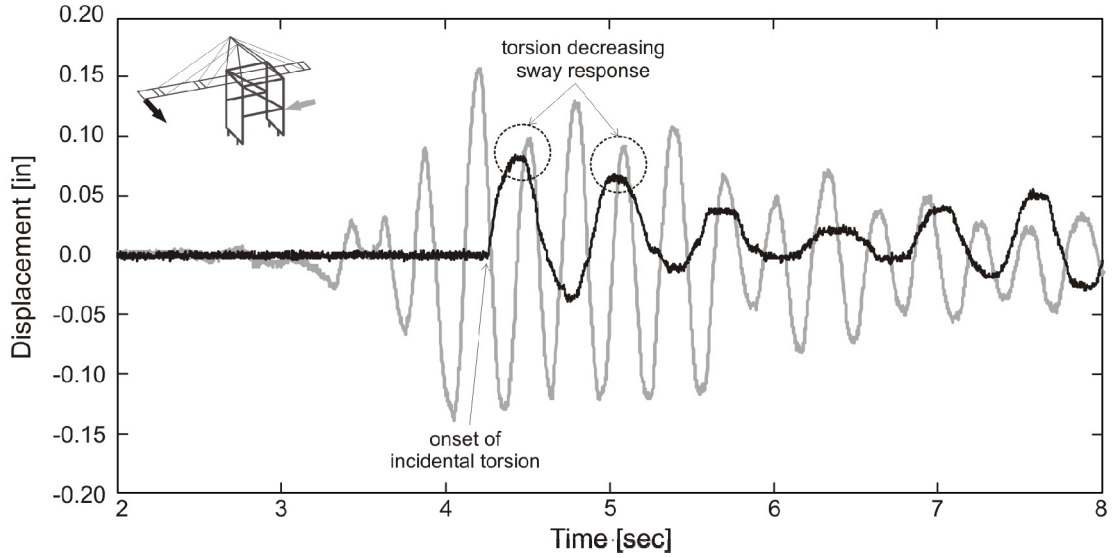

Figure 5.11. Observed portal and boom tip deformation time history, indicating incidental torsion which results in cross-mode contributions for ¼ scale CLE2 excitation.

The settling occurred due to axial imperfections in the experimental columns; some legs were slightly longer than others, resulting in an initial gravity distribution different from assumed, as depicted qualitatively in Figure 5.12. Although a load cell was positioned below each leg base, because the model weight was only a small fraction of the rated load cell capacity (and outside the range of validated calibration), readings were not accurate, and tended to drift upwards. Therefore, the initial load distribution was determined after lifting the crane model using the overhead crane, positioning it on the shake table, and then reading the load cell measurement quickly. Therefore, the initial distribution is known but the axial load measurements during testing are useful only for qualitative purposes. The axial imperfections and resulting incidental torsion also impacted the relative response of each frame, although due to channel limitations, only the North frame is available for response comparisons. In addition, the half-power bandwidth method of estimating damping is imperfect, and could be part of the reason for the overestimation of response by the analytical models at later times (>5s in Fig. 5.10).

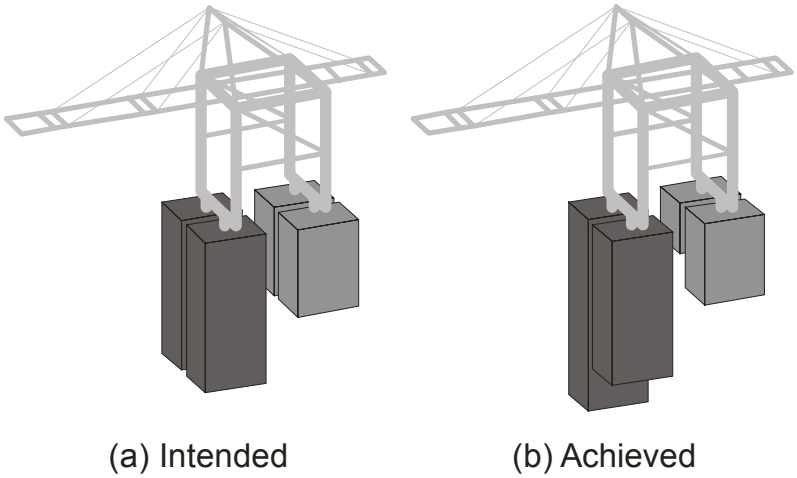

Figure 5.12. Axial load distribution distortion due to length imperfections in crane model.

Considering again Figure 5.10, it can be seen that the response predicted by the 3D and 2D analytical models are nearly indistinguishable, demonstrating that the elastic trolley-travel response can be accurately captured using an appropriate 2D analytical idealization. This result is consistent with previous studies [22]. Because the trolley-travel direction has been shown to be the dominant response, an appropriate 2D model is therefore deemed sufficient to analyze the seismic behavior of container cranes not allowed to uplift, or prior to uplift.

5.5 Coupled Elastic and Uplift Behavior

5.5.1 Coupled Response

When subjected to large enough ground motions, the inertial load is such that the container crane can begin to uplift and exhibit derailment. The observed rocking phenomenon is not rigid rocking, but rather an intimate coupling between elastic structural response and uplift, and tends to increase the period of response, as the rocking

slows the reversals of the dominant sway mode. This response exhibits three general stages, schematically depicted in Figure 5.13[1-3] and described here in further detail: [1] The structure increasingly displaces seaward due to seismic load (a-c). [2] The landside wheels begin to slide when total gravity load transferred to waterside legs (a). As a result, load increases on waterside legs, and they deform further, which then leads to uplift of the sliding legs (b). This causes the uplifted legs to elastically unload and vibrate (c). [3] The landside legs land inboard of the landside rail, and portal sway mode begins to reverse (a). Enough landward portal response causes the waterside legs to slide (and potentially uplift), and land inboard of the waterside rail (b). The result is residual inward displacement of each leg (bowing of the portal frame) (c). This type of response is observed during both experimental and analytical simulations. In all cases, the landside leg (having lower axial load) uplifts first and displaces seaward, though the number of uplift events making up the total rocking response is dependent on the particular ground motion, specifically the duration and amplitude of strong motion.

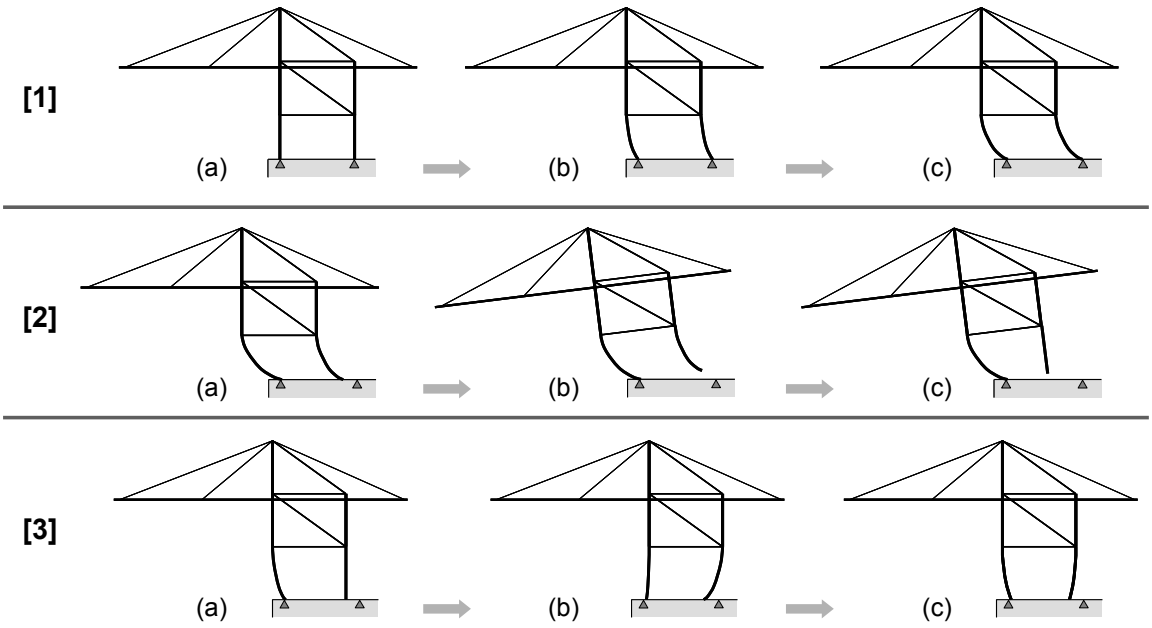

Figure 5.13. Schematic of coupled elastic/uplift behavior of container crane seismic response.

Consistent across ground motions, the container crane rest state after all transients have been damped exhibits inward bowing of the crane legs, such as is shown in Fig. 5.13 [3](c). This lower leg residual drift is observed to vary within the range of 0.5%-1.5%, both physically and experimentally. While the schematic shows both legs settling inside the crane rails, this is not the case for all ground motions. The duration of the uplift event determines the landing point of the uplifted leg. For example, when the crane displaces seaward and the landside leg uplifts, the landside leg will displace seaward if the uplift event is relatively short, such as in Figure 5.13. However, if uplift occurs for a longer duration, the elastic cycle can reverse while the landside leg is uplifted, which can cause the landside leg to land outside the landside rail. An example of this type of behavior is shown in Figure 5.14. Long duration excitation, coupled with long uplift events, can thus cause the crane to "walk" in either direction, as was observed for several cases. However, the inward bowing of the portal frame was the resulting final deformation state of the container crane, regardless of the final locations of the crane leg bases.

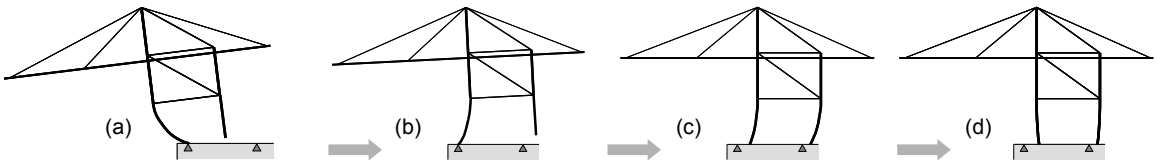

Figure 5.14. Schematic for coupled container crane response during longer duration uplift event.

5.5.2 Uplift Prediction

The onset of uplift and possible derailment is a critical parameter for characterizing a container crane's seismic response. It has been shown [22] that uplift can be successfully related to peak boom acceleration via a static tipping analysis. A simple system is

sketched in Figure 5.15, where H identifies the height to the center of mass, m, of the crane; L_1 the distance between center of mass and waterside leg; L the distance between legs, V_1 and V_2 the vertical reactions at the waterside and landside base, respectively; and a the horizontal threshold acceleration at the center of mass which causes uplift.

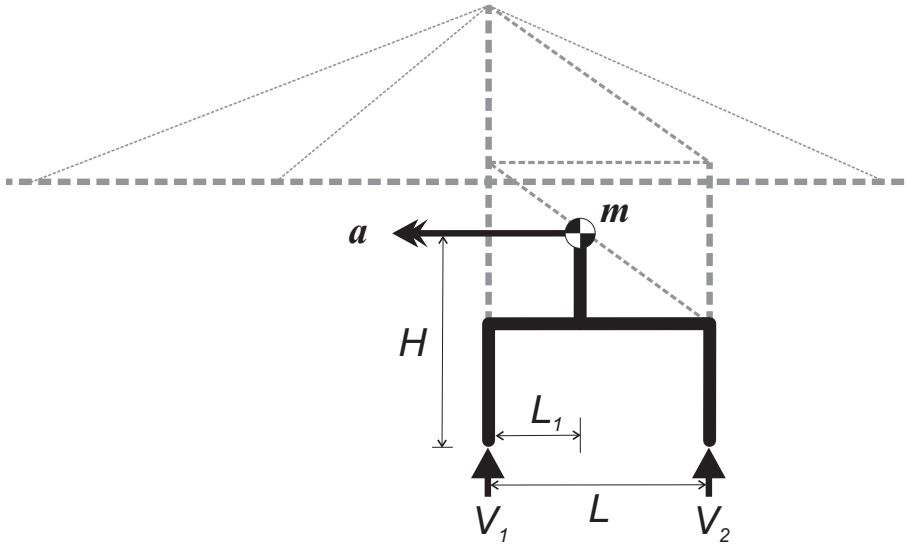

Figure 5.15. Schematic for pseudo-static analysis uplift prediction, adapted from Sugano [22].

The sum of moments can be found at the waterside leg, resulting in Equation 5.1.

$$L \cdot V_2 + H \cdot m \cdot a - L_1 \cdot m \cdot g = 0 \tag{5.1}$$

Because the landside carries less load than the waterside, the landside leg will uplift first, when reaction $V_2 = 0$. Additionally, due to the stiffness of the upper structure of the container crane relative to the portal frame, the acceleration of the center of mass is essentially equal to the acceleration at the boom or the portal beam. The critical acceleration uplift threshold, a_{cr}, can then be evaluated simply using Equation 5.2:

$$a_{cr} = \left(\frac{L_1}{H}\right) g \tag{5.2}$$

Notice that this is consistent with Equation 3.4, repeated below, and introducing the global slenderness parameter (α) from Chapter 3.

$$u_{cr} = \frac{\alpha \cdot g}{\omega^2} = \left(\frac{L_1}{H}\right)\frac{g}{\omega^2} \tag{5.3}$$

The capability to predict this "lift threshold," in terms of either acceleration or displacement, is useful when evaluating seismic capacity, especially from a design perspective. However, the seismic performance and likelihood of downtime relates more to a derailment limit state.

Portal uplift theory, as presented in Chapter 3, indicates that sliding will occur prior to true uplift. Thus, some amount of derailment will occur prior to vertical uplift. This hypothesis is verified in Figure 5.16, which presents the experimental peak displacements of each crane leg for each excitation. It can be seen that significant derailment displacements may occur even with little vertical uplift. Further, there are no situations where significant vertical uplift occurs without derailment. A clear derailment threshold exists at 0.4 in. Below this threshold, horizontal displacements are attributed to the initial "sliding" stage discussed in Chapter 3. Small vertical displacements below the derailment threshold are indicative of slight misalignments of the vertical displacement transducers, and do not indicate true uplift. Therefore, the critical acceleration or deformation value calculated as per Equation 5.2 or 5.3 indicates the onset of initial derailment, confirming the presence of 3-stage behavior as discussed in Chapter 3.

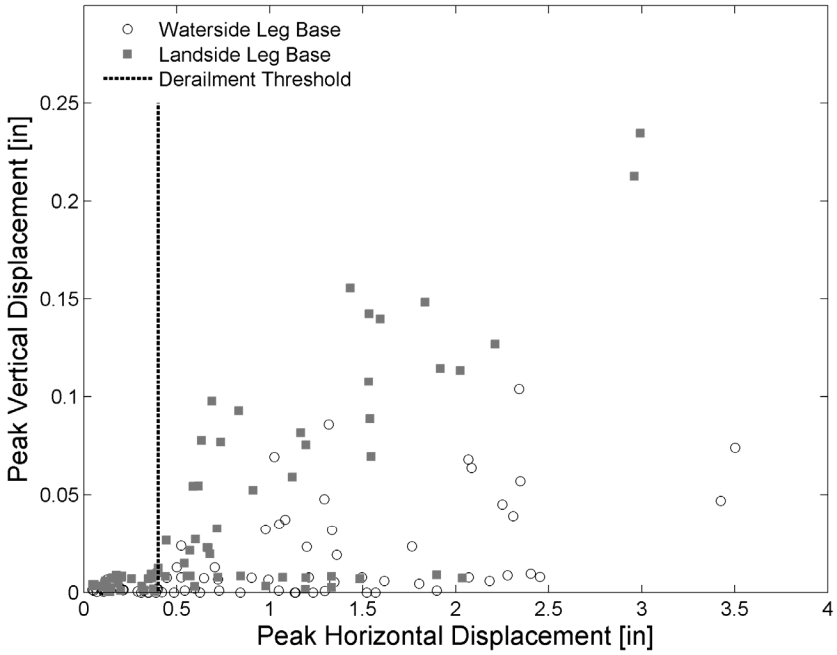

Figure 5.16. Comparison of experimentally observed vertical and trolley-travel (E-W) horizontal displacement of all leg bases under all excitations, indicating a clear derailment threshold.

To confirm that the derailment threshold identified in Figure 5.16 reflects the uplift threshold predicted by Equation 5.2, peak boom acceleration is plotted with respect to the horizontal spectral acceleration of the excitation at the dominant mode (0.306s) and 1.5% damping in Figure 5.17. Solid data points represent experiment runs where E-W horizontal displacement of any leg base surpassed the derailment threshold determined from Figure 5.16, while hollow points are those that did not. As indicated on the figure, the theoretical lift acceleration of the model structure is 0.38g. It is evident that, in general, this predicted lift acceleration is in fact a good indicator of derailment. The two "derailment" data points with near-zero excitation had only vertical excitation, indicating that the effect of vertical motion deserves further consideration. Ignoring these points, a linear trend exists between boom acceleration and input spectral acceleration; thus, uplift

and derailment can in fact be considered in the design stage simply based on design spectra, given that the portal sway mode dominates the critical response.

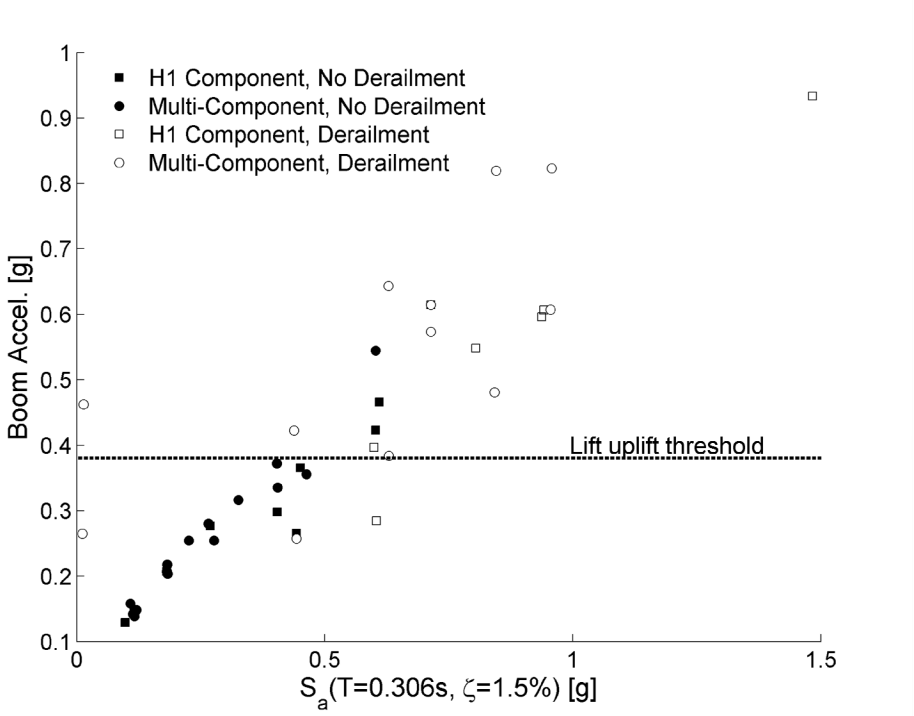

Figure 5.17. Both with and without multiple excitation components, the pseudo-statically determined lift acceleration estimates the onset of derailment well.

5.5.3 Model Comparison with Experiment

For comparing the coupled elastic and uplift response of the experimental and analytical models, the full scale CLE1 excitation having a peak base acceleration of 0.55 g is chosen due to the extent of uplift and derailment response observed. Again, only input in the trolley-travel (E-W) direction is considered.

The observed responses of the experimental and analytical models are in good agreement. Figure 5.18 shows the recorded horizontal and vertical displacements of the waterside and landside leg bases. Both the 3D and 2D analytical models predict the onset and

duration of uplift events and associated translational motion with good accuracy, and capture the 3-stage behavior predicted by the analysis of Chapter 3. In this case, the crane responds lightly in the portal sway mode starting at ~3sec. Just before 6sec, the landside leg "slides" seaward, followed by a reasonably long-duration uplift event which results in the landside leg displacing landward, and landing outside the landside rail. Immediately afterward, the portal sway cycle reverses, causing the seaward leg to slide landward, then uplift a small amount, and finally impact the wharf landward of the waterside rail. This process occurs again just afterward, with further landward sliding and uplift of the landside leg with the accompanied derailment. Finally, after several smaller sliding and uplift events, the crane rests with an inward bowing of the portal legs, where the base of both legs have derailed landward.

Notice that the experiment response of the two parallel frames separates at various times. Early in the excitation, this is caused by the "settling" described earlier due to imperfections in leg lengths. The large recorded offsets of the landside vertical experiment displacements after the primary uplift event are a result of the gages shifting upon impact; one gage rotated while one gage was pushed upwards, leading to imperfect readings with artificial residuals.

In general, the magnitude of translational motion is sensitive to the duration of uplift and the response from elastic structural behavior, both of which are captured well by the analytical models. Overall, both finite element models proved capable of predicting and

capturing the critical response of the elastic crane and its coupling with the uplift/derailment behavior.

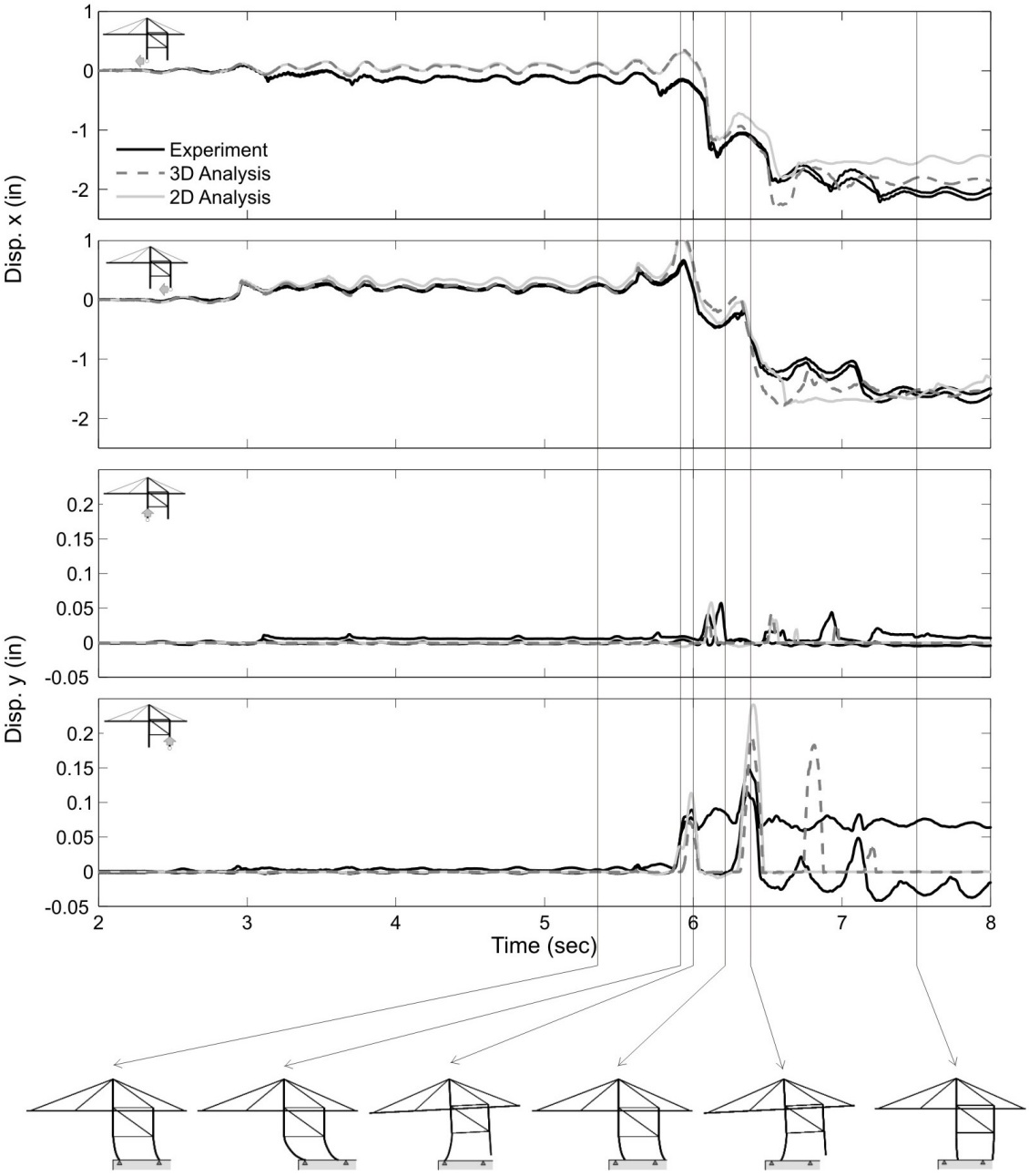

Figure 5.18. Observed vertical and trolley-travel horizontal displacements of waterside and landside leg bases for unscaled CLE1 excitation.

5.6 Impact of Vertical Ground Motion

To determine the impact of vertical ground motion on the response of container cranes, experiments are performed using ground motions both with and without a vertical component. A comparison of the maximum portal observed drifts for these experiments is presented in Figure 5.19. It can be seen that for low levels of excitation (S_a(0.30s) ≤ 0.5 g), the vertical component does not appear to increase maximum portal response. The change in max portal drift (~0.1%) is not outside the expected range of experimental variability. However, for large levels of excitation (S_a(0.30s) > 0.5 g), the vertical component appears to significantly impact the maximum portal drift: as much as 0.5% portal drift. It should be noted that for the large amplitude ground motions, a single record resulted in a decrease in portal drift when the vertical component is considered. Though it is not clear exactly what impact this had, it may be important that this record was the Loma Prieta record, which is the only historical motion recorded on a wharf structure.

With these observations in mind, an analyst or designer considering the effects of large earthquakes should carefully consider the need for including an appropriate vertical component of excitation. Further studies would be helpful in assessing the influence of vertical ground motions to the overall response of a crane, and what constitutes an appropriate vertical motion, given the complex soil-structure interaction and wharf system below the crane. For the purpose of this study, the vertical motion is neglected under the assumption that it will likely be of small amplitude due to the attenuation through the local site effects and the wharf, and that its effect appears important only

where the excitation is large, where estimates of the nonlinear inelastic behavior are made conservative enough that the potential impact from vertical motion will not lead to a generally unconservative analysis.

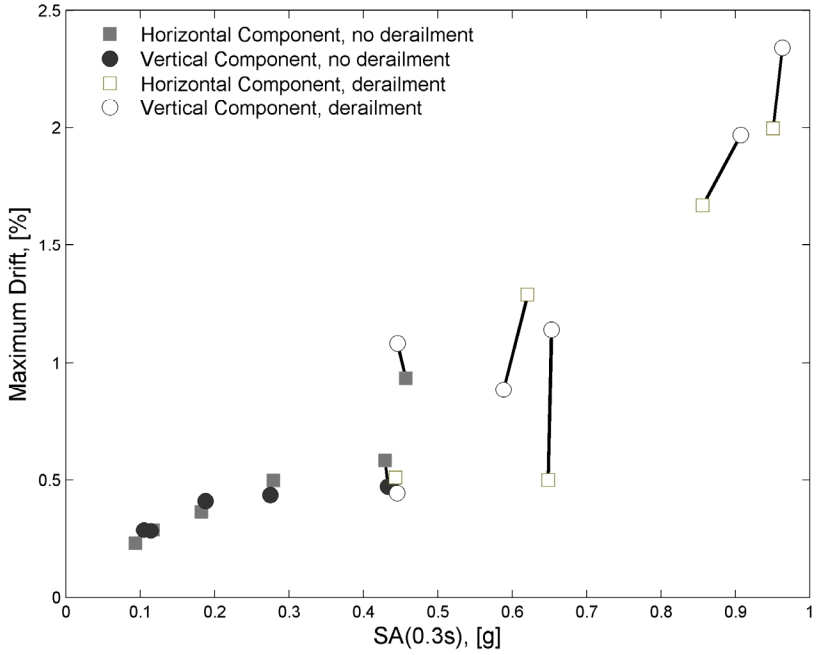

Figure 5.19. Comparison of response pairs, with and without a vertical direction excitation component.

5.7 Summary

The seismic response of a jumbo container crane is complex, and is observed via 1:20 scaled shake-table experiments and finite element simulations. The dominant behavior is controlled by the close coupling between structural response and an uplift/derailment rocking-type phenomenon. The critical structural response is found to be concentrated in the portal sway mode of the trolley-travel direction, which can be captured well by the proposed analytical models. A secondary response includes an obvious torsion mode, but

which does not significantly contribute to the critical portal sway, and in fact does not produce significant contributions to response even when including an off-axis translational excitation component.

Predicting uplift and the possibility of derailment is essential for properly designing and evaluating the seismic response of container cranes. A simple pseudo-static analysis is capable of estimating the critical acceleration or deformation uplift threshold. However, this uplift threshold is actually a derailment threshold, as the 3-stage behavior predicted by Chapter 3 is verified. The occurrence of this derailment is a more appropriate measure of potential post-event downtime.

It is shown that both 3D and 2D analytical models can be constructed which simulate the observed physical behavior, including uplift and derailment response, with good accuracy. Because the portal sway mode is the critical seismic response, to which torsion does not significantly contribute, an appropriate 2D model is sufficient when performing dynamic time-history analysis for evaluating overall behavior. The verified methodology for 2D finite element modeling can then be extrapolated to similarly-constructed prototype-size container cranes for performance evaluation.

Including a vertical component to the excitation is an interesting issue. The inclusion of a vertical ground motion component for the analysis or evaluation of a container crane subjected to a relatively small earthquake may not be necessary. However, it is not clear

how to properly handle a vertical excitation for the case of relatively large earthquakes. Future efforts are required to properly address this issue.

CHAPTER 6

ESTIMATION OF SEISMIC CAPACITY

6.1 Introduction

The preceding chapters described and validated a model which accurately and efficiently captures the critical portal sway response of container cranes. This portal sway mechanism was shown to dominate a crane's deformation-based seismic demand. However, to successfully evaluate the seismic performance of any structure, estimates for both seismic demand and capacity must be available. This chapter considers seismic capacity of container cranes. Consistent with the findings of previous chapters, portal deformation is taken as the critical response of interest for seismic excitations.

Using results and observations from previous research regarding similarly-constructed Japanese steel bridge piers (see Section 2.4), hysteresis rules consistent with the chosen modeling approach are proposed to represent the local inelastic responses. The hysteresis rules are then applied to the portal frame elements of the three case study container cranes presented in Appendix A. Inelastic behavior is captured analytically with rotational springs at the portal joints. Then, overall limit states are defined according to approximate repair methodologies. Finally, the overall limit states are quantified in terms of the critical portal deformation, linked to localized inelastic effects through modified push-over analyses.

6.2 Inelastic Behavior

The portal frames of typical A-frame container cranes are constructed of built-up hollow steel box sections. Due to wheel load restrictions for the crane rails on the underlying wharf, the structural elements of container cranes are optimized by design necessity, rather than simple cost savings. For this reason, the resulting sections typically have extremely slender plate elements, and require longitudinal stiffeners to avoid local buckling prior to bending-induced yielding. Traditionally, section-level elastic stability has been the fundamental design constraint for sizing the stiffeners and setting upper-bound flange/web plate slenderness limits. However, built-up stiffened box sections can exhibit severe local and overall buckling interaction, leading to loss of strength and ductility. This was found to be the case for similarly-constructed steel highway bridge piers in Japan during the 1995 Kobe earthquake [53, 81]. As a result, a number of significant and expansive experimental and analytical research projects were conducted to better understand the underlying inelastic behavior. The most noteworthy of those were reviewed in Section 2.4. The findings and results from these studies are used here to develop and calibrate hysteresis rules appropriate to the chosen modeling methodology and analysis platform.

6.2.1 Calibration Methodology

As described in Section 2.4, the majority of previous research considering the cyclic inelastic behavior of steel stiffened hollow box sections evaluated the load-deflection response of cantilever columns with constant axial load P, height h (split into stub-columns of length a by transverse diaphragm stiffeners), and varying lateral load H, as

shown in Figure 6.1. Local buckling was observed to occur concentrated within the fixed-end stub-column, and progress as described in Table 2.1. Results were typically presented as cyclic load-deflection plots, or as backbone or envelope curves, relating column tip deflection to applied lateral load. Because the Japanese steel bridge piers were typically built as cantilever columns with heavy road decks at the top, this approach was intuitive. However, to be useful for application to container crane portal frame elements, it is convenient to represent the inelastic behavior in a moment-rotation hysteretic curve. Because the buckling and inelastic behavior is concentrated at the column base, a nonlinear and hysteretic rotational spring which captures the key behavioral features, can be developed as depicted in Figure 6.1.

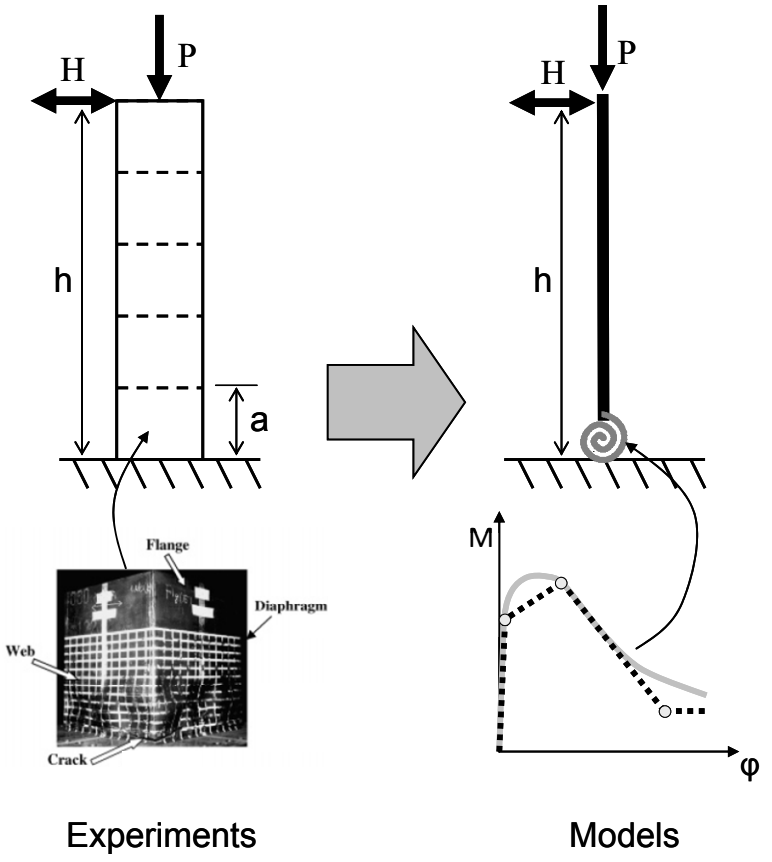

Figure 6.1. Idealized model of experiments, using elastic column and hysteretic rotational spring, which act as a calibration tool for moment-rotation relationship development.

By using an elastic column element and an appropriate moment-rotation relationship, the resulting force-deformation response is the same as the experiment, but the moment-rotation relationship is transferable. In other words, the same moment-rotation relationship developed in the case of the cantilever column can be used in any structure built using the same section. It should be noted, however, that by using an elastic element connected to a rotational spring, the initial stiffness of the rotational spring is essentially infinity. The spring acts as a rigid support such that the elastic column response controls behavior until the initial yield load. From this point on, the rotational spring begins to dominate the force-deformation response.

6.2.2 Hysteresis Rules

To the author's knowledge, no experiments have been performed on steel stiffened hollow box sections identical (or perfectly similar) to the sections used in container crane construction. This is particularly true relative to the relationship between the wall slenderness and the spacing and detailing of the stiffeners. Thus, the hysteretic response must be predicted based on extrapolation from experimental results on somewhat similar specimens and basic mechanics for the individual components.

There are several key aspects of the hysteretic response that must be captured to realistically consider the seismic response of any structure with similar sections, as explored in Section 2.4:

1. Hardening: these sections typically exhibit some significant overstrength, where the maximum capacity can be greater than the initial yield by a very significant margin. This generally means that while behavior is initially dominated by yielding, it is necessary to track many other mechanisms that can take over as hardening occurs.
2. Softening: after reaching the maximum capacity, the strength and stiffness begin to degrade. This decrease can be quite rapid for highly slender sections and lead to significant numerical problems when trying to assess performance in this region.
3. Damage accumulation: repeated cycles at the same deformation level will result in decreased load capacity, an effect which is proportional to the cycle deformation. In other words, there is a path dependency in the hysteretic response. Very little data is available in this area for the slenderness ratios and stiffeners details used in container crane structures.
4. Pinching: the reloading stiffness is softer than the loading stiffness. In other words, the deformation gained during reloading is greater than that recovered during unloading. The effect of this phenomenon on crane performance is unknown.

These response characteristics can be captured by the OpenSees "hysteretic" material (executed using the command `uniaxialMaterial Hysteretic`) applied to a zero-length rotational element defined between two coincident nodes. With the hysteretic material, a (positive and negative) skeleton curve is defined using three points. The unloading behavior is determined by two pinching parameters, as is damage

accumulation. The remainder of this section describes how the skeleton curve is defined for purposes of this study, as well as the appropriate pinching and damage parameters. Based on the review in Section 2.4, this approach has been deemed appropriate and sufficient for defining hysteresis rules in support of this container crane study. This justification is based on the observation that few inelastic cycles are expected to occur due to the uplift response and highly slender member sections.

Initially, the skeleton curve is constructed for the load-deformation response, as depicted in Figure 6.2. The three anchor points are the yield point (Y), the point of maximum ductility (N), and the failed point (Z). The load (H) and deformation (δ) associated with each of these points are determined as described below. The point of maximum capacity (M) is not included in the skeleton curve because the hysteresis model can only utilize three anchor points, but as will be seen later, is still an important quantity.

The first step for defining the skeleton curve is determining typical geometric section properties: area A, moment of inertia I, radius of gyration r, plastic modulus Z, and section modulus S, assuming that the dimensions of the section's component plates are known. It should be understood that the references provided here are examples of relevant literature only, and are not necessarily the origination of the various parameters.

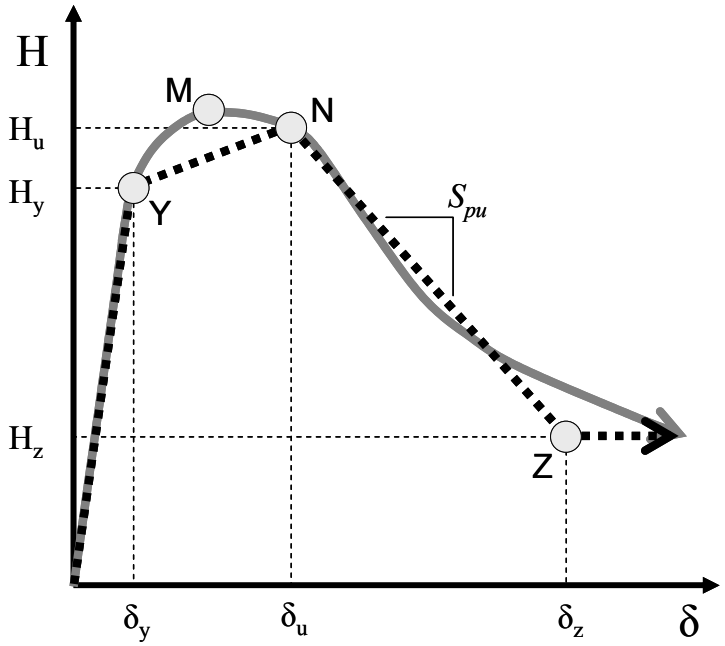

Figure 6.2. Schematic of an envelope curve for slender hollow box section.

6.2.2.1 Yield Point

The yield point is the most straightforward point to estimate. Here, the yield load is determined as

$$H_y = \min\begin{cases} \dfrac{H_{y0}}{0.85}\left(1-\dfrac{P}{P_e}\right)\left(1-\dfrac{P}{P_u}\right) \\ H_{y0}\left(1-\dfrac{P}{P_y}\right) \end{cases} \tag{6.1}$$

where H_{y0} = yield load under no axial load = $F_y S/h$, P_e = Euler buckling load, P_u = ultimate strength, P_y = squash load, and F_y = yield stress [56]. To be consistent with the experiment designs, the ultimate strength is determined from Japanese specification for road bridges [60], and is calculated as

$$\frac{P_u}{P_y} = \begin{cases} 1.0 & \left(\overline{\lambda} \le 0.2\right) \\ 1.109 - 0.545\overline{\lambda} & \left(0.2 \le \overline{\lambda} \le 1.0\right) \\ 1/\left(0.773 + \overline{\lambda}^2\right) & \left(\overline{\lambda} \ge 1.0\right) \end{cases} \tag{6.2}$$

Then, the yield deformation is calculated from beam theory

$$\delta_y = \frac{H_y h^3}{3EI} \tag{6.3}$$

6.2.2.2 Slenderness Parameters

The points of maximum load capacity (M) and maximum ductility (N) have been determined from extensive parametric studies involving large numbers of specimens, both experimental and analytical, depending on a number of useful slenderness parameters. While presented in Section 2.4, they are repeated here for completeness and clarity. First, the flange plate slenderness is defined per Equation 2.1, repeated below [56]:

$$R_f = \frac{B}{t}\sqrt{\frac{12\left(1-\nu^2\right)}{4n^2\pi^2}}\sqrt{\frac{\sigma_y}{E}} \tag{6.4}$$

Also, the traditional column slenderness parameter (Equation 2.2) is important [56]:

$$\overline{\lambda} = \frac{kh}{r\pi}\sqrt{\frac{\sigma_y}{E}} \tag{6.5}$$

The stiffener's equivalent slenderness ratio (Equation 2.11) also plays a role [56]:

$$\overline{\lambda}_s = \frac{1}{\sqrt{Q}}\frac{a}{r_s}\frac{1}{\pi}\sqrt{\frac{\sigma_y}{E}} \tag{6.6}$$

in which r_s = radius of gyration of the T-shape cross section consisting of one longitudinal stiffener and the adjacent subpanels, and Q = local buckling strength of a plate enclosed by two adjacent diaphragms and stiffeners, defined in Equation 2.12 as

$$Q = \frac{1}{2R_f}\left[\beta - \sqrt{\beta^2 - 4R_f}\right] \tag{6.7}$$

When the nondimensionalized compressive residual stress and initial out-of-flatness are (reasonably) assumed to be 1/150, parameter β can be determined from Equation 2.13 as

$$\beta = 1.33R_f + 0.868 \tag{6.8}$$

A modified stiffener equivalent slenderness ratio is defined by Equation 2.14 [83]:

$$\bar{\lambda}_s' = \frac{1}{\sqrt[5]{\alpha}}\bar{\lambda}_s \tag{6.9}$$

where α represents the section aspect ratio of the flange plate between two diaphragms (a/B).

6.2.2.3 Maximum Load Point

The point of maximum load capacity is not explicitly included in the hysteretic skeleton curve because the OpenSees hysteretic material allows at most three anchor points. By removing this point, rather than the point of maximum ductility, the skeleton curve is slightly conservative, cutting off the top of the true peak. Further, because maximum ductility is a more critical parameter for determining seismic capacity than is maximum load, retaining an accurate estimate of the maximum ductility point is crucial. Still, an empirical estimate for the maximum load point is presented, as it is an important parameter for performance-based capacity design and evaluation, discussed further in Chapter 8.

From an extensive database of calibrated and verified finite element models of steel stiffened hollow box sections, Usami et al. [83] present empirical estimates for the load and deformation at the point of maximum load, based on the slenderness parameters

described above. The proposed equations agree well with earlier experimental results [50, 51]. Repeated from Equation 2.15, the maximum load can be determined as

$$\frac{H_{\max}}{H_y} = \frac{0.10}{\left(R_f \bar{\lambda} \bar{\lambda}_s'\right)^{0.5}} + 1.06 \qquad (S = 0.07) \qquad (6.10)$$

where S is the standard deviation of the fit to the database of specimen results. Typical overstrength factors are reported as ranging from 1.3 to 1.7. The corresponding deformation can be determined based on Equation 2.16, repeated below.

$$\frac{\delta_m}{\delta_y} = \frac{0.22}{R_f \sqrt{\bar{\lambda}} \bar{\lambda}_s'} + 1.20 \qquad (S = 0.59) \qquad (6.11)$$

Typical values of ductility at this ultimate load point for tested specimen are reported as varying from 3.0 to 6.0.

6.2.2.4 Maximum Ductility Point

The point of maximum ductility is defined as the point where a potentially unstable progression of local buckling can begin. In other words, after the point of maximum ductility, one cannot reliably count on any meaningful capacity from the section. For these slender stiffened hollow box sections, the current practice is to define it as the deformation at which the load capacity has decreased to 95% of the maximum load (e.g. [83]). Thus, it is on the degrading side of the maximum capacity, but has not yet begun to rapidly degrade. Some local buckling is evident in the plates of a section at its maximum ductility, but it is at the "cusp" of large localized plate or wall buckling. In a nonredundant structure, such as cantilever column or portal frame, this section-level maximum deformation can represent the maximum global capacity prior to complete collapse. Thus, it is important to be slightly conservative on this estimate, which explains

the shift from using the deformation where the load resistance decreases to the yield load, as was done in earlier work (e.g. [51]). This approach is especially important for extremely slender sections, where degradation may be occurring quite rapidly in the region where load capacity has decreased to its yield capacity.

Using the same database as for the point of maximum load, Usami et al. [83] present an empirical relationship for the deformation at maximum ductility, repeated below from Equation 2.17.

$$\frac{\delta_{95}}{\delta_y} = \frac{0.25}{\left(1 + P/P_y\right) R_f \sqrt{\bar{\lambda}\,\bar{\lambda}_s'}} + 2.31 \qquad (S = 0.64) \tag{6.12}$$

Typical maximum ductility values for tested specimens range from 3.5-7.0. The corresponding load is easily calculated based on the ductility definition and Eq. 6.10:

$$H_u = 0.95 \cdot H_{\max} \tag{6.13}$$

6.2.2.5 Failure Point

Experimental evidence [50, 51, 57, 61, 63] from cyclic tests taken to failure, via complete localized buckling or fracture (welds or plates), indicates that some residual load capacity exists even after the identified "failure" point. Thus, the failure point represents the end of the degrading slope, and the beginning of the residual strength plateau. In reality, the transition from degradation to the residual plateau is gradual, as shown in Figure 6.2, so it is difficult to estimate this point with any accuracy. From a qualitative analysis of the past experiments, the residual strength is defined as

$$H_z = \frac{H_y}{3} \tag{6.14}$$

In order to estimate the deformation at this defined failure point, the slope of degradation can be used. It is obvious from experimental results that the degrading slope is much higher for more slender specimens. For example, the skeleton curve idealization depicted in Figure 6.2 represents a significantly more slender section than that depicted in Figure 2.3. With that in mind, a crude empirical relationship was developed to relate the degrading slope after the point of maximum ductility (S_{pu}) to the degrading slope between the maximum load point and the maximum ductility point (S_{95}). A basic model was proposed to relate these slopes as follows:

$$\frac{S_{pu}}{S_{95}} = \frac{1}{\left(\frac{D}{R_f}\right)^A \left(\frac{E}{\bar{\lambda}}\right)^B \left(\frac{F}{\bar{\lambda}_s'}\right)^C} \tag{6.15}$$

To obtain this relationship, the results reported by Usami et al. [83], are first used to graphically estimate the post-ultimate slope from reported envelope curves for each specimen. Then, constants A through D are found such that the norm of the difference between the computed S_{pu} and estimated S_{pu} is minimized. To simplify the model, several samples from Usami's database are not used for this regression. Specimens B6-10, B6-20, and B6-30 are discarded because their only differences lie in the axial load ratio. Specimens B11 and B12 are also discarded because they show little to no strength degradation; in this way, this slope model is essentially weighted towards the more slender specimens. Specimen B18 cannot be used because there is no reported envelope curve. These omissions allow for a simpler slope model, which is still appropriate for use in the desired context, to be used if we recall that (a) the maximum ductility is the crucial parameter, and (b) only a crude estimate of the degrading slope is necessary. Using this methodology, optimal values of the constants were found to be:

$$[A, B, C, D, E, F] = [0.6\ 1.2\ 0.5\ 0.05\ 0.4\ 0.35] \quad (6.16)$$

With this resulting post-ultimate slope model, it is straightforward to determine an estimated deformation value at the failure point.

6.2.2.6 Limitations to Range of Applicable Slenderness Parameters

The reported range [83] of relevance for the empirical estimates of Equations 6.10-6.12 is

$$0.25 \leq R_f \leq 0.56,\ 0.20 \leq \lambda \leq 0.50,\ P/P_y \leq 0.3,\ \gamma/\gamma^* \geq 1.0 \quad (6.17)$$

These ranges are based on the parameter values for the specimens considered. If specimens from other studies whose cyclic behavior are also well-predicted are included, the ranges can be slightly extended to

$$0.25 \leq R_f \leq 0.67,\ 0.20 \leq \lambda \leq 0.71,\ P/P_y \leq 0.4,\ \gamma/\gamma^* \geq 0.85 \quad (6.18)$$

However, it is the author's belief that these upper limits to slenderness parameters should not explicitly limit the use of the empirical strength and ductility equations presented by Usami et al. [83]. Because they are inversely proportional to a product of multiple slenderness parameters, the estimated strength or ductility is essentially exponentially decreasing to some lower bound asymptote (refer back to Figure 2.6 for plots). For very slender sections, the estimated strength or ductility changes very little with even large changes in the slenderness product. In other words, highly slender sections which technically violate the applicable range in either Equation 6.17 or 6.18 are in the "flat" area of the curve. Thus, while there may be greater uncertainty associated with the predicted values, it is reasonable to approximate the strength and ductility values for sections more slender than those used to develop the empirical equations. Clearly some caution and judgment are needed in interpreting final results from this procedure.

6.2.2.7 Pinching Parameters

Two pinching parameters in the OpenSees hysteretic material control the reloading path. By default, the `pinchx` and `pinchy` parameters are unity, resulting in direct reloading as illustrated in Figure 6.3. Altering these parameters allows the reloading to occur in two branches. By selecting a relatively low `pinchx` and relatively high `pinchy` parameters, the reloading path more realistically captures the Bauschinger effect and the associated energy absorption. For this study, values of 0.2 and 0.8 are chosen for `pinchx` and `pinchy`, respectively, as illustrated in Figure 6.3.

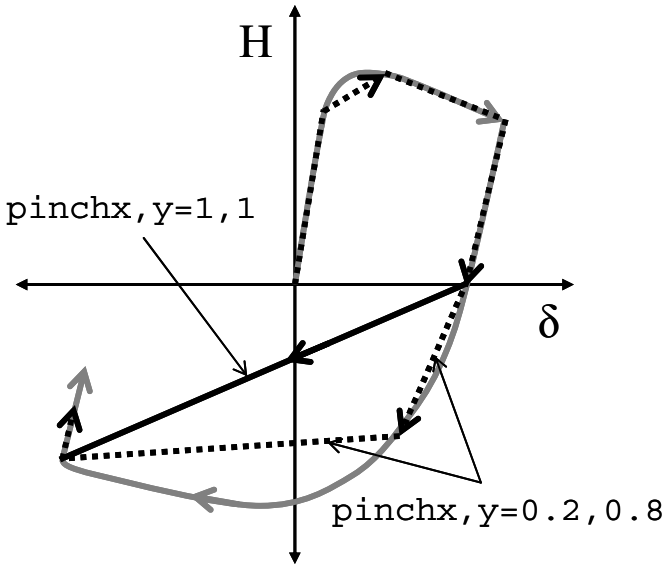

Figure 6.3. Definition of pinching behavior and parameters for hysteretic rules.

6.2.2.8 Damage Parameters

Degradation due to damage accumulation can be controlled in the OpenSees hysteretic material as well. Damage can be defined based on inelastic deformation or energy accumulation. This section explains how these damage terms are defined, based on OpenSees source code (HystereticMaterial v. 1.19). Although the material model can be

used for stress/strain, force/deformation, moment/rotation, etc., it is convenient for this discussion to generalize the axes as `s/e`. Then, the user-defined positive and negative envelope can be illustrated as in Figure 6.4.

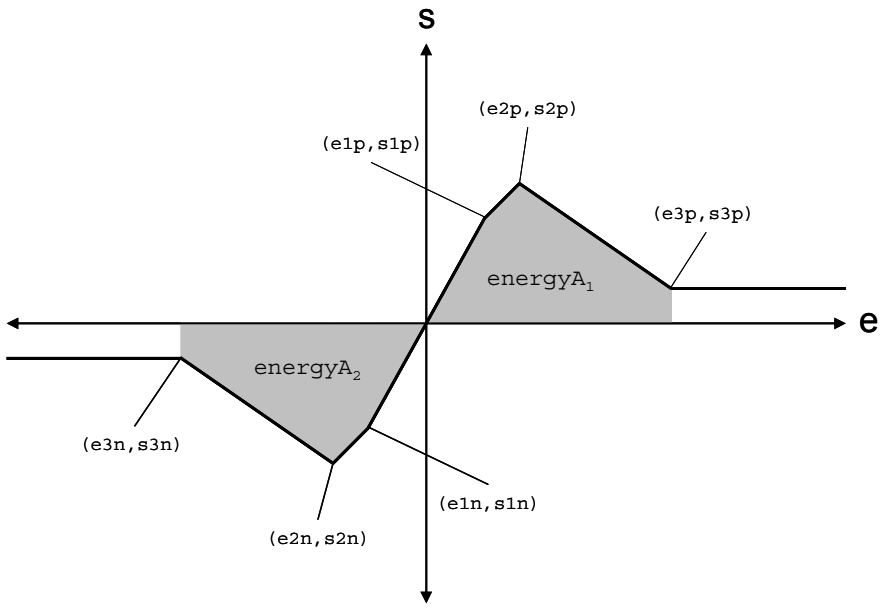

Figure 6.4. Parameter definitions for skeleton curve.

Internally, total damage is defined as

$$D = \beta_1 \frac{e - e1}{e1} + \beta_2 \frac{energy}{energyA} \tag{6.19}$$

Here, β_1 and β_2 are the user-input damage parameters for ductility- and energy-based damage, respectively. The first term contributes damage based on the ratio of a cycle's maximum inelastic deformation ($e - e1$) to elastic deformation ($e1$). This can accumulate from the positive or negative branch. The second term contributes damage based on the ratio of half-cycle accumulated energy (*energy*), normalized with respect to the envelope curve energy ($energyA = energyA_1 + energyA_2$). The half-cycle energy (*energy*) is depicted graphically in Figure 6.5.

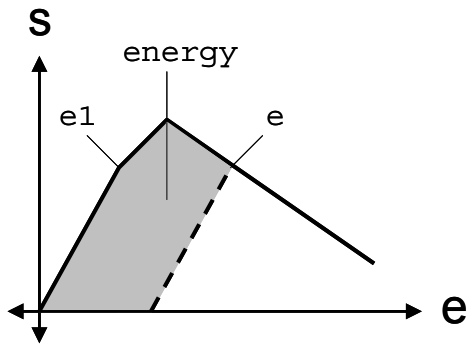

Figure 6.5. Graphical definition of half-cycle energy.

When damage has been determined for one cycle, the next cycle follows a different load path, even if the prescribed displacement is different. The hysteretic rule is best described graphically, as in Figure 6.6.

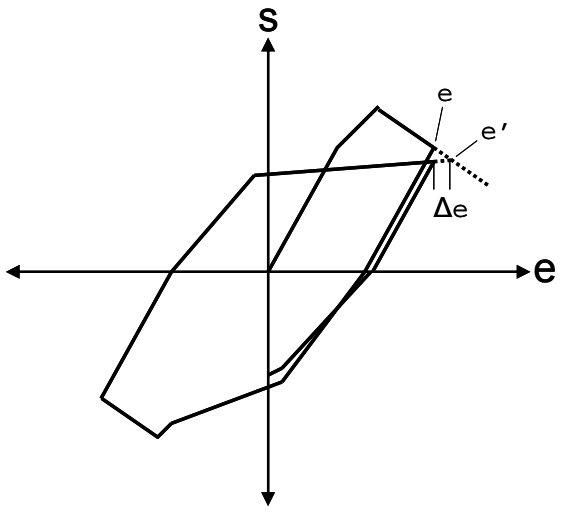

Figure 6.6. Graphical definition of damage-based degradation for hysteretic rules.

Damage is enforced in the hysteresis rule by the following equation:

$$e' = e + \Delta e = e(1 + D) \tag{6.20}$$

Essentially, the additional deformation is proportional to the product of damage and the current deformation. This is somewhat different than other typical damage models, such

as those described in Section 2.4.3.3, in which the additional deformation is proportional to the energy itself:

$$e' = e + \Delta e = e + D \tag{6.21}$$

Therefore, it is impossible to define the OpenSees hysteretic material damage parameters as per recommendations in the literature specifically for steel stiffened hollow box sections.

However, it is still desirable to include some amount of energy-based damage accumulation, as suggested by requirement 3 listed above. Therefore, an energy-based damage parameter with a value of β_2=0.5 is chosen. With this damage accumulation model, significant damage at large deformations can have a very large effect on degradation. Because the post-ultimate slope estimated by Equation 6.15 does not account for this, the deformation at the failure point on the envelope curve is doubled. Therefore, a balance is achieved between envelope-induced degradation and energy-based damage accumulation degradation.

6.2.2.9 Load-Deflection to Moment-Rotation

When the desired hysteresis envelope is defined according to the sections above for the cantilever column, the anchor points must be translated to anchor points for the moment-rotation envelope curve applied to the nonlinear rotational spring. To translate lateral forces to moments is quite simple, as the anchor point moments are simply the lateral loads divided by the load height, or column length.

$$M = H/h \tag{6.22}$$

To translate column tip deformations to concentrated base rotations, it is slightly more complicated because the column has elastic properties of its own, so the initial stiffness of the rotational spring is essentially infinite. Thus, the angle of rotation must be adjusted to remove the elastic contribution to deformation, which is accomplished by the following equations.

$$\phi_y = \tan^{-1}\left[\left(0.01\delta_y\right)/h\right] \tag{6.23}$$

$$\phi_{\max} = \tan^{-1}\left[\left(\delta_m - \frac{H_{\max}}{H_y}\delta_y\right)\Big/h\right] \tag{6.24}$$

$$\phi_u = \tan^{-1}\left[\left(\delta_u - \frac{H_u}{H_y}\delta_y\right)\Big/h\right] \tag{6.25}$$

$$\phi_z = \tan^{-1}\left[\left(\delta_z - \frac{H_z}{H_y}\delta_y\right)\Big/h\right] \tag{6.26}$$

6.2.3 Verification of Calibration

Using the methodology from Sections 6.2.1 and 6.2.2, several models are constructed, each representing one of the analytical or experimental specimens discussed in Section 2.4. These example specimens were chosen from those with relatively high overall slenderness, so that they are as similar to the container crane sections as possible. (As will be seen in Section 6.4, the container crane specimens are quite slender, by all measures.) Table 6.1 presents a summary of the sizes of these example sections, and Table 6.2 summarizes the relevant calculated parameters as presented here and in Sections 6.2.2.2 and 2.4.

Table 6.1. Geometry of example sections from the literature used as points of verification for hysteresis rule calibration.

Column	*Ref.*	*D* [mm]	*B* [mm]	*t* [mm]	*bs* [mm]	*ts* [mm]	*n*	*a* [mm]	*h* [m]	f_y [MPa]	P/P_y
B2	[83]	1344	1344	20	121	20	3	1344	7.54	314	0.15
B4	[83]	1344	1344	20	121	20	3	1344	10.78	314	0.15
B14	[83]	882	882	9	80	6	4	882	3.40	379	0.125
S6	[51]	409	400	4.5	35	3.2	4	350	2.4	292	0.079
S62C5	[50]	286.7	422	4.34	57	4.25	3	423	2.05	309.9	0.2

Table 6.2. Calculated slenderness parameters from example sections in Table 6.1.

Column	R_f	λ	λ_s	λ_s'	γ/γ_{req}	γ/γ^*	t/t_0
B2	0.46	0.35	0.51	0.51	1.01	0.86	1.07
B4	0.46	0.50	0.51	0.51	1.01	0.86	1.07
B14	0.56	0.26	0.63	0.63	0.93	0.93	0.98
S6	0.44	0.36	0.46	0.48	1.58	0.95	2.49
S62C5	0.67	0.43	0.35	0.35	5.42	5.42	0.74

Columns B2 and B4 are quite slender, evidenced by the relatively high slenderness parameters R_f, λ, and λ_s', which leads to rather steep degradation after the point of maximum ductility. The reported hysteretic behavior from two-sided cyclic testing is shown in Figure 6.7 (a) and (c) for columns B2 and B4, respectively. The corresponding response using the hysteresis rules described in Section 6.2.2 are illustrated in Figure 6.7 (b) and (d). Notice that the general shapes are reasonably similar. Most importantly, the point of maximum ductility is predicted well, and cyclic degradation is captured well. As expected, because the point of maximum force capacity is not used on the envelope curve, the model underpredicts capacity during the initial hardening stage.

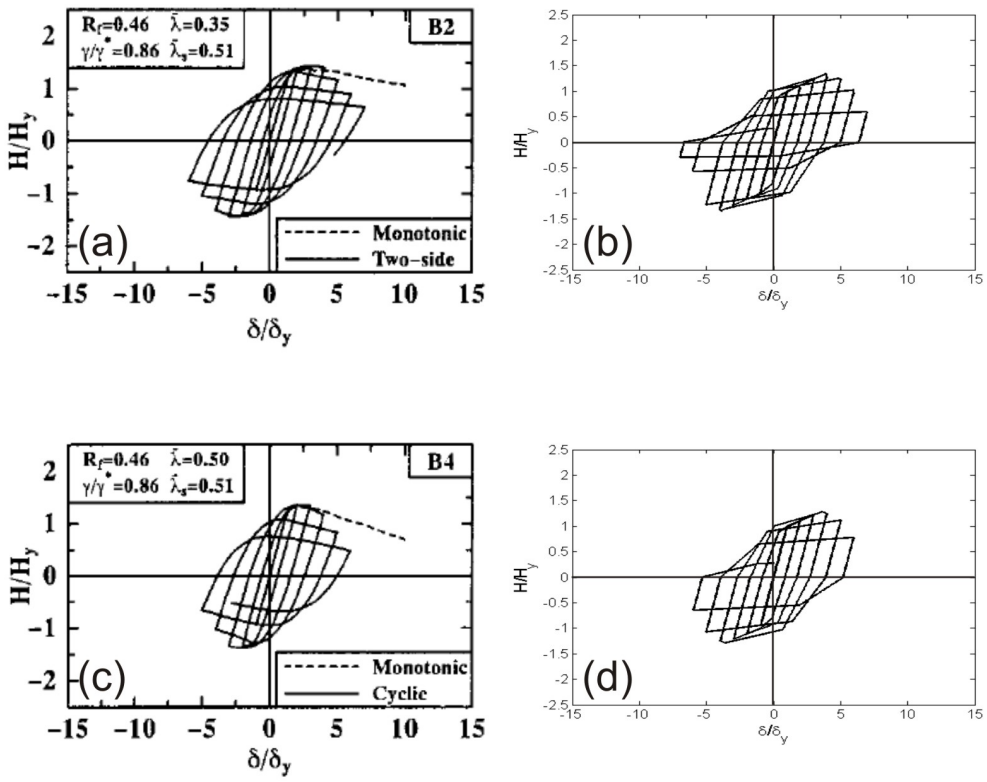

Figure 6.7. Literature reported [83] cyclic behavior (a & c) compared with that predicted by the model used here (b & d), for columns B2 and B4.

One important feature of the hysteretic response is that in reality the maximum force is achieved early in the cycles with large maximum deformation, followed by gradual decrease; this is more evident in B4 than in B2. In the hysteresis model, the load gradually increases instead. The reason for this is clearly evident in Figure 6.3, where the definition of pinching behavior forces this response. While refinements could be made, the hysteresis modeling approach was kept as straightforward and flexible as possible, and avoids having to use experimental results to explicitly calibrate each rotational spring. Recall that the end goal in this context is to have an approximate hysteresis model which captures the broad features of true response, and can be extended to container crane sections for which experimental cyclic test results are not available for calibration.

Because container cranes are not expected to exhibit many cycles during seismic loading due to the uplift response and the rapid degradation due to high slenderness, the predictions shown in Figure 6.7 (c) and (d) are viewed as adequate and appropriate for purposes of performance evaluation.

The γ ratios, which were shown in Section 2.4.2 to be helpful in predicting the buckling potential and controlling local buckling mode, predict overall wall buckling. This in fact was the case for both of columns B2 and B4 [83].

Column B14 presents an interesting case, as it was used by Usami et al. to verify that their new material model, the modified two-surface plasticity model (2SM) [78], provided finite element results which matched experimental cyclic testing [81]. Figure 6.8 (a) illustrates the comparison, and the 2SM model was said to "accurately predict the cyclic behavior" [56]. The prediction of cyclic behavior from the simple hysteretic model used here is shown in Figure 6.8 (b), and provides a reasonable approximation here as well.

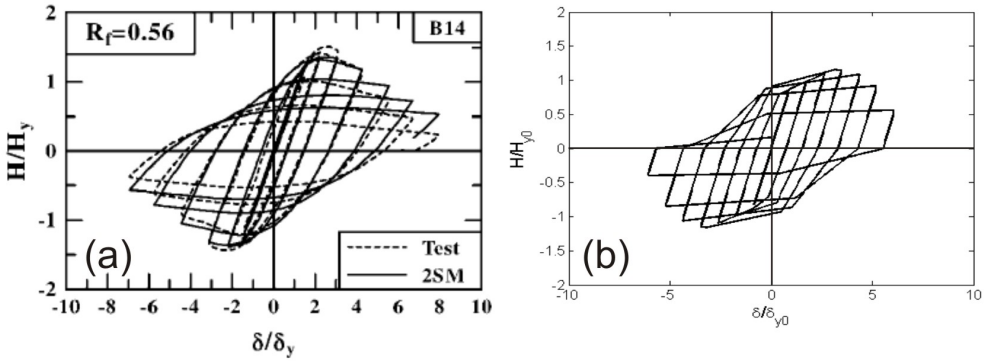

Figure 6.8. Literature-reported [83] cyclic behavior (a) from test and analysis of column B14, compared with that predicted by the model used here (b).

To ensure that the hysteresis model is also capable of predicting the cyclic response of specimens from other experiments, example specimen S6 was chosen from a study done by a research group at an entirely different facility with no shared personnel [51]. The experimental cyclic response is presented in Figure 6.9 (a), as compared with the predicted response in Figure 6.9 (b). In this case, the prediction performs as well as with columns B2, B4, and B14, but most importantly captures the point of maximum ductility quite well.

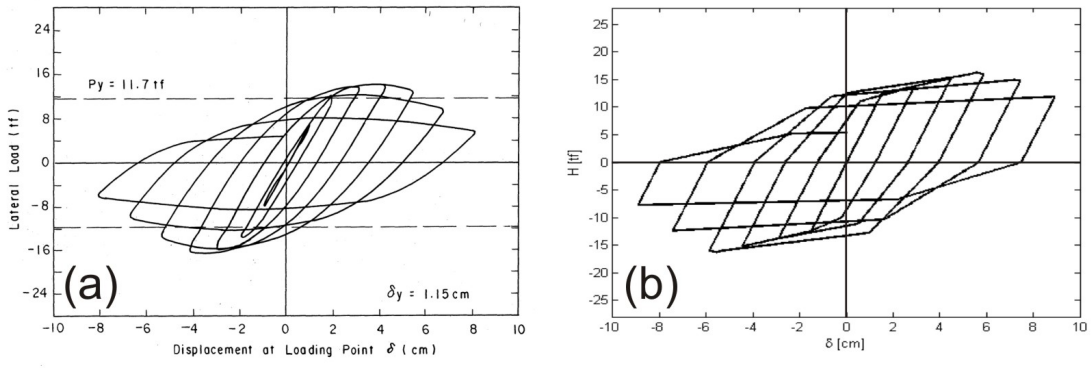

Figure 6.9. Literature-reported [51] cyclic behavior (a) from test and analysis of columnS6, compared with that predicted by the model used here (b).

The examples above present results from tests done with two-sided cyclic testing where only one cycle at each deformation level was performed. Thus, the overall post-ultimate degradation is a result of a combination of back-bone induced and energy-based cyclic degradation. In order to verify that the energy-based damage accumulation causes appropriate degradation, specimen S62C5, which was tested using three cycles at each deformation level, was chosen [50]. Figure 6.10 (a) presents the experimental cyclic response, compared with that predicted by the hysteresis model used here in Figure 6.10 (b). Again, the overall response prediction is reasonable, and captures the important features, including cycle-to-cycle degradation. For the reasons described in Section

6.2.2.8, the energy-based damage accumulation is exaggerated at large deformations, and perhaps underestimated at low deformations. However, due to the nature of the formulation, the damage parameter is chosen so as to balance these effects and leads to an overall reasonable prediction.

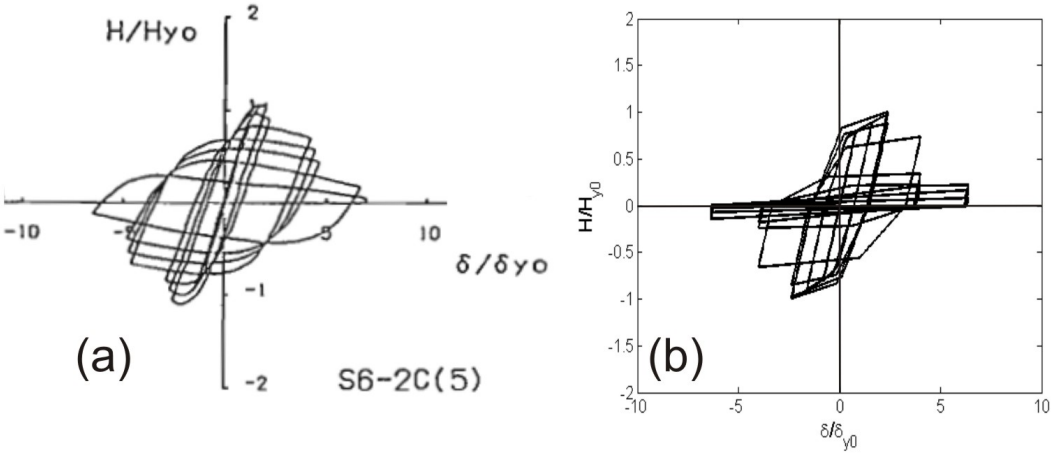

Figure 6.10. Literature-reported [50] cyclic behavior (a) from test and analysis of column S62C5, compared with that predicted by the model used here (b).

It should be noted here that column S62C5 had γ ratios such that type 3 behavior from Section 2.4.2 is predicted, corresponding to failure by fracture. As reported in [50], this was indeed the observed failure at a ductility just less than 5, but that some residual strength remained which can be seen in Figure 6.10 (a).

6.3 Definition of Limit States

As discussed in Chapter 1, port downtime is a critical factor for estimation of business losses following an earthquake. Container crane damage is a key contributor to downtime, and in fact can be the critical path to recovery following crane collapse due to a large seismic event. For these reasons, it is desirable to define limit states in terms of different levels of expected downtime. This can be accomplished by defining limit states

in terms of general repair strategies, which are intimately related to levels of structural damage. These levels of structural damage can be quantified in terms of the chosen global engineering demand parameter (EDP). As discussed in Section 2.5.2, interstory drift is an appropriate EDP. In the context of container cranes, the portal deformation is identified throughout Chapters 2-5 as the critical seismic response. In summary, portal drift is the chosen EDP for quantifying the damage levels corresponding to different repair methods, each of which contribute to port downtime due to the time necessary for the different repairs.

Although only a small number of repairs to container cranes have been required due to seismically induced damage (e.g. Loma Prieta, Kobe), repairs for operational accident damages, such as ships impacting cranes during berthing, are similar. These types of accidents are not uncommon, and much experience has been gained in successful repair strategies for a variety of damages. One engineering firm with expertise in container crane consulting has presented case studies of typical repairs in an internal document [168], which is especially useful. That document, paired with personal discussions with the authors, forms the basis for the repair models used to define the limit states described below.

6.3.1 Derailment (DR)

Derailment occurs when the lateral load is sufficient to reduce the axial reaction of at least one leg base to zero, as explored deeply in Chapter 3, which causes the leg base to be displaced from the wharf-mounted crane rail, illustrated in Figure 6.11. In the past,

derailment has been repaired by the use of mobile cranes and jacking systems to reposition the crane back onto the crane rails [168]. If derailment is the only form of damage, it can be repositioned in a matter of days, assuming that adequate personnel are available and that the wharf structure remains safe. While perhaps not contributing largely to business interruption losses, the days associated with derailment downtime should not be neglected. They can be critical for immediate emergency response if the surrounding area must rely on the delivery of emergency goods through the port immediately following a devastating earthquake.

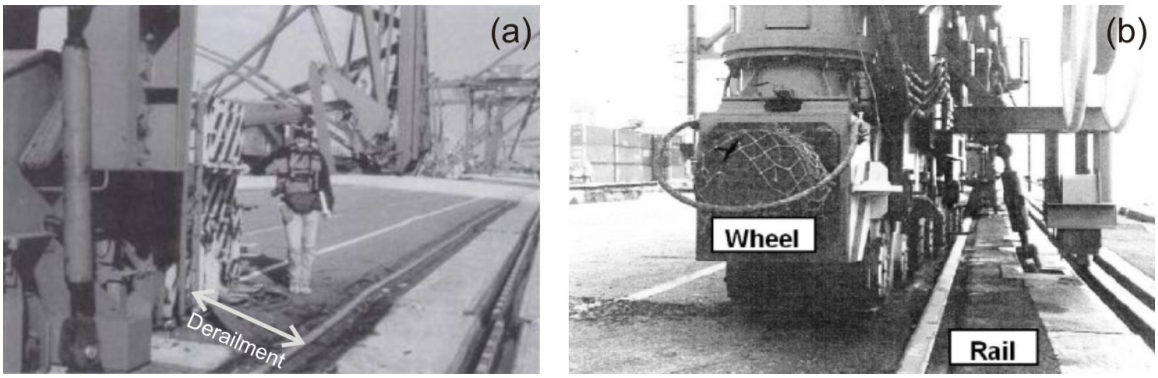

Figure 6.11. Derailment observed following the Kobe earthquake; sourced from [7] (a) and [18] (b).

6.3.2 Immediate Use (IU)

Immediate use represents the state of a container crane being mostly operational, derailment notwithstanding. In other words, the crane has suffered only minor structural damage which would not significantly impact its operational capacity, although derailment may or may not have occurred. Once any amount of derailment has been corrected, the crane may be suitable for immediate, but slightly impaired, use. The lower limit of this state can be quantified as the elastic limit of the portal frame. In this state, some minor buckling of hollow sections (within the portal frame or not) or misalignments

of other structural elements may result, which will need addressing before normal daily use can be resumed long-term. Slight buckling has been successfully and efficiently repaired with careful heat straightening, such as is shown in Figure 6.12 (b). Misalignment or residual "twist" in the structural frame has been successfully corrected using mechanical realignment techniques, using "push-pull" jacking to untwist the frame, such as is shown in Figure 6.12 (a). Typically, these sorts of repairs can be planned and executed in slightly more than one week, under preferential circumstances.

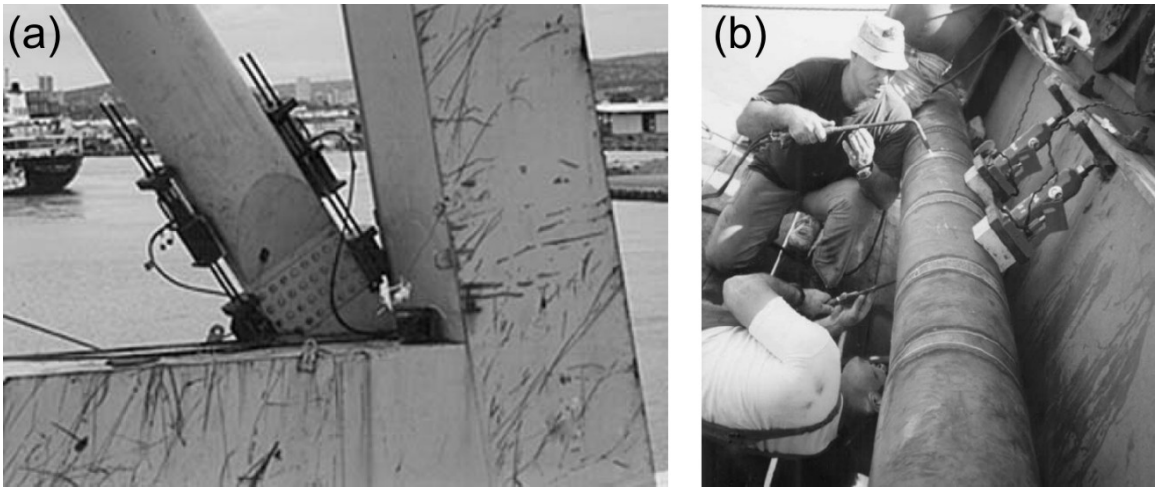

Figure 6.12. Mechanical realignment (a) and heat straightening (b) repairs to container cranes [168].

6.3.3 Structural Damage (SD)

If the crane response reaches the structural damage limit state, but does not collapse, it will be extensively damaged and will not be suitable for use without major repairs. The damage includes large local buckling of structural elements in the flanges and webs, especially critical in the portal frame structure such as is shown in Figure 6.13 (a). This state of structural damage state can be quantified roughly as a portal deformation somewhat less than the deformation at maximum load capacity up to the point of ultimate

ductility. Local buckling has occurred due to ship impact as well, as shown in Figure 6.13 (b), and much has been learned about how to efficiently repair heavy damage.

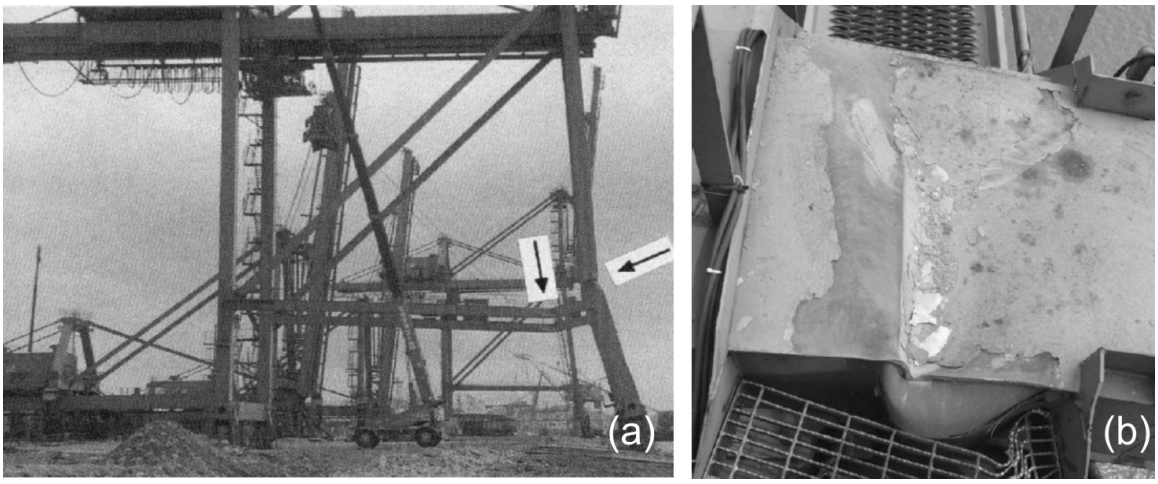

Figure 6.13. Local buckling in container crane portal frame following Kobe earthquake (a) [18] and due to ship impact (b) [168].

Before permanent repairs can proceed, it is generally necessary to provide temporary bracing around the damaged area of the container crane. This is shown in Figure 6.14 (a), where significant damage was caused by inadvertent ship impact. Repairs of heavily damaged sections involve major panel replacement and reconstruction. Often, a wharf is incapable of carrying the large equipment loads needed to lift a container crane for repairs. This could be especially pertinent because wharves may be extensively damaged following a seismic event, or the heavy equipment is unavailable or inaccessible. One effective technique to avoid this challenge is the use of self-supported bracing systems such as is shown in Figure 6.14 (b). Loads are transferred around the damaged section through the bracing system, allowing for safe replacement of the damaged pieces. Repairs such as these may take several months to plan and execute.

Figure 6.14. Temporary bracing (a) and self-supported bracing (b) used to stabilize and repair damaged components of container cranes [168].

6.3.4 Complete Collapse (CC)

If the portal deformation of a container crane surpasses the estimated point of maximum ductility, the local buckling near the portal joints can progress rapidly leading to local instability. Because the portal frame is a nonredundant structure, this local instability can quickly lead to global instability and eventual collapse. Thus, the point of ultimate ductility quantifies the limit state for likely collapse. Collapses container cranes from the Kobe earthquake are shown in Figure 6.15.

In the event of complete collapse of a container crane, replacement is expected to be necessary. Reconstruction is generally not possible. Because the container crane construction market is dominated predominantly by one Chinese manufacturer (ZPMC

controls greater than 80% of international market share [169]), and they are built as semi-custom purchases, replacement can take a year or more.

Figure 6.15. Collapse of container cranes on Rokko Island at the Port of Kobe after the 1995 Hyogoken Nanbu earthquake [170].

6.3.5 Performance Levels

Performance levels are defined as the regions between limit states. Performance levels are defined based on the discussions above as serviceable, derailed, minor damage, major damage, and collapse. The relationship between limit state and performance level is depicted graphically in Figure 6.16.

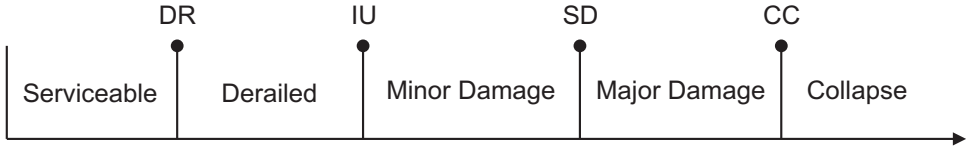

Figure 6.16. Relationship between performance levels and limit states.

6.4 Seismic Capacity Estimates

With the general qualitative limit states defined as above, and the critical features of inelastic behavior identified and modeled, it is possible to quantify the specific limit

states, ranging from simple derailment to complete collapse, for a given container crane. The following sections use a series of push-over analyses, with a load applied at the boom tip of the 2D container crane finite element models (Figure 6.17) for the three specific container cranes described in Appendix A. Nonlinear rotational springs with strength, ductility, and hysteresis rules assigned as described in Section 6.1 are positioned in the critical portal joints. The local behavior captured by these nonlinear portal springs are translated to global response, quantified in terms of portal drift. Pushover analyses are reported in terms of total base shear V_b, nondimensionalized by the crane weight, with respect to portal drift. Because the upper structure of the crane is stiff relative to the lower portal frame, the pushover results are relatively insensitive to the point of load application.

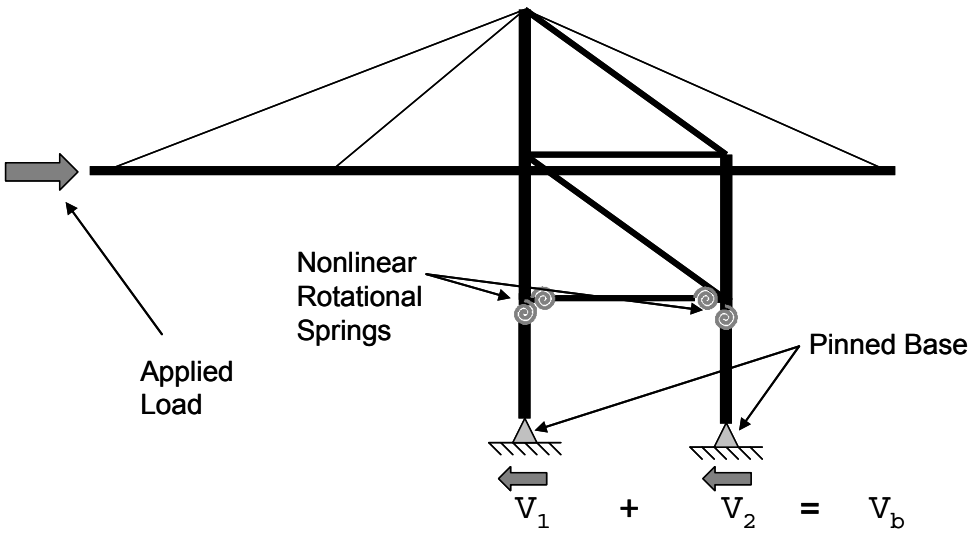

Figure 6.17. Pushover schematic of a container crane to quantify limit states.

A pinned base is used for the pushover tests in order to force large portal deformations during static, displacement-controlled analyses. Otherwise, sliding and tipping occur. Because the structural capacity is independent of the loading, the limit states quantified

using a pinned-base pushover can be applied to dynamic analysis utilizing frictional contact elements. While it may seem counterintuitive to estimate overall capacity limit states from a crane while in contact with the ground, since in reality a failed container crane will likely have exhibited uplift and be resisted by only one side, the general symmetry of the portal frame structure is helpful. Because the waterside and landside legs are typically similar in stiffness and strength, they reach their individual limit states at approximately equal displacements. Thus, by enforcing equal deformations in each leg, the capacity of each can be simultaneously determined and compared. Recall that because the portal frame structure is nonredundant, the onset of a limit state in one leg is equivalent to the limit state being reached for the entire structure.

The derailment limit states are quantified based on the analysis of Chapter 3, where the uplift threshold (perhaps more suitably labeled as the threshold of initial sliding) is determined based on the overall stability of the structure.

Although significant effort has been put forth to determine the limit states and seismic capacity as accurately as possible for each crane, the simplifications required and modeling approaches are imperfect, so the resulting quantified limit states are mean estimates, with some associated variability. That variability is discussed in Chapter 7.

6.4.1 J100 Container Crane

The J100 crane, representing a modern jumbo crane, is designed to service very large container ships, and is vital to stay competitive among leading ports. While it is not

specifically designed for seismic forces, it has a relatively stiff and strong portal sway mode due to operational stiffness requirements and lifting forces. That said, the portal frame elements are extremely slender, though still in the valid design regions of Figure 2.5. The calculated slenderness parameters are shown in Table 6.3 below for cantilever-column representations of the waterside portal leg (WL), landside portal leg (LL), and portal beam (PB).

Table 6.3. Calculated slenderness parameters for portal frame elements of J100 container crane.

Column	R_f	λ	λ_s	λ_s'	γ/γ_{req}	γ/γ^*	t/t_0
WL	0.66	0.50	0.57	0.57	1.72	1.72	0.83
LL	0.95	0.50	0.58	0.58	4.70	4.70	0.58
PB	1.10	0.19	0.62	0.61	6.35	6.35	0.50

Because the portal legs are tapered, the calculation of the column slenderness ratio λ is not as straightforward as Equation 6.5. Bazeos and Karabalis [171] present a methodology which can be used to determine the effective slenderness ratio for a tapered column. The published design charts and interpolation equations consider tapered columns in which the web depth varies linearly, as it does in the case of crane portal legs. Basically, one can find an equivalent column element with uniform section throughout its length. This equivalent section would have the section dimensions of the tapered column at some x_{cr} distance from the smaller end, as shown in Figure 6.18.

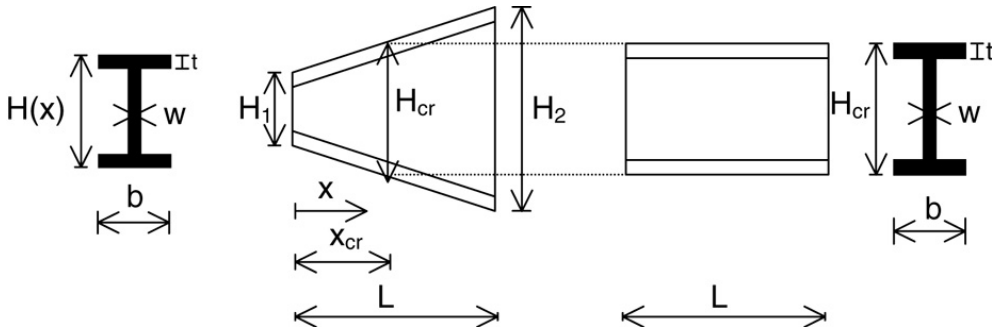

Figure 6.18. Schematic for determining the equivalent prismatic column for calculating the overall buckling load of a tapered column [171].

This critical location can be determined from one of the design charts, or the corresponding interpolation equation, by its relationship to the ratio of H_2/H_1. The reported design charts are shown to be quite accurate in the range of practical interest. Because the web depth varies linearly, it is a simple matter to determine the depth of the column at its critical section as

$$H_{cr} = \left(\frac{x_{cr}}{L}\right)(H_2 - H_1) + H_1 \tag{6.27}$$

Then, the critical moment of inertia is determined from the following equation

$$I_{cr} = \left[bH_{cr}^3 - (b - 2\bar{t}_w)(H_{cr} - 2\bar{t}_f)^3\right]/12 \tag{6.28}$$

where the equivalent flange and web thicknesses are used for simplicity, and found by using an equivalent unstiffened box section. This simplification maintains the same outside dimensions, area, and M_p, and is outlined by Zheng [85], as illustrated in Figure 6.19 and characterized by Equation 6.29.

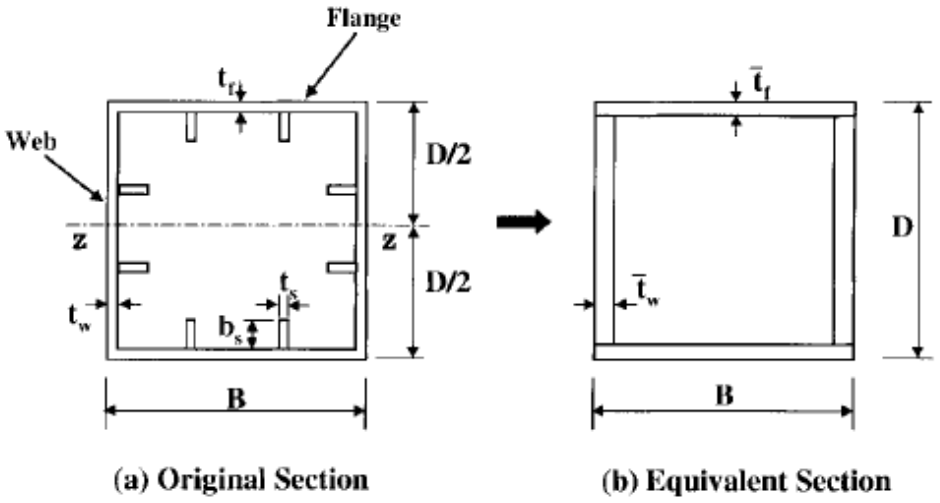

Figure 6.19. Equivalent unstiffened hollow box section [85].

$$\bar{t}_f = \frac{4Z - AD}{2(BD - A)}, \qquad \bar{t}_w = \frac{A - 2B\bar{t}_f}{2(D - 2\bar{t}f)}, \qquad A = BD - (B - 2\bar{t}_w)(H - 2\bar{t}_f) \tag{6.29}$$

Then this I_{cr} is used to determine P_{cr}, as

$$P_{cr} = \frac{\pi^2 EI_{cr}}{(kL)^2} \tag{6.30}$$

It is easily shown that the column slenderness ratio can be represented as

$$\lambda = \sqrt{\frac{P_y}{P_{cr}}} \tag{6.31}$$

Thus, the effective column slenderness ratio of the tapered column can be determined from the squash load and critical load of the equivalent prismatic column.

Using the techniques described in Section 6.1, the overstrength and various ductility measures are calculated, and presented in Table 6.4, assuming an axial load ratio of 10%. The resulting pushover curve is presented in Figure 6.20.

Table 6.4. Overstrength and ductility measures of portal elements of J100 container crane.

	H_{max}/H_y	δ_m/δ_y	δ_u/δ_y	δ_z/δ_y
WL	1.29	2.02	3.16	5.16
LL	1.25	1.77	2.90	4.47
PB	1.34	1.96	3.09	7.78

From the pushover curve, the limit states identified in Section 6.2 are quantified. At approximately 2% portal drift, both columns reach their initial yielding point. This is noteworthy, as the waterside and landside legs are of somewhat different sizes. Because of those differences, a pushover analysis is performed in each direction, applying the load in a seaward and landward direction. However, the resulting deformation response is nearly identical, as indicated by the nearly overlapping pushover curves in Figure 6.20. At 3% portal drift, the deformation has reached a level that indicates structural damage. Complete collapse is likely at a portal drift of approximately 4.5%, as a portal column has degraded to the point of ultimate ductility, where the nonredundant portal structure is susceptible to collapse during the unstable progression of local buckling.

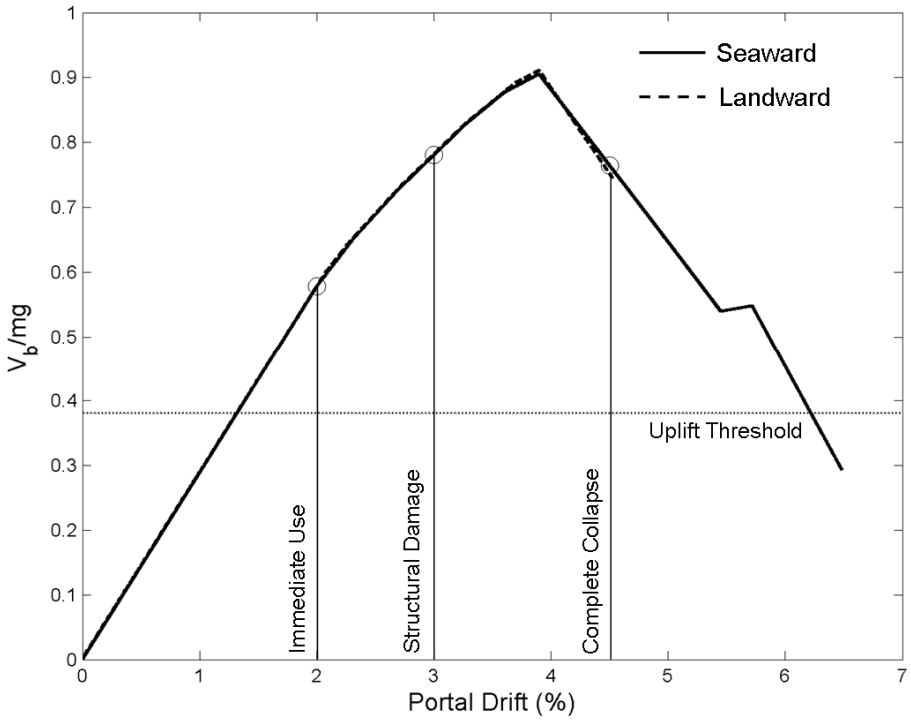

Figure 6.20. Pushover curve and identified limit states for J100 container crane.

Notice that the uplift threshold is lower than the immediate use limit state. This indicates that the container crane portal frame is strong enough to support the initial sliding behavior which occurs just after losing vertical and thus horizontal constraint of one side. Thus, derailment is a valid limit state, and in fact is the first to be surpassed in this case; to determine which limit state will be achieved for a given earthquake, the seismic demand must account for the three-stage portal uplift behavior described in Chapter 3.

6.4.1.1 Alternative Approach

A different approach at estimating ductility capacity was discussed in Section 2.4.4 based on the work of Zheng at al. [84, 85]. In this approach, a strain-based evaluation procedure is used where an effective ultimate strain ε_u for each "critical part" is

determined from an empirical relationship. Then, the ratio of average compression strain to effective ultimate strain over an effective failure length represents a damage index, as written in Equation 6.32. The failure length is assumed as l_e=min[0.7B, l_d] where B is the flange width and l_d is the distance between two adjacent diaphragm stiffeners.

$$D_s = \frac{\varepsilon_a}{\varepsilon_u} \tag{6.32}$$

The "critical parts" are those where potential section failure may occur, and where the associated damage index must be monitored during analysis. In the case of a container crane, the critical parts are the locations where rotational springs were placed in the earlier methodology, as labeled in Figure 6.21.

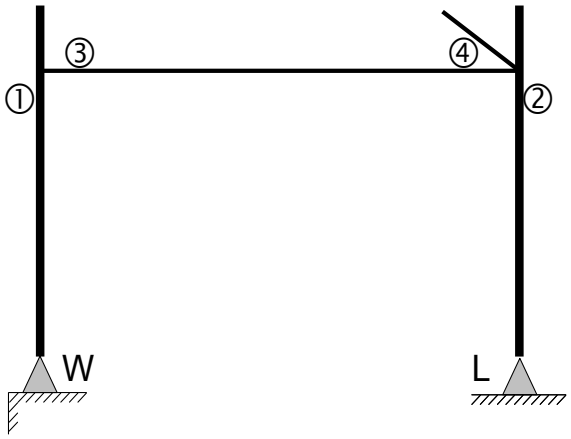

Figure 6.21. Location of critical parts 1 ~ 4.

As earlier, a pushover analysis is used to identify limit states. Using fiber-section representations of the portal frame structural elements, it becomes straightforward to monitor the average strains over the effective failure length at each critical part during analysis. After the analysis, the ultimate strain for each part is calculated at each increment, as the axial load varies. The damage index, then, is calculated for each critical part at each increment with Equation 6.32. These damage indices for critical parts ①-④

are plotted with respect to portal drift in Figure 6.22. Pushing the crane left and right results in negative and positive drifts, respectively.

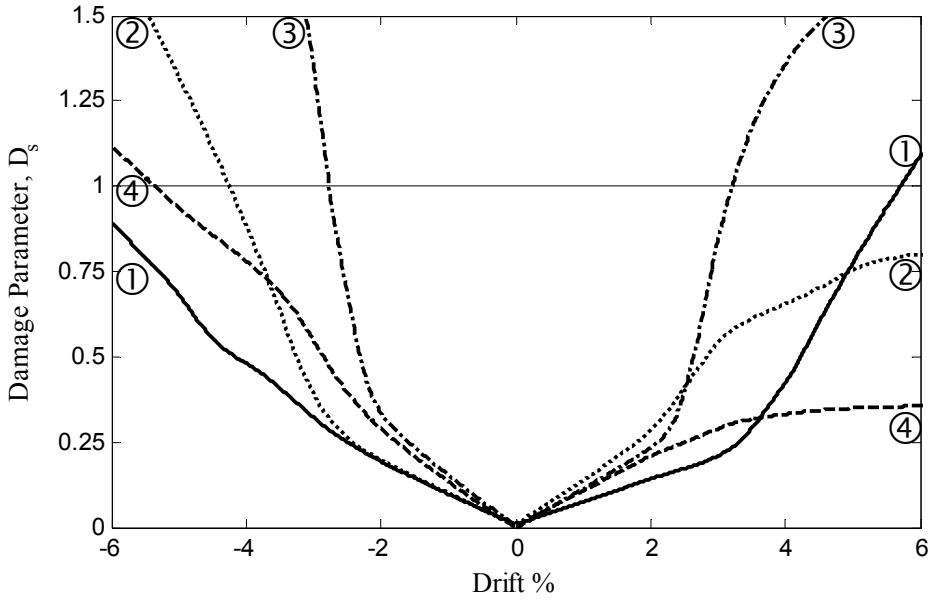

Figure 6.22. Computed damage parameter during pushover analysis for critical parts ① ~ ④.

Using Figure 6.22, the structural limit states can be identified. Recall that the IU state is identified as the drift in each direction that the elastic limit is reached in any member. The CC state is chosen to be the drift in each direction that D_s reaches 1.0 in either of ① or ②, as collapse is not expected to immediately occur with a failure in the portal beam. The SD state must be more subjectively defined; it is identified here as the drift in each direction at which point the damage index begins to increase very rapidly. The drift values associated with each limit state are presented in Table 6.5. The worst-case direction for each limit state is presented, as the direction of maximum response during dynamic loading is unpredictable. However, limit states for the waterside and landside parts are considered separately. It can be seen that the portal beam on the waterside is

more vulnerable than the column, while the opposite is true for the landside. This is expected, as the portal beam has continuous flange width, while the waterside leg has thicker flanges than the landside leg.

Table 6.5. The associated drift (%) for critical parts ① ~ ④ for each of the three limit states. Bold entries indicate limiting values. Collapse prevention does not consider hinging in the portal beam.

	Waterside		Landside	
	①	③	②	④
IU	2.5	**2**	**2**	2
SD	3	**2.5**	**2.5**	3
CC	**5.5**	~~2.5~~	**4**	~~5.5~~

It should be noted that the identified limit states are much the same as those identified from the earlier methodology. This alternative methodology provides a way to estimate the maximum structural system limit states without an explicit representation of each vulnerable component's inelasticity. Thus, it is a feasible concept for fairly rapid seismic evaluations of existing cranes, but does not provide the section-level ductility detail of the rotational spring approach. Thus, it is an important example for demonstration purposes and for further gaining confidence in the rotational spring approach, but is not used for the next 2 crane examples.

6.4.2 LD100 Container Crane

The LD100 crane, representing a typical older jumbo crane, is designed to service large routine container ships, and is the workhorse of many ports worldwide. It was designed according to the assumption that container cranes can uplift, which isolate them from further seismic excitation, and was thus not specifically designed for seismic forces. As a result, the portal frame elements are extremely slender with very low ductility. The

calculated slenderness parameters are shown in Table 6.6 below for cantilever-column representations of the waterside portal leg (WL), landside portal leg (LL), and portal beam (PB).

Table 6.6. Calculated slenderness parameters for portal frame elements of LD100 container crane.

Column	R_f	λ	λ_s	λ_s'	γ/γ_{req}	γ/γ^*	t/t_0
WL	1.25	0.55	1.10	0.99	3.39	3.39	0.44
LL	1.25	0.55	1.10	0.99	3.39	3.39	0.44
PB	1.25	0.38	1.40	1.23	2.16	2.16	0.44

The calculated overstrength and various ductility measures are calculated and presented in Table 6.7, assuming an axial load ratio of 15%. The resulting pushover curve is presented in Figure 6.23.

Table 6.7. Overstrength and ductility measures of portal elements of LD100 container crane.

	H_{max}/H_y	δ_m/δ_y	δ_u/δ_y	δ_z/δ_y
WL	1.18	1.44	2.55	3.42
LL	1.18	1.44	2.55	3.42
PB	1.19	1.43	2.54	3.76

From the pushover curve, the limit states identified in Section 6.2 are quantified. At approximately 1.5% portal drift, both columns reach their initial yielding point. Because both lower legs are identical, only one direction of pushover analysis is required. At 2% portal drift, the deformation has reached a level that indicates structural damage. Complete collapse is likely at a portal drift of approximately 3%, as a portal column has degraded to its point of ultimate ductility.

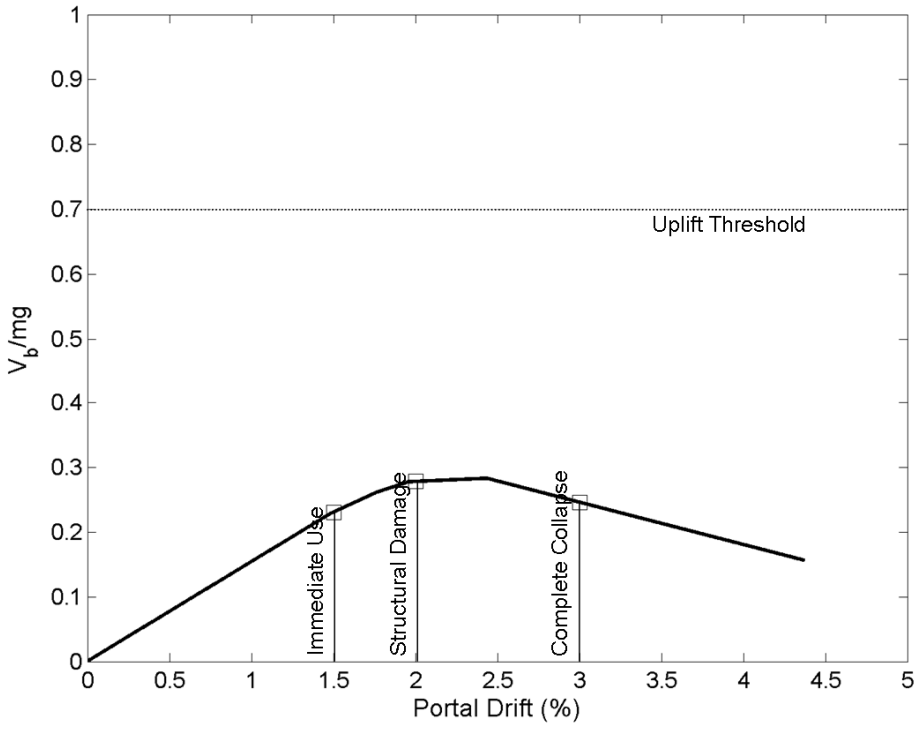

Figure 6.23. Pushover curve and identified limit states for LD100 container crane.

Notice that the uplift threshold is higher than any structural limit state, indicating that this container crane will collapse prior to sliding or uplifting in the context of Chapter 3. Thus, derailment is not a valid limit state for this crane, and need not be considered.

6.4.3 LD50 Container Crane

The LD500 crane, representing a typical older small crane, is designed to service small to moderately-sized ships, and is seldom operated at peak utilization rates at large competitive ports. In the event of collapse, it would likely be upgraded with a newer, more modern jumbo crane if the wharf were deemed sufficient. It is representative of the type of crane from which the "rocking" design assumption was originally based. As such, it is expected to tip prior to suffering significant structural damage during a seismic event.

However, ductility was not seen as a specific design criterion. As a result, the portal frame elements are extremely slender with very low ductility. The calculated slenderness parameters are shown in Table 6.8 below for cantilever-column representations of the waterside portal leg (WL), landside portal leg (LL), and portal beam (PB).

Table 6.8. Calculated slenderness parameters for portal frame elements of LD50 container crane.

Column	R_f	λ	λ_s	λ_s'	γ/γ_{req}	γ/γ^*	t/t_0
WL	0.94	0.57	1.05	0.95	1.57	1.57	0.59
LL	0.94	0.57	1.05	0.95	1.57	1.57	0.59
PB	1.25	0.38	1.08	0.97	3.50	1.57	0.44

The calculated overstrength and various ductility measures are calculated and presented in Table 6.9, assuming an axial load ratio of 15%. The resulting pushover curve is presented in Figure 6.24.

Table 6.9. Overstrength and ductility measures of portal elements of LD50 container crane.

	H_{max}/H_y	δ_m/δ_y	δ_u/δ_y	δ_z/δ_y
WL	1.20	1.53	2.64	3.65
LL	1.20	1.53	2.64	3.65
PB	1.21	1.49	2.60	3.98

From the pushover curve, the limit states identified in Section 6.2 are quantified. At approximately 1.9% portal drift, both columns reach their initial yielding point. Because both lower legs are identical, only one direction of pushover analysis is required. At 2.5% portal drift, the deformation has reached a level that indicates structural damage. Complete collapse is likely at a portal drift of approximately 3.5%, as both portal columns have degraded to their points of ultimate ductility. Note that because the gage length is much smaller, the stiffness of the upper frame is relatively higher than that from

a larger gage crane. Therefore, deformations are even more concentrated in the portal legs. As a result, the portal beam remains elastic, and the portal columns control the seismic capacity, evidenced by the strictly trilinear pushover curve in Figure 6.24. Note that this is exactly opposite than the "strong column weak beam" design philosophy adopted for safe and efficient seismic design.

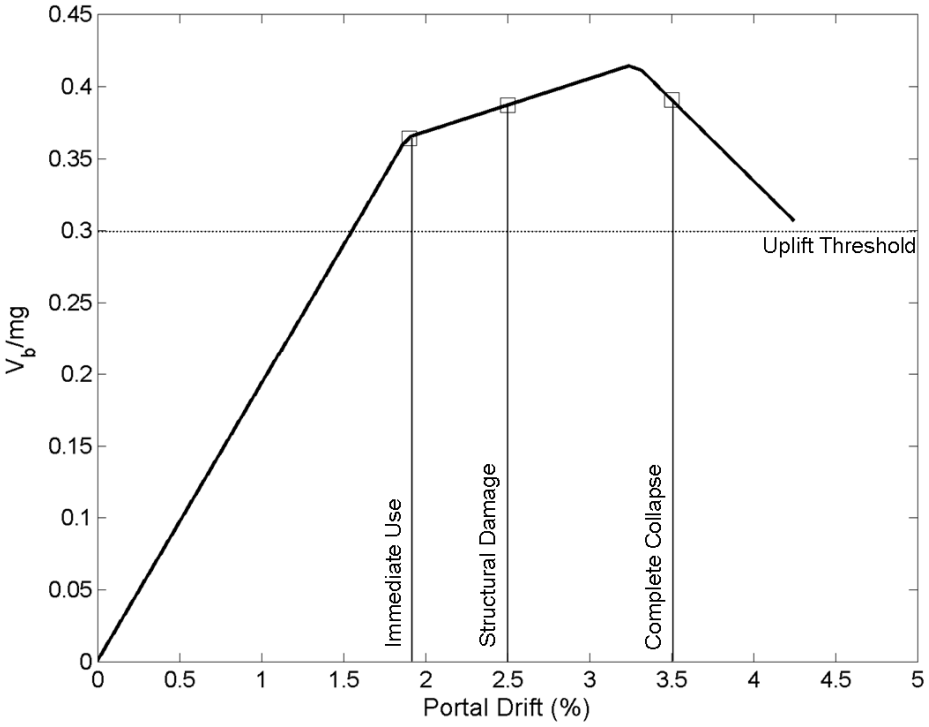

Figure 6.24. Pushover curve and identified limit states for LD50 container crane.

Notice that the uplift threshold is below the immediate use limit state. This indicates that the container crane portal frame is strong enough to support the initial sliding behavior which occurs just after losing vertical and thus horizontal constraint of one side prior to initial yielding of the columns. Thus, derailment is a valid limit state. However, having sufficient strength to reach the uplift stage is not sufficient for ensuring adequate seismic performance. Rather, a performance-based design or evaluation must account for the

three-stage portal uplift behavior described in Chapter 3 when considering the seismic demand.

6.4.4 General Observations

While each crane is unique, and thus has different quantified limit states, it is interesting to compare the identified limit states for the three case study container cranes. The limit states identified above are summarized in Table 6.10.

Table 6.10. Summarized limit states (in terms of portal drift %) of three case study container cranes.

	DR	*IU*	*SD*	*CC*
J100	1.3	2.0	3.0	4.5
LD100	-	1.5	2.0	3.0
LD50	1.5	1.9	2.5	3.5

In general, the relative flexibility of container crane structures is evidenced by the rather high elastic limit portal drifts, in comparison to steel building moment frames. However, the lack of seismic detailing is evident in the low ductility at which significant structural damage and complete collapse may occur ($\mu_{SD} \approx 1.3\text{-}1.5$; $\mu_{CC} \approx 1.8\text{-}2.3$). Because the sections are sized to avoid elastic collapse prior to reaching the yield load, and not to ensure a reasonably level of ductility, they can be extremely slender. This slenderness is predicted to lead to rapid strength degradation due to local buckling interaction. Because the structure's seismic response is controlled by the nonredundant portal frame, a heavily damaged portal leg can greatly impact overall stability. This is further compounded when the deformations are overly concentrated in the portal legs, which can lead to an unfavorable "strong beam weak column" behavior that can cause overall collapse. Fortunately, the same procedures presented here for evaluating seismic capacity can also be used to do detail design for new construction or retrofitting in order to provide greater

ductility and thus increase the SD and CC limit states. This additional detail design is not expected to require significant additional steel. Thus, it should not greatly increase the mass or cost of a new or retrofitted crane.

It is important to realize that the achieved section behavior is rather different than that assumed by typical seismic design guidelines for ports. It is reported that because thin walled hollow box sections typically achieve 40-60% overstrength, they will form a ductile moment frame in container cranes [7]. However, the overstrengths predicted here are significantly less than that assumed amount due to the extreme panel slenderness. Container crane designers should notice that sections can be designed to avoid local buckling prior to reaching the yield point without satisfying the slenderness limits necessary to ensure the assumed overstrength and ductility levels. Thus, a more explicit treatment of slenderness should be taken during design, which account for overstrength and ductility if inelastic behavior is expected under seismic loads.

6.5 Summary

To estimate the seismic capacity of a given container crane in various limit states requires a thorough understanding of the inelastic behavior of the structural elements. This chapter presented a methodology for which the strength, ductility, and hysteresis rules for typical container crane sections could be estimated based on various slenderness parameters that can be calculated for steel stiffened hollow box sections. By calibrating these rules to experimental results of similar cross-section, nonlinear hysteretic rotational

springs are developed to account for the local buckling interaction which often governs the inelastic response of container crane structural elements.

Container crane limit states are defined qualitatively relative to feasible repairs. Repair models based on industry experience allows for limit states to represent estimates of crane downtime in the event of a seismic event, in addition to a more traditional estimate of operational capacity or structural integrity. Four total limit states are defined. First, derailment indicates a crane leg base movement relative to the crane rail. Then, three levels of structural limit states are defined; in order of increasing severity, these are immediate use, structural damage, and complete collapse.

The three case study container cranes are considered in depth, and estimates of their capacity are determined based on pushover analyses of 2D finite element model representations. In general, derailment may or may not be a valid limit state, based on the overall strength and stability of the crane in question. Further, because of the extreme slenderness of container crane structural elements, a result of minimal ductility considerations in design, limit states are rather closely spaced and complete collapse may follow fairly quickly after first yield. In other words, the rapid degradation that the slender sections of container cranes are predicted to exhibit can cause complete portal collapse at levels of only moderate ductility. This is rather different than what current design guideline commentary might suggest.

CHAPTER 7

SEISMIC FRAGILITY ANALYSIS OF CONTAINER CRANES

7.1 Introduction

In order to make informed decisions regarding resource allocation, emergency planning, etc., port stakeholders need to understand the risk and vulnerability of their port's components, including container cranes. Fragility analysis provides just such a tool, representing the probability of a crane reaching a certain limit state, and inferring a certain length of downtime, given that an earthquake of specific intensity occurs. By removing seismic hazard from the overall risk, the vulnerability of the specific component is more transparent. This chapter outlines and demonstrates a fragility methodology for application to seismic fragility analysis of container cranes.

Quantifying uncertainty is critical to successful fragility analysis. First, a sensitivity study is performed in order to characterize the importance of various contributors to overall uncertainty. Based on that, the fragility methodology reviewed in Chapter 2 is further tailored to the treatment of container cranes. Then, the fragility analysis is performed for the three representative container cranes. To do this, the finite element models, seismic demand modeling, capacity estimates, and general approach described in previous chapters is required. It is the author's intent that the developed fragility curves can serve as industry "default" curves for most cranes in existence, but that the generalized approach used can act as a template where more customization is desired or required. The chapter concludes with a basic treatment of expected downtime.

7.2 Sensitivity Study

There are particular uncertainties associated with many input parameters required for seismic performance evaluation of container cranes. These uncertainties cause uncertainty in the predicted response, and therefore performance, of a container crane to seismic loading. The identified sources of input uncertainty that affect response include ground motion profile, ground motion intensity, structural strength and stiffness, mass, damping, as well as others. This study uses simple methodology to present a deterministic sensitivity study of a jumbo container crane subjected to seismic loading. By utilizing a consistent damage index for computing seismic demand, the relative importance of these various variables is investigated in order to better understand the range of performance which can be expected within the range of engineering "certainty."

A deterministic sensitivity study is used to determine the relative significance of uncertainty in each input parameter to uncertainty of the engineering design parameter (EDP). This study employs a tornado diagram approach [118, 172] in which the "swing," or relative importance of each input parameter, is ranked and graphically depicted. The output variable is a known deterministic function of a set of random input variables with assumed probability distributions. In this study, the 2D finite element approximation with frictional contact boundary elements is used as the deterministic function, relying on dynamic time history analysis. For each input variable, assumed independent for simplicity, the best estimate and two extreme values (here, the 10^{th} and 90^{th} percentile) are chosen. The deterministic function is evaluated many times, each evaluation with one

input variable set to one of its chosen extreme values while the rest are set to their best estimates. Doing this produces upper and lower bounds of the output for each input. The absolute difference between these bounds is defined as that input parameter's swing. One then ranks the input variables according to their swing, with larger swings indicating more significance to the output. For this study, the J100 container crane serves as the example crane, as it is a typical but critically important type of crane.

7.2.1 Uncertain Variables

The choice of input variables is dependent on the output variable of interest. For this study, it is desired that the output meaningfully quantify the progression of damage towards failure. For this reason, the ultimate ductility evaluation procedure used in Section 6.4.11 [84] is adopted, with the output parameter identified as the damage indices of the critical parts, according to Figure 6.21.

7.2.1.1 Uncertainty in Ground Motion Intensity

The intensity of an earthquake is considered one of the most important parameters when evaluating seismic performance, and can often have significant uncertainty. Typical intensity measures (IMs) used in earthquake engineering includes measured peak motions and elastic spectral responses, quantified in terms of acceleration, velocity, and displacement. In this study, the spectral acceleration S_a, at the structure's fundamental mode with the structure's estimated damping level, is deemed an appropriate IM. This is because a container crane's response is dominated strongly by the fundamental mode, especially for the chosen EDP, but is moderately sensitive to damping.

The best estimate of earthquake intensity, as defined by the spectral acceleration at the fundamental mode, is set according to the average S_a of the un-scaled chosen motions. In addition, uncertainty in the earthquake intensity is considered. A port-wide ground motion study conducted in 2007 for the POLA/POLB to determine appropriate design level earthquakes and the corresponding design spectra [164, 165] was used for this purpose. Besides the epistemic uncertainty with hazard, reported differences between soil modeling methods, attenuation approaches, the effect of low damping, and other factors lead to a reasonable choice of a normal distribution with COV of 0.2.

7.2.1.2 Uncertainty in Ground Motion Profile

Because a ground motion profile is characterized by many variables, a simple method to consider ground motion characteristics other than the primary intensity measure [172] is used. In this method, one selects a set of ground motion profiles where each of them is scaled according to the target IM selected beforehand. Then, one obtains the EDP value corresponding to each scaled ground motion profile by performing a structural analysis. The set of ground motion profiles can then be ranked according to their respective EDP values. One can then choose the lower and upper bound, and best estimate profiles corresponding to the chosen lower and upper fractiles (e.g. 10^{th} and 90^{th} percentiles), and median, respectively. This process is outlined and effectively demonstrated in Lee & Mosalam [118].

The largest US container port system is the combined Port of Los Angeles and Port of Long Beach. For this reason, ground motion studies and selected ground motions to illustrate sensitivities to seismic vulnerability are chosen to represent most specifically this area. However, this selection is not expected to narrow the applicability of this study. A wide range of ground motion profiles was desired due to the employed methodology for ranking their effect on the damage index. Also, as an EDP related to failure was chosen, a suite of high intensity ground motions was desirable. Therefore, the SAC Steel Project suite of 20 ground motions representing a 2% in 50 years probability of exceedance in the LA region were selected [173]. These motions were then amplitude scaled to achieve consistent spectral acceleration S_a at the structure's fundamental mode of vibration and damping. This suite of ground motions, which are used extensively in this chapter, are described in detail in Appendix B.

Associated with each ground motion is a damage index associated with each flange of each critical structural element of the container crane with all parameters set to their best estimates. Of the four rigid connections in the portal frame, the inside flange at the top of the landside leg consistently shows the highest damage index. This part, then, is chosen as the critical part for which the damage index is calculated throughout this study. The ground motions were then ranked in descending order according to this damage index. The ground motion associated with the median damage index, la24, is assigned the "best estimate" tag, or the 50^{th} percentile response motion. Next, la36 and la31 are tagged as the 90^{th} and 10^{th} percentile motions, respectively. Motion la31 was chosen in favor of la23 due to an undesirable numerical phenomenon exhibited during analysis with la23;

differences in damage indexes associated with la31 and la23 are believed negligible. Table 7.1 provides a summary of the ground motion selection.

Table 7.1. Ground motion records considered for representing the lower-bound, median, and upper-bound time histories, ranked according to the damage index computed with all other uncertain parameters taken at their best estimate.

Record	M	R	S_a	Scaling	D_s
		km	g		
la33	7.1	10.7	0.79	1.91	3.12
la36	7.1	11.2	1.80	0.84	2.11
la40	7.1	1.5	1.56	0.97	1.97
la35	7.1	11.2	1.93	0.78	1.33
la28	6.7	6.4	1.58	0.96	0.94
la30	7.4	1.2	0.99	1.54	0.66
la38	7.1	1.5	1.62	0.93	0.53
la37	7.1	1.5	1.21	1.26	0.51
la39	7.1	1.5	0.90	1.69	0.44
la24	7.0	3.5	1.67	0.91	0.40
la27	6.7	6.4	1.37	1.11	0.35
la32	7.1	17.5	1.96	0.77	0.33
la21	6.9	3.4	2.59	0.59	0.32
la22	6.9	3.4	1.03	1.48	0.32
la29	7.4	1.2	0.79	1.92	0.32
la25	6.7	7.5	1.34	1.13	0.28
la26	6.7	7.5	2.27	0.67	0.26
la31	7.1	17.5	2.44	0.62	0.24
la23	7.0	3.5	0.87	1.75	0.24
la34	7.1	10.7	1.61	0.94	0.20

7.2.1.3 Uncertainty in Structural Properties

Uncertainties in properties which affect the dynamic behavior of a structure, including strength, stiffness, mass, and damping, are characterized largely by imperfect knowledge and simplified understandings. Approaches to realistically quantify and account for these uncertainties are discussed in Section 2.5.1.

Because A709 steel is essentially A592 steel with an additional requirement for Charpy V-notch toughness, reported statistics for the appropriately thick A592 plate steel

reported by Liu [115] are used for characterizing the steel yield strength as normal with mean 393 MPa (57 ksi) and COV of 0.07. Young's modulus is taken as normally distributed with mean 200 GPa (29000 ksi) and COV of 0.06 [114]. As recommended by Ellingwood et al. [116], all mass, computed from dead load, is perfectly correlated and has a normal distribution with COV of 0.1. Rayleigh damping is assumed, with a mean value of 1.5% of critical for the first and third modes and a COV of 0.3 per the recommendations of Porter et al. [172].

7.2.2 Deterministic Sensitivity Study Results

A summary of the input parameters is presented in Table 7.2. The best estimate value is reported as the mean of the assumed normal distribution, and calculated 10^{th} and 90^{th} percentile values are also presented. Table 7.2 also shows the results of the sensitivity study, in terms of calculated damage indices for each parameter's assumed lower and upper bound. Input parameters are listed in increasing order of importance, as measured by their swing. A graphical depiction, in "tornado diagram" form, is shown in Figure 7.1. The damage index using the best estimate values of all parameters is $D_s = 0.40$.

The largest swing is associated with the ground motion record, followed by the magnitude of the earthquake intensity. Of the structural properties considered, the mass has the highest associated swing, while elastic modulus and damping have a similar, low impact. Uncertainty in the coefficient of friction plays a small role when despite having a relatively high assumed COV of 0.2.

Several parameters, such as ground motion characteristics, mass, and elastic modulus exhibit a positive trend in the swing; the upper bound damage index is much further from the best estimate than the lower bound. Because of the slenderness of the portal frame structural elements, the computed damage index grows rapidly once damage begins to "accumulate."

Table 7.2. List of parameters included in the sensitivity study and their lower and upper bound values with the corresponding calculated damage index, listed in order of increasing importance.

Input Parameter	Unit	Mean	10th%	90th%	Swing
			D_s	D_s	
Friction, μ		0.8	0.6	0.99	0.0005
			0.4049	0.4054	
Elastic Modulus, E	GPa	200	185	215	0.0480
			0.3930	0.441	
Damping, ζ		1.50%	2.08%	0.92%	0.0543
			0.3730	0.4273	
Yield Stress, f_y	MPa	393	428	358	0.1908
			0.3159	0.5067	
Mass	ton	1250	1092	1412	0.2296
			0.3207	0.5503	
EQ Intensity, S_a	g	1.51	1.12	1.90	1.1253
			0.2686	1.3939	
GM Profile		la24	la31	la36	1.8698
			0.2406	2.1104	

It should be noted that these results are not unexpected. As discussed in Section 2.5, uncertainty in seismic demand from the randomness in earthquake characteristics often dominates the overall response variability. This is a key result that allows for great simplification in the fragility analysis, as will be seen in Section 7.3.3.1.

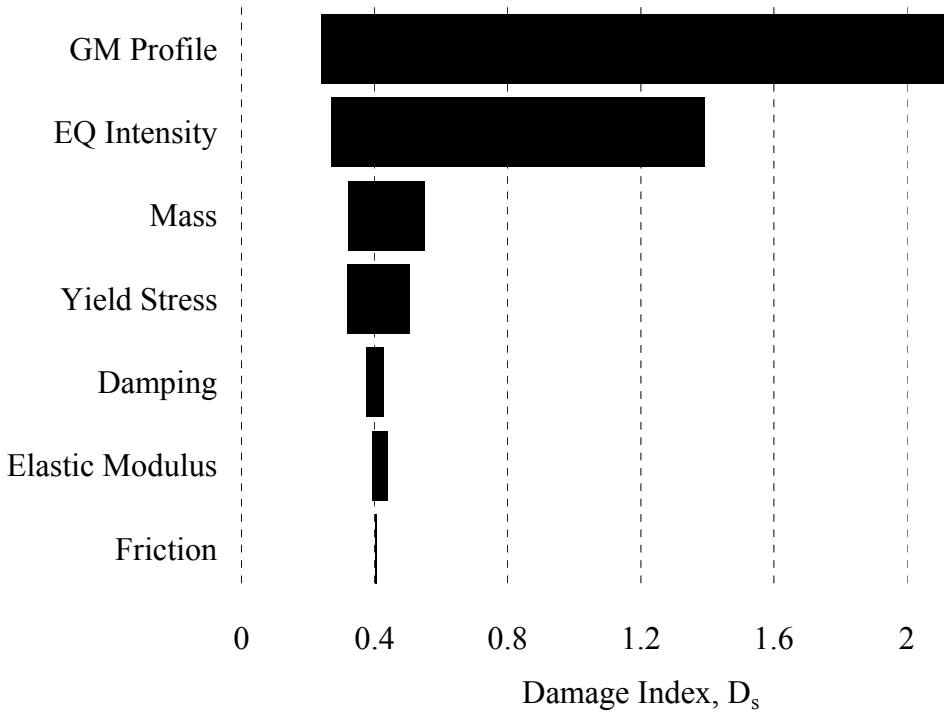

Figure 7.1. "Tornado diagram" graphical depiction of sensitivity study results, indicating relative importance of each considered parameter in terms of its "swing."

7.3 Fragility Formulation

A detailed treatment of the risk and analytical fragility formulation used is presented in Section 2.5 with appropriate references. For completeness of this chapter, a brief review is given in the following sections, supplemented with information that is specific to container cranes and the results of previous chapters.

7.3.1 Risk Framework

Quoting Ellingwood et al. [101], "[t]he concept of risk involves hazard, consequences, and context." The theorem of total probability provides a way to consider all three aspects of risk assessment:

$$P[Loss > c] = \sum_{s} \sum_{LS} \sum_{d} P[Loss > c \mid DS = d] P[DS = d \mid LS] P[LS \mid SI = s] P[SI = s] \quad (7.1)$$

in which P[SI=s] is the probability of a seismic event with SI=s, from the standard hazard curve; P[LS|SI=s] is the probability of reaching a limit state LS, given the occurrence of SI=s (consequence); P[DS=d|LS] the probability of damage state DS, given limit state LS (consequence); and P[Loss>c|DS=d] the probability that loss exceeds c (context), given that DS=d. The fragility term P[LS|SI=s] describes the conditional probability that a limit state is achieved, given a specific earthquake intensity. Here, because local limit states are directly related to global damage states, and that damage states are defined according to repair models with specific estimated downtimes, the fragility term provides a convenient link to estimate the probability of losses in terms of downtime. This concept is further refined and demonstrated in Section 7.5.

Limit states are defined in Chapter 6 in terms of an EDP of maximum portal drift, and spectral acceleration has been shown to be an appropriate measure of seismic intensity for fragility analysis. Thus, the fragility term can be more specifically written as

$$P[D > \theta | S_a = s] \quad (7.2)$$

where D represents the EDP of maximum portal drift, θ is a specific value of D, S_a represents spectral acceleration as the measure of seismic intensity, and s is a specific value of S_a. The traditional assumption of a lognormal cumulative distribution function is assumed for fragility, so that

$$F_R(x) = \Phi[\ln(x / m_R) / \beta] \quad (7.3)$$

where m_R represents the *median* capacity with logarithmic standard deviation β representing the combination of inherent randomness and uncertainty, which is

discretized and further explored in Section 7.3.3. The notation Φ[·] indicates the standard normal probability integral. Variable x here represents the specific value of EDP, described here also as θ. In effect, fragility analysis represents a probabilistic treatment of the overlap of separate distribution functions for demand and capacity. The methodology adopted here is but one way to treat this scenario and analytically develop fragility curves.

7.3.2 Seismic Demand Models

In order to make use of Equation 7.3 to develop analytical fragility curves, a means to relate the seismic intensity (spectral acceleration) to limit states represented in terms of the EDP is necessary. Here, this is done in terms of seismic demand models, which are simply a mathematical construct to relate spectral acceleration to portal drift and quantify the uncertainty related to the choice of demand model. One efficient way of determining a demand model is to fit a function to the data points from a series of nonlinear time history analyses and quantify the dispersion of data points from that assumed function. Generally, a suite of ground motions is used, and a nonlinear finite element model is subjected to each motion individually. In some cases, uncertainty in structural properties must be included in the finite element model, such that a number of different random realizations of the system with uncertain parameters are subjected to each earthquake.

Typically, the seismic demand models are assumed to be log-log linear relationships, defined by the relationship

$$\theta_{\max} = a \cdot S_a^b \cdot \varepsilon \tag{7.4}$$

where ε is a lognormal random variable with median 1 and logarithmic standard deviation $\sigma_{\ln\varepsilon}$. A linear regression on ln $\theta_{\max}$ *vs*. ln S_a is thus used to characterize the mean and standard deviation results in a mean value seismic demand model. While typical, this log-log linear relationship is not by definition required in order to satisfy the assumption of a lognormal cumulative distribution fragility relationship. If evidence or experience suggests a more appropriate model, it may also be valid. In the case of container cranes, Chapter 3 represents a detailed treatment of the seismic demand for uplifting portal frame structures. As such, results and observations from that treatment are drawn upon heavily in the following sections.

7.3.3 Treatment of Uncertainty

The term β in Equation 7.3 represents the combination of inherent randomness and uncertainty present in the all aspects of the fragility formulation. Typically, this factor is on the order of 0.6 [174]. However, it can be broken down into different categories of uncertainty and quantified separately. Specifically, the total uncertainty can be attributed to aleatory randomness and epistemic uncertainty. Epistemic uncertainty stems from lack of knowledge, and can be reduced with further investigation or more detailed analysis. Aleatory randomness stems from physical sources of unpredictable behavior which cannot be reduced by increased knowledge. Aleatory randomness can be further split into randomness in demand and capacity. Mathematically, the combination of effects can be described by the following equation

$$\beta = \sqrt{\beta_{RD}^2 + \beta_{RC}^2 + \beta_U^2} \tag{7.5}$$

where β_{RD} and β_{RC} represent quantified randomness in demand and capacity, respectively, and β_U represents epistemic uncertainty. The following sections describe how each parameter is estimated for application to container crane fragility here. It should be noted that when this sort of discretization of overall uncertainty is performed, the resulting fragility estimates are *mean* estimates, rather than the *median* estimates by a strict interpretation of Equation 7.3.

7.3.3.1 Aleatory Randomness

Aleatory randomness, or variability due to natural phenomenon, can be attributed to inherent randomness in both demand and capacity. Randomness in demand can be quantified based on the dispersion of data points around the assumed seismic demand model. In this case, the logarithmic standard deviation $\sigma_{\ln\varepsilon}$ is used to approximate β_{RD}, sometimes written as $\beta_{D|Sa}$ because it represents the variability in demand given a specific earthquake. Ideally, every identified source of uncertainty would be included in the underlying Monte Carlo analysis, so that many possible system realizations are tested under each ground motion. However, this can become computationally expensive. Thus, the sensitivity study presented in Section 7.2 is useful for identifying which sources of uncertainty are critical to capturing the fundamental features of the demand model and its associated demand randomness. It was determined that of all considered sources of uncertainty, randomness in the ground motion intensity and profile characteristics dominated the overall demand randomness of container cranes. Thus, computational costs can be minimized by performing only one finite element analysis per ground

motion, with all uncertain parameters evaluated at their best estimate (mean/median) value. This simplification is taken advantage of in the following fragility analyses.

Randomness in capacity is a more difficult parameter to quantify. It must capture and quantify the uncertainty associated with the identified limit states of Chapter 6. Namely, it accounts for the assumptions that derailment, immediate use, structural damage, and complete collapse can be identified from static analysis and the various positions on a pushover curve. An assumed value of $\beta_{RC} = 0.25$ has been used as a reasonable estimate for this randomness in capacity [101], though it is assumed here that $\beta_{RC} = 0.2$ based on the additional information from the sensitivity study and the fact that the structural system is comprised of relatively few elements. It is important to mention that this randomness in capacity does not attempt to quantify the uncertainty of estimating limit states due to modeling assumptions, such as the anchor points for the skeleton curve. Those sources of uncertainty are part of the epistemic uncertainty, described next.

7.3.3.2 Epistemic Uncertainty

Epistemic (or scientific) uncertainty envelopes all of the simplifications, assumptions, and analysis limitations present in the previous chapters. While there are a seemingly infinite number of effects contributing, several major ones are as follows. First, the modeling approaches described in Chapter 4 contribute. For example, the finite element platform chosen has built-in limitations and assumptions. Also, the simplification to a 2D finite element model introduces uncertainty, as well as the assumption that the critical response is that of portal deformation. Second, there is the fact that the range of

applicability for the strength, ductility, and hysteresis rules of Chapter 5 must be loosened for application to container cranes. Third, the behavior predicted by Chapter 3 relies on assumptions as well, which must be accounted for. Using a similar modeling and fragility approach as this work, the epistemic modeling uncertainty has been assumed to be β_U = 0.20 [101], which is based on the assumption that, with 90% confidence, the modeling approach predicts performance which is within ±30% of actual [175]. Here, it is assumed that β_U = 0.25 based on the additional uncertainty from modeling uplift.

7.4 Fragility Analysis

The following sections present a seismic demand and fragility analysis for the three representative container cranes of Appendix A, using the formulation described in Section 7.3. The ground motions used are the SAC ground motions used in the sensitivity study of Section 7.1, and described in Appendix B. Limit states for each crane are defined and quantified in Chapter 6.

7.4.1 J100

Recall, the J100 crane represents a large jumbo container crane, capable of servicing some of the largest container ships. From Appendix A, it is known that its global stability parameter is α = 0.38. Cranes such as these have not yet been subjected to a significant earthquake.

Using the methodology developed in Chapter 4 and verified in Chapter 5, a 2D finite element model is built which is capable of capturing the uplift response and the inelastic

section behavior of the portal frame. A nonlinear dynamic time history analysis is performed for each of a series of ground motions. Here, 40 total ground motions are used: 20 motions having a 10% probability of exceedance in 50 years in the Los Angeles region, and 20 having a 2% probability of exceedance. For each analysis, the peak portal deformation is identified. Recall that because of the uplift and derailment response, the waterside and landside portal drift may be different. From Chapter 6, it is understood that each side has approximately equivalent limit states. Thus, the peak of waterside or landside portal drift is identified as the peak portal drift θ_{max} for each earthquake.

One data point from each earthquake is plotted in Figure 7.2 on a logarithmic scale. A log-log linear best fit line (linear regression in log-log space) to the data points is also plotted. Notice that the equation, noted in Figure 7.2, follows the form of Equation 7.4. It should also be noted that three earthquakes caused obvious "collapse," as indicated in the figure, and are not included in the linear regression. These points of collapse are identified based on an unrealistic level of portal drift, on the order of 8-10%. At these levels of drift, the portal columns have reached their residual strength plateau, and are therefore likely to have completely collapsed. Because limit state of complete collapse is more conservatively defined here as a point on the degrading slope (here, $ln(4.5\%)=1.5$), the limit state falls below the earthquake threshold which results in the ignored "collapse" points. The distribution of data points is assumed to be lognormal about the log-log linear best fit line. In this case, the dispersion of data points is quantified by $\beta_{D|Sa} = 0.268$. This demonstrates the typical method of fitting a seismic demand model, generally chosen for mathematical convenience and for lack of further information. Notice,

however, that the log-log linear fit slightly overestimates drift at low (S_a < 0.5g) and high (S_a > 1.2g) seismic intensity, and underestimates in between. Further, this approach assigns a single value of dispersion $\beta_{D|Sa}$, despite the clear trend of increasing dispersion with higher excitation. Because of the greater uncertainty of response at higher excitations (due to uplift, local buckling, etc.), it is expected that dispersion would increase for larger earthquakes. For these reasons, there may be a better choice for a seismic demand model than the typical log-log linear choice. Fortunately, there are physical reasons to choose a different demand model for container cranes.

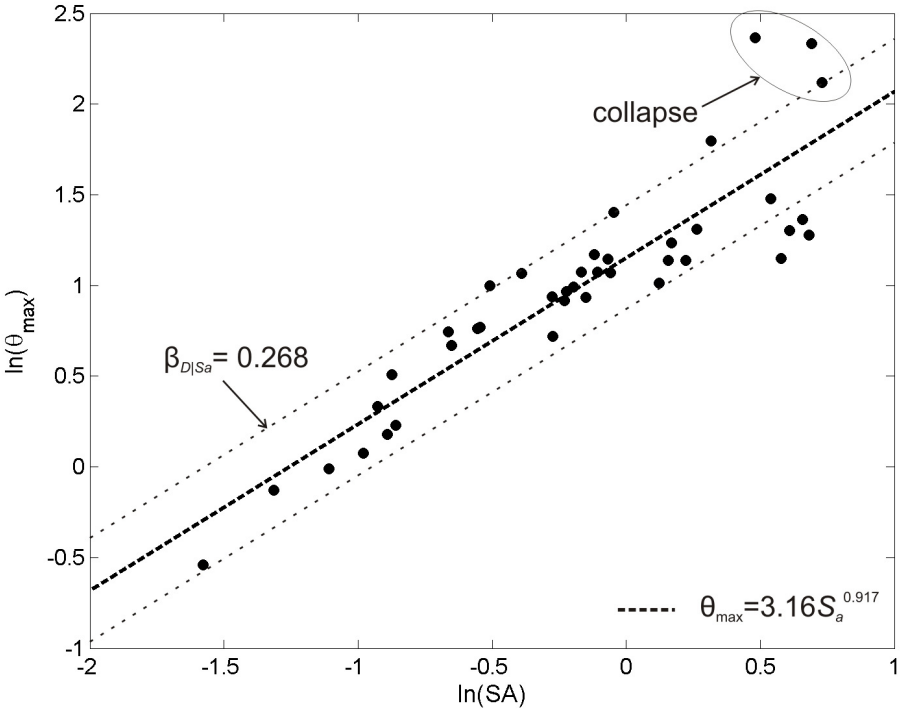

Figure 7.2. Log-log linear seismic demand model of J100 container crane, fit to data points from 2D nonlinear finite element model subjected to SAC LA ground motions.

From Chapter 3, it is known that portal frame seismic behavior exhibits three stages: elastic, sliding, and tipping. Further, the portal deformation at which the response transitions from one stage to another can be estimated from Equations 3.4 and 3.7.

Therefore, the finite element data points can be binned according to the response they exhibit based on the corresponding input ground motion intensity. The data points are replotted in Figure 7.3 accordingly. Then, a log-log linear fit is plotted for each range, the start point enforced as the end point of the previous stage. The equation of each line is shown in the figure, each following the form of Equation 7.3. It is clear that this trilinear fit more realistically follows the data, and better represents the physical container crane behavior. Further, it provides a convenient way to capture the difference in dispersion at low and high seismic intensity. Specifically, the dispersion in the elastic range is quantified as $\beta_{D|Sa} = 0.08$, and in the tipping stage as $\beta_{D|Sa} = 0.301$. So that there is not a discontinuous "jump" between dispersion values, the dispersion in the sliding stage is assumed to linearly vary from 0.08 to 0.301.

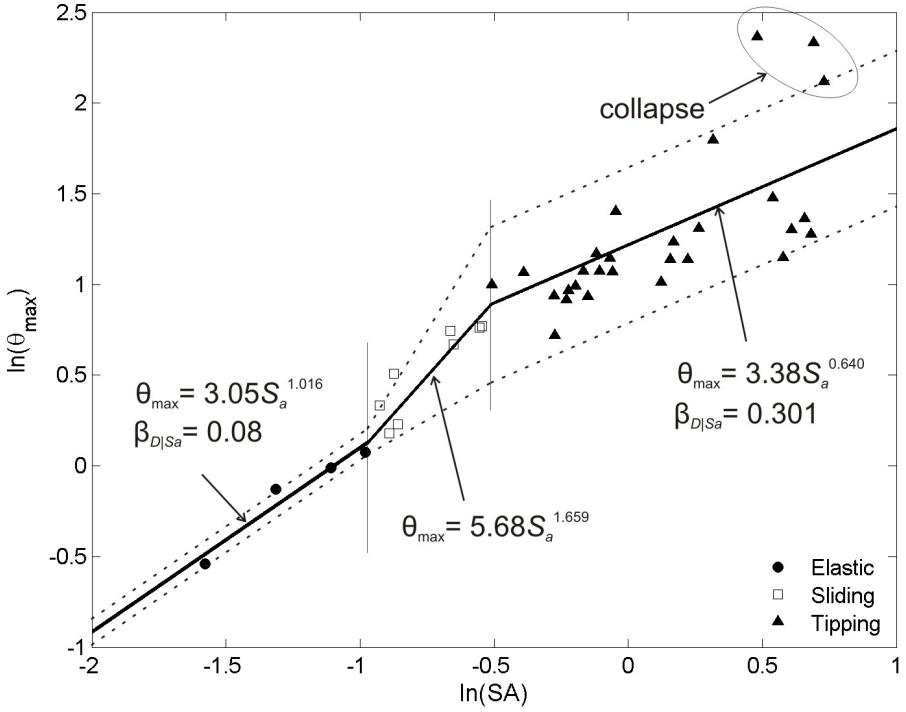

Figure 7.3. Trilinear seismic demand model for J100 container crane.

In addition to deformation limits to define thresholds between response stages, Chapter 3 also provides a methodology for closed-form estimation of seismic demand dependent on system input based on the basic portal geometry. That methodology can be slightly adjusted to provide a seismic demand model relating the predicted maximum portal deformation to spectral acceleration; the process for doing this is summarized here. First, the overall stability factor α is determined based on the location of the crane's center of mass. Then, the maximum predicted portal deformation is evaluated based on a piecewise function, based on the expected three-stage sequential behavior of elastic, sliding, and tipping responses. Quantitatively, this can be expressed as

$$u_{\max} = \begin{cases} u_1, & u_{\max} < u_{cr} \\ u_2, & u_{cr} < u_{\max} < n \cdot u_{cr} \\ u_3, & n \cdot u_{cr} < u_{\max} \end{cases} \tag{7.6}$$

where u_1, u_2, and u_3 describe the maximum during the elastic, sliding, and tipping stages, respectively. Recall that for a portal frame, n = 2, and the critical deformation is determined based from Equation 3.4, repeated below,

$$u_{cr} = \frac{\alpha \cdot g}{\omega^2} \tag{7.7}$$

where g = gravity and ω = natural frequency. Then, deformations u_1, u_2, and u_3 can determined based on the derivations in Chapter 3, but representing the input force using pseudo-displacement. First, the elastic deformation is the pseudo-displacement, directly:

$$u_1 = \frac{S_A(\omega, \xi)}{\omega^2} \tag{7.8}$$

where the spectral acceleration is dependent on natural frequency ω and damping ratio ξ. Then, the maximum deformation during sliding is determined from modified versions of Equation 3.13 and 3.14:

$$u_2 = u_{cr} e^{-\bar{\xi}\phi} \sqrt{1 + n\left[\left(\frac{u_1}{u_{cr}}\right)^2 - 1\right]} \tag{7.9}$$

$$\phi = \frac{\pi}{2} - \tan^{-1}\left\{\left(n\left[\left(\frac{u_1}{u_{cr}}\right)^2 - 1\right]\right)^{-1/2}\right\} \tag{7.10}$$

Recall that modified damping ratio $\bar{\xi} = \xi / n$. Finally, the maximum portal deformation during tipping is determined from modified forms of Equation 3.21 and 3.22:

$$u_3 =_{cr} \left\{\frac{n}{1+\alpha^2} + \frac{\alpha}{\sqrt{1+\alpha^2}} e^{-\zeta\varphi} \sqrt{\frac{n^2\alpha^2}{1+\alpha^2} + \left[\left(\frac{u_2}{u_{cr}}\right)^2 - n^2\right]}\right\} \tag{7.11}$$

$$\varphi = \frac{\pi}{2} - \tan^{-1}\left\{\frac{n\alpha}{\sqrt{1+\alpha^2}}\left[\left(\frac{u_2}{u_{cr}}\right) - n^2\right]^{-1/2}\right\} \tag{7.12}$$

Recall that the damping during the tipping stage is significantly increased, represented by a different damping ratio, repeated from Chapter 3 in a slightly modified form as

$$\zeta = \frac{\xi}{n}\frac{\sqrt{1+\alpha^2}}{\alpha} \tag{7.13}$$

Presented in this way, the predicted deformation for any uplift-capable portal frame structure subjected to a given spectral acceleration can be estimated with relative ease. Taken over a range of excitations for a given natural frequency, damping ratio, and stability factor α, the piecewise function of closed-form estimates provides a seismic demand model more tailored to the type of system considered, in this case a container crane.

Applying this alternative demand model based on portal uplift theory to the J100 container crane, a new solid line is plotted on top of the dashed trilinear best fit in Figure 7.4. It is clear that the portal uplift model is an appropriate seismic demand model, and fits the data very well. The values for dispersion of points around the demand model are assumed to be the same as the trilinear model, due to the closeness of fit.

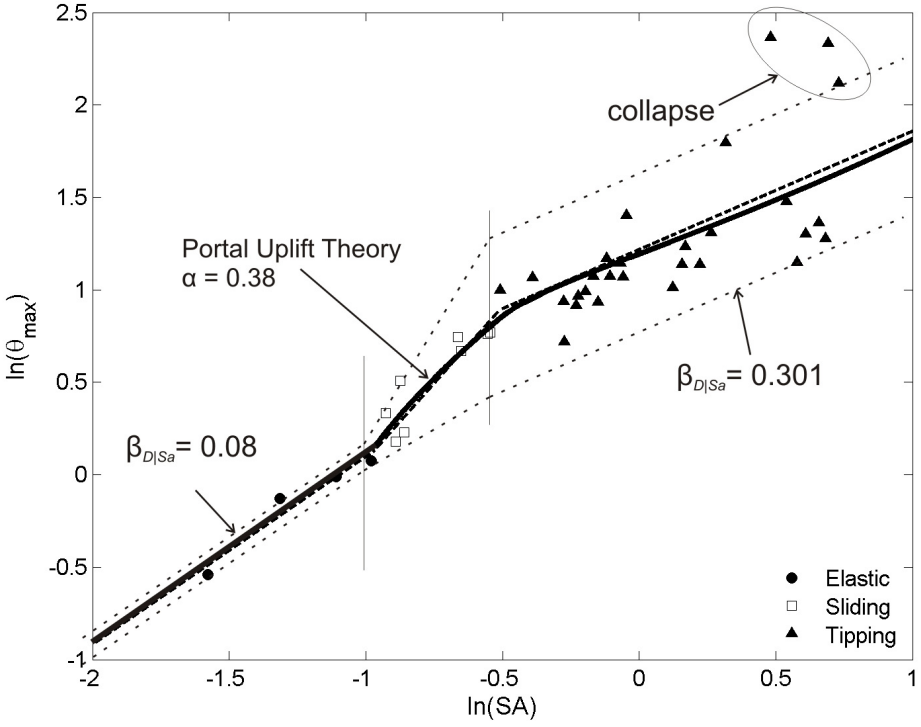

Figure 7.4. Seismic demand model as per portal uplift theory for J100 container crane, plotted on top of the trilinear demand model.

Using the assumption of lognormality, Equation 7.3 can be applied together with the limit states quantified in Chapter 6, the treatment of uncertainty in Section 7.3, and an assumed seismic demand model to determine fragility curves. Recall that the assumption of a lognormal distribution behind Equation 7.3 does not dictate one demand model over any other. Rather, any appropriate demand model can be used in place of variable *x* such that

a comparison between demand and median capacity m_R can be performed. For J100, two sets of fragility curves are presented in Figure 7.5. The dashed curves represent fragility curves assuming that seismic demand follows the log-log linear best fit line, while the solid curves assume that demand follows portal uplift theory as described above. While more traditional in appearance, the dashed curves are misleading in the same way that the log-log linear demand model is. Specifically, the dashed fragility curves overestimate the likelihood of each limit state in their respective range of low and high seismic intensity, and underestimate in between. Because the downtime associated with collapse is large, even relative to the structural damage limit state, overestimating the likelihood of collapse at small earthquakes can significantly but artificially inflate the expected losses. This point is emphasized in Section 7.5.

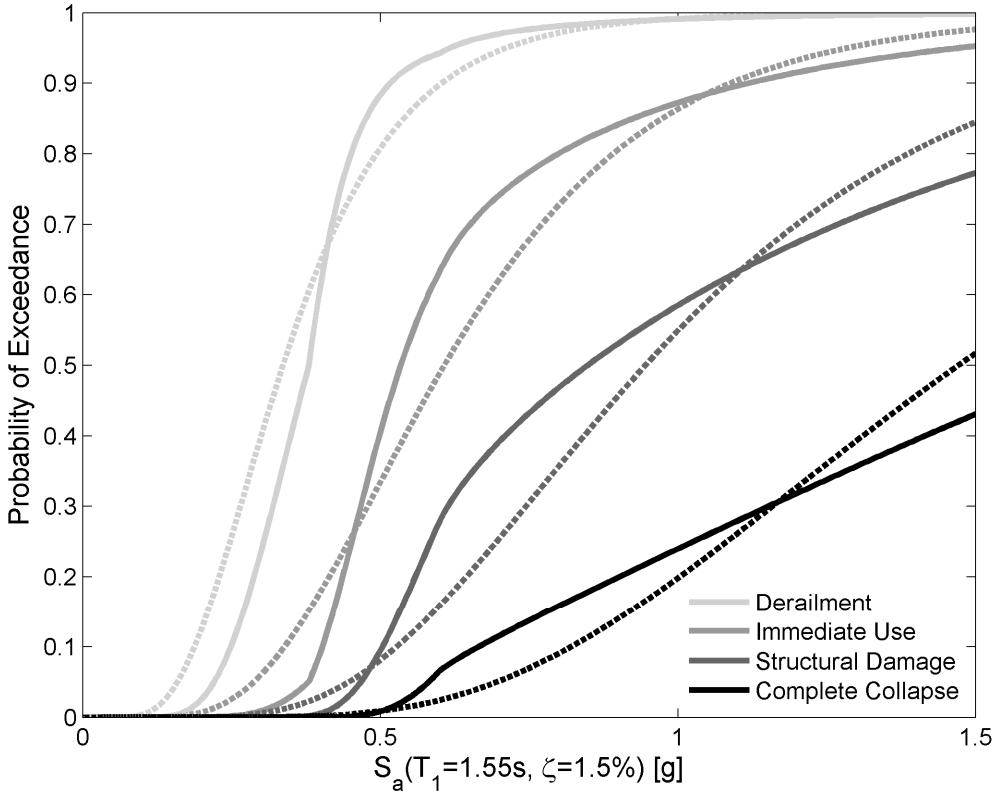

Figure 7.5. Fragility curves for J100 container crane, assuming a log-log linear demand model (dashed lines) or that from portal uplift theory (solid lines).

7.4.2 LD100

Recall, the LD100 crane represents an older jumbo container crane, but the basic "workhorse" of many container ports. From Appendix A, it is known that its global stability parameter is $\alpha = 0.70$.

As with J100, a nonlinear finite element model is built and run for each of a series of ground motions. However, because the capacity of LD100 is much less than J100, only the earthquakes having a 10% probability of exceedance are used. Even still, 4 earthquakes (la9, la11, la18, and la20) cause unrealistically high portal drift (on the order off 10%), and are not included in the demand modeling, similar to with J100.

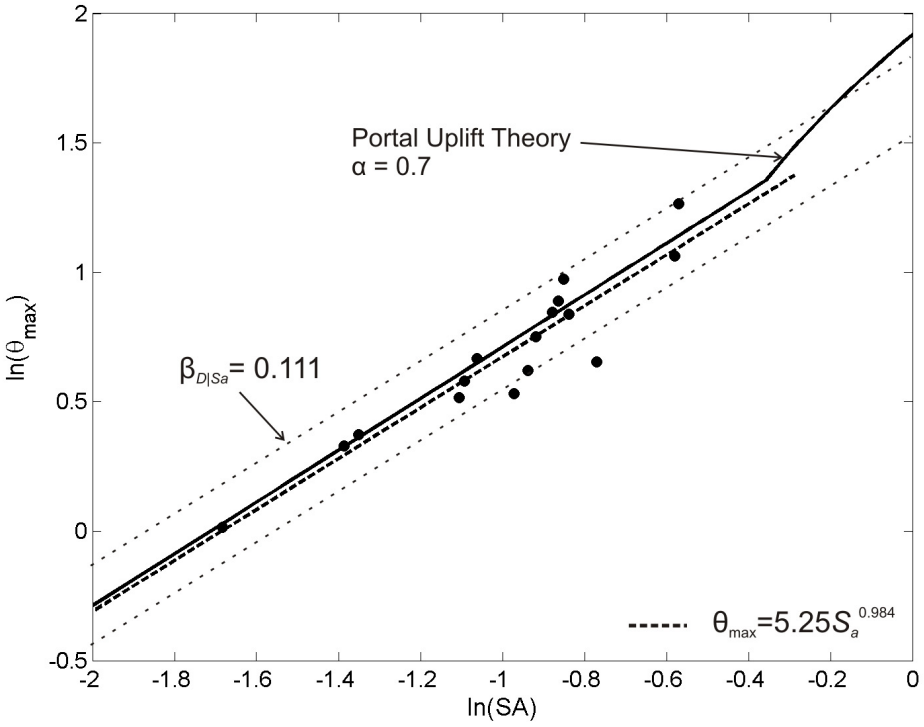

Figure 7.6. Log-log linear and portal uplift theory seismic demand models of LD100 container crane.

Each data point is plotted in Figure 7.6, as are two seismic demand models: log-log-linear and portal uplift theory. Notice that because the overall stability is high, as discussed in Chapter 6, the uplift threshold and thus derailment limit state (3.8%) is above the complete collapse capacity (3.0%). Thus, derailment is not considered as a limit state. Therefore, the log-log linear and portal uplift theory demand models are both linear in the range of interest, and are closely matched. The dispersion from either model in this range is quantified as $\beta_{D|Sa} = 0.111$. To maintain a consistent approach as with J100, the portal uplift theory seismic demand model is chosen for use in the fragility analysis. Fragility curves for the three structural limit states are depicted in Figure 7.7, assuming seismic demand follows portal uplift theory.

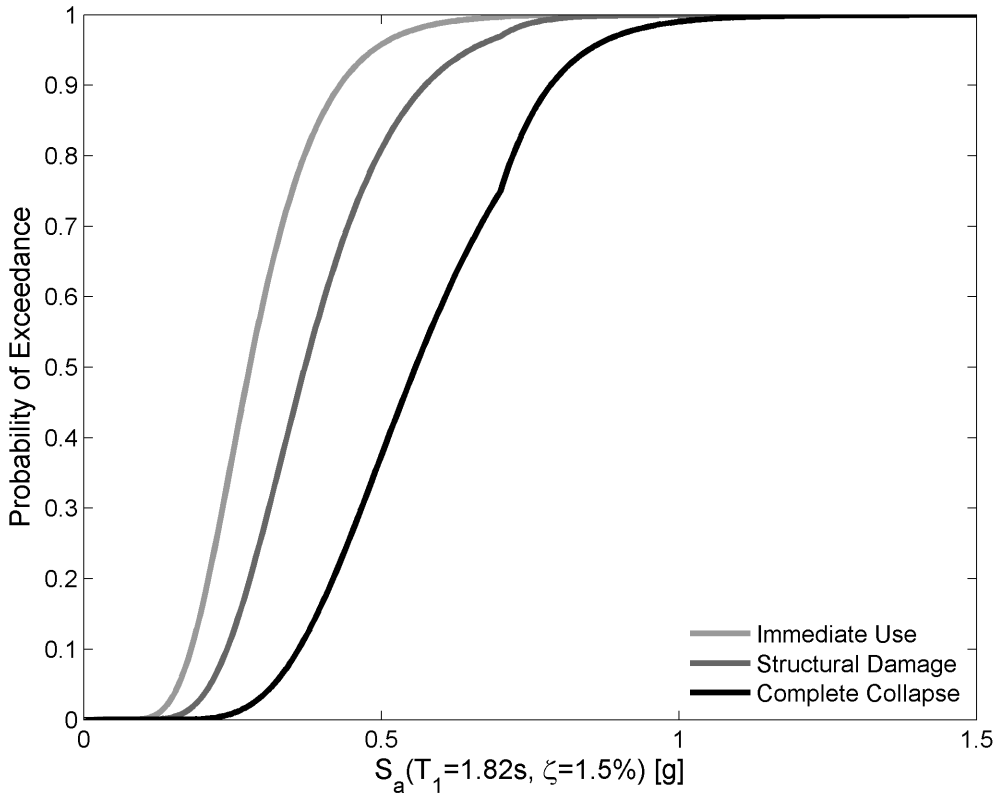

Figure 7.7. Fragility curves for LD100, assuming portal uplift theory seismic demand model.

7.4.3 LD50

Recall, the LD500 crane represents an older small container crane, basically outdated but still useful to service smaller ships when terminals get crowded. Although LD50 may not be as critical to sustained operation of a major port, it is still important to quantify its fragility for comparison purposes, and as another point to be used for verification of the methodology via historic crane seismic performance. From Appendix A, it is known that its global stability parameter is $\alpha = 0.30$.

Based on the excellent predictive ability of the portal uplift theory for J100 and LD100, it is chosen as the seismic demand modeling approach for LD50. Further, because it is an older crane, significant and numerous modifications and repairs have likely been made, making it difficult to determine or assume some current configuration. However, portal uplift theory requires only a basic description of the structure. Thus, this section represents a demonstration of fragility development assuming an existing crane with little known about structural details.

The seismic demand model from portal uplift theory is shown in Figure 7.8. Randomness in demand given the seismic intensity is modeled in the same fashion as with J100, where it is assumed that $\beta_{D|Sa} = 0.15$ in the elastic stage, $\beta_{D|Sa} = 0.40$ in the tipping stage, and linearly varying from 0.15 to 0.40 in the sliding stage. These values are assumed, erring on the side of conservatism, as there are not data points from which it can be quantified. Based on the demand analysis for J100 and the sensitivity study of Section 7.1, these

values are seen as reasonable, and could be used for fragility analysis of other cranes where explicit quantification of dispersion is impossible or computationally prohibitive.

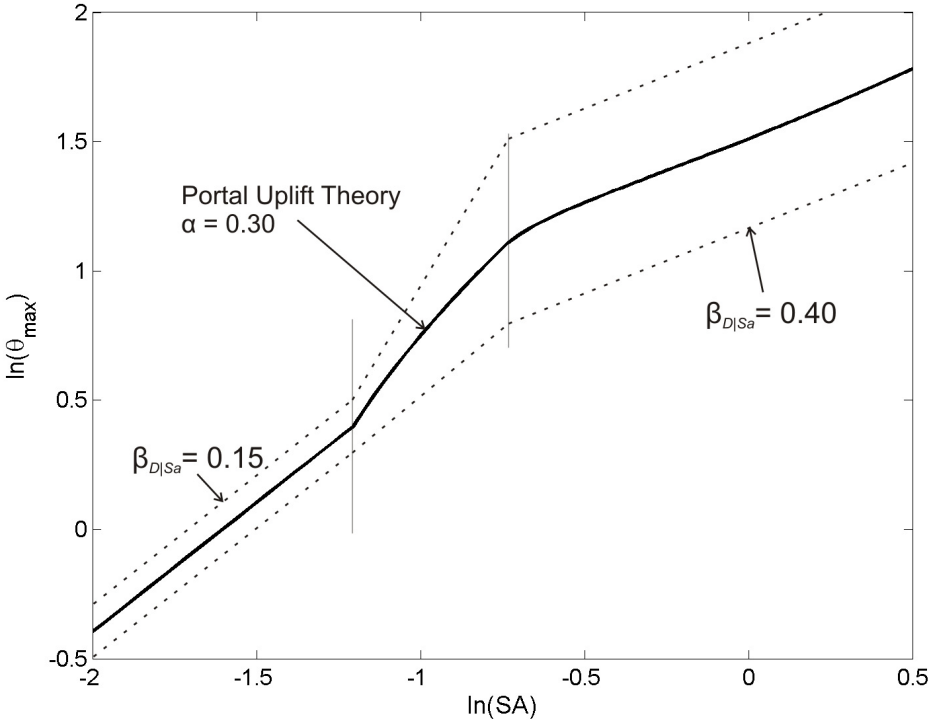

Figure 7.8. Seismic demand model for LD50 assuming portal uplift theory.

Using portal uplift theory as the seismic demand model, the lognormality assumption and Equation 7.3, as well as the limit states quantified in Chapter 6, fragility curves for LD50 are estimated and presented in Figure 7.9. Because LD50 has a fairly low stability parameter α, it requires less capacity than LD100 in order to actually exhibit uplift. Therefore, the three stage behavior predicted by portal uplift theory is valid, and derailment must be considered as a limit state in addition to the three structural limit states.

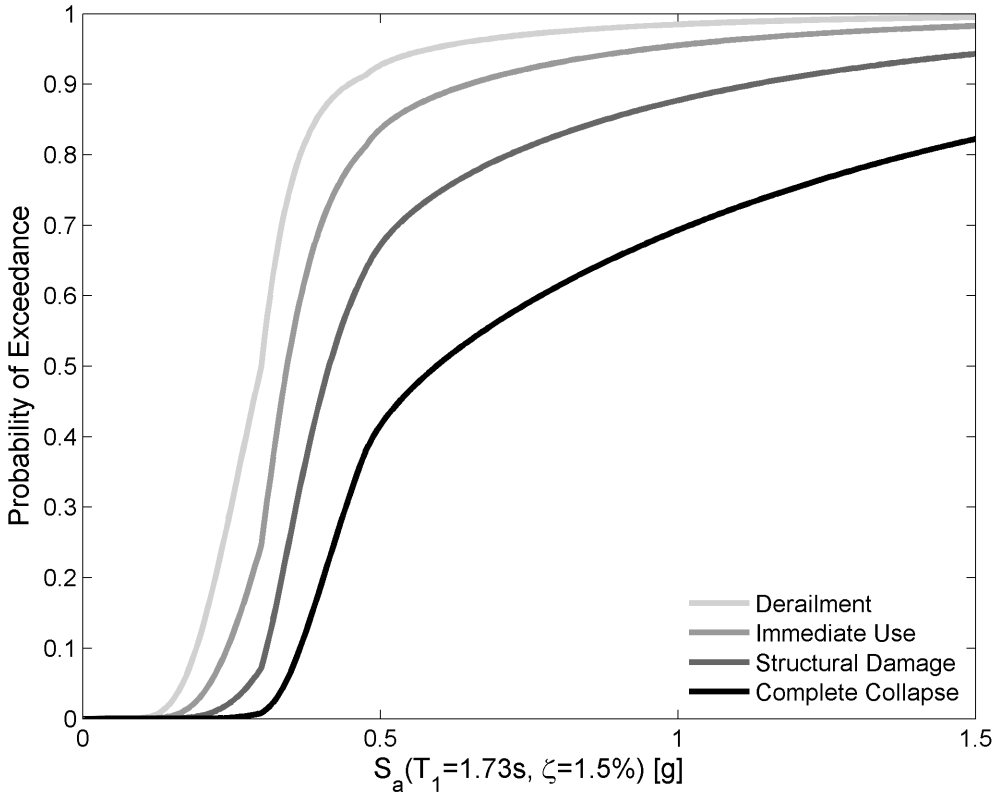

Figure 7.9. Fragility curves for LD50, assuming portal uplift theory seismic demand model.

7.4.4 Hazard Perspective

In order to provide hazard perspective and a context for application of fragility curves, proposed earthquake spectra for different design level earthquakes at the Port of Los Angeles [164] are considered. Two levels of shaking are considered. Under an operating level earthquake (OLE), representing excitation with a 72 year recurrence interval (50% probability of exceedance in 50 years), the 2007 POLA seismic design guidelines require that container cranes remain operable [11]. Under a contingency level earthquake (CLE), representing excitation with a 475 year recurrence interval (10% probability of exceedance in 50 years), the POLA guidelines require that container cranes do not

collapse. The design spectra, for 1.5% of critical damping, are shown in Figure 7.10, annotated with the period of each crane's portal sway mode.

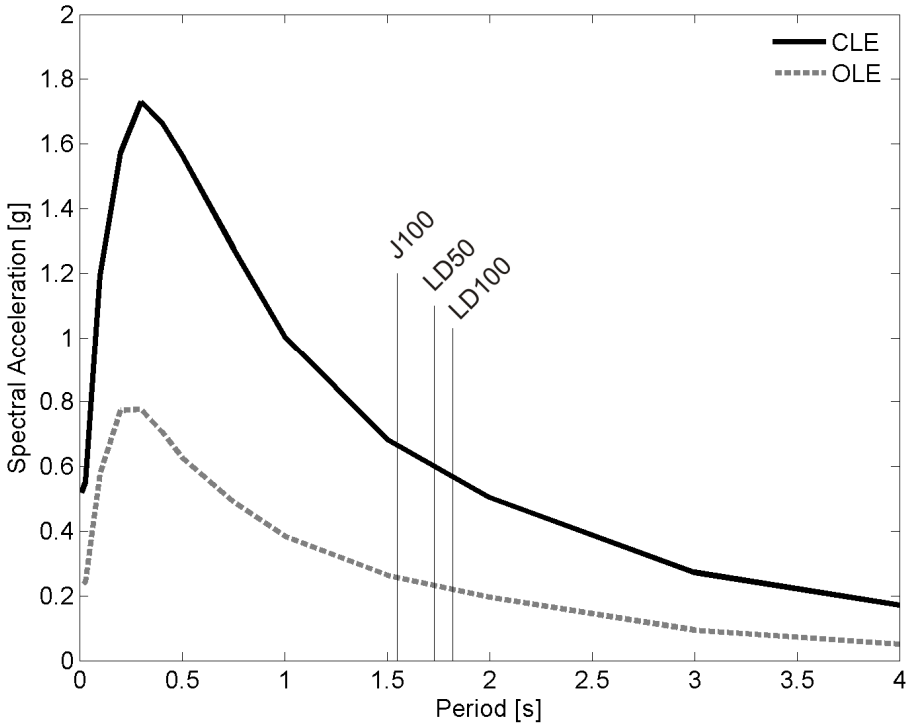

Figure 7.10. Design spectra for OLE and CLE earthquakes for the Port of Los Angeles for 1.5% damping [11], and the fundamental mode of three representative container cranes.

Evaluating the fragility curves of each crane at their respective design level seismic intensity, the likelihood of the different damage states can be determined for each crane. Figure 7.11 depicts the likelihood the J100, LD100, and LD50 container cranes of remaining serviceable, being derailed, suffering minor or major structural damage, or completely collapsing when subjected to Port of Los Angeles OLE and CLE design level earthquakes. It is clear from the figure that all three cranes under an OLE event will remain serviceable, but have significant likelihood of suffering some form of damage requiring downtime. When subjected to a CLE event, the LD100 and LD50 cranes have

a likelihood of collapse slightly above 50%. The J100 crane is broadly distributed, centered in minor damage, with significant (~10%) chance of complete collapse. Therefore, neither container crane performance requirement from the POLA seismic design guidelines is satisfied, especially for a CLE event and the older cranes.

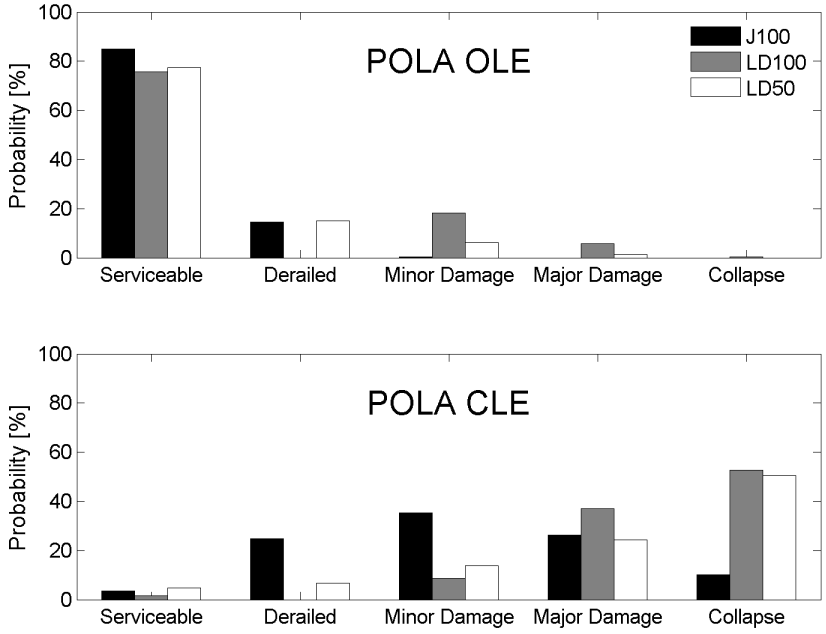

Figure 7.11. Likelihood of identified damage states for POLA OLE and CLE design level motions for each of three representative container cranes.

7.4.4.1 Comparing Demand Models

The effect of different seismic demand models is shown by example, using those determined based on the log-log linear (LLL) best fit line and portal uplift theory (PUT) shown for the J100 container crane. Using the same design level motions as above, the likelihood of achieving different performance levels is depicted in Figure 7.12 for both demand models. As expected based on the discussion of differences in predicted maximum portal drift, the predicted likelihoods are somewhat different. Under the more

frequent OLE event, the log-log linear demand model over-predicts the response when assuming a seismic demand following portal uplift theory, thus leading to higher probability of derailment and minor damage, and less likelihood of remaining serviceable. Thus, the more realistic choice of portal uplift theory is beneficial for evaluating the likelihood of conforming to design guidelines given a crane design. Differences are somewhat more subtle when considering the more intense CLE event. However, because PUT estimates a higher maximum portal drift than LLL in this range of moderate earthquake, the distribution of performance is skewed slightly more towards higher damage levels. Thus, it is unconservative to assume a LLL model when evaluating the potential for major damage or collapse. For these reasons, portal uplift theory is viewed as the superior seismic demand model.

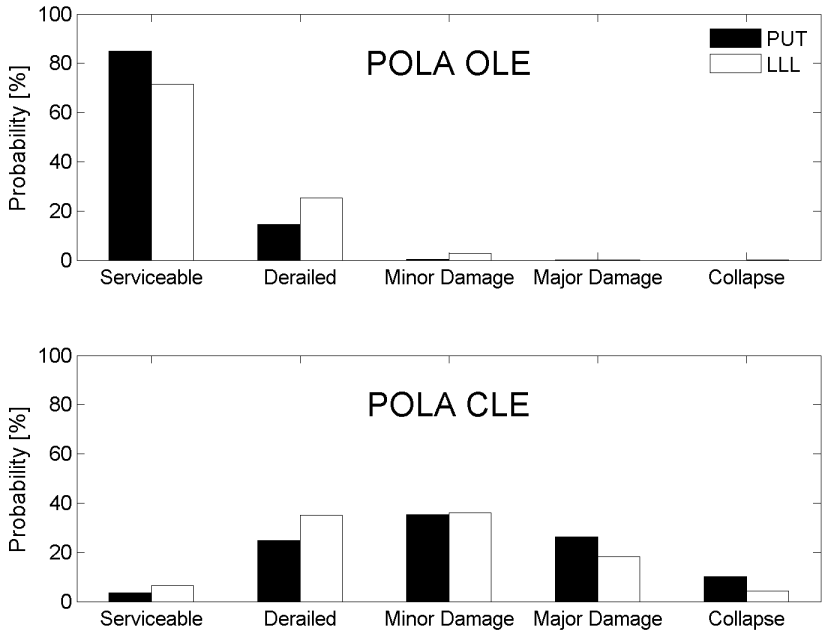

Figure 7.12. Likelihood of identified damage states for POLA OLE and CLE design level motions for J100 container crane using two assumed seismic demand models: log-log linear (LLL) and portal uplift theory (PUT).

7.4.5 General Discussion

Notice that, especially for the LD100 and LD50 container cranes, the fragility curves are relatively closely spaced. This is because the limit states are also closely spaced, a result of significant lack of ductility due to highly slender portal frame structural elements exhibiting strength degradation due to local buckling. Then, if collapse prevention is the goal, it may be possible to decrease the effective slenderness of critical sections in existing cranes enough to increase collapse limit state's portal drift safely beyond the seismic demand. This idea is further explored in Chapter 8.

7.4.5.1 Application of Equal Displacement Rule

At first glance, it may be surprising that portal uplift theory accurately predicts seismic demand in the region of inelastic response, since portal uplift theory is based on an elastic structure. However, recall the well-known "equal displacement rule" [130]: under certain conditions, the maximum deformation of an inelastic system is approximately the same as an elastic system. The conditions are that the structure must have a relatively long period, and not exhibit large degradations. The first condition is satisfied based on the critical portal sway mode of typical container cranes. The second condition is satisfied here because, while still on a degrading curve, the collapse limit state is defined where significant strength remains. Therefore, it is reasonable and even expected that an elastically-derived demand model should match inelastic behavior up to collapse. Beyond collapse, however, this is not the case, as evidenced by the points identified with unreasonably high portal drift for J100.

7.4.5.2 Comparison with HAZUS

As presented in Section 2.5.5, the loss estimation package HAZUS [107] provides fragility curves for rail-mounted port cranes. Damage levels are defined as minor, major, and a combined extensive/complete, defined in terms of the seismic input as described in Section 2.5.5, with some assumed combined uncertainty and randomness. The fragility curves are recreated from this information and depicted in Figure 7.13.

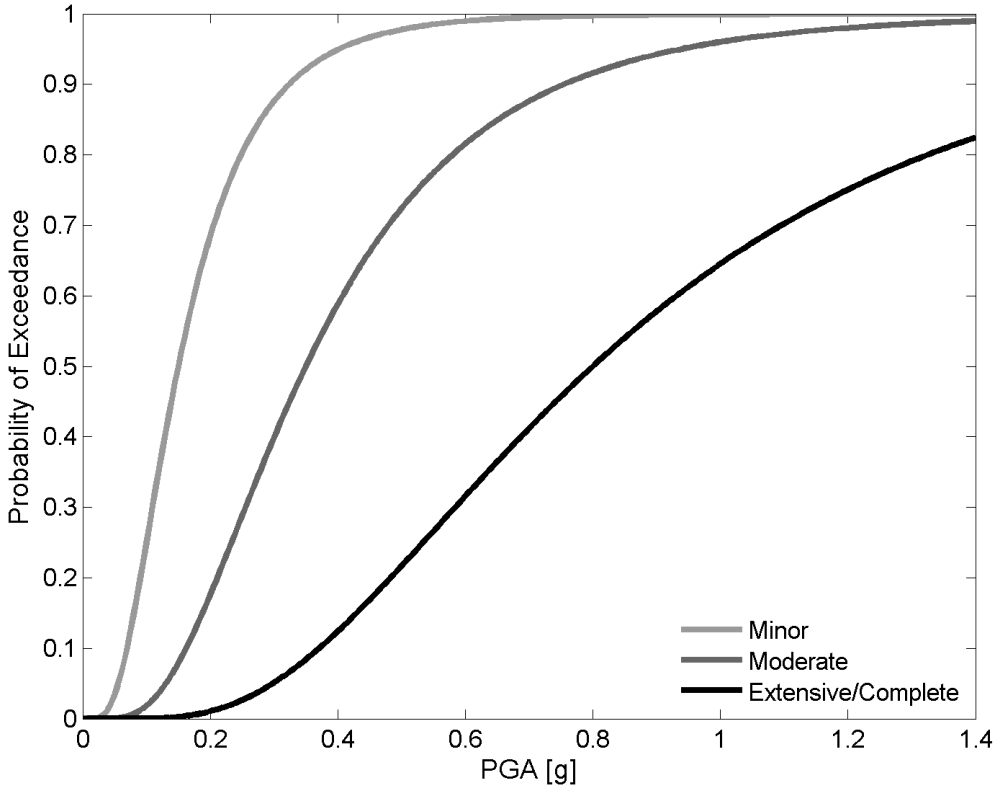

Figure 7.13. Fragility curves for rail-mounted cranes, as defined by HAZUS [107].

Similarities exist in the mathematical form of the fragility curves to the methodology adopted here, particularly an assumed lognormal distribution defined by median capacity and lognormal standard deviation β, but many differences exist. Notably, the fragility curves from HAZUS are based on expert opinion and analysis using the capacity

spectrum method [176]. Perhaps most obviously, however, is that rail-mounted port crane fragility curves related to ground motion are in terms of peak ground acceleration (PGA), rather than some seismic intensity measure such as spectral acceleration. As such, it is difficult and potentially misleading to plot HAZUS fragility curves alongside those developed here, even after making some conversions for consistency. Therefore, damage state probabilities are presented in tabular form for the Port of Los Angeles OLE (PGA = 0.23g) and CLE (PGA = 0.52g) design level motions, comparing the three representative cranes considered here with the hypothetical HAZUS crane. Results for an OLE event are presented in Table 7.3, while Table 7.4 presents results from a CLE event. While the damage levels are defined slightly differently, they can be compared as per the organization in the tables.

Table 7.3. Damage state probabilities for OLE design level event at POLA.

	Serviceable	Derailed	Minor	Major	Complete
	None	Minor		Major	Extensive/Complete
J100	85	15	0.4	0	0
LD100	76	0	18	6	0.3
LD50	77	15	6	1	0
HAZUS	24	54		22	2

Table 7.4. Damage state probabilities for CLE design level event at POLA.

	Serviceable	Derailed	Minor	Major	Complete
	None	Minor		Major	Extensive/Complete
J100	4	25	36	26	10
LD100	2	0	9	37	53
LD50	5	7	14	24	50
HAZUS	2	23		51	24

When subjected to the more frequent OLE event, the predicted likelihood of remaining serviceable is much higher for the three cranes considered here than the HAZUS

interpretation suggests. While the HAZUS model estimates a 54% likelihood of minor damage, the three cranes considered here suggest a 15-21% likelihood. HAZUS also overestimates the likelihood of major damage, and predicts some small chance of collapse where the models here indicate a nearly negligible likelihood.

Under the larger CLE event, the HAZUS model leads predictions centered around major damage. Recall that for LD100 and LD50, collapse was the most likely performance, and for J100, minor damage. Thus, the HAZUS model represents some response between the modern and older cranes under the moderate CLE earthquake. This highlights an important observation: container crane types can respond drastically different under the same earthquake. Thus, it is appropriate to represent container crane types with their own fragility curves, as is done here.

It should be noted that the lognormal standard deviations from the HAZUS model (0.6-0.7) are higher than the total uncertainty β_{TU} considered for cranes J100, LD100, LD50 (0.32-0.51). This is expected, as the HAZUS models were intended to represent the broad group of all container cranes, while the more sophisticated curves developed here represent specific cranes representative of more focused sub-groups. However, this subdivision is important, as different types of cranes built to different standards during different times can perform surprisingly different, as has been shown. Based on the demonstrated simplicity with which specific fragility curves can be developed based on seismic demand predicted by portal uplift theory, it is reasonable to expect that different crane classes can be assigned different fragility.

7.4.5.3 Verification from Historical Performance

One way to verify that fragility curves are reasonable is by comparing historical performance with that predicted by the fragility analysis. While very large container cranes, such as J100, have not yet been subjected to significant earthquakes, several earlier events can be used for this purpose.

LD100 is somewhat similar to cranes which were heavily damaged or completely collapsed at the Port of Kobe in 1995. From Figure 3.10, container cranes were subjected to a spectral acceleration of approximately 1g. From the fragility curves in Figure 7.7, major structural damage or collapse are predicted. Because of the major wharf damage and liquefaction that occurred, however, some isolation of the cranes is expected to have been present [12]. Thus, the fact that the majority of cranes were damaged and that several completely collapsed is in line with predictions from the fragility curves here, which assume an intact wharf.

Cranes such as LD50 exhibited some derailment and minor damages during the Loma Prieta earthquake, especially at the Port of San Francisco [7]. Accelerometers mounted on a wharf deck at the Port of Oakland recorded the event, and believed to be similar to what the Port of San Francisco was subjected. The spectral acceleration that J50 would have been subjected to is approximately 0.23g (see LP spectra in Figure 5.5). Considering the fragility curves in Figure 7.9, the Loma Prieta earthquake is expected to have caused derailment with approximately 22% likelihood and minor damage with approximately 7.5% likelihood. Given that most cranes remained serviceable but that

several exhibited minor derailment and fewer suffered minor structural damage, the fragility curves are judged as reasonable. This is especially noteworthy, because it highlights the fact that the same methodology realistically predicts adequate performance of older cranes while also predicting poor performance of larger, newer cranes under today's expected earthquakes.

7.5 Downtime Analysis

While fragility curves provide more transparency than a total seismic risk assessment, it does not always reflect the desired consequence which non-engineering stakeholders require to make properly educated decisions. Rather, stakeholders are often interested in the probability of reaching certain losses. It is convenient to express loss in terms of replacement cost and downtime (dollars and days). As discussed in Chapter 1, the downtime related to container crane damage and collapse is critical to the recovery of overall port operations following a seismic event. Thus, the following sections address a probabilistic treatment of conditional downtime estimation. The statistics of conditional downtime are presented for each of the three representative container cranes.

7.5.1 Analytical Approach

Given the conditional probability of achieving different limit states, the law of total probability and Equation 7.1 provide a reasonably simple method for evaluating the conditional probability of loss. Here, loss is identified and quantified in terms of downtime. It has been shown [177] that a lognormal distribution of loss is appropriate,

which serves the basis for the analysis presented here. Therefore, the probability of loss can be described by two parameters. More specifically:

$$P\left[L > l \middle| IM\right] = f(\mu, \sigma) \tag{7.14}$$

In other words, the probability that loss L is greater than some threshold l is a function of the mean and variance of the lognormal distribution. These two parameters can be estimated based on the expected loss given a damage state and the associated uncertainty and the likelihood of that damage state given the seismic intensity (fragility). Using the definitions, descriptions, and underlying historical experience of damage states in Section 6.3, the downtime associated with each damage state is assumed to be lognormal. The mean and coefficient of variation of that downtime is presented in Table 7.5, along with a review of the pertinent repairs. Notice that because of being driven by replacement timelines, the collapse state is expected to have an extremely long downtime. However, because the timeline for new purchases is generally more known than repairs, the coefficient of variation for collapse is reasonably low.

Table 7.5. Summary of expected repairs for identified levels of damage, and their expected downtimes and respective coefficient of variations.

	Repair	Mean [days]	COV
Derailed	Jacking and repositioning	6	0.3
Minor	Mechanical realignment, heat straightening, minor plate replacement	10	0.5
Major	Remove and replace damaged elements, self-supporting braced repairs	60	0.5
Collapse	Extensive reconstruction, replacement	330	0.3

Then,

$$E\left[L \middle| IM\right] = \sum_{i=1}^{m} E\left[L \middle| DS_i, IM\right] \cdot P\left[DS_i \middle| IM\right] \tag{7.15}$$

$$\sigma^2[L|IM] = \sum_{i=1}^{m}\left(\sigma_i^2[L|DS_i, IM]\cdot P[DS_i|IM]\right) + \sum_{i=1}^{m}\left(\left(E[L|DS_i, IM] - E[L|IM]\right)^2 \cdot P[DS_i|IM]\right) \tag{7.16}$$

Here, m is the number of considered damage states. For J100 and LD50, which exhibit derailment, $m = 4$. For LD100, which is not expected to uplift, $m = 3$. When $E[L|IM]$ and $\sigma^2[L|IM]$ are properly estimated, the probability of loss can be estimated from the cumulative distribution function of the lognormal distribution:

$$P[L \le l|IM] = \Phi\left[\frac{\ln(l) - \mu_{\ln L|IM}}{\sigma_{\ln L|IM}}\right] \tag{7.17}$$

where

$$\mu_{\ln L|IM} = \ln\left(\frac{E[L|IM]^2}{\sqrt{E[L|IM]^2 + \sigma[L|IM]^2}}\right) \tag{7.18}$$

$$\sigma_{\ln L|IM} = \sqrt{\ln\left[1 + \left(\frac{\sigma[L|IM]}{E[L|IM]}\right)^2\right]} \tag{7.19}$$

7.5.2 Example Container Cranes

When downtime is chosen as the quantifier for loss, as is the case for container cranes in this study, loss is designated here as L_t. Then, Equation 7.15 and 7.16 are evaluated for each of cranes J100, LD100, and LD50 in order to estimate the parameters for a lognormal distribution of downtime. Figure 7.14 presents the earthquake-dependent curves for $E[L|IM]$ and $\sigma[L|IM]$ for each representative container crane.

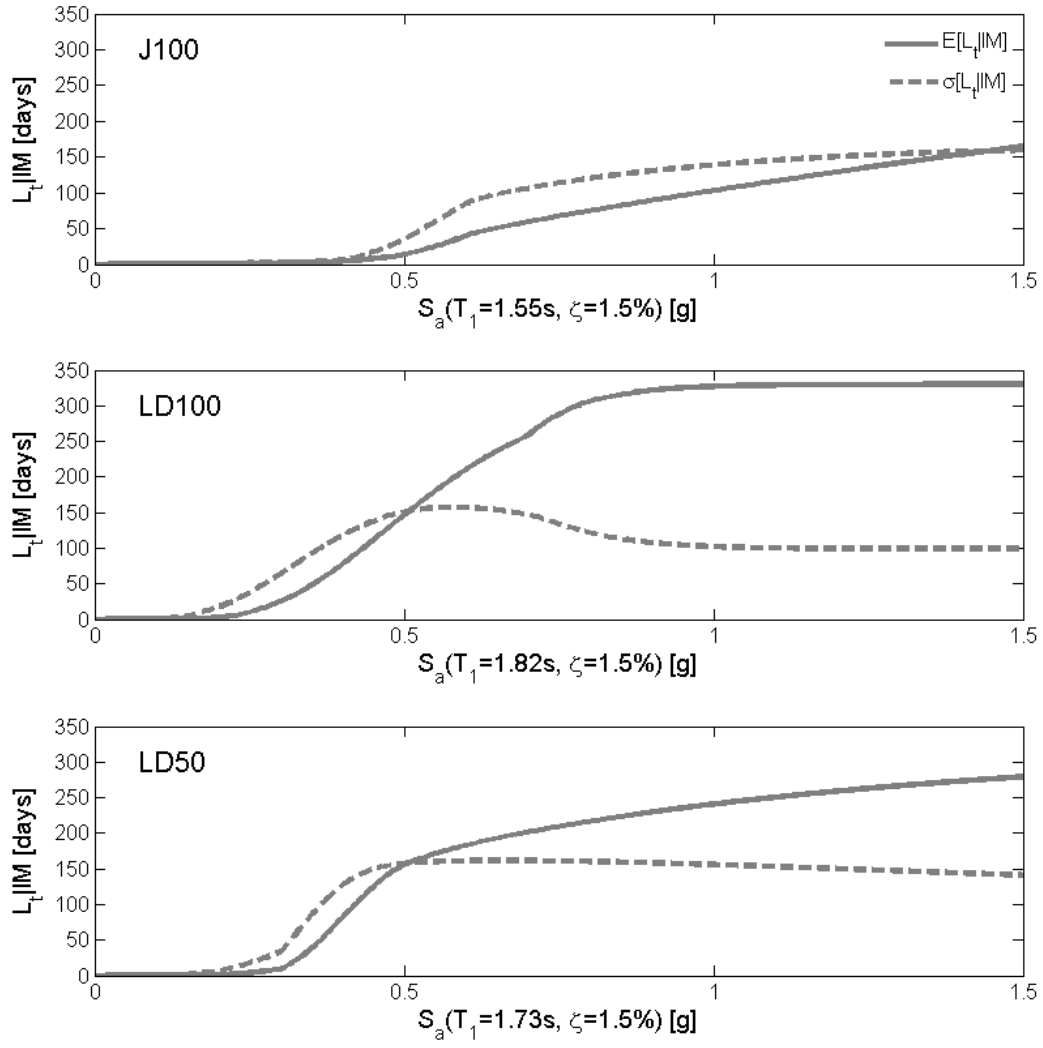

Figure 7.14. Expected downtime curves for three representative container cranes.

Notice that, because the expected value of downtime for collapse is significantly higher than for other damage levels, the overall downtime curves are predominantly controlled by the collapse limit state. As a consequence, where collapse is not the most likely damage, but where there is some nonzero probability of collapse, the variability of downtime is very large, and in fact higher than the expected value. Thus, one is forced to at least partially consider collapse when designing to achieve a specific performance level with certain confidence.

Again, the Port of Los Angeles OLE and CLE design level earthquakes, this time to provide context for expected levels of downtime. Table 7.6 presents the lognormal statistics of expected downtime for each crane under both design level earthquakes. Notice that for each crane subjected to an OLE event, the measure of variability is significantly greater than the expected downtime. This is also true for the J100 crane subjected to a CLE event. While not greater than the expected value, the variability of downtime for LD100 and LD50 subjected to a CLE event are still quite high. This is a result of the collapse downtime exhibiting a sort of "low risk high consequence" behavior, as there is still some small risk of collapse even at low earthquakes.

Table 7.6. Expected value and variability measure of downtime for representative container cranes due to design level OLE and CLE events.

	POLA OLE			POLA CLE		
	J100	LD100	LD50	J100	LD100	LD50
$E[L_t\|IM]$	1	5	2.5	54	193	182
$\sigma[L_t\|IM]$	2	24	12	101	158	161

According to the POLA 2007 seismic design guidelines [11], downtime should be essentially negligible for an OLE event. Table 7.6 indicates that this may not be the case, as there is some non-negligible expected downtime for each crane considered, and with significant variability. The design guidelines indicate that collapse should not occur for a CLE event, presumably so that repairs could be performed which would not take longer than the expected 60-90 days. However, Table 7.6 echoes the results of Table 7.4, indicating that this performance goal may not be met by any of the considered cranes, especially LD100 and LD50.

7.6 Summary

A methodology for appropriately quantifying uncertainty and developing fragility curves for container cranes is presented and applied to three representative container cranes. Based on results from verified finite element models, the seismic demand predicted by portal uplift theory is an appropriate model. Paired with the limit states defined in Chapter 6, this approach is used to develop the presented fragility curves. It is intended that these fragility curves can be used as industry standard "default" curves for the represented classes, or the methodology applied as a template for individual crane designs. Because the different types of cranes can response quite differently under varying levels of excitation, the lumping of all container cranes into a single fragility curve such as is done with HAZUS is inappropriate given the large consequence that collapse can have on port recovery following a seismic event.

Based on design level ground motions, existing container cranes similar to those considered are not expected to completely meet performance requirements presented in design guidelines. There is a significant risk of some form of damage for all considered cranes under typical small earthquakes, and an unacceptably large risk of collapse, especially for older cranes, if exposed to a moderate-to-large earthquake. Port stakeholders can and should consider similarly developed fragility curves, or the associated downtime estimate curves, to help in making risk-informed decisions.

CHAPTER 8

CONCEPTS FOR PERFORMANCE-BASED DESIGN

8.1 Introduction

In the previous chapters, emphasis was placed on the analysis and methodology necessary for evaluating the seismic performance of container cranes. It was demonstrated that many container cranes are potentially vulnerable to damage or collapse during a significant seismic event. Further, the desired performance under design level earthquakes may not be met with sufficient reliability given the current design approach. Fortunately, the tools, simplified methods, and results developed and presented for performance evaluation can also be used to address the problem of reliably meeting performance-based design guidelines, both for new cranes and for potentially correcting existing cranes. In particular, the new understanding of seismic demand of uplift-capable container cranes provided by portal uplift theory allows for a convenient and simple estimation of the critical structural deformation to be used in preliminary design calculations.

This chapter presents and demonstrates a methodology for applying this and other ideas discussed in previous chapters to address the challenge of seismic design and retrofit of container cranes. First, design guidelines consistent with the port industry accepted criterion are discussed and adopted. Then, a capacity approach to design is proposed, using portal deformation as the critical parameter for preliminary seismic design. Finally, the approach is demonstrated through example for a new and existing container crane.

8.2 Performance-Based Guidelines

For purposes of this study, emphasis is placed on seismic design guidelines for US ports, although much of what is discussed is also applicable to international ports. Ports find themselves in a difficult position regarding governing design codes. While building codes are often applied to non-building structures, such as port structures, it is debatable about whether code-writing officials intended for or would agree with their application. Engineers familiar with traditional port structures (piers, wharves, etc.) are quick to point out the fundamental differences between traditional building code requirements and functional requirements of port structures. Perhaps most notably among several is the idea that building codes are anchored in providing "life safety," while port engineers are most concerned with economic sustainability, as port downtime can have a devastating economic effect. Thus, any economically unrepairable physical port damage can be classified as "collapse" regardless of whether the "life safety" non-collapse intended by building codes is met or not. As a result, the port industry has been active in developing their own design guidelines in order to uniquely address their own perceived challenges. Port engineers Johnson and Hardy [178] provide a narrative of this code development environment as well as the history of applicable seismic design codes for traditional port structures, the relevant parts of which are discussed below.

Due to the economic incentives (one could say requirements) to retain as much operational capacity after a seismic event as realistically possible, ports located in areas of high seismicity adopted performance-based design practices as early as the 1980's

[178]. Here, multiple design level earthquakes are defined for a given port, and performance objectives are set for each design level. For years, each port developed and used their own seismic codes, which used different earthquake levels and different performance objectives, with the Port of Oakland, the Port of Los Angeles, and the Port of Long Beach apparently the technical leaders [178]. Because of the complicated business interactions between owner/operator/user port entities, local building commissions, and contracted engineering consultants, these guidelines require extensive efforts to create, maintain, and modify. Thus, consistency and consensus among port stakeholders for a unified design approach is attractive. In 2006, the state of California adopted the Marine Oil Terminal Engineering and Maintenance Standards (MOTEMS) [179] as law, which included seismic evaluation and design guidelines for port structures very similar to those developed by POLA and POLB [11]. Currently, the American Society of Civil Engineers (ASCE) has a specially-formed standards committee charged with creating a new consensus document regarding seismic design criteria for port structures [178], but this effort is expected to take much time and deliberation.

Currently, the typical performance-based port seismic design guideline uses two earthquake levels. When subjected to a small, fairly common earthquake, the performance objective for traditional port structures is such that any minimal damage shall not contribute to interruption of daily operations. Then, for some larger, less frequent earthquake, some amount of damage is tolerable as long as it can be repaired in some acceptable period of time. This approach, or similar, is taken by MOTEMS, ASCE, the US Navy, Japan, Spain, Eurocode, New Zealand, and others [6]. Much of the code

development was spurred by damage to the Port of Kobe in 1995 [180]. How each entity defines the two earthquake levels varies, however. In the US, it is most common to define the two earthquake levels as two of the following: operating level earthquake (OLE), contingency level earthquake (CLE), and ultimate level earthquake (ULE), also referred to as the maximum credible earthquake (MCE). The likelihood and frequency of these events are summarized in Table 8.1.

Table 8.1. Typical design level ground motions for port seismic guidelines.

Earthquake	*Probability of Exceedance*	*Return Period*
OLE	50% in 50 years	72
CLE	10% in 50 years	475
ULE/MCE	2% in 50 years*	2475*

*NOTE: The ULE/MCE earthquake is often scaled or otherwise modified, which alters its likelihood and return period.

Although port seismic design guidelines have been developed predominantly with traditional port structures in mind, ancillary structures such as container cranes have recently begun to gain attention [10]. To the author's knowledge, only the Port of Los Angeles explicitly sets dual-level performance objectives for container cranes currently [11], while the Port of Long Beach, Port of Oakland, Port of Tacoma, and the ASCE standard in development all specify a single performance objective, either for an OLE-type event or for the largest design earthquake [10]. It is interesting to note that, while traditional port structures are commonly required to perform with repairable damage due to a CLE-type event, no current code explicitly requires comparable performance from container cranes.

Given the importance of container cranes to port operations and the potential for extended downtime in the event of collapse, it would seem prudent to require container

cranes to perform to the same standard as the piers and wharves. Requiring full operational capacity for an OLE-type event may appear to some in the building industry as likely to lead to adequate performance under a CLE-type event. However, considering the closeness of limit states identified for three representative container cranes in Chapter 6, it is clear that this may not be the case for container cranes. Along the same lines, it is perhaps unreasonable to expect that a performance objective of "no collapse" under a ULE/MCE-type event will inevitably lead to adequate performance at lesser excitation. Thus, a dual level approach to seismic design of container cranes should be taken, using earthquake levels similar to the defined OLE and CLE events.

The performance objective for an OLE event should be complete operational capacity. Intuitively, this equates to no structural damage, especially in the portal frame. Allowing derailment or not under this earthquake level is a more difficult matter to decide. Although past experience has shown that jacking and repositioning a crane after derailment has occurred is a fairly quick process [168], this is based on accidental events such as ship collision. After an earthquake, personnel may not be immediately available to perform this specialized task. Thus, ports that do not, or can not, have signed agreements with contractors for preferential treatment in the event of an emergency may require that container cranes do not derail during an OLE event. Further, it is perhaps wise to require that the most critical container cranes do not derail, ensuring that at least some port capacity is immediately available following an event. For the purposes of this study, the performance requirement adopted for an OLE event is full operational capacity, meaning no yielding and no derailment.

Consistent with the performance objective of piers and wharves, a CLE event should not result in collapse. While some structural damage can be tolerated, it should be confined to repairable areas, and limited to what can be realistically and economically repaired using the repair strategies outlined in Chapter 6. Had some form of a ULE/MCE event been chosen as the earthquake level, the possibility would exist for a damaged wharf to be repaired reasonably quickly only to have to wait nearly a year before the collapsed crane could bring the wharf back into service. Again, this highlights the importance of downtime. Although the capital expense of a container crane does not put it in the same realm of financial importance as a wharf structure, its potential for causing debilitating downtime makes it of the utmost importance.

8.3 Capacity Approach to Design

Displacement-based, or deformation-based seismic design has been in use for wharf design in the US since the late 1990's, and is now the standard practice [178]. Seismic design of container cranes, however, is generally force-based, but industry leaders are beginning to suggest the possibility of deformation-based design for future cranes [9, 153]. Still, without a model for estimating the deformation demand of an uplift-capable portal frame structure, this is a challenging prospect. Even the most recent recommendations from respected container crane consulting engineers have implied that designing to tip elastically is sufficient to provide adequate seismic performance. However, as discussed throughout the previous chapters, this is not necessarily true. According to the portal uplift theory derived, demonstrated, and verified in this study, the

seismic demand increases with larger earthquake excitation, even after the uplift threshold. Fortunately, portal uplift theory provides a simplified method to estimate the seismic demand, and can be used to modify the common response spectra to depict the seismic demand of an uplift-capable portal frame-type structure for any given earthquake. Then, deformation-based evaluation can be done by comparing the seismic demand with a pushover analysis. This can be conveniently accomplished using the capacity spectrum method [176], specifically considering the portal frame deformation critical to seismic performance.

8.3.1 Design Factors for Capacity and Demand

Because calculated deformations, both in terms of capacity and demand, are not exact and perfect, but rather estimates with some associated uncertainty, it is not enough to simply compare mean or median estimates of capacity and design to satisfy performance objectives. Rather, the distribution of possible values should be considered, so that performance objectives may be met with some quantifiable level of reliability. True reliability-based performance design is still a long way from reality, however. Instead, it is more accepted to use load and resistance factors to target certain levels of reliability. The basic approach adopted here, for the basic case assumed of "one-resistance one-load," is to use characteristic values of demand (D_k) and capacity (C_k), defined as

$$D_k = \gamma_D \mu_D \,,\; C_k = \phi_C \mu_C \tag{8.1}$$

where γ_D and φ_C represent demand and capacity factors. Thus, the characteristic safety factor,

$$\lambda_k = \frac{\phi_C \mu_C}{\gamma_D \mu_D} \tag{8.2}$$

is fundamentally different than the central safety factor,

$$\gamma_0 = \frac{\mu_C}{\mu_D} \tag{8.3}$$

which represents the safety factor if design were done with mean demand and capacity values. While convenient and useful for practical design, characteristic values have no fundamental meaning [113], and so can be determined in a number of ways, so long as it is done consistently. Here, as with many examples of codified design, the 5th and 95th percentiles are used from the distributions associated with capacity and demand, respectively. Thus, a characteristic safety factor greater than one implies that the 5th percentile of capacity is greater than the 95th percentile of demand, depicted graphically in Figure 8.1.

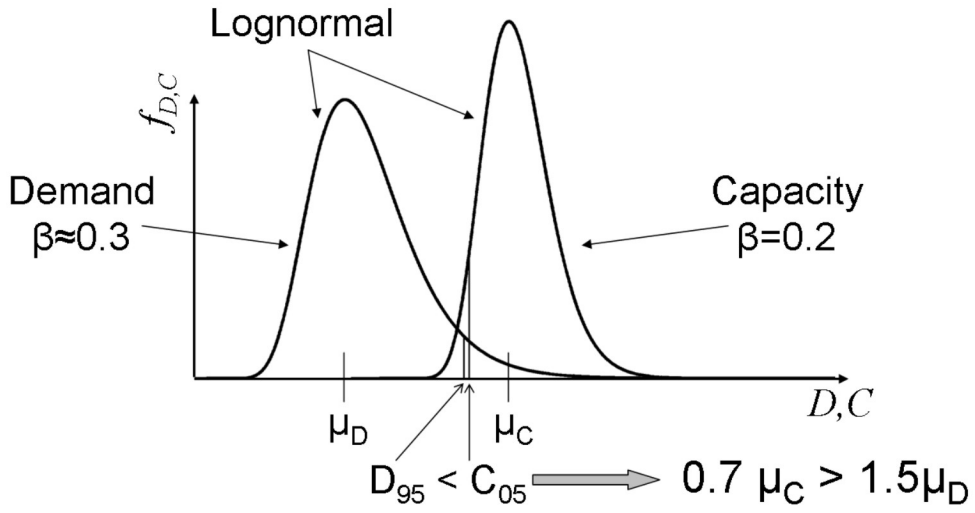

Figure 8.1. Schematic for determining capacity and demand factors using characteristic values of lognormally distributed parameters.

As discussed earlier, demand and capacity are assumed to follow a lognormal distribution. Further, it was assumed that variability of capacity could be estimated with $\beta_C = 0.2$, and that variability in demand could range from $\beta_D = 0.27$-39 for increasing levels of damage.

Thus, the 5th percentile capacity value is equal to $0.7080\mu_C$, and the 95th percentile value of demand could range from 1.49 μ_D to 1.73 μ_D. For simplicity, the capacity and demand factors are estimated as 0.7 and 1.5, respectively. While 1.5 is on the low end of possible values of demand factor, it should be noted that the higher values come from greater uncertainty with larger seismic excitation. It is believed that a somewhat higher risk may be tolerated for these larger events, and thus for consistency and simplicity, a single value of 1.5 is chosen. When these characteristic values are used as the design values (characteristic safety factor $\lambda_k = 1.0$), the central safety factor is approximately $\lambda_0 = 2.14$.

It is possible, and useful, to relate the safety factor to the probability of limit state violation p_f. Although no general solution is possible because it is dependent on the probability distributions associated with demand and capacity, the assumption of lognormality again proves convenient. Under this assumption, limit state violation probability can be determined as [113]

$$p_f = \Phi(-\beta) = \Phi\left(-\frac{\ln\left\{\lambda_0 \left[\left(1+V_D^{\,2}\right)/\left(1+V_C^{\,2}\right)^{1/2}\right]\right\}}{\left\{\ln\left[\left(1+V_C^{\,2}\right)\left(1+V_D^{\,2}\right)\right]\right\}^{1/2}} \right) \tag{8.4}$$

where β is the typical "safety index," the notation $\Phi[\cdot]$ again indicates the standard normal CDF, and V_D and V_C are the coefficient of variation for demand and capacity. Because β_D and β_C are assumed less than 0.3, it is reasonable to approximate $V_{D,C}$ as $\beta_{D,C}$. When the factored demand and capacity are assumed as the design values (such that the central safety factor $\lambda_0 = 2.14$), this results in a safety index of 2.22 and a p_f equal to 0.0133. Although this is still less reliable than typical building codes, where a safety index near 3 is more typical, it provides a first step in providing reliability in light of

large randomness and uncertainty in seismic demand and capacity of container cranes. It is recommended for seismic design of container cranes, therefore, that a load factor of 1.5 be applied to the seismic demand estimate provided by portal uplift theory, and a resistance factor of 0.7 be applied to the calculated pushover curve representing seismic capacity.

8.3.2 Capacity Spectrum Method for Uplift-Capable Container Cranes

Having discussed the merit of a performance-based seismic design approach using deformation (rather than stresses or forces) as the critical response parameter, and with recommended capacity and demand design factors defined, a method to compare factored capacity and demand estimates is required. As mentioned above, the capacity spectrum method (CSM) [176, 181] provides a convenient method to do this, especially given the first-mode dominance exhibited by container cranes under seismic loads. Although many modifications, complexities, and adjustments have been proposed since its development in the 1970's the core principle is to plot the capacity and demand spectra on the same plot, graphically depicting the interaction between them to evaluate expected performance of the structure in question [182]. That basic structure is adopted here. The author believes that, if presented as straight-forward and uncluttered as possible, designers will be more apt to understand and correctly apply the procedure to the greatest benefit. Briefly described in more detail below, the common approach with spectral acceleration plotted with respect to spectral acceleration is implemented.

In design or evaluation of any structure, it is assumed that some elastic design spectra is available or can be obtained from standard hazard maps, site hazard analysis, or similar. When evaluating response in the inelastic range, it is often beneficial to reduce the demand spectra to reflect the additional energy dissipation provided by that inelastic response. While this is often done simply by considering higher damping ratios corresponds to increased ductility levels, and graphically iterating to find the limit state violation "solution" crossing-point of the demand and capacity spectra (e.g. [181]). However, there has been debate that approach, and a push from academics to use more appropriate and mechanics-based demand spectra modification techniques, such as by explicitly using inelastic earthquake response spectra (e.g. [183]). For container cranes dominated by a flexible portal sway mode, the inelastic response follows the "equal displacement rule" [130] (demonstrated in Chapter 7), and an elastic spectra is a reasonable and adequate representation of response, even without adjustments to the damping level. Still, classic elastic response spectra are not appropriate, as demand changes due to the uplift phenomenon. As demonstrated in Section 3.9 though, portal uplift theory provides a straight-forward methodology for modifying response spectra to include the effect of portal uplift behavior. Figure 8.2 depicts the design level OLE and CLE earthquakes from Figure 7.10, but modified to reflect uplift behavior and plotted in CSM form (S_a vs. S_d), and reflecting a factored spectral deformation of 1.5 from the recommendations above.

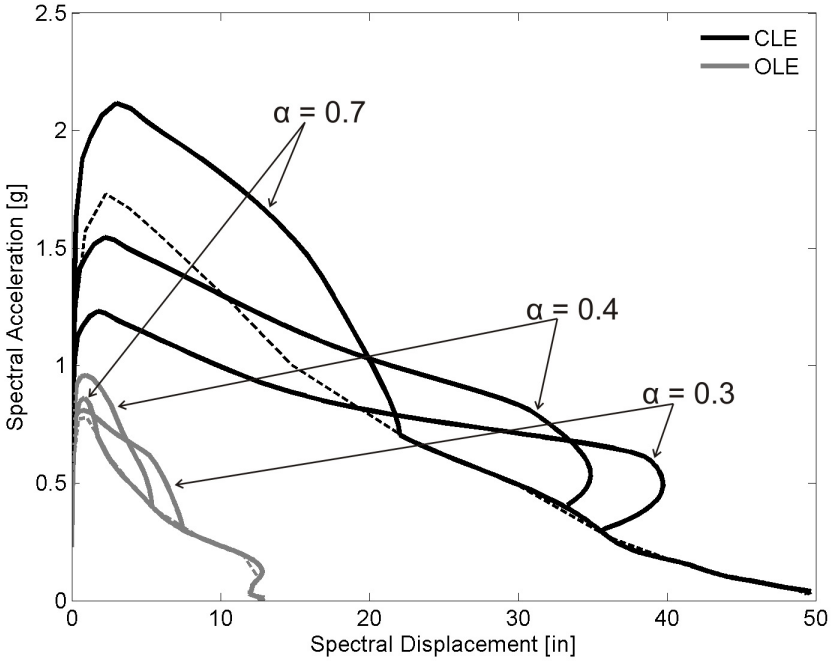

Figure 8.2. CSM demand spectra for POLA elastic response spectra (dashed lines) and modified for uplift (solid lines) of structures with different overall stability.

Capacity spectra can be determined based on simplified pushover curves of the simple frame model described in Section 4.5.2. Because emphasis is placed on preliminary conceptual design or evaluation with limited information, the pushover curve for this purpose can be defined by two points: the yield point and the point of collapse. The yield point can be estimated based on the structure's period T, crane weight W, the height of the portal h, and the yield moment of the portal legs M_y. First, the base shear at initial yield is determined:

$$V_b = 2M_y / h \tag{8.5}$$

Then, the corresponding spectral acceleration to the base shear at yield is

$$S_{a1} = V_b / W \tag{8.6}$$

Finally, the spectral displacement at yielding is found from the period, multiplied by the capacity factor suggested above and accounting for the fact that the critical portal deformation can be estimated as 0.95 times the deformation at the mass (modeled at the center of mass of the structure), as

$$S_{d1} = \frac{0.7}{0.95}\left(\frac{T}{2\pi}\right)^2 S_{a1} \tag{8.7}$$

The point of collapse can be estimated using the calculated properties of the portal legs, using the methodology of Chapter 6. Equation 6.10 is used to determine the overstrength factor. Recall that the point of ultimate ductility is defined as the point where the load capacity has reduced to 95% of its peak. Additionally, the mean minus one standard deviation should be used for conservatism in a preliminary design or evaluation, since many other contributing factors to demand and capacity are not included in this stage of analysis. Thus, the spectral acceleration at the collapse point of a conceptual design can be initially estimated as

$$S_{a2} = 0.95 \cdot S_{a1}\left(\frac{H_{\max}}{H_y} - 0.07\right) \tag{8.8}$$

Likewise, the corresponding deformation can be estimated from the point of ultimate ductility for the portal legs via Equation 6.12, again subtracting the standard deviation:

$$S_{d2} = S_{d1}\left(\frac{\delta_{95}}{\delta_y} - 0.64\right) \tag{8.9}$$

This methodology for approximation of the capacity spectra is demonstrated for the three representative container cranes in Figure 8.3.

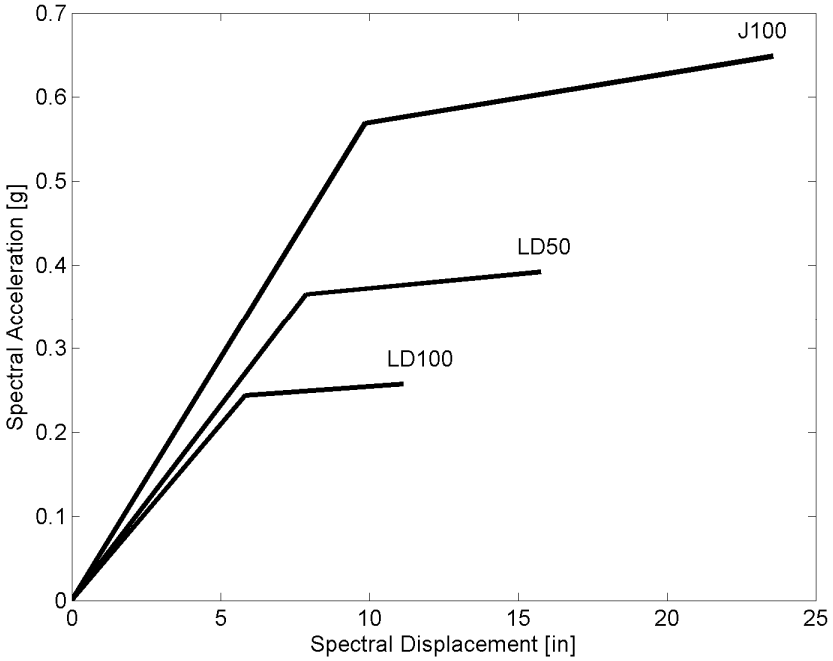

Figure 8.3. CSM capacity spectra estimated for three representative container cranes.

Having defined a simplified methodology for estimating the capacity spectra for container cranes, they can be directly compared with the demand spectra adjusted for uplift using portal uplift theory in order to verify reliable compliance with performance objectives. The following sections demonstrate the approach through example, first for a new conceptual design and then for modifications to an existing container crane.

8.4 New Crane - Preliminary Design Example

Consider a new container terminal that the port owner would like to outfit to service the largest ships of today. The owner requires that the crane be designed to the performance-based guidelines of Sections 8.2 and 8.3, using the design spectra of POLA. They have decided that derailment is tolerable during an OLE event. The standard 100 ft rail gage is specified, and for operational reasons, the portal sway mode must be limited to a

maximum of 1.5 seconds [14]. The boom is required to be at a height of 140 ft, and the portal beam must be 65 ft above the wharf deck for clearance. Based on past experience and the desired lifting capacity, a weight of 2900 kips is assumed. The general relevant configuration is depicted in Figure 8.4, with an assumed location of the center of mass, in the vertical middle of the second story and 1/3 of the gage length away from the waterside leg.

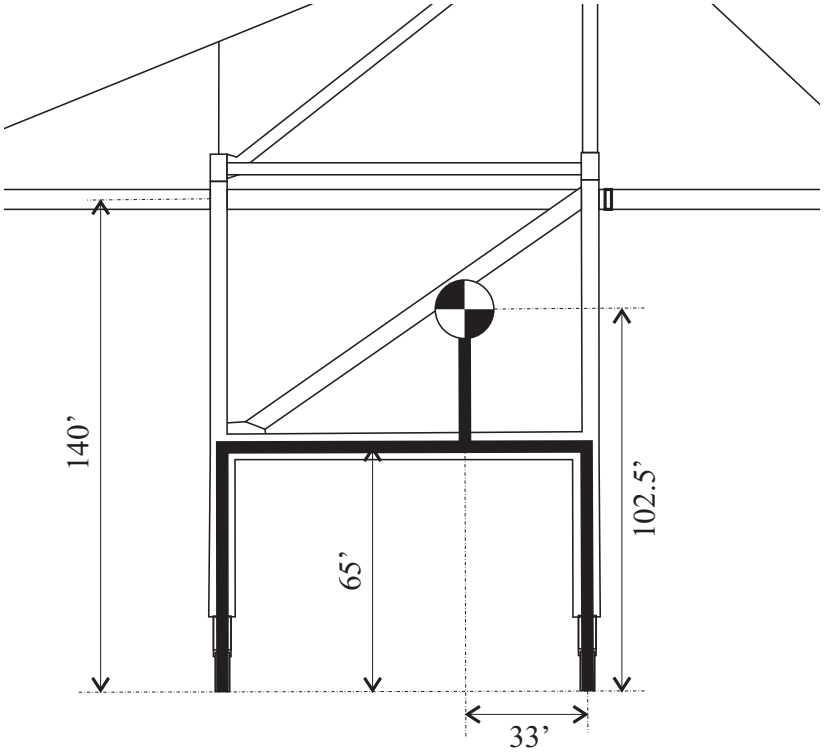

Figure 8.4. General configuration of example crane for preliminary seismic design.

Given the assumed center of mass, the overall stability factor α = 0.32. Then, the factored demand spectra for OLE and CLE events can be determined from portal uplift theory, presented in Figure 8.5. An elastic (factored) capacity line at the assumed period T = 1.5sec is also shown. From the figure, it is clear that in order to remain elastic during

an OLE event, the structure must have more than 7 inches of unfactored elastic deformation capacity. Because the critical deformation, calculated from Equation 3.4, is approximately 5.6in and less than the 7in OLE demand, derailment is likely to occur under the OLE event. Also shown in Figure 8.5 is a proposed design target capacity curve, assuming reasonable targets of mean overstrength, ultimate ductility, and column yield moment of 1.3, 3.5, and 400,000 kip-in respectively. This target achieves the performance objectives with factored demand and capacity.

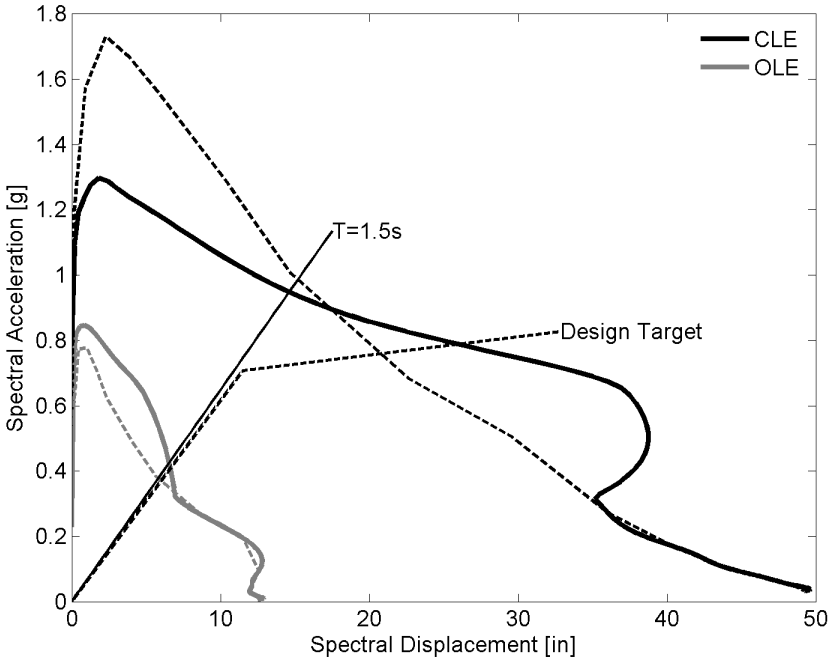

Figure 8.5. Design demand spectra and initial design target capacity spectra achieving performance objectives under POLA design level earthquakes, accounting for uplift.

With the design target in mind, an initial section design is determined to achieve the assumed yield moment, overstrength, and ductility. First, a built-up hollow box section 118.11in (3000 mm) deep and 59.06in (1500 mm) wide is chosen in order to provide the necessary moment capacity, built using ASTM A709 steel with an expected yield stress

of 57ksi. To keep weight down, the thickness of flange plate is chosen as 0.787in (15mm), and the web plate is sized at 0.5in thick. Then, according to Equation 2.3, longitudinal stiffeners are required to maintain a suggested subpanel width-to-thickness ratio: 3 on the flange and 7 on the web. The column is separated into nine "stub-columns" with the use of lateral "diaphragm" stiffeners, and the longitudinal stiffeners are sized as 5.9in long and 0.59in thick in order to satisfy the γ-ratio requirements graphically depicted in Figure 2.5. Additionally, an axial load ratio of 15% of the squash load is assumed. The resulting calculated slenderness parameters, defined and described in Chapters 2 and 4, are summarized in Table 8.2, as well as the resulting overstrength and ultimate ductility. Because the overstrength, ductility, and yield moment all exceed the target values, the section is acceptable to meet the performance objectives for the preliminary design. From the γ-ratios and Figure 2.5, the design is in a valid range, and overall wall buckling is expected to be the dominating mode of strength and stiffness degradation after the point of ultimate ductility.

Table 8.2. Calculated slenderness parameters, overstrength, ductility, and yield moment for column.

R_f	λ	λ_s	λ_s'	γ/γ_{req}	γ/γ^*	t/t_0	H_{max}/H_y	δ_u/δ_y	M_y
0.43	0.32	0.51	0.51	1.30	0.77	1.28	1.36	4.06	433160 kip-in

Notice that the slenderness is much lower than the columns of J100, although the amount of steel is not significantly more. The largest difference is the addition of one longitudinal stiffener, and shorter stub-columns resulting from an additional lateral stiffener. This highlights the fact that, for seismic design, detailing can have a large impact on expected seismic performance.

Following this basic preliminary seismic design, the rest of the structure can then be designed accordingly. After a more complete, detailed design is performed (presumably to satisfy operational loads), a true pushover analysis should be performed in order to check that the resulting lateral capacity is sufficient. Further, the fundamental period should be verified as less than or equal to 1.5sec. In general, all the assumptions used to perform this preliminary design should be checked, and design iterations should be performed when assumptions are violated until convergence occurs.

8.5 Existing Crane – Conceptual Retrofit Example

Consider a moderately-sized port in a seismic zone that is heavily reliant on LD100 container cranes for daily operations. The port stakeholders have recognized their potential vulnerability from poor expected seismic performance of these cranes, and have requested an inexpensive retrofit to bring the performance as close to the deformation objectives laid out in Sections 6.2 and 6.3. Portal clearance should not be affected, either in height or nominal clear distance between the legs. In order to improve operational efficiency, it is acceptable to stiffen the structure and thus decrease the portal sway period.

Recall that LD100 has a portal height equal to 47.7ft, gage length of 100ft, and a global stability factor α = 0.7. The steel sections are built using A36 steel with an expected yield stress of 42ksi. Section dimensions are provided in Appendix A, and the calculated slenderness parameters, overstrength, and ductility are calculated and shown in Table 8.3. The approximate capacity curve for this original section is graphically compared to the demand curves in Figure 8.6, and found to be deficient in terms of both performance

objectives. A target capacity is also defined and plotted, which assumes a period shift to T = 1.5s, overstrength of 1.35, a ductility of 5, and an increase in yield moment to 80,000 kip-in. Then, additions to the section are made one at a time, iterating towards an acceptable section. For ease-of-construction and access, only section modifications which can be done externally are proposed.

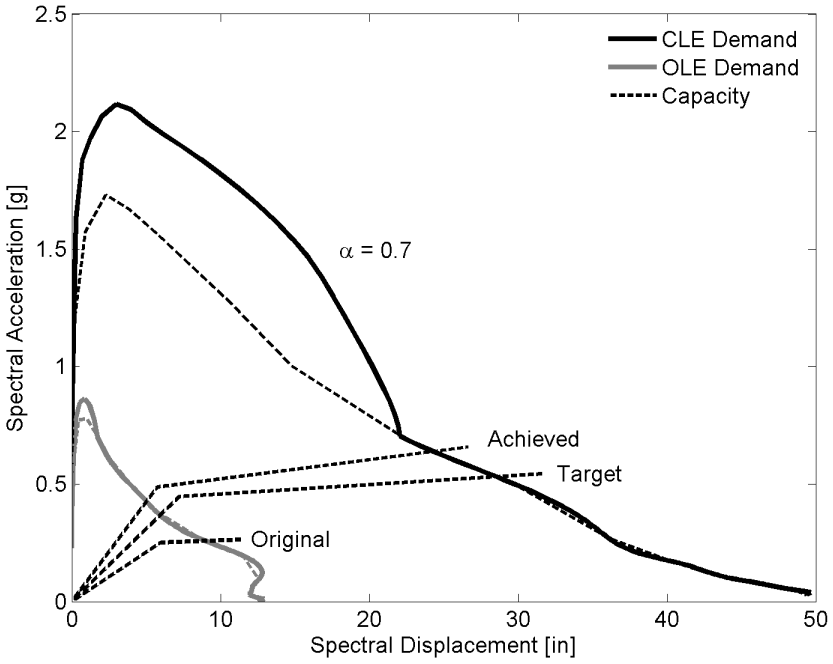

Figure 8.6. Design demand spectra of POLA design level earthquakes accounting for uplift, and the original, target, and achieved estimates of capacity spectra for retrofit concept.

Because the target strength increase is quite significant, it is addressed first. Section A assumes that additional 0.375in plates are welded to the outer faces of the flanges, effectively doubling the flange thicknesses. As can be seen in Table 8.3, this reduces causes the existing stiffeners to be insufficient to prevent overall section buckling prior to yield, and the width-thickness ratio of the subpanels are still too large. Thus, structural section B includes 3 longitudinal stiffeners 5in deep and 0.75in thick added, evenly

spaced, to the external face of the flanges of section A. While these stiffeners provide sufficient stiffness to the subpanels, the resulting ductility still falls short of the target. For section C, these stiffeners are replaced with 8in deep, 0.75in thick stiffeners. This modification leads to a section that meets and exceeds all of the target values, and should degrade through overall wall buckling after the point of ultimate ductility.

Table 8.3. Calculated slenderness parameters, overstrength, ductility, and yield moment for original column section and design iterations toward target values.

Section	R_f	λ	λ_s	λ_s'	γ/γ_{req}	γ/γ^*	t/t_0	H_{max}/H_y	δ_u/δ_y	M_y [kip-in]
Original	1.25	0.55	1.10	0.99	3.39	3.39	0.44	1.18	2.55	44872
A	0.62	0.51	1.06	0.95	0.48	0.48	0.88	1.24	2.82	69851
B	0.31	0.52	0.61	0.55	1.00	0.28	1.77	1.40	4.08	81725
C	0.31	0.53	0.36	0.33	3.39	0.96	1.77	1.49	5.26	87249

By making the modifications to create section C, the portal leg stiffness increases as well. The effect of that on portal sway period should be checked and compared with the initial assumption of reaching 1.5sec. It is found that the modifications increase the section moment of inertia by a factor of 2.09. In addition, the added steel increases the total weight of the crane by 2%. Thus, the shift in portal sway period can be approximated by a factor $\sqrt{(1.02/2.09)}=0.70$. The resulting portal sway period is estimated as 1.28sec, significantly lower than the assumed 1.5sec, so it may be expected that a higher seismic demand is necessary. The estimated seismic capacity curve achieved by using section C for the portal legs is plotted Figure 8.6. Despite the shift in period, the achieved capacity is sufficient to reliably meet the performance objectives for the two design level earthquakes.

As with the previous example, the above design is a preliminary, conceptual design only. Following a more detailed design, including sizing the rest of the structure (notably, the

portal beam) to compatible strength and ductility levels, a more accurate capacity curve can be developed which may dictate minor changes to the portal leg design. Further, detailing of connections, welds, transitions, etc. must still be performed. Still, this example demonstrates several important points. First, a container crane can be retrofitted to meet modern performance objectives without extensive reconstruction. Rather, retrofits can be designed which, once completed, do not hinder operations. Even to drastically improve expected seismic performance, the additional steel represents only a small fraction of overall crane weight, and is thus not likely to overload the crane rails and wharf below. While extensive and reasonably costly on-site welding may be necessary, the retrofits represent significant value as they will greatly reduce expected downtime in the event of an earthquake.

8.6 Summary

Performance-based design is already part of the seismic design guidelines for many of the largest US container ports in terms of wharf and pier response. However, similar performance should be required from the container cranes in order to achieve overall port performance consistent with written objectives. A deformation-based approach is recommended for container cranes, as the critical seismic response can be quantified in terms of first-mode portal deformation. In order to produce reliable designs, capacity and demand design factors of 0.7 and 1.5, respectively, are proposed given the randomness and uncertainty in predicting response behavior.

The capacity spectrum method provides an efficient way to directly compare factored capacity and demand in order to reliably achieve performance objectives given design-level earthquakes. This direct comparison provides an intuitive relationship between demand and capacity which designers are likely to appreciate if specific demand and capacity spectra can be determined in a simple and straightforward manner. In this context, the traditional elastic demand spectra can be easily modified to account for uplift response using portal uplift theory. The capacity spectra can be approximated by simple section slenderness analysis of the portal legs and the general configuration and dynamics of the container crane under consideration. This approach can be applied both for new design and for conceptual retrofit of existing cranes. It is shown that seismic performance can be greatly improved with only a small sacrifice in weight and material, and that a successful retrofit can be envisioned which does not require large-scale reconstruction efforts.

CHAPTER 9

SUMMARY, CONCLUSIONS, AND IMPACT

9.1 Summary and Conclusions

Container cranes represent a vital component of container ports worldwide, which in turn play a critical role in local, regional, and national economies by acting as gateways for international trade. Unfortunately, the largest of US seaports such as Los Angeles, Long Beach, Seattle, Oakland, Charleston, and Savannah are at risk to significant seismic activity. It is well known that earthquake damage at a port has the potential to cause major business interruption losses due to the downtime associated with repairs. The case of the Port of Kobe following the earthquake in 1995 is a poignant example of the lasting impact that port seismic damage can have. While significant efforts have gone into improving the behavior of wharves and piers to seismic loads, the seismic response of container cranes has gone largely ignored. This is especially surprising given the fact that replacement in the event of crane collapse could take a year or more. However, port stakeholders are beginning to understand the importance that cranes have to continued daily operations, and are starting to question their expected seismic performance.

The main objective of this work was to develop a robust understanding of the seismic performance of container cranes and use that knowledge to develop fragility curves for three representative cranes. This work is critical and timely as the physical size of new container cranes has grown rapidly in recent years, paralleling the growth of container ships, and they have been built without a mature and complete understanding of their

seismic behavior. In this work, two areas of key importance to understanding the seismic behavior of container cranes were identified. First, the effect of allowing container cranes to uplift, a phenomenon that has not been well understood. Second, the expected ductility and cyclic response of a crane's critical components, another issue in which substantial unknowns remain unexplored.

Since the 1960's, it was assumed that by allowing container cranes to uplift during seismic excitation, a "safety valve" was being provided which limited the transfer of seismic energy to the crane as that which causes uplift. However, this assumption ignores the fact that during uplift, the effective stiffness of the structure decreases. In this work, the effect of uplift on structural response was reconsidered from a theoretical perspective, solving the equations of motion for the basic case of an uplifting portal frame during each of three identified stages: elastic, sliding, and tipping. It was shown that, rather than the assumed situation of "isolation" from uplift, an uplifting portal frame can actually exhibit increased structural demands due to uplift. This effect is amplified for more stable structures. Thus, older smaller cranes are affected to a lesser extent, explaining why they have historically performed reasonably well during small-to-moderate earthquakes. However, today's modern jumbo cranes can be significantly more stable and thus be subject to significantly higher seismic demands than would be predicted by the classic design assumption. This new treatment of uplift where the effective shear stiffness is reduced was termed "portal uplift theory," and verified using finite element and experimental models with complex boundary conditions which allow for derailment during uplift events.

To be able to capture the identified uplift behavior using finite element models, frictional contact elements were adapted for use as structural boundary elements and specific analysis methodologies were developed. This approach was applied to 3D finite element models of representative container cranes, as well as various modeling simplifications including 2D and simple portal frame representations. The results of a 1:20 scaled elastic shake table experiment of a jumbo container crane were used to verify and validate the response predicted by the finite element models and by portal uplift theory. From the coupled experimental/analytical analysis of this jumbo crane, several conclusions were made in regards to the seismic response of container cranes, including the following:

- In general, the structural deformation at the level of the portal beam is the critical container crane response under seismic loads, regardless of the excitation components included.
- An uplift threshold determined from a simple static analysis is capable of predicting the onset of derailment, equally reflected by experimental and analytical observations.
- The long-period torsion response typical of container cranes generally does not significantly contribute to the critical portal deformation, and can be neglected for general seismic analysis.

Based on these conclusions, the 2D finite element model was found to be sufficient for evaluating the seismic performance of typical container cranes. For many purposes, the simple frame was determined to be as satisfactory.

Finite element models were developed for three representative container cranes using the verified methodology from the scaled experiment: a modern jumbo crane (J100), a heritage jumbo crane (LD100), and a heritage compact crane (LD50). Nonlinear rotational springs were placed in the portal joints representing the inelastic behavior. The skeleton curve and hysteresis rules for these springs were based on experimental and shell-element model analysis of similarly-constructed Japanese steel bridge piers found in the literature. From defined slenderness parameters, the overstrength, ductility, damage accumulation, and envelope degradation were estimated for each structural element. Then, limit states were defined based on repair models from industry experience: derailment, immediate use, structural damage, and complete collapse. Expressed in terms of portal drift, the limit states were quantified from modified pushover analyses. It was found that in general, because they were designed only to resist local buckling until reaching the initial yield point, the portal elements of the three representative container cranes are extremely slender, and are not expected to exhibit significant ductility. Rather, they are expected to exhibit rapid strength and stiffness degradation due to local buckling, with only marginal overstrength. This highlights the need to probabilistically evaluate the expected seismic performance of each representative container crane.

A sensitivity study was conducted in order to identify the sources of uncertainty which most affect the response of a container crane. It was found that the ground motions dominate the randomness with respect to seismic demand. Thus, seismic demand models were defined based on models using mean estimates of all structural parameters subjected to a suite of ground motion, so that dispersion from the mean demand was a result of

randomness in ground motion. It was found that the closed-form estimate of seismic demand predicted by portal uplift theory provided an accurate representation, and is therefore used as the default method for estimating seismic demand throughout this work. Using probabilistic methods and assuming a lognormal distribution for capacity and demand, fragility curves were developed for each identified limit state for each representative container crane. The randomness in demand with respect to ground motions was included, as was randomness in capacity and epistemic uncertainty encompassing modeling errors, skewed assumptions, etc. These fragility curves were used to define point estimates of limit state exceedance probability for example design-level earthquakes, and were compared with those presented by HAZUS. In addition, estimates for the expected value of downtime and its associated standard deviation were presented, conditioned on earthquake intensity. Several conclusions can be drawn from the fragility curves, damage level probabilities, and downtime estimates, including:

- LD50 cranes can derail fairly easily, but that does not completely "save" them from structural damage at higher earthquake levels. Although they performed well during Loma Prieta, an earthquake of higher intensity is likely to cause fairly significant damage. That said, they are nearing the end of their functional life at modern ports, and are unlikely to be the recipient of any retrofit attention.
- LD100 cranes exhibit relatively high overall stability, but low capacity. Thus, they can completely collapse prior to reaching the uplift threshold. At many ports, these are still the "workhorse" cranes, and may therefore be the focus of retrofit efforts. Fortunately, a conceptual retrofit strategy was demonstrated as feasible,

and which could achieve performance objectives consistent with port seismic guidelines for wharf construction.

- J100 cranes were the least vulnerable crane type, despite being perceived as the most worrisome by some port stakeholders. That said, they do not reliably meet performance objectives consistent with wharf criterion due to increased demands due to the uplift response.
- Damage state probabilities based on HAZUS fragility curves in general over-predict probability of damage under an operating level earthquake, but significantly under-estimate the probability of collapse for LD100 and LD50 under a contingency-level earthquake. Because different cranes can respond very differently under the same earthquake, fragility curves for different crane classes should be used for port risk models, such as those developed in this work.
- For each crane, the downtime estimate was dominated by the collapse limit state due to the disproportionately high downtime associated with replacement. Further, until the mean response is collapse, the standard deviation of downtime is larger than the mean. This observation strengthens the argument that for economic reasons, collapse prevention should be the primary performance objective.

Based on the risk of damage and/or collapse of each container crane considered, performance-based design concepts are advocated which are consistent with wharf performance objectives. A deformation-based approach evaluating the critical portal deformation is proposed, and design factors are recommended to ensure sufficient reliability. To promote implementation, a basic application of the intuitive capacity

spectrum method is described, using portal uplift theory to define the demand spectrum and defining the capacity spectrum based on ductility and overstrength analysis of the portal legs. Using this approach, crane designers can easily perform the preliminary seismic design of a new container crane or quickly evaluate the performance of an existing crane and propose cost-effective retrofit concepts to achieve desired performance.

9.2 Impact

This work represents a detailed approach to evaluating the seismic behavior of typical and representative container cranes allowed to uplift, both from the perspective of demand and capacity. It defines a new state-of-the-art for evaluating the seismic performance of container cranes, and provides the guidance necessary to develop safer, more robust container cranes for ports worldwide. One primary contribution of the work is the pioneering development of methodologies to model the true effect that portal uplift has on seismic demand, either using closed-form estimation techniques or finite element models incorporating frictional contact elements. Additional benefits of the research and contributions include the following:

- The current understanding regarding the seismic performance of container cranes has been largely based on an idea about uplift "isolation" that is not completely applicable to the typical modern container crane. This study reconsiders that basic assumption and provides the first systematic and comprehensive assessment of seismic performance evaluation of modern jumbo container cranes.
- While specifically applied to container cranes, the developed portal uplift theory can be applied by researchers or practitioners more generally to any structure

which exhibits reduced shear stiffness due to loss of horizontal constraint during uplift, such as when an anchor system fails.

- An enhanced understanding of inelastic and hysteretic effects of slender built-up steel stiffened hollow box sections allows ductility estimates for sections previously designed based on elastic strength requirements. The adopted methodology allows for efficient estimation of deformation capacities for existing or new container crane portal frames.
- The development of fragility curves for representative container cranes provides insight to the seismic vulnerability of existing cranes. Port stakeholders can use the developed fragility curves, underlying methodologies, uncertainty characterizations, and downtime estimates to evaluate the risk to their own cranes, and make decisions regarding potential retrofit or replacement to cost-effectively reduce their seismic risk. The definition of limit states related to repair models provides transparency to the decision-maker about the economic consequences associated with each damage level.
- Using the capacity spectrum method as described in this work, practitioners can effectively achieve performance objectives parallel to those recommended for the underlying wharf structure and thus reduce overall risk of downtime to that expected by port stakeholders. By using the developed capacity and demand design factors, practitioners can confidently provide designs with known reliability of achieving the targeted performance objectives.

9.3 Future Research

The insights and framework provided by this work suggests several avenues to extend and refine the research and resulting conclusions, including the following:

- The methodologies developed and adopted here were specifically applied to typical A-frame container cranes. Future studies could evaluate their relevance for the seismic performance evaluation of less typical container crane types, such as low-profile and elevating-girder container cranes.
- With the discovery that uplift may increase seismic demand, retrofitting of wharves may be pursued to provide capacity for the tensile loads required to use tie-downs. Or, in regions such as Charleston, which are at risk to both hurricanes and earthquakes, tie-downs may be in use in the event of an earthquake. Thus, an understanding of the seismic performance of tie-downs could be pursued.
- Due to the number of cranes in use worldwide now understood to be at risk to seismic damage, it is expected that this research will lead to a significant demand for cost-effective retrofit solutions. An innovative approach to significantly reduce seismic demand or increase capacity could have a large market.
- This work assumed that the input acceleration spectra to the base of the crane were known. Coupled crane/wharf/soil analyses could provide perspective regarding the holistic port system seismic risk.
- Given the perpetual quest for efficiency in container handling, there is a large potential for a brand new type of container crane configuration exhibiting operational efficiency and seismic resistance to have market success.

APPENDIX A

TERMINOLOGY AND REPRESENTATIVE CRANES

A.1 Introduction

In general, most container cranes are constructed in a very similar fashion, and in very similar configurations (with the exception of low-profile cranes, which are vastly outnumbered by the more traditional A-frame type [8]). In many contexts, any given A-frame container crane will respond very similarly to any other of a similar operational classification. Thus, it is prudent to consider the seismic behavior of several representative cranes in depth, which can then serve as the models for the analysis and evaluation of other, similar cranes.

This appendix serves as a reference for the chapters preceding. First, a brief introduction to typical container crane terminology is presented. Second, operational classifications are defined, and the distribution of existing container cranes at real ports amongst these classifications is discussed. Finally, a general description of several representative container cranes is presented, which are used significantly throughout the preceding chapters, especially for probabilistic seismic performance assessment.

A.2 Background

Many readers may not be familiar with container cranes, so a very brief introduction is presented here. Port container cranes are positioned at the waterline of every container terminal worldwide. They are the sole means for ship-to-shore (STS) operations (loading

and unloading) of international container trade. Cranes are positioned with their boom perpendicular to the berth docking line, and can travel parallel to the waterline (gantry). Most often, several cranes service any given docked container ship. The operator sits in the crane's trolley, and controls the spreader which they raise and lower to move containers in a parabolic motion from a docked ship to the wharf. From there, containers are loaded on waiting trucks and/or trains for intermodal transport or are moved to storage. A typical large container crane, pictured as a pair unloading a large ship, is presented in Figure A.1.

Figure A.1. Typical container crane, photo courtesy of Dr. Eduardo Miranda.

A.2.1 Terminology

Certain terminology is helpful for the descriptions, discussion, and analysis pertaining to container cranes in this study. Typical referenced dimensions are labeled in Figure A.2, and defined in Table A.1. Likewise, key structural and nonstructural elements are labeled and defined similarly. The terms presented, while depicted specifically for one crane, are generic terms that can be used with the majority of container cranes.

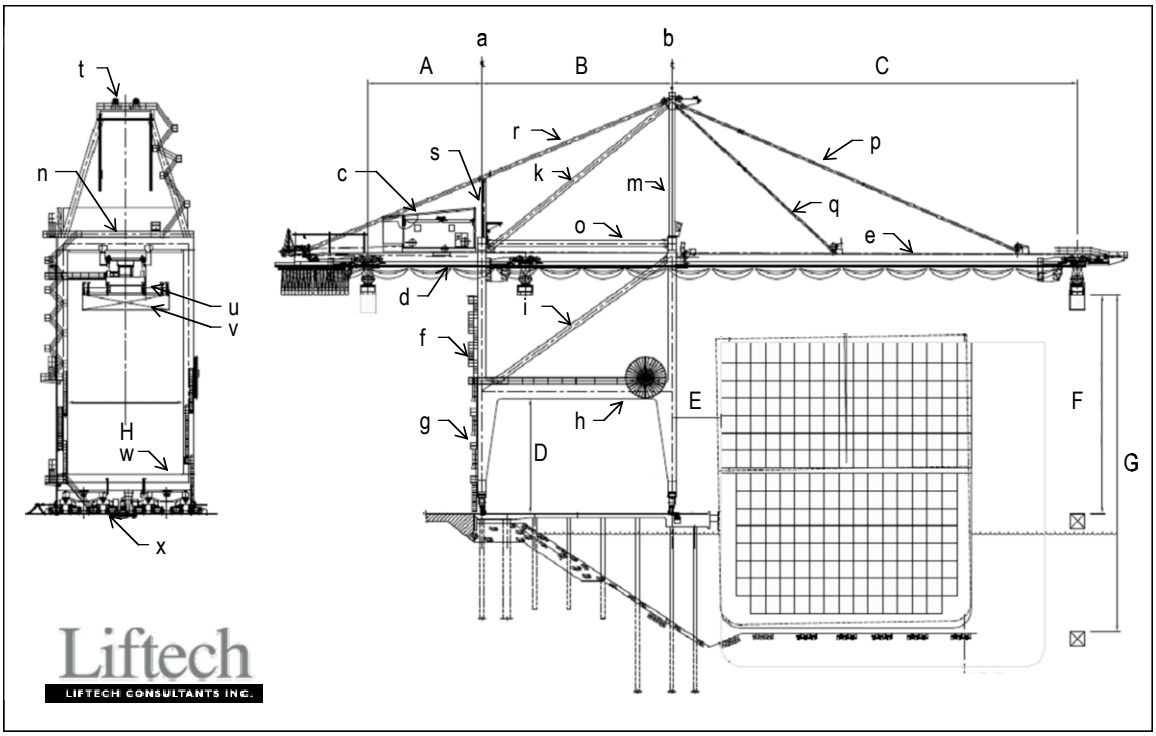

Figure A.2. Container crane dimensions (capital letters) and elements (lowercase letters) labels. Labels are defined in Table A.1 (base figure courtesy Liftech, Inc.)

Table A.1. Terminology of labeled dimensions and elements of Figure A.1

Dimension		Element	
A	Backreach	a	Landside (LS) Rail
B	Gage	b	Waterside (WS) Rail
C	Outreach	c	Machinery House
D	Portal Clearance	d	Trolley Girder
E	Setback	e	Boom
F	Clear Under Spreader	f	Upper Leg
G	Total Lift Height	g	Lower Leg
H	Clearance Between Legs	h	Portal Beam
		i	Lower Diagonal
		k	Upper Diagonal
		m	A-Frame
		n	Trolley Girder Support Beam (TGSB)
		o	TGSB Tie
		p	Outer Forestay
		q	Inner Forestay
		r	Backstay
		s	Backstay Strut
		t	Top Beam
		u	Spreader
		v	Container
		w	Sill Beam
		x	Balance Beam/Truck System

A.2.2 Operational Classifications

Container cranes are operationally characterized by their outreach, which dictates the widest ship which can be accommodated for STS activities. The ships width, or beam, dictates the number of rows of containers on board. Operational designations are defined:

Panamax: The current width of the Panama Canal can accommodate ships as wide as 106', generally holding 12-13 containers wide.

Post-Panamax: Any ship wider than can be accommodated in the Panama Canal is technically classified as Post-Panamax, though in practice this designation generally refers to ships only as wide as 18-20 containers (approximately <185').

Super Post-Panamax: Ships which hold more than 20 containers abeam are termed Super Post-Panamax, but generally hold 21-22 containers across.

Suezmax: Generally 23 containers across, though crossing restrictions in the Suez Canal are actually set by wetted area (Suez Canal Authority) rather than width.

Malaccamax: The Straight of Malacca is a potential bottleneck for future ship growth, and limits ships to 24 containers wide.

There are some conflicting reports of maximum widths for different classes and operational designation, especially where maximum width is a function of draught (wetted area). Therefore, operational designations are characterized for this study in an explicit, quantifiable way, as described in the following section.

A.2.3 Size Distribution

The discussion of crane size distribution is based on an extensive survey of published port capacities as of April 1, 2008 by undergraduate research assistant Lynne Schleiffarth [184]. Surveyed US ports include: Charleston, Long Beach, Los Angeles, New York, New Jersey, Oakland, Savannah, Seattle, Tacoma, and Virginia. International ports include Bremerhaven, Germany; Colombo, Sri Lanka; Dubai, UAE; Keelung, Taiwan; La Havre, France; Laem Chabang, Thailand; Nagoya, Japan; and Tanjung Pelepas, Malaysia. A total of 504 cranes were surveyed, 313 of which were from the US. Because the US list is more complete, it is used for analyzing the distribution, though results do not change if the whole sample is considered.

The surveyed US container cranes are binned corresponding to the approximate width of ship, in terms of containers across. It is assumed that the average outreach a container crane capable of servicing a ship with N containers wide is:

$$4\text{ft} + 9\text{ft}*N \tag{A.1}$$

For example, a 16-container crane might have an average outreach of 148ft.

A histogram describing the distribution of container crane size in the US is presented according to the above operational designation in Figure A.3. Many early *Panamax* and

small *Post-Panamax* cranes still exist, as evidenced by the fairly uniform distribution of cranes for 11-15. A large number of 16-container cranes is apparent, and represent a reaction of port owners/operators to the beginning of ship growth. The next generation of cranes built was of the 18/19-wide variety. Now, 22-wide or slightly larger have shown up in large numbers. Current orders and future purchases will likely be of the 22+ variety, as there are no signs that ship growth has stopped. Still, smaller cranes are valuable to a port, as they can more efficiently service the older, smaller ships which still act as the workhorse of the container shipping industry for much of the world's trading nations.

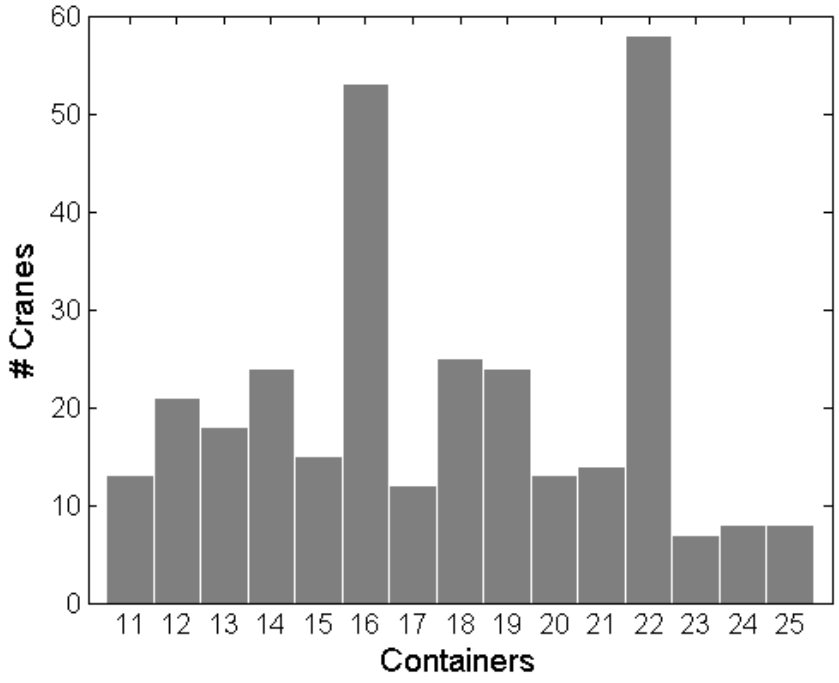

Figure A.3. Histogram of the maximum width (# containers) of surveyed US container cranes.

Operational designations of container cranes are quantified from this histogram and Equation A.1, as outlined in Table A.2.

Table A.2. Operational classification of container cranes.

Designation	*Outreach*	*# Containers Wide*
Panamax & Small Post-Panamax	0 – 135 ft	≤ 14
Large Post-Panamax	135.01 – 185 ft	14 - 20
Super Post-Panamax	185.01 – 200 ft	20 – 22
Suezmax	200.01 - ∞	≥ 22

The smaller cranes were built with either a 50’ or 100’ gage distance, while most modern cranes are have a 100’ gage or somewhere close. Several cranes elsewhere in the world have 150’ gage, but this requires significant modifications or complete redesign of the underlying wharf structure and/or berthing channel, and is therefore not expected to be widespread in the US for years to come.

A graphical representation of the US crane size distribution by operational designation, with distinctions shown for 50’ and 100’ gage cranes, is shown in Figure A.4. It is clear that *Suezmax* cranes are still a relatively small fraction of cranes in use in the US. However, *Large Post-Panamax* (along with the structurally similar *Super Post-Panamax*) category represents the largest portion of cranes in use, are still able to service the majority of ships in use (but not the largest, most modern ships, which may become the typical ship in future years), and are thus very important for sustained port operations in the near-term. The *Panamax & Small Post-Panamax* category represents a significant fraction of cranes used, though they are of lesser importance due to their operational limitations, and likely would be replaced with a significantly larger crane in the event of collapse.

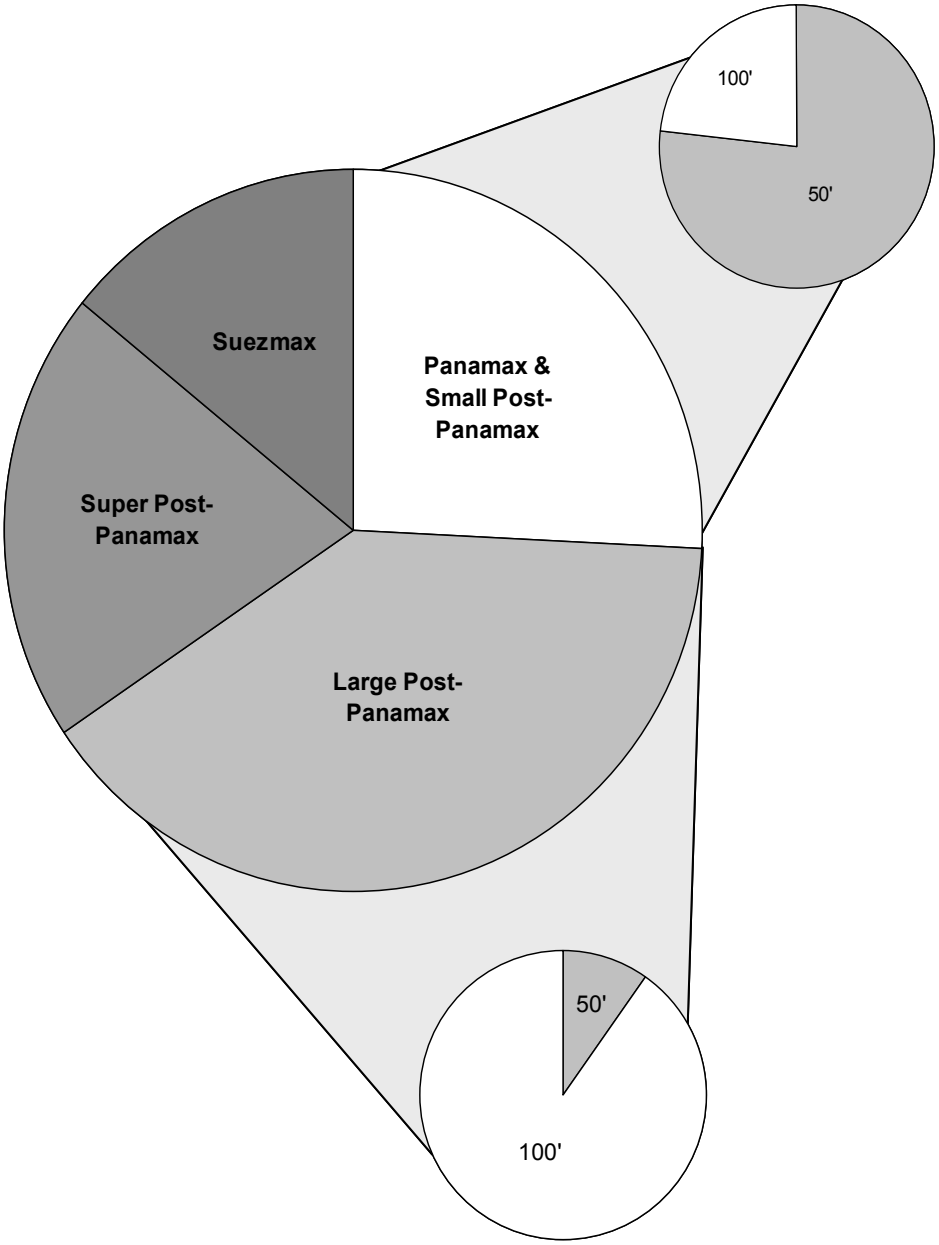

Figure A.4. Graphical representation of US container crane operational size distribution.

A.3 Case Study Container Cranes

Three typical container cranes based on existing cranes are considered in depth, and their characteristics relevant to seismic performance are presented in the following sections. These three container cranes together represent the majority of cranes in use, and span a

range of expected seismic behavior. As a set, they are intended to provide sufficient example information to evaluate any given A-frame crane of typical construction.

Each container crane is built using some combination of the following steel sections: built-up hollow boxes, tubes, and built-up wide-flange shapes. The dimensions of the different shapes are defined in Figure A.5. Built-up hollow box sections have outside dimensions of B and D, with flange and web thicknesses of t_f and t_w respectively, and rectangular stiffeners of length b_s and thickness t_s. Often, the hollow boxes utilize longitudinal stiffeners; thus, n_f (or n_w) indicate the number of longitudinal stiffeners equally spaced along the flange (or web) of a given box section. Round tubes have diameter D and wall thickness t. Built-up wide-flange shapes have flange dimensions B and t_f and web dimensions of D and t_w.

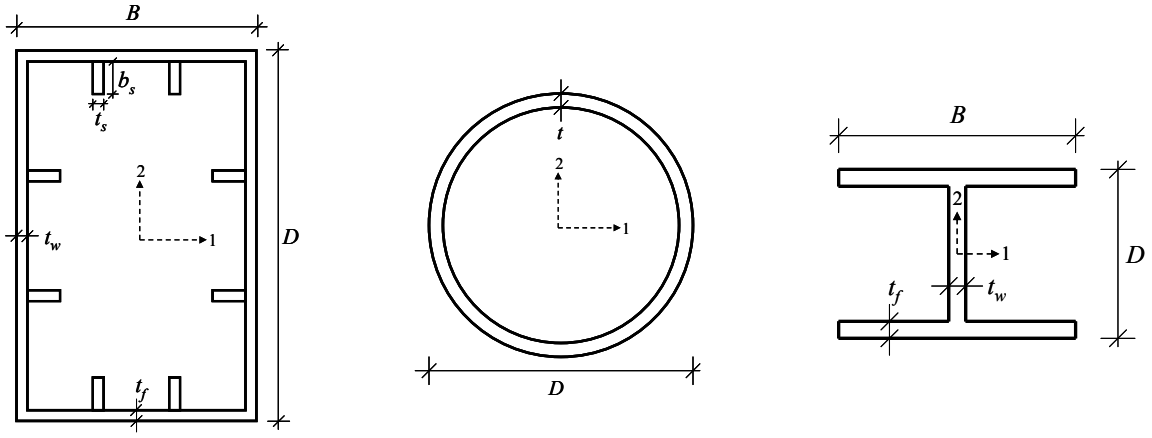

Figure A.5. Cross-sections employed in the case study container cranes and their dimensions.

The mass of a crane is attributed to the mass of structural members and their attachments, as well as major machinery and equipment. The mass of attachments along structural members are accounted for by multiplying the area of each structural element by a dead load factor, defined separately for each member. The appropriate dead load factors for

each member of each crane are defined in the following sections. The mass of major equipment and their locations are indicated graphically, along with the location of the center of mass. Each crane evaluated is assumed to have a damping ratio of 1.5% in the critical portal sway mode, based on industry experience [9] and previous research [13, 16, 21].

A.4 Modern Jumbo Crane (J100)

The J100 crane is representative of cranes ranging from large 100' *Large Post-Panamax* up to moderate *Super Post-Panamax* cranes. Typical of large cranes built circa 2000, it could be operationally classified as *Suezmax*, as defined in Section A.2.3, but its main structural frame is believed to be more reflective of cranes with slightly less operational capacity. It is built using ASTM A709 steel.

A.4.1 Geometry

The overall dimensions of the J100 crane are depicted in Figure A.6, as well as the section definitions of the major structural elements. Dimensions for the referenced section definitions are presented in Table A.3 (built-up hollow boxes), Table A.4 (tubes), and Table A.5 (built-up wide-flange shapes).

All portal frame stiffeners are L-shaped, oriented with the long dimension perpendicular to the plate being stiffened. To ease the computation for analysis purposes, these stiffeners are replaced with 7.87x0.394in flat stiffeners, which have an equivalent moment of inertia and radius of gyration as the L-shaped stiffeners that they replace. In

this way, they will contribute towards the overall section slenderness ratios in the same way as the true stiffeners.

Table A.3. Dimensions of J100 built-up hollow box sections.

Section	B [in]	t_f [in]	n_f	D [in]	t_w [in]	n_w
A-A	60.00	0.625	1	90.00	0.375	2
B-B	60.00	0.500	1	90.00	0.328	2
C-C	52.76	1.102	1	80.94	0.709	2
C'-C'	52.76	1.102	1	80.94	0.787	2
D-D	52.76	1.102	1	80.94	0.630	2
D'-D'	52.76	1.102	1	80.94	0.787	2
E-E	52.76	0.472	1	67.87	0.394	2
F-F	52.76	0.787	1	68.50	0.630	2
G-G	111.34	1.024	2	68.19	0.551	2
H-H	52.76	0.630	2	68.19	0.630	2
I-I	111.81	0.787	2	68.50	0.787	2
J-J	52.76	1.417	1	101.26	0.787	2
J'-J'	52.76	1.417	1	101.26	0.945	2
K-K	52.76	0.787	1	100.00	0.551	2
K'-K'	52.76	0.787	1	100.00	0.630	2
L-L	67.56	0.472	2	119.06	0.315	4
M-M	49.61	0.787	1	72.44	0.630	2
N-N	52.76	0.945	2	68.82	0.787	2

Table A.4. Dimensions of J100 tube sections.

Section	D [in]	t [in]
a-a	39.37	0.630
b-b	47.24	0.630
c-c	19.69	0.394
d-d	39.37	0.551

Table A.5. Dimensions of J100 built-up wide-flange sections.

Section	B [in]	t_f [in]	D [in]	t_w [in]
e-e	11.81	0.630	13.07	0.472
f-f	16.54	0.787	15.35	0.630

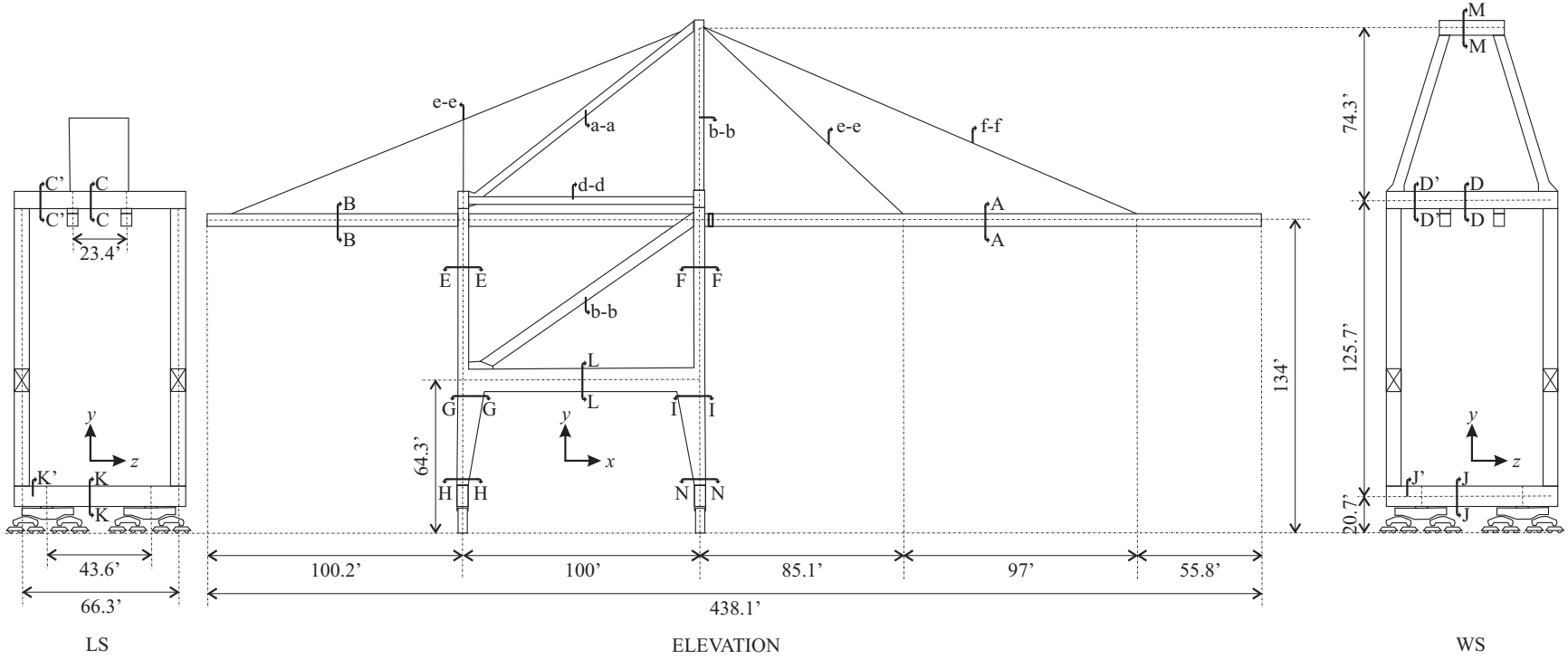

Figure A.6. Overall dimensions and section assignments (defined in Tables A.3-5) of J100 container crane.

A.4.2 Mass

The dead load factors for the J100 crane are defined in Table A.6, which accounts for the distributed nonstructural mass attached to each member. Table A.7 describes a summary of the overall weight, including the major equipment and machinery. Locations of the major equipment are identified in Figure A.7, as is the center of mass.

Table A.6. Dead load factors for J100 structural members.

Member	*Factor*
Legs	1.30
Sill	2.00
Portal Beam	1.30
Landside TGSB	1.76
Waterside TGSB	2.00
Pipes	1.00
Top Beam	4.50
Boom	1.65
Trolley Girder	2.00
Forestays	1.00
Boom Ties	1.30

Table A.7. Weight summary for J100, including major equipment.

Item		*Weight* [kip]
	Structural Frame	2039.1
1	Stairs 1	10.7
2	Stairs 2	40.0
3	Stairs 3	19.0
4	Trucks (x4)	62.7
5	Machinery House (MH) (x2)	174.2
6	Service Crane	3.9
7	½ Festoon	8.8
8	Snag Device	30.9
9	Boom Hoist Rope	17.0
10	Trim & List	4.4
	TOTAL	**2773**

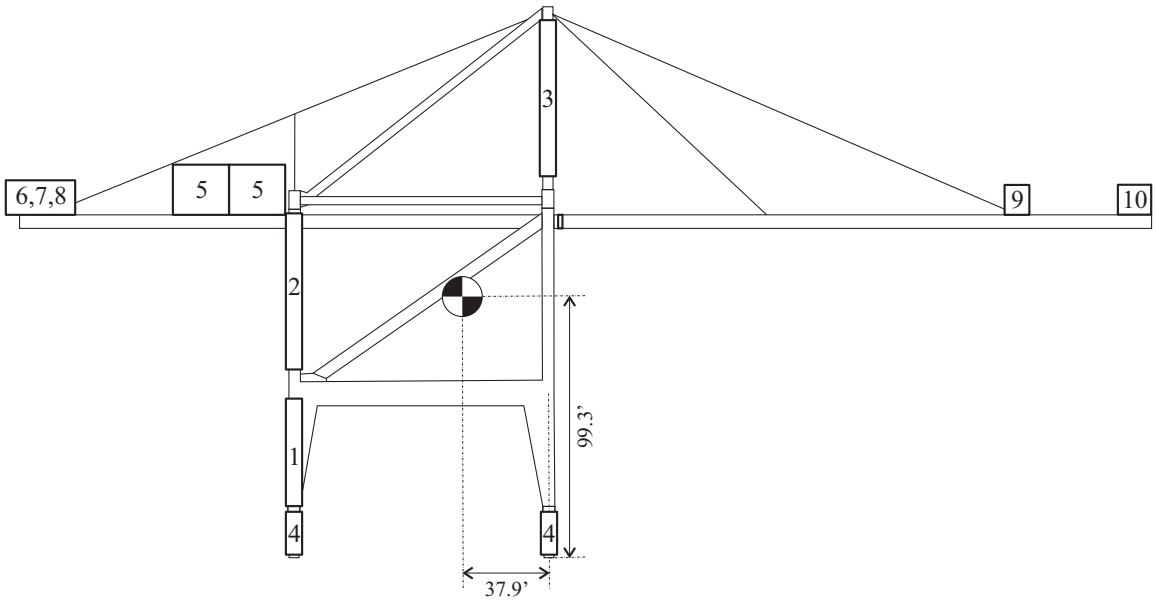

Figure A.7. Location of center of mass and major equipment of J100.

A.5 Heritage Jumbo Crane (LD100)

The LD100 crane is representative of a small 100' *Large Post-Panamax* or *Small Post-Panamax*, circa 1980. While this specific crane would typically be operationally designated as a *Panamax* crane, similar cranes have been retrofitted with longer booms to service larger ships without modifications to the structural frames. It is built using ASTM A36 steel.

A.5.1 Geometry

The overall dimensions of the LD100 crane are depicted in Figure A.8, as well as the section definitions of the major structural elements. Dimensions for the referenced section definitions are presented in Table A.8 (built-up hollow boxes) and Table A.9. All stiffeners are constructed using flat plates; the stiffeners in the portal beam and sill beams are 0.6125x4in, and the leg stiffeners are 0.375x5in.

Table A.8. Dimensions of LD100 built-up hollow box sections.

Section	B [in]	t_f [in]	n_f	D [in]	t_w [in]	n_w
A-A	47.50	0.500	1	47.50	0.438	2
B-B	47.50	0.500	1	47.50	0.438	2
C-C	47.50	0.500	1	71.50	0.375	2
C'-C'	47.50	0.500	1	71.50	0.375	2
D-D	47.50	0.625	1	71.50	0.375	2
D'-D'	47.50	0.500	1	71.50	0.375	2
E-E	47.50	0.375	1	47.50	0.500	1
F-F	47.50	0.375	1	47.50	0.500	1
G-G	47.50	0.375	1	47.50	0.375	1
H-H	47.50	0.375	1	47.50	0.500	1
I-I	47.50	0.375	1	47.50	0.375	1
J-J	47.50	0.500	1	59.50	0.375	2
K-K	47.19	0.313	1	46.25	0.300	1
L-L	47.50	0.375	1	47.50	0.313	1
M-M	47.50	0.375	1	47.50	0.313	1
N-N	47.50	0.375	1	47.50	0.625	1

Table A.9. Dimensions of LD100 tubes.

Section	D [in]	t [in]
a-a	24.00	0.375
b-b	30.00	0.313
c-c	18.00	0.250

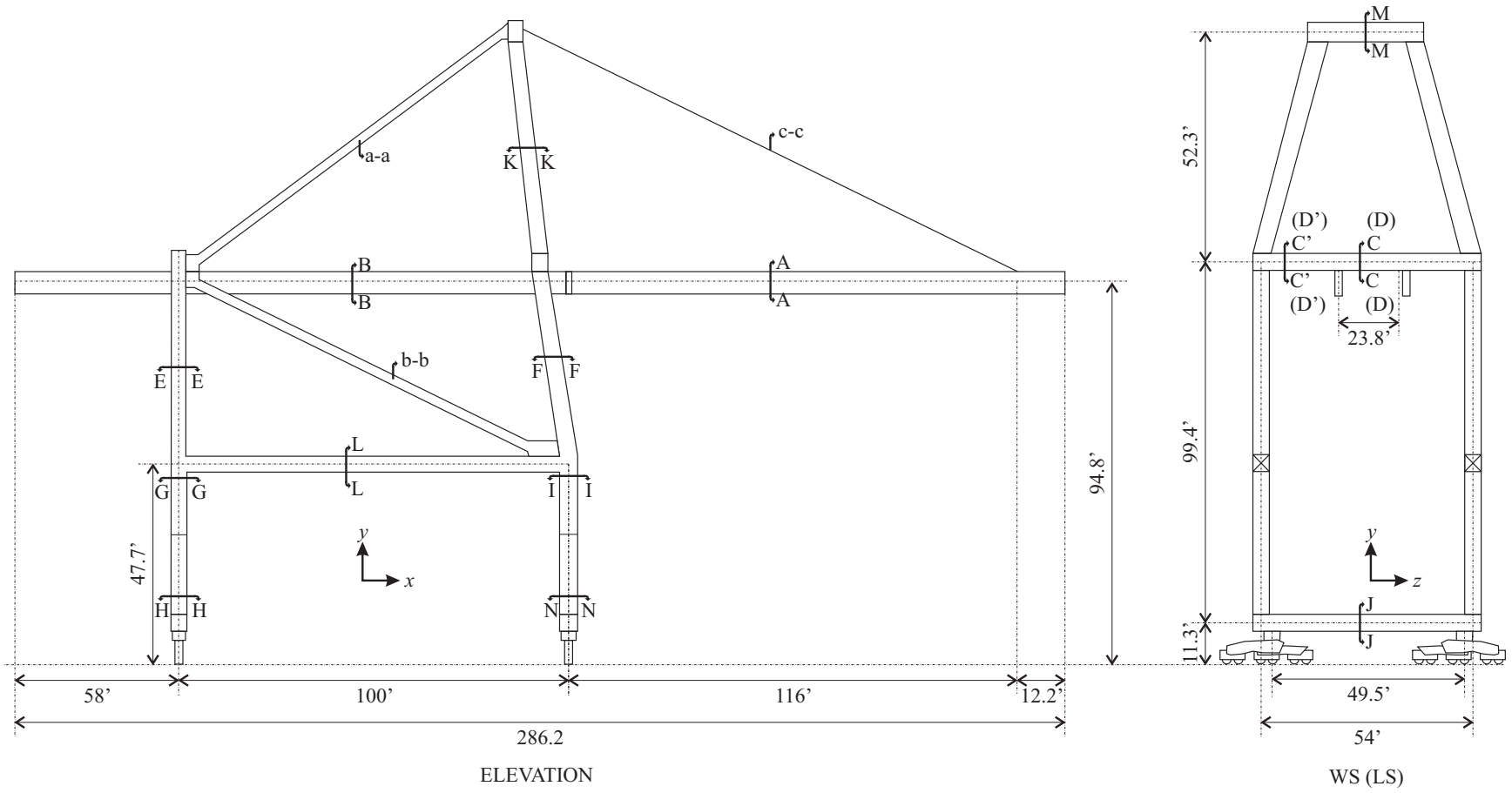

Figure A.8. Overall dimensions and section assignments (defined in Tables A.8-9) of LD100 container crane.

A.5.2 Mass

The dead load factors for the LD100 crane are defined in Table A.10, which accounts for the distributed nonstructural mass attached to each member. Table A.11 describes a summary of the overall weight, including the major equipment and machinery. Locations of the major equipment are identified in Figure A.9, as is the center of mass.

Table A.10. Dead load factors for LD100 structural members.

Member	*Factor*
Legs	1.30
Sill	2.00
Portal Beam	1.30
Landside TGSB	1.75
Waterside TGSB	2.00
Pipes	1.00
Top Beam	5.30
Boom	1.65
Trolley Girder	1.30
Forestay	1.00
Boom Ties	1.30

Table A.11. Weight summary for LD100, including major equipment.

Item		*Weight* [kip]
	Frame	750.4
	Misc. Distr. Structural & Electrical	120
1	Trolley	20
2	Stairs & Ladders	16.4
3	Trucks (x4)	35 (x4)
4	Machinery House (MH) (x2)	103 (x2)
	TOTAL	**1252.8**

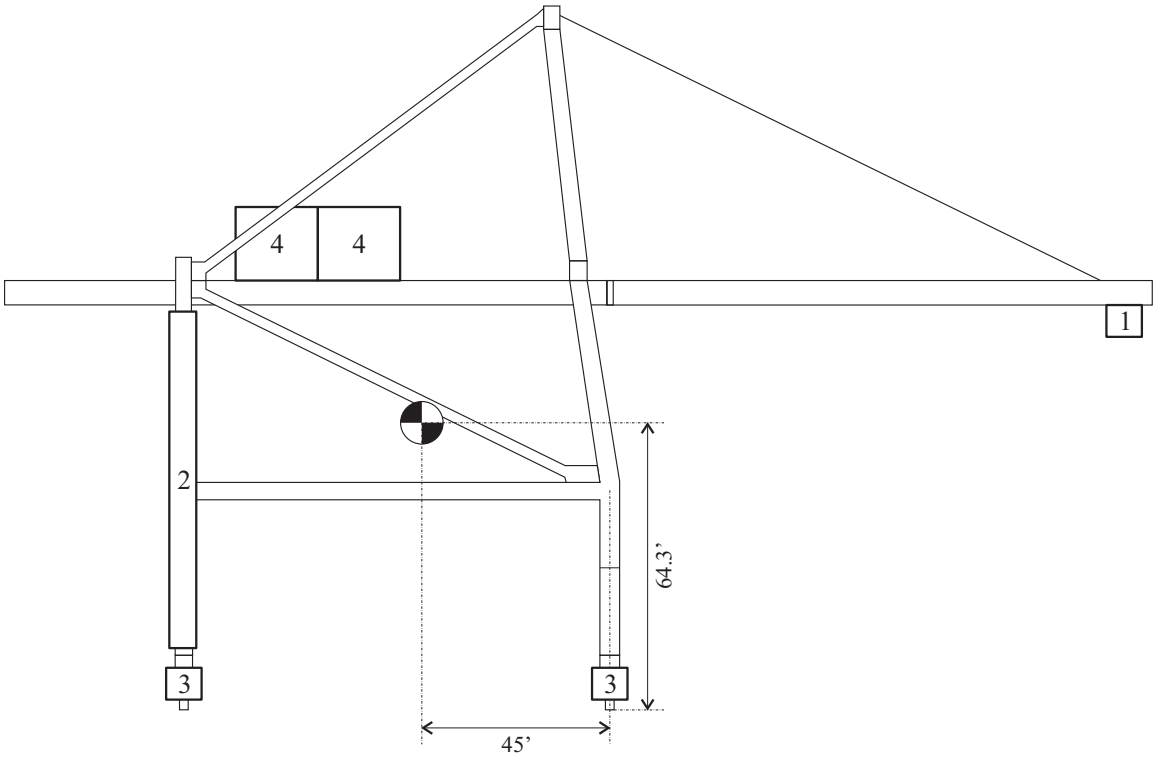

Figure A.9. Location of center of mass and major equipment of LD100.

A.6 Heritage Compact Crane (LD50)

The LD50 is a typical 50' *Small Post-Panamax* crane, circa 1970. While a small crane like this typically would have a truss-type boom, a twin box-section boom with a comparable weight is assumed, but with the same length. It is built using ASTM A36 steel.

A.6.1 Geometry

The overall dimensions of the LD50 crane are depicted in Figure A.10, as well as the section definitions of the major structural elements. Dimensions for the referenced section definitions are presented in Table A.12 (built-up hollow boxes) and Table A.13. All stiffeners are 0.375x5in flat plates, oriented perpendicular to the stiffened plate.

Table A.12. Dimensions of LD50 built-up hollow box sections.

Section	B [in]	t_f [in]	n_f	D [in]	t_w [in]	n_w
A-A	47.50	0.500	1	47.50	0.438	2
B-B	47.50	0.500	1	47.50	0.438	2
C-C	47.50	0.375	1	71.50	0.375	2
D-D	47.50	0.750	1	71.50	0.500	2
E-E	47.50	0.375	1	47.50	0.375	1
F-F	47.50	0.375	1	47.50	0.375	1
G-G	47.50	0.500	1	47.50	0.375	1
H-H	47.50	0.375	1	47.50	0.500	1
I-I	47.50	0.500	1	47.50	0.375	1
J-J	47.50	0.500	1	47.50	0.375	1
K-K	47.50	0.500	1	47.50	0.375	1
L-L	47.50	0.375	1	47.50	0.375	1
M-M	47.50	0.500	1	47.50	0.500	1
N-N	47.50	0.380	1	47.50	0.500	1
O-O	47.50	0.313	1	47.50	0.313	1

Table A.13. Dimensions of LD50 tubes.

Section	D [in]	t [in]
a-a	24.00	0.375
b-b	30.00	0.313
c-c	18.00	0.250

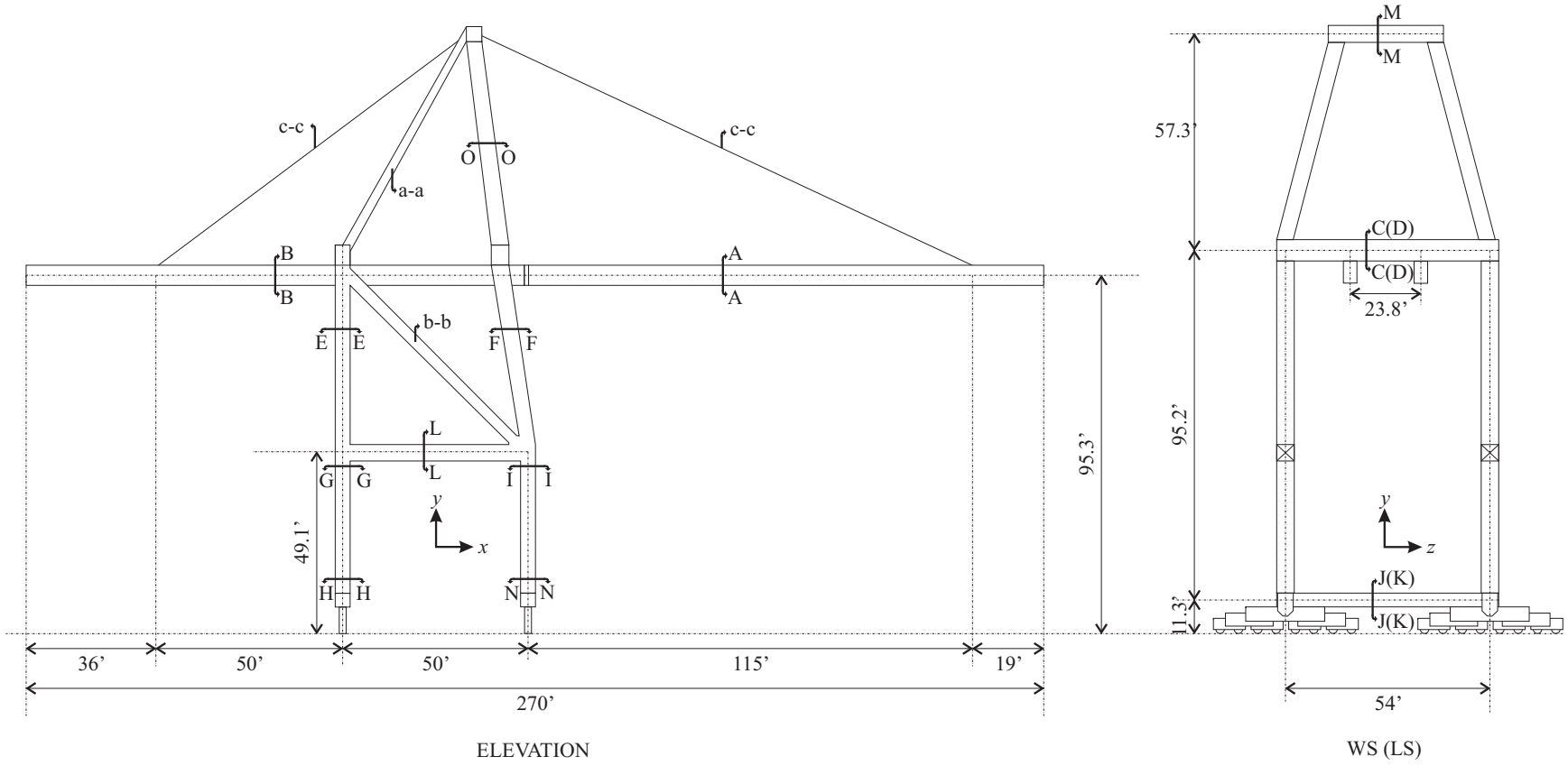

Figure A.10. Overall dimensions and section assignments (defined in Tables A.12-13) of LD50 container crane.

A.6.2 Mass

The specific details regarding the weight of attached machinery is not explicitly known for the LD50 crane. However, it is known that the total weight is 1282.3kip, and that the center of mass is located as per Figure A.11.

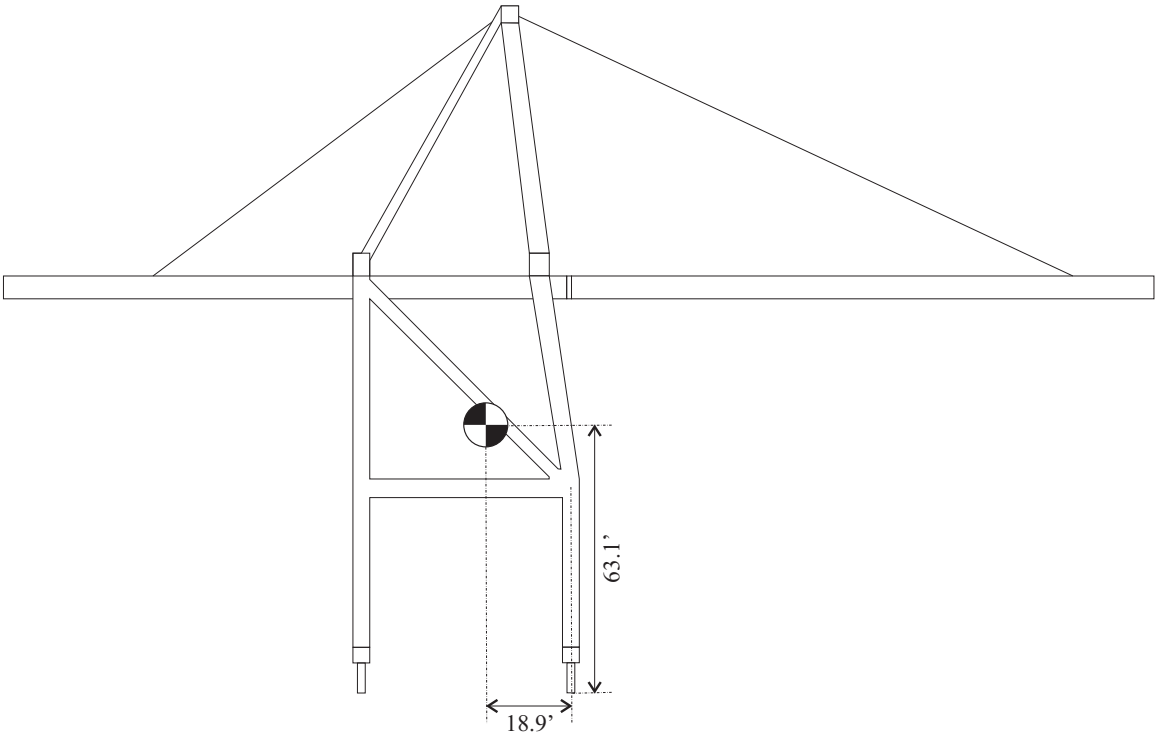

Figure A.11. Location of center of mass of LD50.

A.7 Summary

Container cranes have been built over the years according to the largest foreseeable container ships. Therefore, a large number of cranes with vastly different operational capabilities exist. The distribution of US container cranes according to quantitative operational definitions is explored. While there is a large range of overall size, they can be binned according to four major operational classes.

Fortunately, most (A-frame) container cranes share the same overall structural configuration, but with differing sizes. Three representative container cranes are presented for use in this study which are based on three existing container cranes. These case study cranes together represent the majority of cranes in existence, from small 50' gage *Panamax* to modern 100' gage *Super Post-Panamax* container cranes. In order to analyze their seismic performance, their overall and section dimensions are presented, as well as their mass distributions, specifically highlighting the crucial center of mass.

APPENDIX B

DESCRIPTION OF GROUND MOTIONS USED

B.1 Introduction

The suite of Los Angeles ground motions from the SAC project [173] were used in this study, especially in Chapter 7. For completeness, those ground motions are described briefly in this appendix. Further details regarding their context and development can be found online [185].

B.2 Ground Motion Details

Details regarding the ground motions described in these pages are split into two categories: the ground motions representing a 10% probability of exceedance in 50 years and those representing a 2% probability of exceedance in 50 years for the Los Angeles region. For each category several important features are tabulated for each earthquake (Tables B.1 and B.2): designation, location recorded, magnitude of event, distance from source, scale factor used to reach the desired intensity, recording time-step, duration of record, and peak ground acceleration. Then, the individual response spectra are plotted together along with their mean value (Figures B.1 and B.6). Finally, the time history is plotted for each record, 5 per figure (Figures B.2-5 and B.7-10).

Table B.1. Details of Los Angeles ground motions, 10% probability of exceedance in 50 years.

Name	*Record*	*Mag.*	*Dis.* [km]	*Scale Factor*	*dt* [sec]	*Duration* [sec]	*PGA* [g]
LA01	Imperial Valley, 1940, El Centro	6.9	10	2.01	0.02	40	0.46
LA02	Imperial Valley, 1940, El Centro	6.9	10	2.01	0.02	40	0.68
LA03	Imperial Valley, 1979, Array #05	6.5	4.1	1.01	0.01	40	0.39
LA04	Imperial Valley, 1979, Array #05	6.5	4.1	1.01	0.01	40	0.49
LA05	Imperial Valley, 1979, Array #06	6.5	1.2	0.84	0.01	39	0.30
LA06	Imperial Valley, 1979, Array #06	6.5	1.2	0.84	0.01	39	0.23
LA07	Landers, 1992, Barstow	7.3	36	2.17	0.02	80	0.42
LA08	Landers, 1992, Barstow	7.3	36	2.17	0.02	80	0.43
LA09	Landers, 1992, Yermo	7.3	25	1.79	0.02	80	0.52
LA10	Landers, 1992, Yermo	7.3	25	1.79	0.02	80	0.36
LA11	Loma Prieta, 1989, Gilroy	7	12	1.79	0.02	40	0.67
LA12	Loma Prieta, 1989, Gilroy	7	12	1.79	0.02	40	0.97
LA13	Northridge, 1994, Newhall	6.7	6.7	1.03	0.02	60	0.68
LA14	Northridge, 1994, Newhall	6.7	6.7	1.03	0.02	60	0.66
LA15	Northridge, 1994, Rinaldi RS	6.7	7.5	0.79	0.005	15	0.53
LA16	Northridge, 1994, Rinaldi RS	6.7	7.5	0.79	0.005	15	0.58
LA17	Northridge, 1994, Sylmar	6.7	6.4	0.99	0.02	60	0.57
LA18	Northridge, 1994, Sylmar	6.7	6.4	0.99	0.02	60	0.82
LA19	North Palm Springs, 1986	6	6.7	2.97	0.02	60	1.02
LA20	North Palm Springs, 1986	6	6.7	2.97	0.02	60	0.99

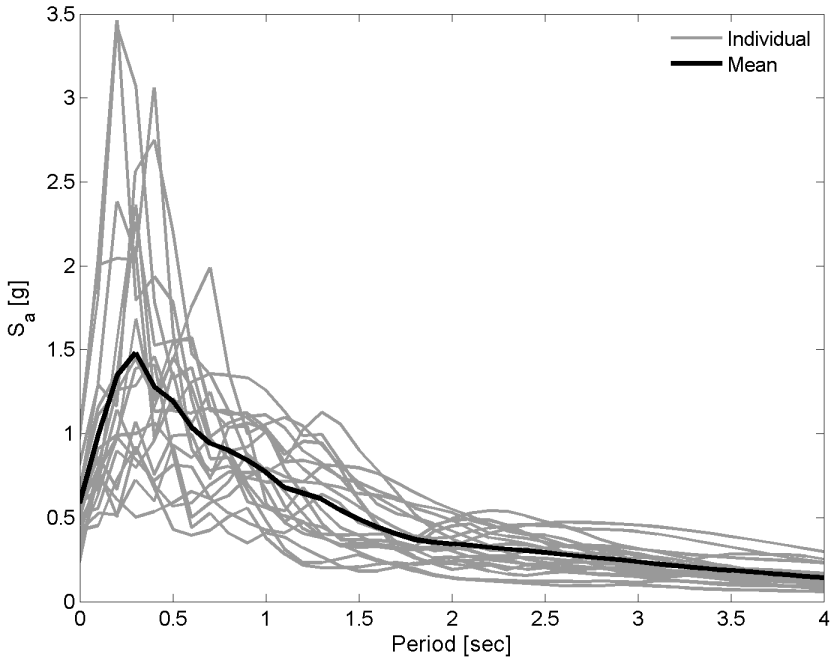

Figure B.1. Response spectra, 10% probability of exceedance in 50 years.

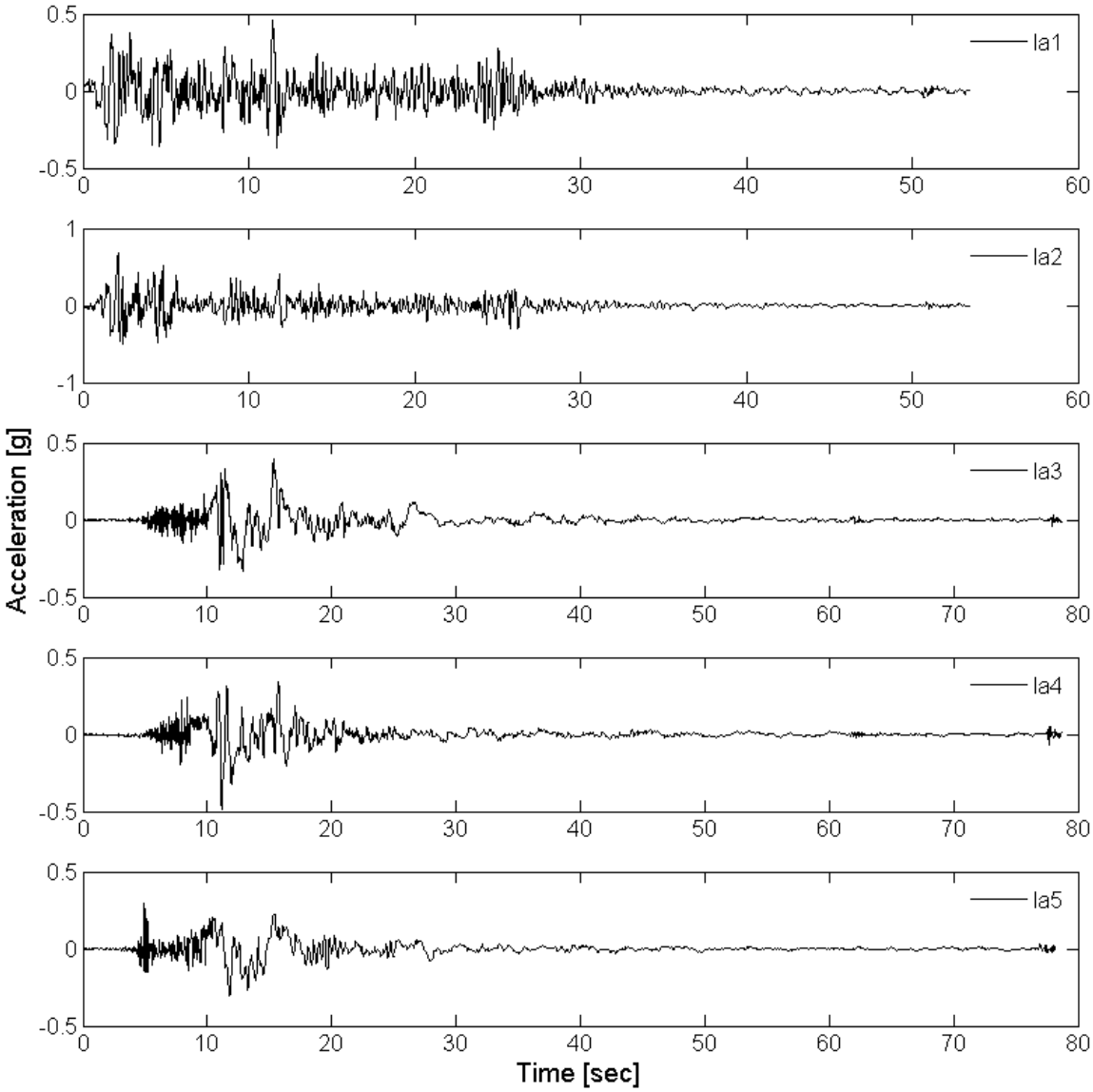

Figure B.2. Ground motion time histories, LA1-5.

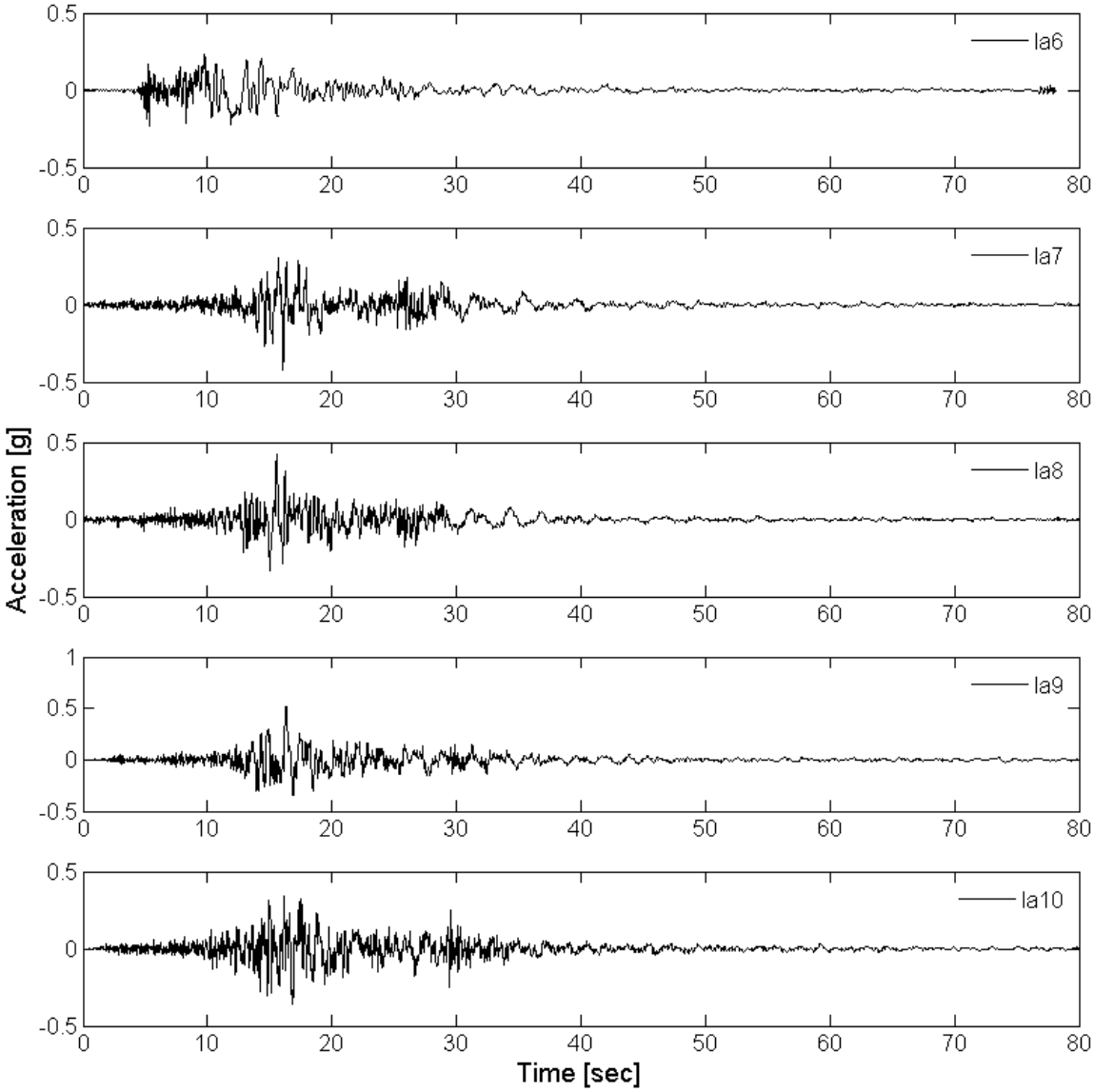

Figure B.3. Ground motion time histories, LA6-10.

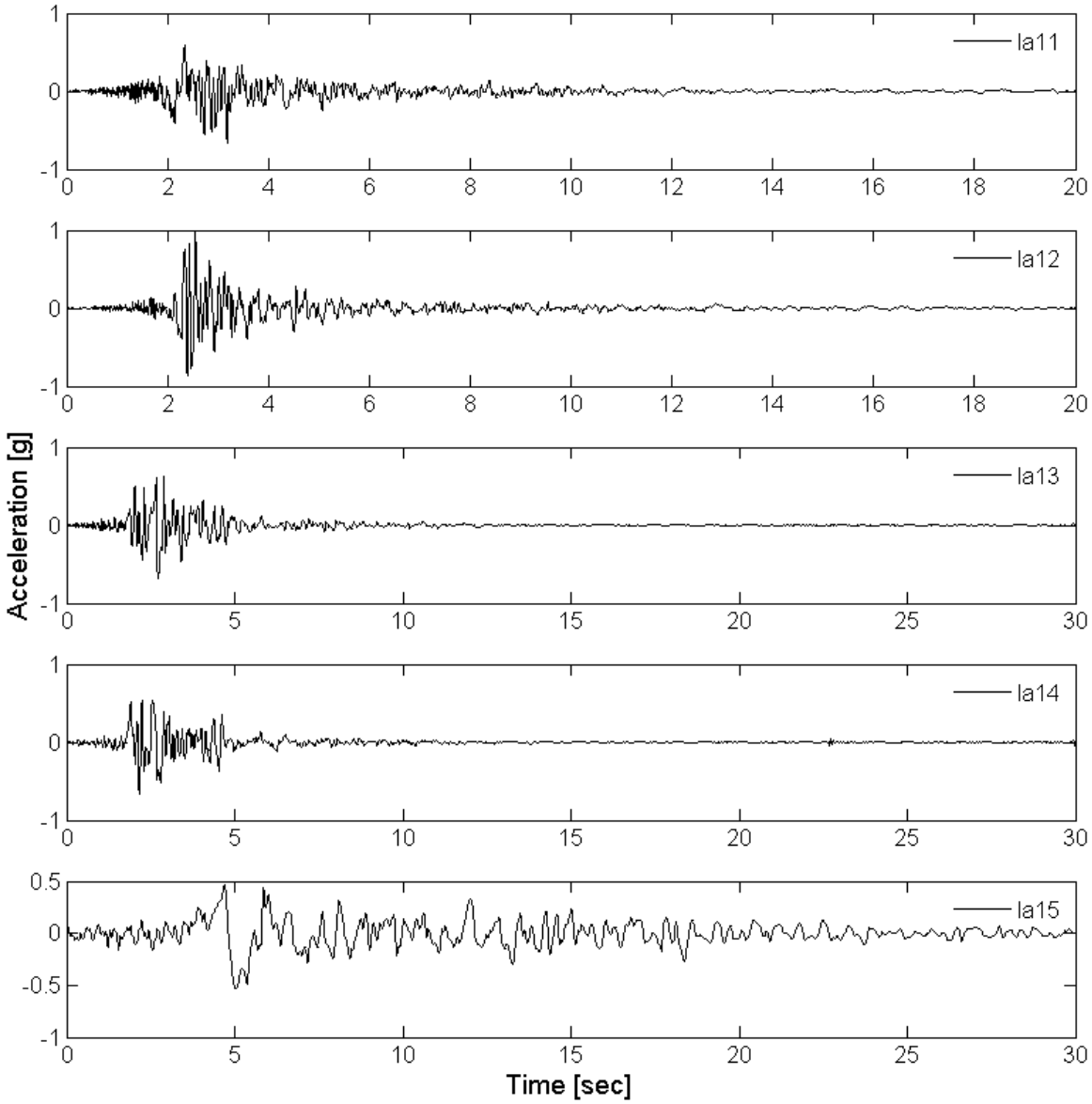

Figure B.4. Ground motion time histories, LA11-15.

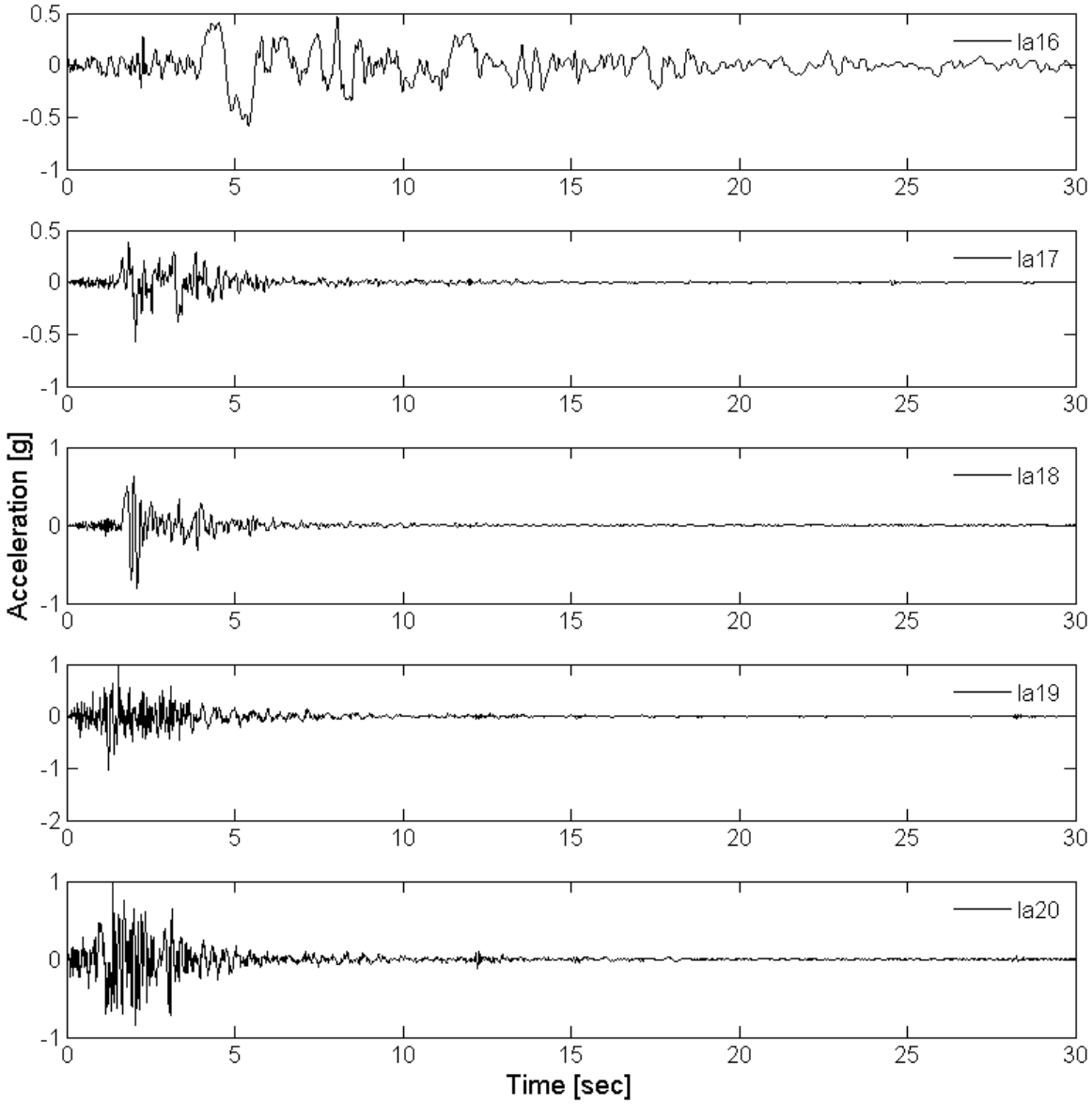

Figure B.5. Ground motion time histories, LA16-20.

Table B.2. Details of Los Angeles ground motions, 2% probability of exceedance in 50 years.

Name	*Record*	*Mag.*	*Dis.* [km]	*Scale Factor*	*dt* [sec]	*Duration* [sec]	*PGA* [g]
LA21	1995 Kobe	6.9	3.4	1.15	0.02	60	1.28
LA22	1995 Kobe	6.9	3.4	1.15	0.02	60	0.92
LA23	1989 Loma Prieta	7	3.5	0.82	0.01	25	0.42
LA24	1989 Loma Prieta	7	3.5	0.82	0.01	25	0.47
LA25	1994 Northridge	6.7	7.5	1.29	0.005	15	0.87
LA26	1994 Northridge	6.7	7.5	1.29	0.005	15	0.94
LA27	1994 Northridge	6.7	6.4	1.61	0.02	60	0.93
LA28	1994 Northridge	6.7	6.4	1.61	0.02	60	1.33
LA29	1974 Tabas	7.4	1.2	1.08	0.02	50	0.81
LA30	1974 Tabas	7.4	1.2	1.08	0.02	50	0.99
LA31	Elysian Park (simulated)	7.1	17.5	1.43	0.01	30	1.30
LA32	Elysian Park (simulated)	7.1	17.5	1.43	0.01	30	1.19
LA33	Elysian Park (simulated)	7.1	10.7	0.97	0.01	30	0.78
LA34	Elysian Park (simulated)	7.1	10.7	0.97	0.01	30	0.68
LA35	Elysian Park (simulated)	7.1	11.2	1.1	0.01	30	0.99
LA36	Elysian Park (simulated)	7.1	11.2	1.1	0.01	30	1.10
LA37	Palos Verdes (simulated)	7.1	1.5	0.9	0.02	60	0.71
LA38	Palos Verdes (simulated)	7.1	1.5	0.9	0.02	60	0.78
LA39	Palos Verdes (simulated)	7.1	1.5	0.88	0.02	60	0.50
LA30	Palos Verdes (simulated)	7.1	1.5	0.88	0.02	60	0.63

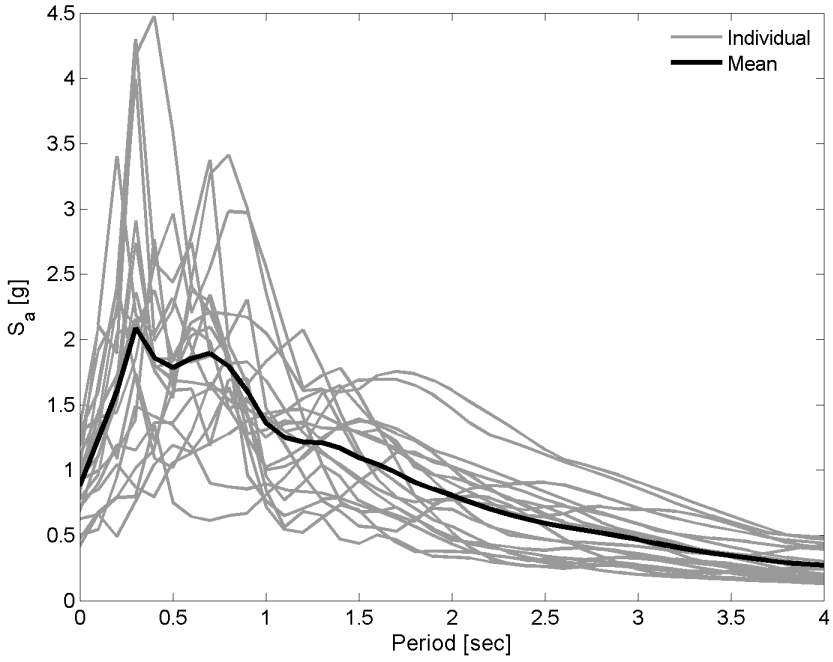

Figure B.6. Response spectra,2% probability of exceedance in 50 years.

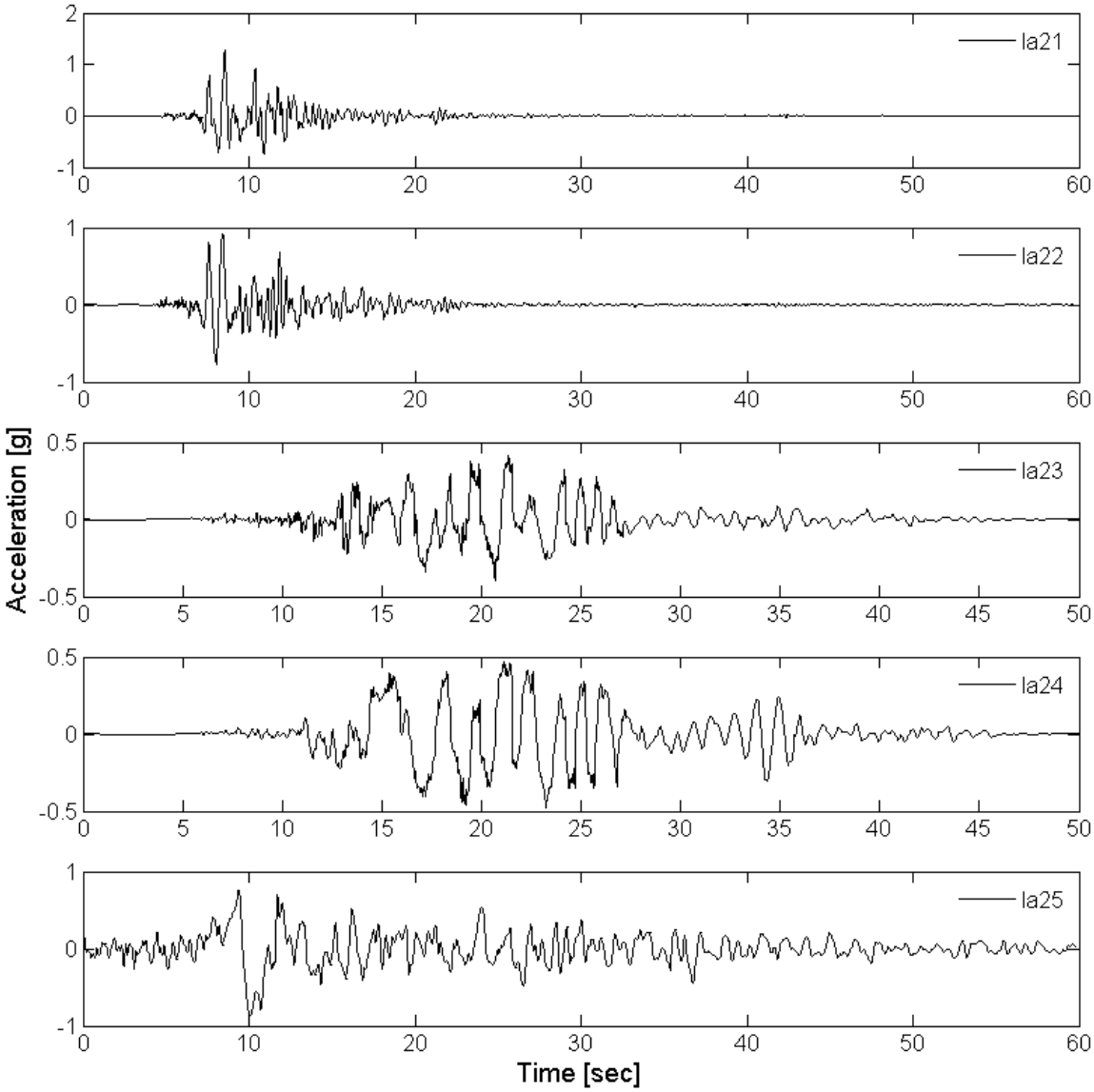

Figure B.7. Ground motion time histories, LA21-25.

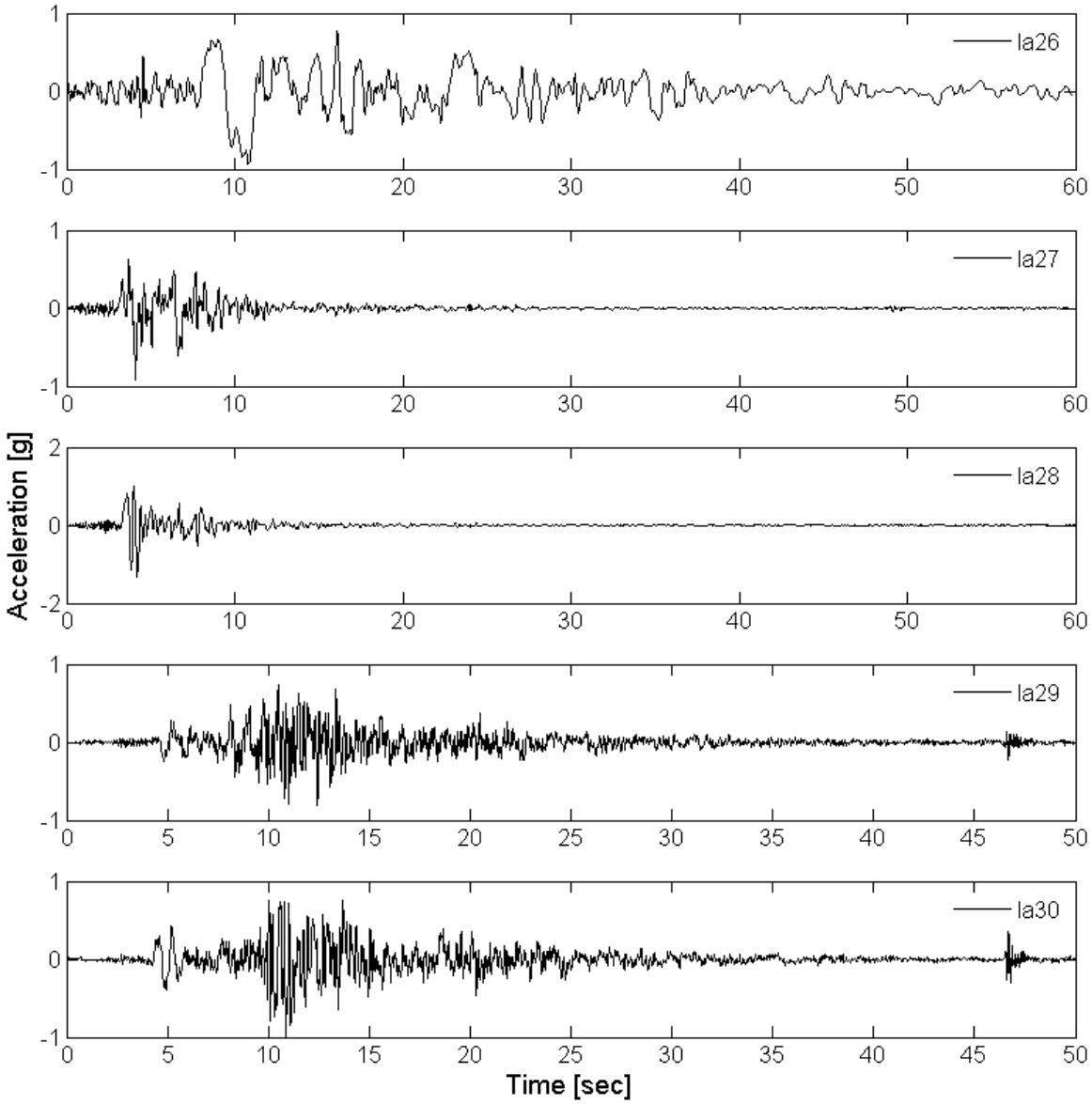

Figure B.8. Ground motion time histories, LA26-30.

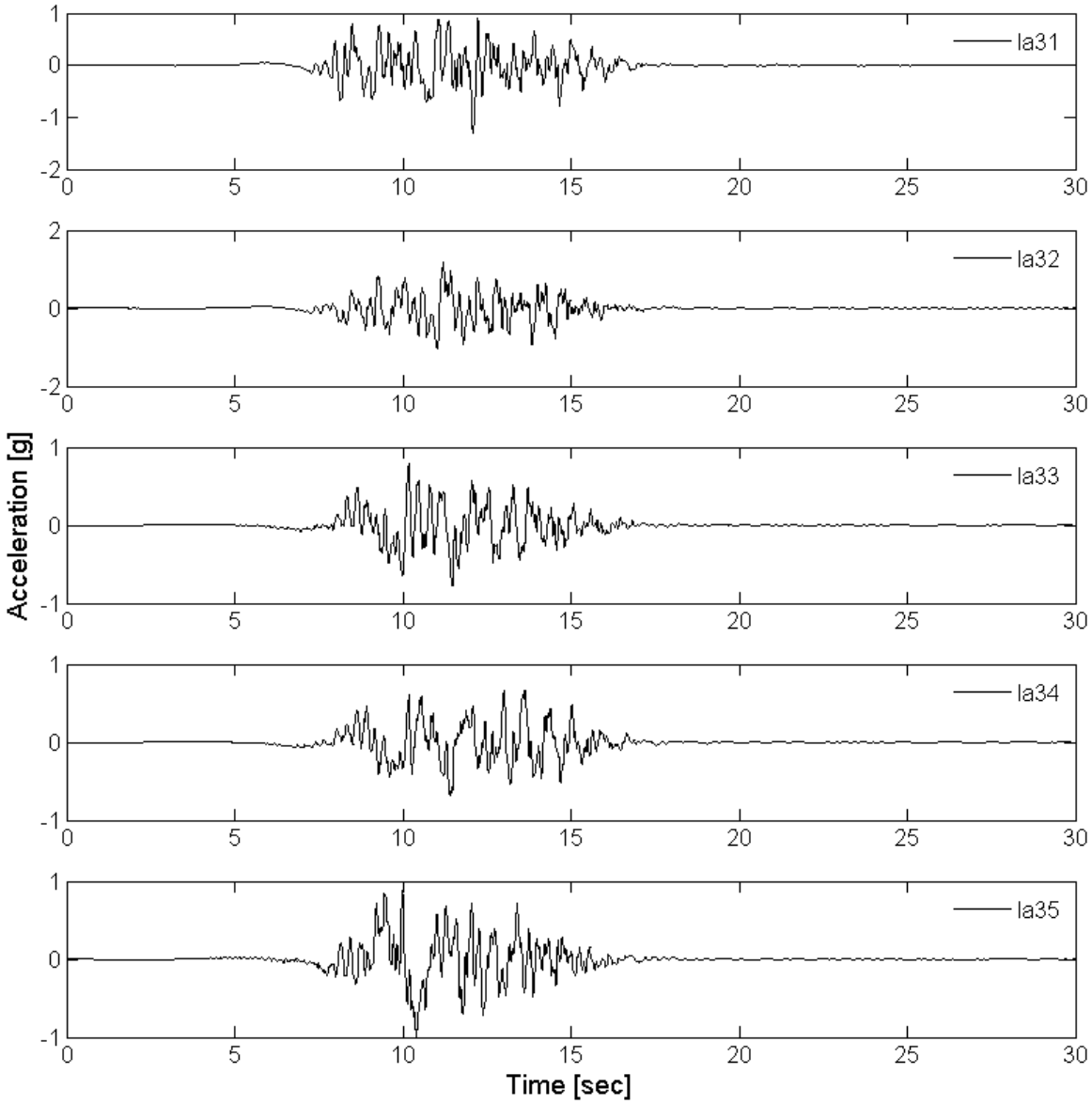

Figure B.9. Ground motion time histories, LA31-35.

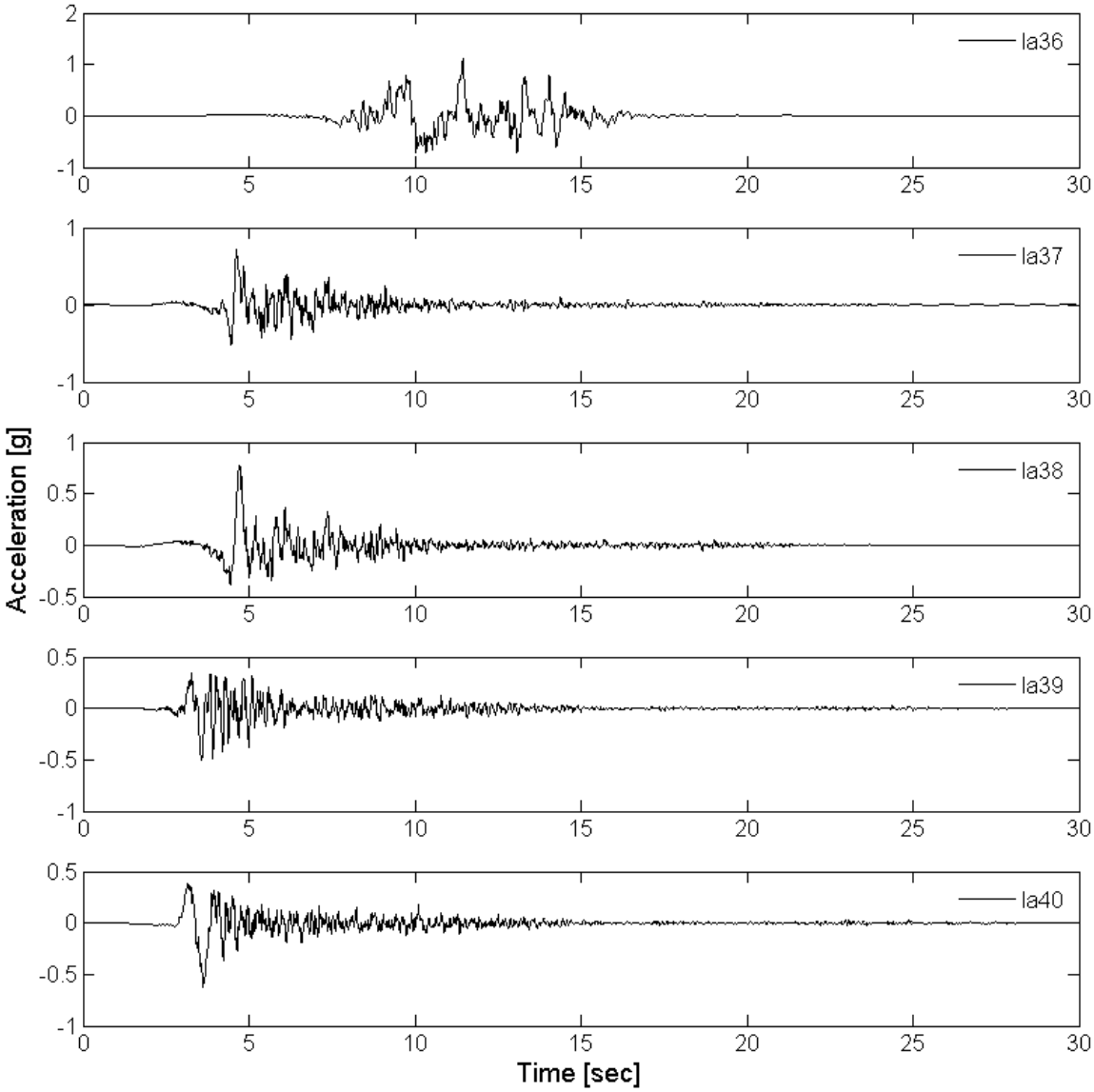

Figure B.10. Ground motion time histories, LA36-40.

REFERENCES

[1] CalTrade, "ILWU Calls for May 1 Dock Walkout," www.caltradereport.com, March 14, 2008. [accessed July 2009]

[2] S. E. Chang, "Disasters and transport systems: loss, recovery and competition at the Port of Kobe after the 1995 earthquake," *Journal of Transport Geography*, vol. 8, pp. 53-65, 2000.

[3] M. O. Eberhard, S. Baldridge, J. Marshall, W. Mooney, and G. J. Rix, "The Mw 7.0 Haiti Earthquake of January 12, 2010: USGS/EERI Advance Reconnaissance Team Report v1.1," USGS/EERI Feb. 23 2010.

[4] BBC News, "Haiti port opening raises hopes for quake victims." http://news.bbc.co.uk, January 22, 2010. [accessed February 2010]

[5] MarineLog, "Titan Salvage works to open up Port-au-Prince," www.marinelog.com, February 12, 2010. [accessed February 2010]

[6] International Navigation Association (PIANC), *Seismic Design Guidelines for Port Structures*. Leiden: Balkema, 2001.

[7] S. D. Werner, *Seismic Guidelines for Ports*. Reston, VA: American Society of Civil Engineers, 1998.

[8] N. Zrnic, "Development of Design of Ship-to-Shore Container Cranes: 1959-2004," in *International Symposium on History of Machines and Mechanisms, Proceedings HMM2004*, M. Ceccarelli, Ed. Dordrecht: Kluwer Academic Publishers, 2004, pp. 229-242.

[9] E. Soderberg and M. Jordan, "Seismic response of jumbo container cranes and design recommendations to limit damage and prevent collapse," presented at Ports 2007: 30 Years of Sharing Ideas 1977-2007; Proceedings of the Eleventh Triennial International Conference, San Diego, CA, 2007.

[10] E. Soderberg, J. Hsieh, and A. Dix, "Seismic Guidelines for Container Cranes," in *TCLEE 2009*. Oakland, CA: ASCE, 2009.

[11] Port of Los Angeles, "The Port of Los Angeles Seismic Code for Port Structures (POLA Code 07)," POLA, Los Angeles 2007.

[12] JSME, "The Machines and Industrial Equipments Damage due to the South Hyogo-Prefecture Earthquake," 1996.

[13] D. Dinevski, M. Oblak, and A. Novak, "Experimental verification of the container crane natural frequencies," Rhodes, Greece, 1997.

[14] M. Jordan, "Megacranes: Holding Sway," in *Port Development International*, 1998, pp. CC10-11.

[15] T. Kanayama and A. Kashiwazaki, "Study on the dynamic behavior of container cranes under strong earthquakes," presented at Pressure Vessels and Piping Conference, Fairfield, NJ, USA, 1998.

[16] T. Kanayama, A. Kashiwazaki, N. Shimizu, I. Nakamura, and N. Kobayashi, "Large shaking table test of a container crane by strong ground excitation," presented at Pressure Vessels and Piping Conference, Fairfield, NJ, USA, 1998.

[17] H. Kuribara and N. Kobayashi, "Seismic Response of Large Flexible Structure Including Contact Problem," presented at Design Engineering Technology Conference, 1999.

[18] N. Kobayashi, H. Kuribara, T. Honda, and M. Watanabe, "Nonlinear seismic responses of container cranes including the contact problem between wheels and rails," *Journal of Pressure Vessel Technology, Transactions of the ASME*, vol. 126, pp. 59-65, 2004.

[19] T. Tanabe, T. Etou, S. Yamamoto, T. Sugano, M. Miyata, and A. Kashiwazaki, "Experiment on Behavior of Container Cranes during Strong Earthquakes," *Transcations of the Japan Society of Mechanical Engineers, Part C*, vol. 66, pp. 205-212, 2000.

[20] S. Yamamoto, T. Sugano, and T. Tanabe, "The shaking table test of the interaction between the pier type wharf and the container crane during earthquakes," *Nippon Kikai Gakkai Ronbunshu, C Hen/Transactions of the Japan Society of Mechanical Engineers, Part C*, vol. 68, pp. 3209-3216, 2002.

[21] T. Sugano, T. Shibakusa, K. Fujiwara, K. Tokunaga, Y. Makimoto, and T. Fujiki, "Study on the Seismic Performance of Container Crane - Development of the Container Crane with Isolation System," *Report of the Port and Airport Research Institute*, vol. 42, pp. 221-250, 2003.

[22] T. Sugano, M. Takenobu, T. Suzuki, and Y. Shiozaki, "Design procedures of seismic-isolated container crane at port," presented at 14th World Conference on Earthquake Engineering, Beijing, China, 2008.

[23] G. W. Housner, "The Behavior of Inverted Pendulum Structures During Earthquakes," *Bulletin of the Seismological Society of America*, vol. 53, pp. 403-417, 1963.

[24] C. K. Yim, A. K. Chopra, and J. Penzien, "Rocking response of rigid blocks to earthquakes," *Earthquake Engineering & Structural Dynamics*, vol. 8, pp. 565-587, 1980.

[25] Y. Ishiyama, "Motion of rigid bodies and criteria for overturning by earthquake excitations," *Earthquake Engineering & Structural Dynamics*, vol. 10, pp. 635-650, 1982.

[26] I. N. Psycharis and P. C. Jennings, "Rocking of slender rigid bodies allowed to uplift," *Earthquake Engineering & Structural Dynamics*, vol. 11, pp. 57-76, 1983.

[27] M. Apostolou, G. Gazetas, and E. Garini, "Seismic response of slender rigid structures with foundation uplifting," *Soil Dynamics and Earthquake Engineering*, vol. 27, pp. 642-654, 2007.

[28] A. Palmeri and N. Makris, "Response analysis of rigid structures rocking on viscoelastic foundation," *Earthquake Engineering & Structural Dynamics*, vol. 37, pp. 1039-1063, 2008.

[29] C. Harden, T. Hutchinson, and M. Moore, "Investigation into the Effects of Foundation Uplift on Simplified Seismic Design Procedures," *Earthquake Spectra*, vol. 22, pp. 663-692, 2006.

[30] American Society of Civil Engineers (ASCE), "Prestandard and Commentary for the Seismic Rehabilitation of Buildings," Federal Emergency Management Agency, FEMA-356, Washington DC 2000.

[31] N. Makris and D. Konstantinidis, "The rocking spectrum and the limitations of practical design methodologies," *Earthquake Engineering & Structural Dynamics*, vol. 32, pp. 265-289, 2003.

[32] J. W. Meek, "Effects of Foundation Tipping on Dynamic Response," *Journal of the Structural Division*, vol. 101, pp. 1297-1311, 1975.

[33] S. C.-S. Yim and A. K. Chopra, "Dynamics of Structures on Two-Spring Foundation Allowed to Uplift," *Journal of Engineering Mechanics*, vol. 110, pp. 1124-1146, 1984.

[34] A. K. Chopra and S. C.-S. Yim, "Simplified Earthquake Analysis of Structures with Foundation Uplift," *Journal of Structural Engineering*, vol. 111, pp. 906-930, 1985.

[35] I. N. Psycharis, "Effect of Base Uplift on Dynamic Response of SDOF Structures," *Journal of Structural Engineering*, vol. 117, pp. 733-754, 1991.

[36] A. A. Huckelbridge and R. W. Clough, "Seismic Response of Uplifting Building Frame," *Journal of the Structural Division*, vol. 104, pp. 1211-1229, 1978.

[37] M. Midorikawa, T. Azuhata, T. Ishihara, and A. Wada, "Shaking table tests on seismic response of steel braced frames with column uplift," *Earthquake Engineering & Structural Dynamics*, vol. 35, pp. 1767-1785, 2006.

[38] M. Pollino and M. Bruneau, "Dynamic seismic response of controlled rocking bridge steel-truss piers," *Engineering Structures*, vol. 30, pp. 1667-1676, 2008.

[39] M. Eatherton, J. F. Hajjar, G. G. Deierlein, X. Ma, S. Billington, and H. Krawinkler, "Steel-Framed Rocking Structural Systems for Moderate Seismic Zones," presented at ASCE/SEI Structures Congress, Austin, TX, 2009.

[40] T. G. Leech, R. J. Conner, E. J. Kaufman, and J. McHugh, "The Kinzua decoded, the forensic investigation of the July 21, 2003 collapse," presented at Forensic Engineering, Cleveland, OH, 2007.

[41] B. F. Maison and K. Kasai, "Dynamics of pounding when two buildings collide," *Earthquake Engineering & Structural Dynamics*, vol. 21, pp. 771-786, 1992.

[42] S. A. Anagnostopoulos, "Equivalent viscous damping for modeling inelastic impacts in earthquake pounding problems," *Earthquake Engineering & Structural Dynamics*, vol. 33, pp. 897-902, 2004.

[43] K. T. Chau and X. X. Wei, "Pounding of structures modelled as non-linear impacts of two oscillators," *Earthquake Engineering & Structural Dynamics*, vol. 30, pp. 633-651, 2001.

[44] R. Jankowski, "Analytical expression between the impact damping ratio and the coefficient of restitution in the non-linear viscoelastic model of structural

pounding," *Earthquake Engineering & Structural Dynamics*, vol. 35, pp. 517-524, 2006.

[45] S. Muthukumar and R. DesRoches, "A Hertz contact model with non-linear damping for pounding simulation," *Earthquake Engineering & Structural Dynamics*, vol. 35, pp. 811-828, 2006.

[46] H. Nakai, T. Kitada, and T. Miki, "EXPERIMENTAL STUDY ON ULTIMATE STRENGTH OF THIN-WALLED BOX STUB-COLUMNS WITH STIFFENERS SUBJECTED TO COMPRESSION AND BENDING," *Doboku Gakkai Rombun-Hokokushu/Proceedings of the Japan Society of Civil Engineers*, pp. 87-97, 1985.

[47] H. Nakai, T. Kitada, and T. Miki, "INTERACTION CURVE OF THIN-WALLED BOX STUB-COLUMN SUBJECTED TO COMPRESSION AND BENDING FOR APPLYING TO OVERALL BUCKLING ANALYSIS OF COLUMNS," *Doboku Gakkai Rombun-Hokokushu/Proceedings of the Japan Society of Civil Engineers*, pp. 65-73, 1985.

[48] H. Nakai, T. Kitada, and T. Miki, "ULTIMATE STRENGTH OF THIN-WALLED BOX STUB-COLUMNS," *Doboku Gakkai Rombun-Hokokushu/Proceedings of the Japan Society of Civil Engineers*, pp. 25-35, 1985.

[49] T. Kitada, H. Nakai, and M. Kunihiro, "Ultimate strength of box stub columns under combined actions of compression, bending and torsion," *Journal of Constructional Steel Research*, vol. 13, pp. 153-168, 1989.

[50] T. Usami, Y. Imai, T. Aoki, and Y. Itoh, "An experimental study on the strength and ductility of steel compression members under cyclic loading," *JSCE Journal of Structural Engineering*, vol. 37A, pp. 93-106, 1991.

[51] K. Kawashima, G. A. MacRae, and K. Hasegawa, "The Strength and Ductility of Steel Bridge Piers Based on Loading Tests," *PWRI Journal of Research*, vol. 29, 1992.

[52] T. Usami, M. Wada, M. Kato, and H. Ge, "Ultimate compressive strength of plate assemblies," *International Conference on Steel and Aluminium Structures*, pp. 471, 1991.

[53] T. V. Galambos, "Guide to Stability Design Criteria for Metal Structures," 5 ed. New York: Wiley, 1998.

[54] H. Degee, A. Detzel, and U. Kuhlmann, "Interaction of global and local buckling in welded RHS compression members," *Journal of Constructional Steel Research*, vol. 64, pp. 755-765, 2008.

[55] Y. B. Kwon, N. G. Kim, and G. J. Hancock, "Compression tests of welded section columns undergoing buckling interaction," *Journal of Constructional Steel Research*, vol. 63, pp. 1590-1602, 2007.

[56] H. Ge, S. Gao, and T. Usami, "Stiffened steel box columns. Part 1: Cyclic behaviour," *Earthquake Engineering and Structural Dynamics*, vol. 29, pp. 1691-1706, 2000.

[57] K. Kawashima, K. Hasegawa, G. A. MacRae, T. Ikeuchi, and K. Oshima, "Ductility of Steel Bridge Piers from Dynamic Loading Tests," presented at U.S.-Japan Joint Seminar on Stability and Ductility of Steel Structures under Cyclic Loading, Osaka, Japan, 1991.

[58] DIN 4114, *Stahbau, Stabilitatsfalle (Knickung, Kippung, Beulung), Berechnungsgrundlagen*, vol. Blatt2. Berlin: Deutsches Institut fur Normung (DIN), Richtlinien, 1953.

[59] G. A. MacRae and K. Kawashima, "Estimation of the Deformation Capacity of Steel Bridge Piers," presented at U.S.-Japan Joint Seminar on Stability and Ductility of Steel Structures under Cyclic Loading, Osaka, Japan, 1991.

[60] JRA, "Specifications for Highway Bridges," Japan Road Association, Tokyo, Japan 1990.

[61] G. A. MacRae and K. Kawashima, "Seismic Behavior of Hollow Stiffened Steel Bridge Columns," *Journal of Bridge Engineering*, vol. 6, pp. 110-119, 2001.

[62] T. Usami, T. Aoki, S. Mizutani, and Y. Itoh, "Steel and Concrete-Filled Steel Compression Members under Cyclic Loading," presented at U.S.-Japan Joint Seminar on Stability and Ductility of Steel Structures under Cyclic Loading, Osaka, Japan, 1991.

[63] T. Usami, S. Mizutani, T. Aoki, Y. Itoh, and H. Yasunami, "An experimental study on the elasto-plastic cyclic behavior of stiffened box members," *JSCE Journal of Structural Engineering*, vol. 38A, pp. 105-117, 1992.

[64] Y. Fukumoto, *Guideline for Stability Design of Steel Structures*. Japan: JSCE, 1987.

[65] M. Ikeda, A. Ichikawa, M. Yamada, A. Taira, and M. Yasuhara, "Ductility and Hysteresis Model of Steel Column Members," *Quarterly Report of RTRI*, vol. 40, pp. 177-182, 1999.

[66] M. Suzuki, U. Tsutomu, T. Masahiro, T. Itoh, and K. Saizuka, "Hysteresis Models for Steel Bridge Piers and their Application to Elasto-Plastic Seismic Response Analysis," *Journal of Structural Mechanics and Earthquake Engineering*, vol. 549, pp. 191-204, 1996.

[67] S. Kumar and T. Usami, "Damage Evaluation in Steel Box Columns by Cyclic Loading Tests," *Journal of Structural Engineering*, vol. 122, pp. 626-634, 1996.

[68] T. Usami and S. Kumar, "Damage Evaluation in Steel Box Columns by Pseudodynamic Tests," *Journal of Structural Engineering*, vol. 122, pp. 635-642, 1996.

[69] S. Kumar and T. Usami, "An evolutionary-degrading hysteretic model for thin-walled steel structures," *Engineering Structures*, vol. 18, pp. 504-514, 1996.

[70] Y.-J. Park, A. H. S. Ang, and Y. K. Wen, "SEISMIC DAMAGE ANALYSIS OF REINFORCED CONCRETE BUILDINGS," *Journal of Structural Engineering*, vol. 111, pp. 740-757, 1985.

[71] H. Krawinkler and M. Zohrei, "CUMULATIVE DAMAGE IN STEEL STRUCTURES SUBJECTED TO EARTHQUAKE GROUND MOTIONS," *Computers and Structures*, vol. 16, pp. 531-541, 1982.

[72] Q. Liu, A. Kasai, and U. Tsutomu, "Parameter Identification of Damage-based Hysteretic Model for Pipe-section Steel Bridge Piers," *JSCE Journal of Structural Engineering*, vol. 45A, pp. 1005-1016, 1999.

[73] T. Usami and S. Kumar, "Inelastic seismic design verification method for steel bridge piers using a damage index based hysteretic model," *Engineering Structures*, vol. 20, pp. 472-480, 1998.

[74] Q. Liu, A. Kasai, and U. Tsutomu, "Inelastic response spectra for seismic design verification of pipe and stiffened box steel bridge piers," *JSCE Journal of Structural Engineering*, vol. 46A, pp. 641-652, 2000.

[75] Q. Liu, A. Kasai, and U. Tsutomu, "Comparative Study of Four Hysteretic Models for Pipe-Section Steel Bridge Piers," *Structural Eng./Earthquake Eng.*, vol. 16, pp. 111s-142s, 1999.

[76] Q. Liu, A. Kasai, and U. Tsutomu, "Two hysteretic models for thin-walled pipe-section steel bridge piers," *Engineering Structures*, vol. 23, pp. 186-197, 2001.

[77] I. H. P. Mamaghani, C. Shen, E. Mizuno, and T. Usami, "Cyclic Behavior of Structural Steels. I: Experiments," *Journal of Engineering Mechanics*, vol. 121, pp. 1158-1164, 1995.

[78] C. Shen, I. H. P. Mamaghani, E. Mizuno, and T. Usami, "Cyclic Behavior of Structural Steels. II: Theory," *Journal of Engineering Mechanics*, vol. 121, pp. 1165-1172, 1995.

[79] Y. F. Dafalias and E. P. Popov, "A Model of Nonlinearly Hardening Materials for Complex Loading," *Acta Mechanica*, vol. 21, pp. 173-192, 1975.

[80] T. Usami, S. Gao, and H. Ge, "Elastoplastic analysis of steel members and frames subjected to cyclic loading," *Engineering Structures*, vol. 22, pp. 135-145, 2000.

[81] T. Usami, Y. Zheng, and H. B. Ge, "Recent research developments in stability and ductility of steel bridge structures: General Report," *Journal of Constructional Steel Research*, vol. 55, pp. 183-209, 2000.

[82] T. Usami and H. B. Ge, "Cyclic behavior of thin-walled steel structures - numerical analysis," *Thin-Walled Structures*, vol. 32, pp. 41-80, 1998.

[83] T. Usami, S. Gao, and H. Ge, "Stiffened steel box columns. Part 2: Ductility evaluation," *Earthquake Engineering and Structural Dynamics*, vol. 29, pp. 1707-1722, 2000.

[84] Y. Zheng, T. Usami, and H. Ge, "Ductility of thin-walled steel box stub-columns," *Journal of Structural Engineering*, vol. 126, pp. 1304-1311, 2000.

[85] Y. Zheng, T. Usami, and H. Ge, "Ductility evaluation procedure for thin-walled steel structures," *Journal of Structural Engineering*, vol. 126, pp. 1312-1319, 2000.

[86] I. H. P. Mamaghani, "Seismic Design and Ductility Evaluation of Thin-Walled Steel Bridge Piers of Box Sections," *Transportation Research Record: Journal of the Transportation Research Board*, vol. 2050, pp. 137-142, 2008.

[87] T. Aoki and K. A. S. Susantha, "Seismic Performance of Rectangular-Shaped Steel Piers under Cyclic Loading," *Journal of Structural Engineering*, vol. 131, pp. 240-249, 2005.

[88] O. T. Cetinkaya, S. Nakamura, and K. Takahashi, "Ultimate strain of stiffened steel box sections under bending moment and axial force fluctuations," *Engineering Structures*, vol. 31, pp. 778-787, 2009.

[89] T. Usami and H. Ge, "Ductility of Concrete-Filled Steel Box Columns under Cyclic Loading," *Journal of Structural Engineering*, vol. 120, pp. 2021-2040, 1994.

[90] H. B. Ge, K. A. S. Susantha, Y. Satake, and T. Usami, "Seismic demand predictions of concrete-filled steel box columns," *Engineering Structures*, vol. 25, pp. 337-345, 2003.

[91] K. Nishikawa, S. Yamamoto, T. Natori, K. Terao, H. Yasunami, and M. Terada, "Retrofitting for seismic upgrading of steel bridge columns," *Engineering Structures*, vol. 20, pp. 540-551, 1998.

[92] T. Kitada, M. Matsumura, and Y. Otoguro, "Seismic retrofitting techniques using an energy absorption segment for steel bridge piers," *Engineering Structures*, vol. 25, pp. 621-635, 2003.

[93] K. A. S. Susantha, T. Aoki, T. Kumano, and K. Yamamoto, "Applicability of low-yield-strength steel for ductility improvement of steel bridge piers," *Engineering Structures*, vol. 27, pp. 1064-1073, 2005.

[94] H. L. Hsu and J. L. Juang, "Performance of thin-walled box columns strengthened with internal braces," *Thin-Walled Structures*, vol. 37, pp. 241-258, 2000.

[95] P. Pan, D. Zamfirescu, M. Nakashima, N. Nakayasu, and H. Kashiwa, "Base-Isolation Design Practice in Japan: Introduction to the Post-Kobe Approach," *Journal of Earthquake Engineering*, vol. 9, pp. 147-171, 2005.

[96] H. Gu and Y. Itoh, "Seismic Response of Steel Bridge Piers with Aged Base-Isolated Rubber Bearing," *JSCE Journal of Structural Engineering*, vol. 52A, pp. 537-546, 2006.

[97] B. R. Ellingwood, "Probability-based codified design: past accomplishments and future challenges," *Structural Safety*, vol. 13, pp. 159-176, 1994.

[98] B. R. Ellingwood, "Earthquake risk assessment of building structures," *Reliability Engineering and System Safety*, vol. 74, pp. 251-262, 2001.

[99] A. Der Kiureghian, "SEISMIC RISK ANALYSIS OF STRUCTURAL SYSTEMS," vol. 107, pp. 1133-1153, 1981.

[100] J. M. O'Connor and B. Ellingwood, "RELIABILITY OF NONLINEAR STRUCTURES WITH SEISMIC LOADING," *Journal of structural engineering New York, N.Y.*, vol. 113, pp. 1011-1028, 1987.

[101] B. R. Ellingwood, O. C. Celik, and K. Kinali, "Fragility assessment of building structural systems in Mid-America," *Earthquake Engineering and Structural Dynamics*, vol. 36, pp. 1935-1952, 2007.

[102] U.S. Nuclear Regulatory Commission (U.S. NRC), "A Guide to the Performance of Probabilistic Risk Assessments for Nuclear Power Plants," Washington D.C. NUREG/CR-2300, 1983.

[103] A. Amendola, "Recent paradigms for risk informed decision making," *Safety Science*, vol. 40, pp. 17-30, 2001.

[104] F. Casciati and L. Faravelli, *Fragility analysis of complex structural systems*. Somerset, UK: Research Studies Press, Wiley, 1991.

[105] R. P. Kennedy and M. K. Ravindra, "SEISMIC FRAGILITIES FOR NUCLEAR POWER PLANT RISK STUDIES," *Nuclear Engineering and Design*, vol. 79, pp. 47-68, 1984.

[106] Applied Technology Council, "Earthquake damage evaluation for California," ATC-13, Redwood City, CA 1985.

[107] Federal Emergency Management Agency (FEMA), "Multi-hazard loss estimation methodology, Earthquake model," HAZUS-MH MR4 Technical Manual, Washington DC 2003.

[108] M. Shinozuka, M. Q. Feng, J. Lee, and T. Naganuma, "Statistical Analysis of Fragility Curves," *Journal of Engineering Mechanics*, vol. 126, pp. 1224-1231, 2000.

[109] A. Singhal and A. S. Kiremidjian, "Method for Probabilistic Evaluation of Seismic Structural Damage," *Journal of Structural Engineering*, vol. 122, pp. 1459-1467, 1996.

[110] Y. K. Wen, B. R. Ellingwood, and J. M. Bracci, "Vulnerability Function Framework for Consequence-based Engineering," Mid-America Earthquake Center, Champaign, IL Technical Rep. DS-4, 2004.

[111] C. A. Cornell, F. Jalayer, R. O. Hamburger, and D. A. Foutch, "Probabilistic Basis for 2000 SAC Federal Emergency Management Agency Steel Moment

Frame Guidelines," *Journal of Structural Engineering*, vol. 128, pp. 526-533, 2002.

[112] B. R. Ellingwood, "LRFD: Implementing structural reliability in professional practice," *Engineering Structures*, vol. 22, pp. 106-115, 2000.

[113] R. E. Melchers, *Structural Reliability Analysis and Prediction*, 2nd ed. Chichester, UK: Wiley, 1999.

[114] T. V. Galambos and M. K. Ravindra, "PROPERTIES OF STEEL FOR USE IN LRFD," vol. 104, pp. 1459-1468, 1978.

[115] J. Liu, R. Sabelli, R. L. Brockenbrough, and T. P. Fraser, "Expected yield stress and tensile strength ratios for determination of expected member capacity in the 2005 AISC seismic provisions," *Engineering Journal*, vol. 44, pp. 15-25, 2007.

[116] B. R. Ellingwood, T. V. Galambos, J. G. MacGregor, and C. A. Cornell, "Development of a Probability-Based Load Criterion for American National Standard A58," National Bureau of Standards, Washington, DC 1980.

[117] O.-S. Kwon and A. Elnashai, "The effect of material and ground motion uncertainty on the seismic vulnerability curves of RC structure," *Engineering Structures*, vol. 28, pp. 289-303, 2006.

[118] T.-H. Lee and K. M. Mosalam, "Sensitivity of Seismic Demand of a Reinforced Concrete Shear-Wall Building," presented at Ninth International Conference on Application of Statistics and Probability in Civil Engineering (ICASP 9), San Francisco, California, USA, 2003.

[119] J. E. Padgett and R. DesRoches, "Sensitivity of Seismic Response and Fragility to Parameter Uncertainty," *Journal of Structural Engineering*, vol. 133, pp. 1710-1718, 2007.

[120] J. Song and B. R. Ellingwood, "Probabilistic modeling of steel moment frames with welded connections," *Engineering Journal*, vol. 36, pp. 121-128, 1999.

[121] S.-Y. Yun, R. O. Hamburger, C. A. Cornell, and D. A. Foutch, "Seismic performance evaluation for steel moment frames," *Journal of Structural Engineering*, vol. 128, pp. 534-545, 2002.

[122] C. A. Cornell, "Engineering Seismic Risk Analysis," *Bulletin of the Seismological Society of America*, vol. 58, pp. 1583-1606, 1968.

[123] A. H.-S. Ang and W. H. Tang, *Probability Concepts in Engineering Planning and Design*, vol. 1-Basic Principles. New York: Wiley, 1975.

[124] A. Gupta and H. Krawinkler, "Relating the seismic drift demands of SMRFs to element deformation demands," *Engineering Journal*, vol. 39, pp. 100-108, 2002.

[125] H. Krawinkler, R. Medina, and B. Alavi, "Seismic drift and ductility demands and their dependence on ground motions," *Engineering Structures*, vol. 25, pp. 637-653, 2003.

[126] A. Gupta and H. Krawinkler, "Estimation of seismic drift demands for frame structures," *Earthquake Engineering & Structural Dynamics*, vol. 29, pp. 1287-1305, 2000.

[127] N. Shome, C. A. Cornell, P. Bazzurro, and J. E. Carballo, "Earthquakes, records, and nonlinear responses," *Earthquake Spectra*, vol. 14, pp. 469-500, 1998.

[128] P. Giovenale, C. A. Cornell, and L. Esteva, "Comparing the adequacy of alternative ground motion intensity measures for the estimation of structural responses," *Earthquake Engineering and Structural Dynamics*, vol. 33, pp. 951-979, 2004.

[129] K. Kinali and B. R. Ellingwood, "Seismic fragility assessment of steel frames for consequence-based engineering: A case study for Memphis, TN," *Engineering Structures*, vol. 29, pp. 1115-1127, 2007.

[130] A. S. Veletsos and N. M. Newmark, "Effect of inelastic behavior on the response of simple systems to earthquake motions," presented at 2nd World Conference on Earthquake Engineering, 1960.

[131] S. K. Ramamoorthy, P. Gardoni, and J. M. Bracci, "Seismic Fragility and Confidence Bounds for Gravity Load Designed Reinforced Concrete Frames of Varying Height," *Journal of Structural Engineering*, vol. 134, pp. 639-650, 2008.

[132] S. K. Ramamoorthy, P. Gardoni, and J. M. Bracci, "Probabilistic Demand Models and Fragility Curves for Reinforced Concrete Frames," *Journal of Structural Engineering*, vol. 132, pp. 1563-1572, 2006.

[133] P. Gardoni, A. Der Kiureghian, and K. M. Mosalam, "Probabilistic capacity models and fragility estimates for reinforced concrete columns based on experimental observations," *Journal of Engineering Mechanics*, vol. 128, pp. 1024-1038, 2002.

[134] J. Park, P. Towashiraporn, J. I. Craig, and B. J. Goodno, "Seismic fragility analysis of low-rise unreinforced masonry structures," *Engineering Structures*, vol. 31, pp. 125-137, 2009.

[135] B. G. Nielson and R. DesRoches, "Analytical seismic fragility curves for typical bridges in the central and southeastern United States," *Earthquake Spectra*, vol. 23, pp. 615-633, 2007.

[136] J. E. Padgett and R. DesRoches, "Retrofitted bridge fragility analysis for typical classes of multispan bridges," *Earthquake Spectra*, vol. 25, pp. 117-141, 2009.

[137] J. Song and B. R. Ellingwood, "Seismic reliability of special moment steel frames with welded connections: II," *Journal of Structural Engineering*, vol. 125, pp. 372-384, 1999.

[138] K. R. Collins, W. Yi-k Wei, and D. A. Foutch, "Dual-level seismic design: a reliability-based methodology," *Earthquake Engineering and Structural Dynamics*, vol. 25, pp. 1433-1467, 1996.

[139] Y. K. Wen, "Building reliability and code calibration," *Earthquake Spectra*, vol. 11, pp. 269-269, 1995.

[140] A. Whittaker, M. Constantinou, and P. Tsopelas, "Displacement estimates for performance-based seismic design," *Journal of structural engineering New York, N.Y.*, vol. 124, pp. 905-912, 1998.

[141] D. Vamvatsikos and C. A. Cornell, "Incremental dynamic analysis," *Earthquake Engineering and Structural Dynamics*, vol. 31, pp. 491-514, 2002.

[142] D. Vamvatsikos and C. A. Cornell, "Applied incremental dynamic analysis," *Earthquake Spectra*, vol. 20, pp. 523-553, 2004.

[143] P. McCarthy, E. Soderberg, and A. Dix, "Wind damage to dockside cranes: Recent failures and recommendations," Oakland, CA, United states, 2009.

[144] P. N. Patel and C. C. Spyrakos, "Uplifting-sliding response of flexible structures to seismic loads," *Engineering Analysis with Boundary Elements*, vol. 8, pp. 185-191, 1991.

[145] S. Mazzoni, F. McKenna, M. Scott, and G. L. Fenves, "The OpenSees Command Language Manual: version 2.0," Pacific Earthquake Engineering Center, University of California, Berkeley, 2009.

[146] A. K. Chopra, *Dynamics of Structures*, 2 ed. Upper Saddle River, NJ: Prentice Hall, 2001.

[147] F. McKenna, "Object-Oriented Finite Element Programming: Frameworks for Analysis, Algorithms and Parallel Computing," PhD Thesis, Department of Civil Engineering, University of California, Berkeley, 1997.

[148] B. Welch, K. Jones, and J. Hobbs, *Practical Programming in Tcl and Tk*, 4th ed: Prentice Hall, 2003.

[149] M. H. Scott, G. L. Fenves, F. McKenna, and F. C. Filippou, "Software Patterns for Nonlinear Beam-Column Models," *Journal of Structural Engineering*, vol. 134, pp. 562-571, 2008.

[150] A. Neuenhofer and F. C. Filippou, "Geometrically Nonlinear Flexibility-Based Frame Finite Element," *Journal of Structural Engineering*, vol. 124, pp. 704-711, 1998.

[151] D. A. Foutch and S.-Y. Yun, "Modeling of steel moment frames for seismic loads," *Journal of Constructional Steel Research*, vol. 58, pp. 529-564, 2002.

[152] R. M. de Souza, "Force-based finite element for large displacement inelastic analysis of frames," PhD Thesis, Department of Civil Engineering, University of California, Berkeley, 2000.

[153] E. Soderberg and M. Jordan, "Dockside Ship-to-Shore Cranes; Seismic Risk and Recommended Design Criteria." Oakland: Liftech Consultants Inc., 2007.

[154] S. A. Anagnostopoulos, "POUNDING OF BUILDINGS IN SERIES DURING EARTHQUAKES," *Earthquake Engineering & Structural Dynamics*, vol. 16, pp. 443-456, 1988.

[155] M. A. Crisfield, *Non-linear Finite Element Analysis of Solids and Structures*, vol. 1. Chichester: Wiley, 1996.

[156] N. M. Newmark, "Method of computation for structural dynamics," *ASCE -- Proceedings -- Journal of the Engineering Mechanics Division*, vol. 85, pp. 67-94, 1959.

[157] T. J. R. Hughes, *The Finite Element Method; Linear Static and Dynamic Finite Element Analysis*. Mineola: Dover, 2000.

[158] T. J. R. Hughes, "ANALYSIS OF TRANSIENT ALGORITHMS WITH PARTICULAR REFERENCE TO STABILITY BEHAVIOR." New York, NY: North-Holland Comput Methods in Mech. v 1 Amsterdam, Neth and, 1983, pp. 67-155.

[159] H. M. Hilber, T. J. R. Hughes, and R. L. Taylor, "Improved numerical dissipation for time integration algorithms in structural dynamics," *Earthquake Engineering & Structural Dynamics*, vol. 5, pp. 283-292, 1977.

[160] A. C. Ruge, "The Determination of Earthquake Stresses in Elastic Structures by Means of Models," *Bulletin of the Seismological Society of America*, vol. 24, pp. 169-230, 1934.

[161] H. G. Harris and G. Sabnis, *Structural Modeling and Experimental Techniques*, 2nd ed. Boca Raton, FL: CRC Press, 1999.

[162] P. D. Moncarz and H. Krawinkler, "Theory and Application of Experimental Model Analysis in Earthquake Engineering," The John A. Blume Earthquake Engineering Center, Stanford University, Report No. 50, June 1981.

[163] SEESL, "Structural Engineering and Earthquake Simulation Labortatory (SEESL) Manual." University at Buffalo: Department of Civil, Structural, and Environmental Engineering, 2007.

[164] A. K. Arulmoli, I. P. Lam, B. A. Schell, N. A. Abrahamson, J. S. Ana, and P. Yin, "Port-Wide Ground Motion and Palos Verdes Fault Study, Port of Los Angeles (POLA), California," Earth Mechanics, Inc., Fountain Valley, CA EMI No. 02-131-11, December 22 2006.

[165] A. K. Arulmoli, I. P. Lam, B. A. Schell, N. A. Abrahamson, J. S. Ana, and P. Yin, "Port-Wide Ground Motion Study, Port of Long Beach (POLB), California," Earth Mechanics, Inc., Fountain Valley, CA EMI No. 01-143, August 7 2006.

[166] G. Wang, "Frictional Contact Element for OpenSees," University of California, Berkeley, 2001.

[167] E. Soderberg, "Megacranes: Holding Sway - Boom Motions," *Port Technology International*, vol. 20, pp. 103-106, 2003.

[168] Liftech Inc., "On the Mend," vol. 2009. Oakland, CA, 2008.

[169] ShippingChina, "ZPMC's Era of Heavy Industry." Shanghai, China: Kaiji Press Co., Ltd., 2009.

[170] Geo-Engineering Extreme Events Reconnaissance (GEER), "Geotechnical Reconnaissance of the Effects of the January 17, 1995 Hyogoken-Nanbu Earthquake, Japan," www.geerassociation.org 1995. [accessed February 2010]

[171] N. Bazeos and D. L. Karabalis, "Efficient computation of buckling loads for plane steel frames with tapered members," *Engineering Structures*, vol. 28, pp. 771-775, 2006.

[172] K. A. Porter, J. L. Beck, and R. V. Shaikhutdinov, "Sensitivity of building loss estimates to major uncertain variables," *Earthquake Spectra*, vol. 18, pp. 719-743, 2002.

[173] P. G. Somerville, N. Smith, S. Punyamurthula, and J. Sun, "Development of ground motion time histories for phase 2 of the FEMA/SAC steel project," SAC Joint Venture, Sacramento, California SAC/BD-97/04, 1997.

[174] B. R. Ellingwood, "Reliability-Based Assessment of Seismic Performance of Buildings," Georgia Institute of Technology Structures Seminar, October 23, 2009.

[175] Y. K. Wen, B. R. Ellingwood, D. Veneziano, and J. M. Bracci, "Uncertainty Modeling in Earthquake Engineering (white paper)," University of Illinois at Urbana-Champaign, Urbana,IL MAE Center Project FD-2 Report, 2003.

[176] S. A. Freeman, "Development and use of capacity spectrum method," presented at 6th U.S. National Conference on Earthquake Engineering, Seattle, WA, 1998.

[177] H. Aslani and E. Miranda, "Probabilistic Earthquake Loss Estimation and Loss Disaggregation in Buildings," John A. Blume Earthquake Engineering Center, Stanford University Report No. 157, 2005.

[178] G. S. Johnson and S. P. Hardy, "History of Seismic Design Codes for Piers and Wharves," presented at TCLEE 2009, Oakland, California, 2009.

[179] MOTEMS, "Marine Oil Terminal Engineering and Maintenance Standards," California State Lands Commission May 2002.

[180] A. Nozu, K. Ichii, and T. Sugano, "Seismic Design of Port Structures," *Journal of Japan Association for Earthquake Engineering*, vol. 4, pp. 195-208, 2004.

[181] S. A. Freeman, "The Capacity Spectrum Method as a Tool for Seismic Design," presented at 11th European Conference on Earthquake Engineering, Paris, France, 1998.

[182] S. A. Freeman, "Review of the Development of the Capacity Spectrum Method," *ISET Journal of Earthquake Technology*, vol. 41, pp. 1-13, 2004.

[183] A. K. Chopra and R. K. Goel, "Capacity-Demand-Diagram Methods Based on Inelastic Design Spectrum," *Earthquake Spectra*, vol. 15, pp. 637-656, 1999.

[184] L. Schleiffarth, "Survey of Global Container Crane Sizes," Georgia Institute of Technology, 2008.

[185] SAC Joint Venture Project, "Suites of Earthquake Ground Motions for Analysis of Steel Moment Frame Structures," in *http://nisee.berkeley.edu/data/strong_motion/sacsteel/ground_motions.html*. Pasadena, CA: Woodward-Clyde Federal Services, 1997. [accessed March 2010]